MECHANICAL AND BIOLOGICAL EVALUATIONS OF SMART ANTIBACTERIAL NANOSTRUCTURED TI-6AL-7NB IMPLANT

ALIREZA RAFIEERAD

THESIS SUBMITTED IN FULFILLMENT OF THE REQUIREMENTS FOR THE DEGREE OF DOCTOR OF PHILOSOPHY

FACULTY OF ENGINEERING
UNIVERSITY OF MALAYA
KUALA LUMPUR

2017

UNIVERSITY OF MALAYA

ORIGINAL LITERARY WORK DECLARATION

Name of Candidate: ALIREZA RAFIEERAD

Matric No: KHA140101

Name of Degree: Doctor of Philosophy

Title of Project Paper/Research Report/Dissertation/Thesis ("this Work"):

"MECHANICAL AND BIOLOGICAL EVALUATIONS OF SMART ANTIBACTERIAL NANOSTRUCTURED TI-6AL-7NB IMPLANT"

Field of Study:

Engineering Design/Mechanics and Metal works (Smart orthopedic and dental implant with enhanced mechanical, corrosion, antibacterial and biological properties)

I do solemnly and sincerely declare that:

(1) I am the sole author/writer of this Work;
(2) This Work is original;
(3) Any use of any work in which copyright exists was done by way of fair dealing and for permitted purposes and any excerpt or extract from, or reference to or reproduction of any copyright work has been disclosed expressly and sufficiently and the title of the Work and its authorship have been acknowledged in this Work;
(4) I do not have any actual knowledge nor do I ought reasonably to know that the making of this work constitutes an infringement of any copyright work;
(5) I hereby assign all and every rights in the copyright to this Work to the University of Malaya ("UM"), who henceforth shall be owner of the copyright in this Work and that any reproduction or use in any form or by any means whatsoever is prohibited without the written consent of UM having been first had and obtained;
(6) I am fully aware that if in the course of making this Work I have infringed any copyright whether intentionally or otherwise, I may be subject to legal action or any other action as may be determined by UM.

Candidate's Signature Date:

Subscribed and solemnly declared before,

Witness's Signature Date:

Name:

Designation:

ABSTRACT

Increased demands of artificial bone let the severe plastic deformation (SPD)-processed titanium bioalloys to be widely used as orthopedic and dental implants due to appropriate mechanical, tribocorrosion and biological properties. Based on the literature available on laboratory and animal studies, the related β-type substrates can provide higher bone functionality with some economic limitations. In this study, biomedical grade of near β Ti-6Al-7Nb alloy (Ti67IMP) was selected as implant substrate. Nevertheless, these metallic prosthesis still cannot meet all requirements and surface modifications that are required to promote the biofunctionality and minimize failure risk. Hence, multilayer metallic/ceramics/carbon-based topographies were developed to improve Ti67IMP performance. Application of Taguchi design of experiments (DOE) and multi-objective particle swarm optimization employed to maximize the coating outputs. Highly ordered mixed oxides TiO_2-Nb_2O_5-Al_2O_3 nanotubes anodically grown on as-deposited physical vapor deposition (PVD) niobium (Nb)/Ti67IMP surface. Synthesized few-layered graphene oxide (GO), concentrations of silver nanoparticles decorated GO (AgNPs-GO) and thermally exfoliated mono-layer graphene (TGr) functionalized arginine amino acid (Arg-Gr) transparently spin-coated tubular film. Microstructural features of layer-by-layer have been analyzed by physicochemical characterizations. The mechanical, corrosion, wettability and *in-vitro* bioactivity properties of designed surfaces were assessed as well antibacterial activity against cultured Gram-negative bacteria e.g. Escherichia coli (*E. coli*) and Gram-positive e.g. Staphylococcus aureus (*S. aureus*). Moreover, biocompatibility interaction of seeded human osteoblast (hFOB) cells checked after 1, 3, 5 and 7 day bioassay proliferation. Quantitative and quantitative cytotoxicity, cell growth, adhesion and morphology followed to determine the bone implant feasibility of biostructures. From the results, thick bone-like apatite layers successfully formed on treated Ti67IMP surfaces. The poor antibacterial ability of GO martial limited its

application. Besides, the distributed non-degradable AgNPs increased the toxicity trend affected by concentration within culture time. The competitive bactericidal ability of non-expensive organic large-area Arg-Gr biomorphology in compare with risky AgNPs was highlighted. Superior mechanical stability of single-layer TGr attached functional groups rather than defected GO increase hardness and corrosion resistance of bare Ti67IMP from 1.795 to 5.345 GPa and 7.719×10^{-1} to 3.743×10^{-7} mm $year^{-1}$ respectively. In a nutshell, the reasonable introducing of smart bioactive antibacterial Arg-Gr/mixed oxides/Nb/Ti67IMP composite-implant system with enhanced characteristics and drug delivery potential may contribute to facilitate rapid osseointegration and long-term replacement without infection signs.

ABSTRAK

Permintaan yang tinggi pada tulang tiruan menyebabkan bio-bahan seperti titanium diubah suai menggunakan proses *severe plastic deformation (SPD)* dan digunakan secara meluas dalam peralatan ortopaedik dan pergigian. Hal ini demikian kerana, sifat bahan titanium seperti mekanikal, kakisan serta biokompatibilitas amat bersuaian dengan aplikasi yang disebutkan tadi. Berdasarkan kajian yang dibuat di makmal dan pada haiwan, substrat jenis **β** memberikan fungsi tulang yang lebih tinggi tetapi dengan batasan ekonomi. Dalam kajian ini, gred biomedikal aloi Ti-6Al-7Nb (Ti67IMP) iaitu aloi substrat jenis **β** telah dipilih sebagai substrat implan. Walaubagaimanapun, logam ini masih tidak dapat memenuhi semua keperluan dan pengubahsuaian permukaan yang diperlukan untuk meningkatkan biofungsionaliti dan meminimumkan risiko kegagalan. Oleh itu, topografi pelbagai lapisan logam / seramik / topografi berasaskan karbon telah dibangunkan bagi meningkatkan performa Ti67IMP. Di dalam kajian ini, teknik *Taguchi (DoE)* telah digunakan dalam merangka eksperimen manakala pengoptimuman penganjur zarah pelbagai objektif yang digunakan untuk memaksimumkan output salutan. Oksida bercampur TiO_2-Nb_2O_5-Al_2O_3 nanotiub telah ditanam di atas lapisan (Nb)/Ti671MP yang sebelumnya dihasilkan oleh teknik PVD. Di dalam kajian ini, kami telah menghasilkan beberapa lapisan Graphene oxide (GO), silver nanopartikel yang menghiasi GO (AgNPs-GO) dan mono-lapisan termal terkelupas *graphene (TGr)* berfungsi arginine amino acid (Arg-Gr) filem berbentuk tiub. Ciri-ciri mikrostruktur lapisan demi lapisan ini telah dianalisis oleh ciri-ciri fizikokimia. Keadaan mekanikal, kakisan, pembasahan, sifat-sifat bioaktiviti in-vitro permukaan juga dinilai. Manakala, aktiviti antibakteria terhadap bakteria Gram-negatif seperti *Escherichia coli (E. coli)* dan Gram-positif *Staphylococcus aureus (S. aureus)* telah dikaji. Selain itu, interaksi biokompatibilitas sel osteoblas (hFOB) manusia diperiksa selepas proliferasi bioassay iaitu pada 1, 3, 5 dan 7 hari. Sitotoksik, pertumbuhan sel, tahap kelekatan dan morfologi diikuti dengan keupayaan

biostruktur tulang implant telah dijalankan. Selepas ujikaji, kami mendapati, lapisan tebal apatit menyerupai tulang telah berjaya dihasilkan di atas permukaan Ti671MP yang dirawat. Walaubagaimanapun, keupayaan antibakteria yang lemah dari GO telah membatasi aplikasi penggunaan GO. Selain itu, tahap kecenderungan keracunan AgNPs dipengaruhi oleh faktor kepekatan. Keupayaan bakteria bagi bio-morfologi Arg-Gr berbanding dengan AgNPs telah diketengahkan dalam kajian ini. Kestabilan mekanikal satu lapisan TGr daripada meningkatkan lagi nilai kekerasan Ti 67IMP iaitu daripada 1.795 hingga 5.345 GPa bagi nilai dan nilai tahap rintangan hakisan iaitu dari 7.719×10^{-1} to 3.743×10^{-7} mm tahun-1. Kesimpulannya, Pengenalan bio-anti-bakteria Arg-Gr/ campuran oksida/ Nb/Ti67 komposit-implan sistem yang komprehensif dengan ciri-ciri yang lebih baik boleh menyumbang kepada osseointegrasi dan penggantian implant pada jangka masa yang panjang dan bebas daripada jangkitan.

ACKNOWLEDGMENTS

First and foremost, I would like to thank God Almighty for giving us the health and knowledge. I have great pleasure in acknowledging my gratitude to my supervisors *Associate Prof. Dr. Bushroa Binti Abd Razak*, Faculty of Engineering and *Prof. Dr. Jamuna Vadivelu*, Faculty of Medicine for their invaluable guidance and great support throughout my graduate study. Moreover, would like to appreciate *Prof. Dr. Mohd Hamdi Abd Shukor* for his support to this project.

I want to acknowledge University of Malaya and UCLA also thanks my friends for their useful suggestions.

Finally, great thanks and gratitude to my family especially my dear parent for their always support and encouragement in spite of the long distances between us.

TABLE OF CONTENTS

LIST OF FIGURES

LIST OF TABLES

LIST OF SYMBOLS AND ABBREVIATIONS

NH_4F	Ammonium fluoride
Arg-Gr	Arginine functionalized Graphene
AuNPs	Gold nanoparticles
HfO_2	Hafnium(IV) oxide
HCl	Hydrochloric acid
HA	Hydroxyapatite
Lys	Lysine
DMF	N,N-Dimethylformamide
O_SO_4	Osmium tetroxide
H_3PO_4	Phosphoric acid
Ag_2O	Silver oxide
$H2_SO_4$	Sulfuric acid
TaO	Tantalum oxide
Ta_2O_5	Tantalum pentoxide
TiO_2-Nb_2O_5-Al_2O_3	Titania-niobia-alumina
Ti67IMP	Ti-6Al-7Nb alloy
TGr	Thermally exfoliated graphene
WS_2	Tungsten disulfide
WO_3	Tungsten trioxide
E	Young's modulus
ZrO_2	Zirconia (Zirconium oxide)
ALP	Alkaline phosphates
ANOVA	Analysis of variance
AI	Artificial intelligence

β-TCP	Beta tricalcium phosphate
C/P	Calcium phosphate
CNT	Carbon nanotube
CVD	Chemical vapor deposition
COF	Coefficient of friction
CP Ti	Commercially pure titanium
CA	Contact angle
CPD	Critical drying process
DI	Deionized water
DOE	Design of experiment
DC	Direct current
ddH_2O	Double distilled water
DRIs	Drug-releasing implants
EPD	Electrophoretic deposition
EDS	Energy-dispersive X-ray spectroscopy
EG	Ethylene glycol
FESEM	Field emission scanning electron microscopy
FHA	Fluorohydroxyapatite
FT-IR	Fourier transform infrared spectroscopy
GEP	Gene expression programing
GPa	Gigapascal
AuNPs	Gold nanoparticles
GO	Graphene oxide
HV	Hardness Vickers
hFOB	Human fetal osteoblastic cell
iPSC	Induced pluripotent stem cell

JCPDS	Joint committee on powder diffraction and standards
LST	Laser spallation technique
LDDS	localized drug delivery system
MTT	Methyl thiazole tetrazolium
MOPSO	Multi-objective particle swarm optimization
MWCNT	Multiwall carbon nanotube
OD	Optical density
PSO	Particle swarm optimization
PBS	Phosphate-buffered saline
PVDMS	Physical vapor deposition magnetron sputtering
PEO	Plasma electrolytic oxidation
PLA	Polylactic acid
RF	Radio frequency
rGO	Reduced graphene oxide
SOP	Safety Operating Procedure
SPD	Severe plastic deformation
SWCNT	Single wall carbon nanotube
SBF	Simulated body fluid
SD	Standard deviation
TEM	Transmission Electron Microscopy
XRD	X-ray diffraction
XPS	X-ray photoelectron spectroscopy

LIST OF APPENDICES

CHAPTER 1: INTRODUCTION

1.1 Background of Study

Musculoskeletal disorders have become a widespread human health problem due to societal development, improved living conditions and focusing on rehabilitation. To this end, appropriate biomaterials play a vital role to facilitate rapid osseointegration, healing process and successful long-term replacement. Recently, with increased aged population, number of patients which are living with artificial organs has dramatically raised from 4.9 million in 2002 to 39.7 million cases in 2010 as estimated. In 2011, more than 600,000 number of knee-replacement surgery were performed in United States of America, which this trend has been progressed until now and expect toward promoting in the future (Geetha, Singh, Asokamani, & Gogia, 2009; Leskinen, Eskelinen, Huhtala, Paavolainen, & Remes, 2012). From Global Information report, orthopedic device markets as major biomaterial-providing regions, generated approximately $115 billion in 2008 and predict, which this amount increased to around $252 billion in 2014. The finding indicates the 20 % demand increment for diverse orthopedic biomaterials per year (Boland, Espy, & Bowlin, 2004; Moussy, 2010; L.-N. Wang et al., 2014). Due to rehabilitation importance, the quality of bone tissue materials are required to improve for orthopedic and dental applications. Towards advances in bone graft materials, suited features were addressed interfering successful surgery with minimum failure risk.

The human skeletal system is composed of a diverse hierarchical architecture of various tissues and cellular components. In case of severe injuries to the skeletal system, bone grafts are required to repair damage. Generally, in body organism, bone is able to completely regenerate though, requires small fracture space or any sort of assisted scaffold materials. Among bone repair process, natural materials such allografts, xenografts and mostly autografts, are preferred which harvested from a different body part of a patient. Autografts, regarded as one of the safest patterns because these materials

pose low risk of disease transmission due to containing high amount of a patient's bone-growing cells and proteins. However, autografts are limited by insufficient available tissues, additional costs, and intensive surgical procedures. Advances in biomaterials and nanotechnology provide potential stable structures to rehabilitate the bone defects. This functions should exhibit biocompatibility and mimic natural bone properties to match with a damaged tissue by providing stable bonding between artificial tissues and natural bone. According to *in-vivo* responses, bone biomaterials categorized to: (I) bioinert structures that do not exhibit interaction between implants and bone; (II) bioactive structures that interact chemically with bone after these materials are implanted for a particular range of time; and (III) bioresorbable materials that are gradually resorbed and completely replaced with new bone ingrowths (Carta, Pickup, Knowles, Smith, & Newport, 2005; Yelten, Yilmaz, & Oktar, 2012). Generally, mechanical stability, corrosion, antibacterial and biocompatibility properties are corresponded as main implant requirements. The considered biofunctionality resulted to avoid weakening, allergic immune reactions and release of toxic ions from the implant surface into physiological media. This bone materials also are required to provide the possibility of machining process to form in the complex geometrical targets (Black, 2005). Various metals, ceramics, polymers, carbon-based and composite structures incorporated to adapt as artificial tissues (Domb & Kumar, 2011; El-Meliegy & van Noort, 2011; Höland et al., 2006; Ratner, Hoffman, Schoen, & Lemons, 2004; Wong & Bronzino, 2007). Among this martials, biometallic substrates have been widely used for bone implant fixation since exceed 100 years ago (Lane, 1895).

Based on clinical reports, metallic devices shown more reasonable satisfactions of implant materials within existing choices. Therefore, clinical grades of stainless steels (Rodríguez-González, 2009; Winters & Nutt, 2003), cobalt-chrome alloys (Disegi, Kennedy, & Pilliar, 1999), magnesium (Staiger, Pietak, Huadmai, & Dias, 2006),

tantalum (Zardiackas, Kraay, & Freese, 2006) and titanium alloys (Brunette, 2001; Geetha et al., 2009; Oshida, 2007) were generated. The development of titanium and its alloys perfectly reflect the alternative materials with better biofunctionality. Pure titanium provide safe performance rather than stainless steels and Co-Cr alloys with of harmful composition such nickel or chrome. In contrary, mechanical properties of pure Ti is limited remarkably in hard tissue replacements or under intensive wear use. Such strengths restrictions were somewhat modified by α + β-type alloys such Ti-6Al-4V (Ti64). However, Ti64 alloy is composed of toxic vanadium element. To overcome the limitations, V-free near-β bioalloys such Ti-6Al-7Nb (Ti67IMP) manufactured with good biomedical satisfaction. Recently, low modulus β-type products such Ti-Nb-Ta-Zr alloys were generated with more closed properties to bone. Nevertheless, application of this class of materials is to some extent limited with economic constrains. The Young's modulus (E) characteristics superiority of Ti67IMP lead to higher bone attachment (Textor, Sittig, Frauchiger, Tosatti, & Brunette, 2001). Durability of potential metallic devices still is required to enhance bone degradation. Figure 1.1 illustrates the elastic modulus information of common materials used in bone tissue engineering.

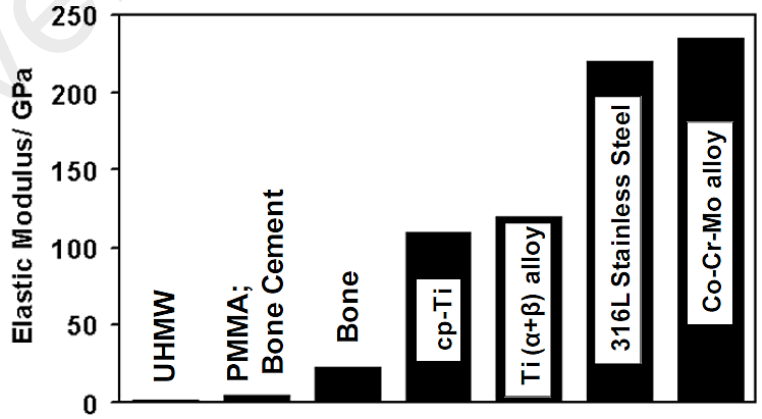

Figure 1.1: Elastic modulus of some widely used orthopedic and dental biomaterials (Niinomi, Hattori, & Niwa, 2004).

Following table presents a comparison between the related properties of Ti with the metallic bone-like material counterparts.

Table 1.1: Property comparison of three major metallic bone materials (Nouri, Hodgson, & Wen, 2010)

Characteristics	Stainless Steel	Cobalt-Chromium	Titanium
Stiffness	High	Medium	Low
Strength	Medium	Medium	High
Corrosion resistance	Low	Medium	High
Biocompatibility	Low	Medium	High

With progress in materials, functional structures proposed to enhance the implant properties trough multilayer thin film and composite structures. Surface modification have been directed to improve bone performance using physico-chemical coating treatments such magnetron sputtered biofilms and 1D anodic nanoconfigurations. Concerned with principles of applied parameters in microstructural and mechanical characteristics, robust design of experiment and optimization algorithms were largely employed to optimize of coating conditions. In addition, corporation of various carbon-based nanomaterials can raise the performance. Attachment of antibacterial agents to implant component effectively protect bone tissues interfacing against both Gram-positive and Gram-negative bacteria. Noted to smart function of nanomaterials in medicine, the high-balanced interest referred to graphene (G), its deviations such graphene oxide (GO) and functionalized topographies largely investigated in biomedical approaches (Parcharoen, Termsuksawad, & Sirivisoot, 2014; Tanurat & Sirivisoot, 2015b; Yan et al., 2015). Moreover, attachment of silver nanoparticle (AgNPs) with carbon-based nanomaterials obtained bactericidal and anticancer conditions (Setyawati, Yuan, Xie, & Leong, 2014; Shi et al., 2016; Yallappa et al., 2016). Whether, based on background of *vivo* experiments, the releasing of Ag^{+} ions in cell's membrane lead to appear cytotoxicity effects, incites immunological and disrupts cell growth activity (De Jong et al., 2013; Qin et al., 2014; Zadorozhnyy et al., 2016). Current limitation has been somewhat decreased with lower toxicity thought chemical reactions of converting Ag^{+} ions into lower particle size and rich nanostructured Ag^{0} phase, but the consequence may not completely stop to inflict cell damage (M. V. Park et al., 2011; Setyawati et al., 2014).

To possess appropriate biological and immune responses including both reasonable biocompatibility and antibacterial ability, carbon-based structures reinforced with additive bioactive hybrid or composite interactions (Cha, Choi, Jang, Choe, & Choi, 2016; G. Shim, Kim, Park, & Oh, 2016; Upadhyay, Naskar, Bhaskar, Bose, & Basu, 2016; Xie, Zhang, Han, & Li, 2016). Hence, implant bone graft with smart nanoengineered surface can facilitate the safe tissue implantation with long-term desired operation. Figure 1.2 demonstrates metallic bone implants and fixation accessories.

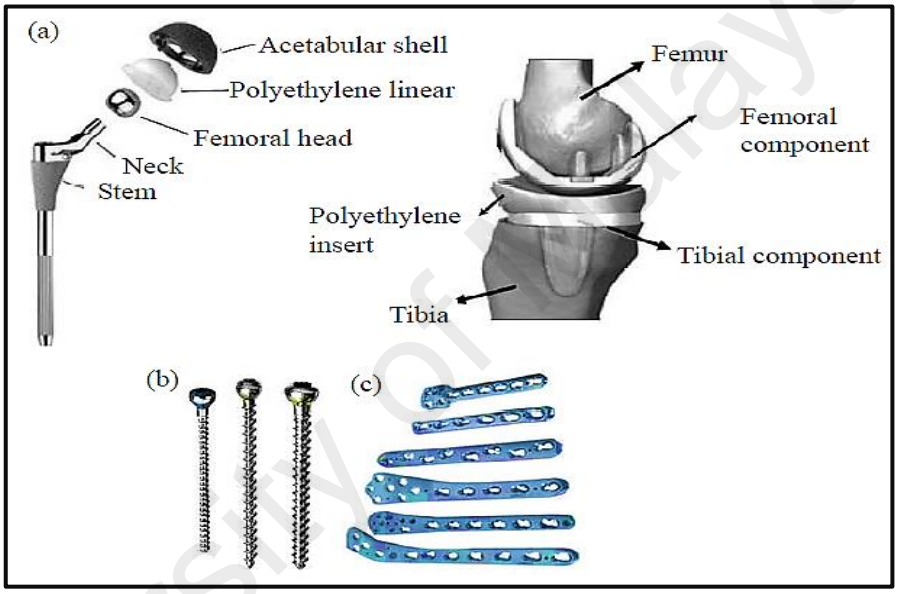

Figure 1.2: Some applications of Ti implants: hip and knee replacements screws and plates (Izman et al., 2012).

1.2 Motivation and Aim of Study

Bone injuries aggravated by malformations, disease, developmental deformity, trauma, or adverse effects from medical treatments have increased the demand of improved bone implant materials (L. L. Hench & Polak, 2002). Affected bones are repaired using surgical techniques with autogenous grafts, internal/external fixation devices, electrical stimuli, and implantable replacement. Recent progress, introduced the application of various biomaterials for bone-like tissue replacements. Among them, biometallic devises can provide more favorable implant characteristics. Industrial

production with refining coarse-grained metals through severe plastic deformation (SPD) techniques such rolling mostly employed to process high-density metallic substrates as a pillar indications of insufficient thickness for orthopedics, orthodontia and alveolar usage. From clinical studies, functionally graded Ti67IMP was corresponded high fracture toughness, low strength-to-weight ratio, controlled corrosion and biocompatibility. Whereas, properties improvement still requires to achieve stable implant materials with appropriate sequences. So, it would be very exciting to propose not-yet-designed applicable products that can impact on physical and psychological elements of patient's health. Appropriate bone-like tissues with nanopatterned texture are supposed to be fully enhance targeted biofunctionality.

The aim of this study is to introduce the multilayer thin biofilms incorporated smart antibacterial nanocomposite-Ti67 implant system which may promote the clinical setting with drug delivery potential.

1.3 Objectives and Scope of Study

In this project, overall improvement of mechano-biological Ti67IMP properties was pointed with commercialization view. Following with the two-side biocompatibility of AgNPs-GO materials with probable unbalanced toxicity effect of designed implant, hFOB cell culture assay assisted to determine the cytotoxicity features. In addition, implant possibility of novel hybrid Arg-Gr structure anchored tubular topography checked to determine the optimum solution for Ti67IMP reinforcement. With the matter of positively charged and electrostatic adsorption of functionalized amino acid materials, inhibition zone measurements against both-type bacteria executed to confirm mediation of generated layer-by-layer morphology as well as cell performance and mechanical stability. Application of designed smart composites can consider as programing location for drug delivery attachment. The main objectives are listed as follow:

1. To fabricate optimized crystalline mixed oxide TiO_2-Nb_2O_5-Al_2O_3 nanotubes on Taguchi-MOPSO treated Nb/Ti67IMP surface.
2. To evaluate the mechanical, wettability, corrosion, *in-vitro* bioactivity, antibacterial and biological cell properties of different concentrations AgNPs-GO/mixed oxides/Nb/Ti67IMP.
3. To synthesize large-area single-layer graphene sheets functionalized Arg amino acid.
4. To design novel smart antibacterial multilayer Arg-Gr/mixed nanotubes/Nb/Ti67 biocomposite-implant system.
5. To confirm the enhanced bone functionality of Ti67IMP.

The scope of this study is to develop multilayer metallic/ceramics/carbon-based biomaterials to improve the biofunctionality of Ti67IMP alloy. The biocompatibility and antibacterial performance of functionalized organic Arg-Gr were compared with GO and two different concretions of AgNPs-GO topographies. These biomaterials have been chosen due to their comprehensive applications in improving bone implant materials.

1.4 Organization of This Thesis

This thesis is presented within five chapters as follow:

Chapter One highlights the background of study and the existing problems in research area, which served as the motivation of project. This chapter also pointed the existing gap, novelty and the main objectives of project.

Chapter Two includes literature review section on fabrication methods, feasibility of related nanostructured and composites biomaterials with over view on emphasized bone-implant properties.

Chapter Three describes the applied materials, methodology and experimental procedures in this project. The details of mathematical modeling, optimization, coating, synthesis, mechanical, corrosion, bioactivity, cytotoxicity bioassay, hFOB morphology and antibacterial characterization protocols were explained accordingly.

Chapter Four analyze the step-by-step obtained results and discussions in comparable mode. The achieved comprehensive improvement of Ti67IPM performance were completely discussed in this chapter.

Chapter Five gathers overall summary of conclusions, project finding and recommendations for future works. The originality aspects of project is also summarized in the current chapter.

CHAPTER 2: LITERATURE REVIEW

2.1 Overview of Biomaterials

Generally, biomaterials are mostly categorized into bioactive metals, 1D ceramics, polymers and 2D carbon-based and composites. In recent years, the ultrafine-grain and nanopatterned biostructures have been attracted for prosthetic devises due to their peculiar and fascinating properties compared with coarse-sized conventional materials. Among the artificial bone choices, metallic implants have been taken into consideration to replace disordered orthopedic tissues where the medical prosperity is subjected. Hence, it is directly relevant to the primitive structural and functional connection between living bone and the surface of a load-bearing artificial implant (osseointegration) which itself affected by surface features. Potential biometallic Ti67IMP substrate will not create adheres tissue tolerance reactions, shows high compatibility to be ingrowth to human body and creates fewer giant cell nucleus. This materials contribute in bony functions corresponding to their appropriate biocompatibility, mechanical and corrosion performance with young modulus of 90-100 GPa (Y. Li et al., 2014; Oldani, Dominguez, & Eli, 2012). Nonetheless, many studies have reported that elastic modulus of α-type and some α + β Ti-based alloys (near to α-type) such Ti64 is much higher than natural bone, which can cause stress shielding effect. Hence, β and near β-type low modulus Ti-based alloys such Ti-35Nb-7Zr-5Ta and Ti-13Nb-13Zr respectively have been developed with elastic modulus clos to bone (48-55 GPa) compared with conventional Ti64 alloy (around 114 GPa), which can provide enhanced performance with concern in product pricing (Y. Li et al., 2014). Table 2.1 and 2.2 categorized different Ti alloys also mechanical property of natural bone as well as elastic modulus.

Table 2.1: Some developed Ti alloys for biomedical applications (Niinomi et al., 2004).

Composition	Type
Pure Ti	α
Ti-6Al-4V ELI (ASTM F136084, F620-87)	$\alpha+\beta$
Ti-6Al-4V (ASTM F1108-88)	$\alpha+\beta$
Ti-6Al-7Nb	$\alpha+\beta$
Ti-5Al-2.5Fe	$\alpha+\beta$
Ti-5Al-3Mo-4Zr	$\alpha+\beta$
Ti-15Sn-4Nb-2Ta-0.2Pd	$\alpha+\beta$
Ti-15Zr-4Nb-2Ta-0.2Pd	$\alpha+\beta$
Ti-13Nb-13Zr	near β (low modulus)
Ti-12Mo-6Zr-2Fe	β (low modulus)
Ti-15Mo	β (low modulus)
Ti-16Nb-10Hf	β (low modulus)
Ti-15Mo-5Zr-3Al	β (low modulus)
Ti-15Mo-2.8Nb-0.2Si-0.26O	β (low modulus)
Ti-35Nb-7Zr-5Ta	β (low modulus)
Ti-29Nb-13Ta-4.6Zr	β (low modulus)
Ti-40Ta, Ti-50Ta	β (high corrosion resistance)

Table 2.2: Compressive properties of human cortical bone, N being the number of bones tested and n, the number of machined specimens obtained from them (Niinomi et al., 2004).

Tissue Source	Age	N	n	Ultimate Strength (MPa)	Elastic modulus (GPa)	Hardness (MPa)
Tibia osteons (longitudinal)	57/61	2	2	–	22.5	614
Tibial interstitial Lamellae (longitudinal)	57/61	2	2	–	25.8	736
Femur	20-89	19	95	194	17.6	–
Tibia	30–89	11	38	195	28.0	–

Bioceramics are maily classified to bioactive, bioinert and biodegradable structures (Bakheet, 2016; L. L. Hench & Wilson, 1993; Popat, Leoni, Grimes, & Desai, 2007). Bioactive and somehow bioinert ceramics can provide stable phases with no significant chemical change or degradation in long interaction with natural bone (Bakheet, 2016). Whereas, metal oxides can provide higher mechanical stability compared with than TCP patterned ceramics with optimum resorption rate. Biopolymer which can be formed through linking a variety of elements in chemical reactions are also

utilized for biodegradable functionality. The organic polymers such polyethylene (PE) and polylactic acid (PLA) are mainly composed with corporation of a cored monomer molecule and carbon attachments at central atomic spaces. For orthopedic and endosseous implants, the biopolymer-derived structures with moderate mechanical performance are used to satisfy antibacterial approaches (Evans, Irvin, Safranski, & Gall, 2016; Jun Liu et al., 2016). To meet higher cellular capability of implant, hybrid polymer-carbon based structures improved metallic substrates (Biasetto, Elsayed, Bonollo, & Colombo, 2016; Upadhyay et al., 2016). Based on the recent literature on artificial bone materials, bioactive ceramics have been mostly highlighted as stable patterns for bone tissue regeneration. The interaction of bioceramics with smart carbon-based nanostructures contributed to promote implant requirements (Tanurat & Sirivisoot, 2015a).

2.2 Surface Modification of Ti-based Implants

To date, various coating treatments were employed to improve the performance of bone-like materials (Lacefield, 1998). The considered modifications have been mostly obtained by application of physical vapor deposition magnetron sputtering (PVDMS), electrochemical anodization, electrophoretic deposition (EPD), plasma electrolyte oxidation (PEO), electrochemical deposition, sol-gel, chemical vapor deposition (CVD), hydrothermal, spin coating and biomimetic precipitation. Notably, the surface properties and chemistry of implant materials can largely effect on their biological and antibacterial behavior. For this, several treatments studied to modify interaction between bone and implantable tissues (Mazaheri, Eslahi, Ordikhani, Tamjid, & Simchi, 2015). Development of the unique bioactive materials with controlled morphology contributed to accelerate bone integration and rapid healing process (Shalabi, Gortemaker, Van't Hof, Jansen, & Creugers, 2006). With progress in nanotechnology, bone implants benefit improved condition of nanostructured surfaces (L. Zhang & Webster, 2009). Looking to background, coated biofilms have been widely utilized to raise functionality of Ti-based

bone prosthesis (W.-C. Chen et al., 2014; Ciganovic et al., 2012; Jimbo et al., 2012; Kirmanidou et al., 2016; Le Guéhennec, Soueidan, Layrolle, & Amouriq, 2007; L. Zhao, Chu, Zhang, & Wu, 2009). Though, the coating treatments contain some limitations and are required to be adjusted for appropriate performance (Maleki-Ghaleh, Khalil-Allafi, Aghaie, & Siadati, 2015). The related constrains include the residual stresses generation between the substrates and thin films, coating interfaces, micro cracks formation, inconsistency in coated surfaces, the layered configuration, economic aspects and poor mechanical properties. Amid proposed coating techniques, magnetron sputtering processes are well suited to deposit both types of metallic and ceramic films with controllable thickness (E. Marin et al., 2016). Due to this, the conventional attitudes have been generally utilized to achieve adequate adhesion strength between coatings, interfaces and the substrates (Yu, Wang, Cheng, & Zhang, 2008). Contrary with sputtering benefits, these processes are required such trial and error experimentations to find coating parameters, which are very time-consuming and costly. Considering the complex conditions of sputtering process with nonlinear relations, estimating the accurate output values is not possible without progressing the large quantities of run. Development an efficient method to model, predict and optimize the coating outputs has been recently concerned. In fact, using a reliable and behavioral model to estimate the reasonable design of experiment (DOE) of PVDMS parameters would result in the optimum condition of as-sputtered films with minimum number of experiments.

Nowadays, artificial intelligent (AI) techniques such as Fuzzy Inference System (FIS) (Jaya, Hashim, & Rahman, 2010; Khorasani, Faraji, & Kootsookos, 2012), Artificial Neural Network (ANN) (Danaher, Dudziak, Datta, Hasan, & Leung, 2013; Dobrzański, Staszuk, & Honysz, 2010; Kwaśny, Sitek, & Dobrzański, 2007), and etc., have been applied for modeling of coating processes as behavioral machine learning methods. Although the previous studies have been reported that the applied AI-based

models have high accuracy in prediction, however, they are suffered with black box tools, which, are unable to provide an explicit mathematical model based on the independent variables. Since, coating treatments are mostly associated with complex equipment, providing the highest possible results in the shortest time is objective. It is well understood that obtaining the reasonable outputs of coating through complicated series of test is not perused. Hence, application of such efficient, fast and robust methods to optimize the dependent variables of coating is inevitable. Taguchi method suggests appropriate design of experiments based on process inputs and statistical analysis which results to find the normal range of outputs. However, this method is not able to provide the mathematical predictive model and optimal value(s). Therefore, proposing an accurate multi-objective optimization algorithm can be very useful in solving engineering problems. Application of metaheuristic optimization approaches was extensively studied for different processes (Sadollah & Bahreininejad, 2011).

Based on current literature, various approaches such as Taguchi method (Verma, Kant, & Suri, 2016), the grey-fuzzy Taguchi (Songsorn, Sriprateep, & Rittidech, 2016), genetic algorithms (Böke, Giner, Keller, Grundmeier, & Fischer, 2016), grey relational analysis (Guo, Zhang, Wang, & Hu, 2016), and expert systems (Kramar, Cica, Sredanovic, & Kopac, 2016) were employed to find the optimum conditions. Due to the high possibility of AI-based methods in engineering process, several studies focused to fuzzy inference system (FIS) (Zalnezhad, Sarhan, & Hamdi, 2013), artificial neural network (ANN) (Danaher et al., 2013), adaptive neuro-fuzzy inference systems (ANFIS) (Datta, Pratihar, & Bandyopadhyay, 2013) and support vector machine (SVM) (Barletta, Gisario, Palagi, & Silvestri, 2014). Even though, the above mentioned approaches do not provide accurate predictable models and generate an explicit mathematical models. This problem has been solved by application of gene expression programing (GEP) method with offer mathematical formulations of independent variables (Mollahasani, Alavi, &

Gandomi, 2011). However, the major difficulties for applying GEP-based approaches still remained with too many control parameters and quite sensitivity to initial values. Therefore, inherent complexity of controlling parameters in GEP method is involved a non-negligible increase of efforts for tuning the control parameters properly. Recently, applying PSO algorithm has been noticed in various branches of engineering to optimize problems that are irregular, noisy and changing over time (dos Santos Coelho, 2010). To settle this issue, an evolutionary algorithm (EA) like PSO as a robust optimization method with few control parameters were applied on predefined quadratic mathematical model to formulate of output properties, followed by experiments. Recently, applying multi-objective swarm particle optimization (MOPSO) as an accurate and robust method has been noticed in various branches of engineering to optimize problems that are irregular, noisy and changing over time (dos Santos Coelho, 2010; Khorasani, Asadnia, & Saadatkia, 2013).

Many studies have been also conducted on the preparation of nanostructured polycrystalline bioceramics such as rod, wire and tube morphologies that are in principle tunable by varying the diameter and chirality. The reasonable mechanical resistance and biocompatibility aspect are expected for bone-like materials under physiological conditions. Nanopatterned biostructures provided remarkable benefit of cell viability coordination and control bacterial proliferation affects by increased specific area (Bhardwaj & Webster, 2017; Justin et al., 2017; A. Tan, Pingguan-Murphy, Ahmad, & Akbar, 2012; A. W. Tan et al., 2016). Bioceramics firstly were introduced to implant market in form of thin film coatings on metallic substrates to achieve longer usability and rapid osseointegration. Thus, electrochemical anodization gives rise to a thin hybrid layer able to improve the implant surface features (Alsawat, Altalhi, Gulati, Santos, & Losic, 2015). Without restraint, clinical Ti-based alloys have received more consideration and exhibit a desirable alternative classification model to create more effectual implantable

devices. Highly-ordered TiO_2 nanotubular array could be promptly developed on Ti-based implants to fulfill the obligation for medical approaches (J. Li et al., 2016). In addition, the electrochemical self-assembly method could be applied for a wide range of biometallic materials such as Ti, Nb, Al, Ta, Ag, zirconium (Zr), hafnium (Hf), tungsten (W) and their alloys. They are capable of forming self-ordered nanostructured metal oxide coatings for clinical targets. Despite the applicability of PVDMS and electrochemical anodization to design multilayer nanoconfigurations, few studies have empirically examined the potential impacts of the combined approach on the development of mixed oxide nanotubes on metallic implants (Ghicov, Aldabergenova, Tsuchyia, & Schmuki, 2006).

Bioactive ceramics may contribute in apatite formability through absorption of Ca and P ions around the implant materials, when surrounded by bioliquid which result to enhance bone regeneration compared with metallic alloy surfaces. Besides, the formed fibrous tissues amid natural bone and bioinert and biodegradable implant provide weak bonding strength and required to be improve mechanical strength. Over the last two decades, bioactive ceramics have been extensively investigated regarding to their direct bonding with natural bone without forming fibrous tissues around bioactive implants. Meanwhile, due to the focus of advanced biomaterials towards the tissue engineering, a need to better define for specific biocompatibility interaction between developed structures and tissue components is required. Advances science in carbon-based materials has been rapidly emerged as a new discipline that employs high properties of nanoscale functions (Hu, Shenderova, Hu, Padgett, & Brenner, 2006). Therefore, attachment of carbon-based morphologies on the surface of Ti-based substrates obtained by electrochemical deposition (C. Liu, Y. Teng, et al., 2011; C. Liu, Wang, Luo, Tang, & Chen, 2011; Yan et al., 2015). Likewise, smart thin films formation and hybrid structures loaded bulk surfaces using spin-coating without conductivity effects (Becerril et al.,

2008; Prabakar, Hwang, Bae, Lee, & Pyo, 2013). This class of organic materials have been reinforced by the nanotubular bioceramics due to excellent features for biomedical functionality (Moon et al., 2013; X. Wang, Zhi, & Müllen, 2008; Zhu et al., 2010).

Development of new biocomposites by current organic materials with metallic nanoparticle such Ag was also addressed corresponded to achive excellent antibacterial mediation (B.-K. Kim, Jo, & Shim, 2012; Rangari et al., 2010; Weng, Wu, Chen, Ho, & Ding, 2010). Despite providing antibacterial property, the Ag-corporation led to increase the cytotoxicity after short period of implantation (De Jong et al., 2013). Many researches have been investigate to balance and optimize the effects of Ag in alive organs (S. Marin et al., 2015; M. V. Park et al., 2011; Qin et al., 2014; Setyawati et al., 2014). In the recent years, there is a not absolute conclusion regarding to Ag applicability in implant materials still such an unequal two-side literature was existed particularly for *in-vitro* cell culture (Johnston et al., 2010; Reidy, Haase, Luch, Dawson, & Lynch, 2013). It was reported that the optimum concentrations and chemical stability of Ag in biological systems can largely control the harmful signs (Jia et al., 2016). On the other hand, some reports clarified the related cytotoxicity in case of body surgeries (Ahamed, AlSalhi, & Siddiqui, 2010). It was reported that human mesenchymal stem cells display pre-tissue, multipotent cells found in dissimilar tissues such fat, bone marrow or muscle. Under cell culture conditions, they can be cultivated over numerous passages (Pittenger et al., 1999). Since, the related stem cells are an essential factor concerning rapid tissue regeneration and wound healing, they are in close contact to bone implant surfaces and may be exhibited to AgNPs coatings consecutively (Hackenberg et al., 2011).

2.3 Coating Techniques

There is direct relation between the surface roughness of metallic Ti-based implants and osteoblast cell adhesion amid proliferation bioassay (Dale, Hamilton,

Dunlop, Lemoine, & Byrne, 2009). Many single-layer, hybrid and composite structures can be developed on boney prosthesis with controlled thickness to enhance properties and future perspectives. In the current section, most popular methods of thin film hard coatings on biosubstrates have been reviewed.

2.3.1 Physical vapor deposition magnetron sputtering

The known PVDMS is well suited method of thin film deposition to promote gradient coatings, nanocrystalline layer materials, metastable coatings, multilayer or superlattice films, and multicomponent coatings (Holleck & Schier, 1995; E. Marin et al., 2016). PVDMS technology can deposit homogenous metallic and ceramic solid films onto the various substrates. So that, direct current (DC) and radio frequency (RF) power supply apply for conductive and insulators materials respectively. The fabricated thin films by PVDMS method result to enhance the properties of coated substrates depends on the sputtered materials (E. Marin et al., 2016). This flexible deposition technique possessed the possibility of improving the mechanical properties of coated substrate with facilities of high-purity hybrid and multi sputtered well-adhered layers with high deposition rates and coating uniformity. The PVDMS process potentially provides dense films with controllable thickness and adequate adhesion strength in case of proper parameters. This method has been widely applied in case of deposition of various films such palladium (Pd) (Checchetto, Bazzanella, Patton, & Miotello, 2004), tantalum oxide (TaO) (Rahmati et al., 2016), Nb (Fenker, Kappl, Banakh, Martin, & Pierson, 2006), Ag (W. Chen et al., 2006), Ta (Masoud Sarraf et al., 2016), Ti (Zalnezhad et al., 2016), Zr (Baradaran et al., 2014), Al (M Sarraf et al., 2014), molybdenum (Mo) (Audronis, Leyland, Kelly, & Matthews, 2008) and hydroxyapatite (HA) (Mohseni et al., 2015) for biomedical approaches.

2.3.2 Electrochemical Anodization

Do date, numerous techniques have been applied with aim of forming the nanoscale structures on the surface of Ti-based implants. In this regards, irregular morphology of biomaterials has been appeared through specific coating conditions. Two-electrode electrochemical anodization process was generated as the novel strategies to produce controlled vertically aligned nanoconfigurations (S. He et al., 2010; Kaczmarek et al., 2016; Y. J. Park, Liu, Yoo, & Park, 2012). The self-organization through pitting formation presents a versatile and convenient approach to prepare tunable 1D oxide topographies with high yield. Anodic reactions involve the oxidation of a non-noble metal in a certain electrolyte by the withdrawal of electrons at a solid/electrolyte interface. To enhance the mechano-biological properties of fabricated biomaterials, the significant study has been performed to obtain in advanced biocompatible morpholgies. Due to the oxidation potential of metals issued by self-organizing anodization incorporated the passive layers, various ceramic structures such TiO_2, Nb_2O_5, Al_2O_3, ZrO_2, Ta_2O_5, silver oxide (Ag_2O), tungsten oxide (WO_3), hafnium oxide (HfO_2) were possibility defined within growing mechanism. From the reaction, it was confirmed the pitting process originates from ordered porous oxide by a “pore-wall-splitting” operation which affected by applied voltage, time and electrolyte conditions. Based on the current literature, self-assembly in fluoride-based electrolytes has been widely reported with different pore diameters (15- <300 nm) and lengths up to 5µm (Albu, Ghicov, Macak, & Schmuki, 2007; Assefpour-Dezfuly, Vlachos, & Andrews, 1984; Baradaran et al., 2014; Beranek, Hildebrand, & Schmuki, 2003; Berger, Jakubka, & Schmuki, 2009; Mohamed & Rohani, 2009; Ng, Ye, Ng, & Amal, 2010; Roy, Berger, & Schmuki, 2011; M Sarraf et al., 2014; Wei et al., 2010; Zwilling et al., 1999). More details regarding the current electro-chemical process and effective parameters in controlling the morphologies were comprehensively reviewed for various nanoconfigurations (Roy et al., 2011). The

possibility of amorphous nanostructures, phase transformation, and effect of shifted crystallization on the wettability performance of formed biofilms were studied (W.-G. Kim, Choe, Ko, & Brantley, 2009; Macak et al., 2007; Anca Mazare, Dilea, Ionita, & Demetrescu, 2014; A Mazare et al., 2012; Minagar, Berndt, Gengenbach, & Wen, 2014; Rafieerad et al., 2015). The distribution of performed researches on considered anodic elements for biomedical applications was presented in Figure 2.1.

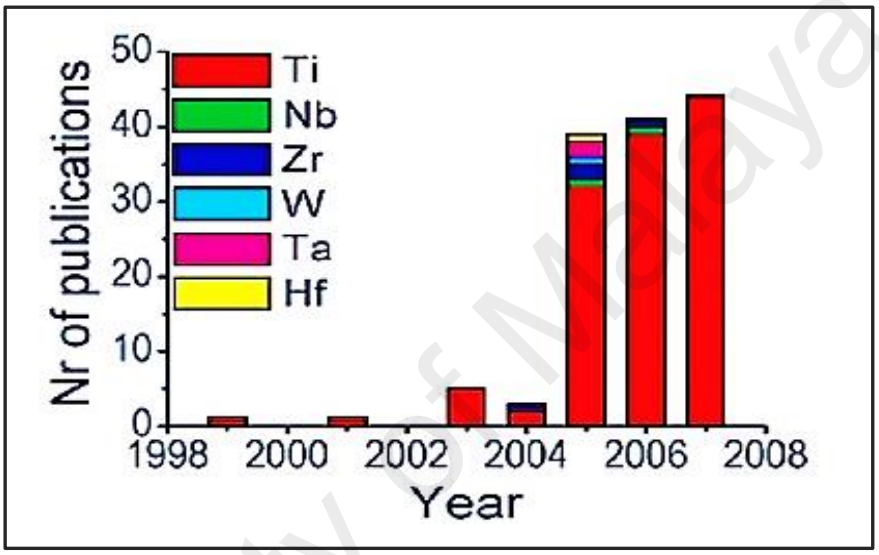

Figure 2.1: The number of articles published on valve metal oxide nanostructures via electrochemical anodization process (Ghicov & Schmuki, 2009).

2.3.3 Electrophoretic deposition (EPD)

EPD was generated as versatile economic method to deposit charged metals, ceramics, polymers, carbon-based and composite structures on bulk substrates. Whereby two-electrode EPD technique, the morphology and thickness can be altered with controlling deposition parameters such voltage, time and pH of suspension. The application of EPD for bone implant has been widely investigated due to high deposition rate, stoichiometry control, uniform 3D treatment and large-area coating (Boccaccini, Keim, Ma, Li, & Zhitomirsky, 2010). Therefore, various thickness of calcium-phosphate based materials (CaP) biofilms such HA obtained through EPD have been reported (Sridhar, Eliaz, Mudali, & Raj, 2002).Contrary with economic and uniform coating , EPD

technique is limited with poor adhesion strength even after sintering issued post-process shrinkage . The weakness was partially modified with incorporation of reinforced materials and composite structure with enhanced mechanical properties (Albayrak, El-Atwani, & Altintas, 2008; Farrokhi-Rad, 2016; Khalili et al., 2016; J. U. Lee, Park, Kim, Bae, & Lee, 2016). The improved stability of coated martials in EPD method is to some extend affected by parametric optimization and subsequent sintering treatment.

2.3.4 Plasma Electrolytic Oxidation (PEO)

PEO process is addressed as one of the significant method to deposit bioactive Ca/P based ceramic layers such HA, on metallic implant surfaces. PEO can largely provide the capability of Ca and P ions attachment to reinforce biological performance as well as corrosion resistance of composite structures. Based on the current literature, applied voltage, electrolyte composition, current density, times and annealing conditions are highly effect the PEO process (Ooi, Hamdi, & Ramesh, 2007; Shin, Ko, & Shin, 2011; Søballe, Hansen, B-Rasmussen, Jørgensen, & Bünger, 1992; D. Williams, 1987). Microstructural functionality of coated substrates with various geometrics and reasonable adhesion strength is highlighted as the advantages of PEO in case of proper parameters. Occasionally, to find the optimum outputs, PEO has been combined with other coating methods through hybrid processes (Abbasi, Golestani-Fard, Mirhosseini, Ziaee, & Mehrjoo, 2013).

2.3.5 Electrochemical Deposition (Electrodeposition)

Electrodeposition is an economic coating technique which can be generated with convenient control of coating complex geometries under low temperature (Eliaz, Kopelovitch, Burstein, Kobayashi, & Hanawa, 2009; Manso, Jimenez, Morant, Herrero, & Martınez-Duart, 2000). To date, Electrodeposition has been considered as unique three-electrode method to fabricate the uniform layers on conductive substrates. The

morphology of formed thin films was controlled by varying the electrolyte concentration and electrochemical potential (Kuo & Yen, 2002). Investigations of this method were widely carried out in district of biomaterials on biometallic substrates such Ti and magnesium (Mg) alloys through *vitro* also *vivo* orthodontic practices (Le Guéhennec et al., 2007; Rigo et al., 2004; Tian & Liu, 2015; Vijayaraghavan & Bensalem, 1994; Zanin et al., 2013). According to conducted research, electrodeposition method was applied to coat archwires with Ni film impregnated with inorganic fullerene-like nanospheres of tungsten disulphide (WS_2) to reduce the frictional force (Redlich et al., 2008). Furthermore, the electroplated Ta film on NiTi alloy reported to evaluate the effect of coating on corrosion resistance than untreated alloys (El Abedin, Welz-Biermann, & Endres, 2005). Elsewhere, developed HA and HA-ZrO_2 nanocomposite coating on NiTi substrate used electrodeposition technique with same target of improved corrosion (Qiu, Wang, & Yin, 2010). The electrodeposition functionality of bone-like implants via were also examined to assess the enhanced biological, antibacterial and drug delivery properties (Ordikhani, Zustiak, & Simchi, 2016; C.-C. Yang, Lin, & Yen, 2011).

2.3.6 Sol-Gel

Sol-gel method is referred to the chemical process which was used to develop possible structures such glass, hybrid glass-ceramic and ceramic-based composites through low- temperature experiment (Cotolan et al., 2016; Mackenzie & Bescher, 2000; Patil, Hwang, Kim, Chang, & Park, 2004; Peláez-Vargas, 2005). Sol-gel is being performed in aqueous solutions of species undergo polymerization responses, which lead to form a gelatinous network for densification of coated products. The method has provided greatest potential for coating organic thin films (CHEMISTS, 1992). The current process has been widely generated to coat metallic bone implants with enhance mechano-biological features (Greer, Lim, Brydone, & Gadegaard, 2016; Shimizu et al., 2016; Tran, Fox, & Tran, 2017). It was reported that synthesis of hybrid TiO_2-ZrO_2 biocomposite

structure on derived Ti-based tissue obtained by so-gel technique (García-Galván, Jiménez-Morales, Hickman, Perry, & Galván, 2016). Likewise, the fabrication of glass-like cerium modified biodegradable Ca/P nanomaterials on biocompatible coating was examined (Reyes, Durán, & Castro, 2016; Usinskas, Stankeviciute, Beganskiene, & Kareiva, 2016).

2.3.7 Chemical Vapor Deposition (CVD)

The CVD method operates with the various chemical reactions which can be taken place around the hot surface targets to deposit various thin films materials. The chemically productions and their further exhaustion out of the related devise chamber tackle with unreacted precursor gases follows the process. CVD action has been attracted due to its distinctive advantages including controllable thickness through high-rate deposition, potential of using for large materials with desired purity. However, similar with other methods, CVD also faces some limitations such lies in properties of the precursors, since they are required to be volatile at around room temperatures, which is beneficial for large number of chemical elements. Other drawbacks is mainly issued regarding to toxic, expensive, corrosive and explosive precursors which can coat layers at high-temperatures, deposition (B. E. Williams & Stiglich Jr, 1992). Based on the current literature, CVD has been applied to deposit biofilms on Ti-based substrate for orthopedic applications (Strąkowska, Beutner, Gnyba, Zielinski, & Scharnweber, 2016; Tripi, Bonaccorso, & Condorelli, 2003; Tripi et al., 2002). Surface modification of dental burs and endodontic devises was reported with using CVD approach was reported (Lima, Motisuki, Santos-Pinto, Santos-Pinto, & Corat, 2006). Elsewhere, the electrochemically assisted to develop HA on Ti-based implants in biological performance with cell interaction (Strąkowska et al., 2016). Modified plasma treated CVD method for metallic substrates improvement was also examined the effect amino acid functionalization in bioactivity of implant (Lu et al., 2016).

2.3.8 Hydrothermal Method

Generally, hydrothermal method is used to synthesize materials at high temperature and high pressure by using chemical supersaturated solutions (Jingbing Liu et al., 2003). Hydrothermal processing involves the use of a solvent (with precursor soluble ions), which is heated in a sealed vessel. The main solvent in this process is water. Solvent temperature can be increased to above boiling point because autogenous pressure in a sealed vessel exceeds ambient pressure. Variations in solvent and reactant properties (e.g., solubility) at increased temperature indicate that experimental variables can be controlled to a high degree. In this regards, the related reactions become more predictable because crystal nucleation, growth, and aging can be regulated. It should be mentioned that, calcination is not required in this method. In low-temperature methods, such as wet chemical precipitation and sol–gel synthesis, post-heat treatment is required to crystallize HA, whereas crystalline HA can be produced in one step via hydrothermal and solvothermal syntheses. Yields approaching 100%, relatively low-cost reagents, and short reaction times have also been reported for these processes. This method was suited to structure HA nanotube, microtube, and nanorod with a micro length for biomedical applications (Chandanshive, Rai, Rossi, Ersen, & Khushalani, 2013; C. Chen et al., 2011; D. K. Lee, Park, Kim, & Jang, 2011; Lester et al., 2013; Jingbing Liu et al., 2003). Likewise, in case of metallic implant modification, the evaluation of microstructural features and *in vitro* biocompatibility of hydrothermally coated fluorohydroxyapatite (FHA) on clinical AZ80 Mg Alloy was reported (S.-H. Wang, Yang, & Lee, 2016).

2.3.9 Spin Coating

Spin coating is the predominant technique employed to produce uniform thin films of photosensitive organic materials with coating thickness in micro and nanometer orders (Sahu, Parija, & Panigrahi, 2009). The pioneering analysis of spin coating was performed more than fifty years ago by Emil *et al* (Emslie, Bonner, & Peck, 1958) who considered

the spreading of a thin axisymmetric film of Newtonian fluid on a planner substrate rotating with constant angular velocity. In many cases the coating material is polymeric and is applied in the form of a solution from which the solvent evaporates. Spin coating was firstly studied for coating of paint and pitch (Meyerhofer, 1978). This economic method has been used for several decades for development of various thin film. A typical process involves depositing a small puddle of a fluid resin onto the center of a substrate a hen spinning the substrate at high speed. Centripetal acceleration will cause the resin to spread to, and eventually off, the edge of the substrate leaving a thin film of resin on the surface. One of the most important factors in spin coating is repeatability. Subtle variations in the parameters that define the spin process can result in drastic variations in the coated film (Tyona, 2013). The advantages of spin coating are the simplicity and relative ease with which a process can be set up coupled with the thin and uniform coating that can be achieved. Due to the ability to have high spin speeds the high airflow leads to fast drying times which in turn results in high consistency at both macroscopic and nano lengthscales. The disadvantage of spin coating is that it is an inherently batch (single substrate) process and therefore relatively low throughput compared to roll-to-roll processes. The fast drying times can also lead to lower performance for some particular nano-technologies which require time to self-assemble and/or crystallize. Finally, the material usage is typically very low at around 10% or less with the rest being flung off the side and wasted. Whilst this is not usually an issue for research environments it is clearly wasteful for manufacturing. Despite these drawbacks, spin coating is usually the starting point and benchmark for most academic and industrial processes requiring a thin and uniform coating. So, layer-by-layered assemblies used spin coating technology to find facile distribution of homogenies thin films (S.-S. Lee et al., 2001). Recently, implant materials have been reinforced with some advanced composites such carbon nanotubes (CNT) attached ceramic structure and G–Al_2O_3 through thin film coatings methods (Gopi,

Shinyjoy, Kavitha, & Rajeswari, 2016; Jian Liu et al., 2016). Based on our best knowledge, no obvious research was reported the development of carbon-based thin films on coated nanotubular ceramics using spin coating.

2.4 Mechanical Properties

2.4.1 Adhesion Strength of Coated Ti-based Implants

With modification view, single and composite-phase biomaterials have been developed to improve the properties of artificial hard tissues such Ti-based implants (L. Zhang & Webster, 2009). Therefore, the coating structures are required to be correlated with more appropriate methods for higher functionality. However, there is still some limitations which have induced researchers to promote the optimized conditions of processes (Maleki-Ghaleh et al., 2015). The reasonable fabrication may contribute to enhance the coating outputs such adhesion strength which resulted in higher mechanical properties. It is notified that, the coating outputs are extensively influenced the implant stability as well as undesired properties. This matter would be more highlighted in case of coated metallic implants with homogeneous morphologies (E. Marin et al., 2016). So, appropriate adhesion strength between coated films, interlayers and substrates is labeled as an important requirement. Various techniques have been applied to characterize the adhesion feature of layers, including peel test (Horgnies, Willieme, & Gabet, 2011), the bulge analysis (Lynch, Mlack, Correia, Brown, & Muhlstein, 2000), the laser spallation technique (LST) (J. Shim, Hagerman, Wu, & Gupta, 2008), the coating tensile assessment (Hoffman, 1988), and the scratch examination (Bull & Berasetegui, 2006; Gonczy & Randall, 2005; Laugier, 1984). Among these methods, the LST analysis can provide an accurate measurement for adhesion strength of coated layers, while, it requires the specific equipment. Afterward, scratch analysis is considered as a common quantitative assessment of the thin film's adhesion. So, many researches have been wildly studied the characteristics of coated metallic implants (Lei, Mittal, & Yu, 2016; S. Liu, Li, Liang,

Wang, & Qiao, 2016; Meischel et al., 2016). Recently, the adhesion optimization of Taguchi designed Nb PVD film on Ti-implant has been investigated. Elsewhere, the adhered bonding of different fabricated layers has been evaluated due durability impact of coated implants (Cools et al., 2016; S. Liu et al., 2016; Ong, Lucas, Lacefield, & Rigney, 1992; Piveteau, Gasser, & Schlapbach, 2000).

2.4.2 Mechanical Hardness

Modification of bone interfaces is an open problem in appropriate mechanical stability of cementless fixed implants. Adequate mechanical properties such hardness are well suited for engineered tissues trough coating treatment (Giavaresi et al., 2002). The enhanced stability expect to promote bonding strength with minimizing the mismatch between the coated layers and treated substrates (Ding et al., 2016). Due to the related mechanical effects on *in-vivo* results, interfacial bone microhardness of collagen-coated Ti-implant in rabbit models has been widely studied (Calciolari, Donos, & Mardas, 2016; Fini, Giavaresi, Rimondini, & Giardino, 2002; Morra et al., 2005). Related article was reviewed the mechanical hardness, tensile strength and modulus aspects of orthopedic devises (Frigg, Schavan, & Hehli, 2001; Geetha et al., 2009). Recently, in situ plasma fabrication of ceramic-like structures on polymeric implant with enhanced surface integrity, cytocompatibility and antibacterial behavior considerably examined (Jun Liu et al., 2016). So, application of thin film hard coating contributed to enhance the strength of Ti-based bioalloys (Baradaran et al., 2014; Mehrali et al., 2016; Sasikumar & Rajendran, 2017). Likewise, the effect of as-sputtered layers on Ti-based substrates significantly modified the mechanical parameters (Movassagh-Alanagh, Abdollah-zadeh, Aliofkhazraei, & Abedi, 2017; Musil, Zenkin, Čerstvý, Haviar, & Čiperová, 2017). From literature, current features of EPD coated hybrid HA-multi wall carbon nanotubes (MWCNT) composite provided higher stability of treated NiTi alloys (Khalili et al., 2016). Incorporation of metallic dental implant using cubic ZrO_2 nanocoating executed

boosted bioperformance (I. Das, Chattopadhyay, Mahato, Kundu, & De, 2016). Based on reported research, biological features of Ti-base implant osseointegration as well as its mechanical resistance were clearly influenced by as-coated structure (Veronesi et al., 2017).

2.5 Corrosion Resistance

To date, various topographies of metallic, ceramic and carbon-based morphologies have been generated for oral implants and joint replacements due to high strength, ductility and toughness. There is no doubt that these potential biomaterials can enhance long-term implant performances (Gilbert, Buckley, & Jacobs, 1993; Rafieerad et al., 2015). However, the chemical reactivity of treated components even into physiological media (typically as a 37 ºC aqueous solution at pH of 7.4) may restrict their life span of bone implants. The application of nanostructures shown desired advantages of interaction within body media (such as dissolved gases, electrolytes, cells and proteins). Since, reinforced metallic implants with corrosive agents may cause localized anodic reactions which effects the mechanical loading and patient's activities. Meanwhile, the anticorrosion behavior is associated with the surrounding space to postpone the gradual deterioration. The subjected reactions can be chemical, electrochemical, physical or their combination (Uhlig, 1948). There is three main factors related to study of the corrosion phenomenon: the material, the environment and the interfaces. Although corrosion can also effect the surface of ceramics and polymers, but, the corrosive reaction of metallic materials is well referred in the most common sense. It has been corresponded to occur through chemical processes specified dissolution and oxidation. From obtained results in literature for corrosion resistance of bone implants largely affected by surface coating (X. Liu, Chu, & Ding, 2004). From corrosion point of view, implanted materials are continuously facing with corrosive conditions under direct blood, interstitial and synovial fluids contact. Therefore, implantable materials are

required to be satisfy in anticorrosion aspect (Miura et al., 2016; Sekine, 1989; Stergioudi, Vogiatzis, Pavlidou, Skolianos, & Michailidis, 2016; B. Zhao, Wang, Qiao, Wang, & Hu, 2017). Compositions of body media involve chains bonded of protein and amino acid branches which may accelerate the corrosion damage (Merritt & Brown, 1988; R. L. Williams, Brown, & Merritt, 1988). It is notified that, declined pH to around 5 within hard bone-like tissue after implantation reaches to around 7 within 14 days of immersion (L. Hench & Ethridge, 1975). Toxicity and allergy may affect *vivo* analysis, if metallic materials are corroded by body fluids, leading to the release of metal ions for a long period and ions combining with biomolecules. Thereby, the corrosion resistance of metallic alloys is considered as vital artificial bone tissues requirements. Formation of a native TiO_2 film can protects the metal's surface from further oxidation to provide reasonable surface removal of Ti-based orthopedic system (Gonzalez & Mirza-Rosca, 1999; Mueller & Greener, 1970). Corrosion properties of bulk metallic substances into simulated corrosive condition has been largely studied (Aziz-Kerrzo, Conroy, Fenelon, Farrell, & Breslin, 2001; Durgalakshmi, Rakkesh, & Balakumar, 2015; Janković et al., 2015; Marimuthu et al., 2014; J. Pan, Leygraf, Thierry, & Ektessabi, 1997; Yan et al., 2015).

2.6 Biological Evaluation

2.6.1 *In-vitro* Bioactivity

Rapid ingrowth of biomedical implants in simulated media is a main key feature is form apatite layer resulting the bone regenerations. It is therefore vitally important that the *in-vitro* studies examine the bioactivity of nanostructured morphologies in view of apatite-induced effect. In this regards, formation of hybrid rich SiO_2 and Ca/P films on biosurfaces carried out to follow adequate bonding with body bone carried out. The reproducing Ca/P-based layer in a buffer solution at pH 7.4 (including of Tris hydroxymethylaminomethane and hydrochloric acid) within *vivo* experiments (Ogino, Ohuchi, & Hench, 1980). The related report, investigated the possibility of rich layer SiO_2

on glass-ceramic structures, while the formation bone apatite coating on surface in living body may provide the real bone integration (Kitsugi et al., 1987). Known literature used micro X-ray diffraction technology to identify the related Ca-P film as crystalline apatite structure. Moreover, in 1990, the *in vivo* apatite appearing on glass-ceramic surfaces interfacing an acellular saturated simulated body fluid (SBF) with ion composition close to the human blood plasma reported. Bioactivity of modified Ti-based implants with nanotubular ceramic structure was assessed by evaluating in SBF mineralization (Kokubo & Takadama, 2006). There are large number of researches about the ability of crystalline and carbon-based nanostructures to induce the quick bone-like formation by soaking (Uchida, Kim, Kokubo, Fujibayashi, & Nakamura, 2003). The physicochemical changes on biometallic tissue surfaces perform based on heterogeneous nucleation phenomenon. If the solution supersaturation and the substrate condition are appropriately controlled, nucleation and crystallization of apatite layer appear the treated surfaces. The reviewed absorption mechanism reactions of apatite formation facilitate the rapid osseointegration and implant fixation without any pretreatment trough interfacing in alkaline solutions or *vivo* media (Siriphannon, Kameshima, Yasumori, Okada, & Hayashi, 2000, 2002).

2.6.2 Antibacterial Activity

A major burden for orthopedic implant success is due to chronic infections, which can cause the implant failure and revision surgeries. Based on the reports, surface modification of implants has resulted to reduce bacteria attachment and allow tissue integration. Comparison of the conventional bare Ti substrate with its modified surfaces by nanoroughing through electron beam evaporation was reported (Yao, Slamovich, & Webster, 2008). Their results has investigated the reduction of *S. aureus*, *S. epidermidis*, and *P.aeruginosa* bacteria which provide higher bone functionality. The same approach can be applied to examine the antibacterial properties of nanotubular bioceramics. The

reinforced ceramics with carbon-based materials also has been attended due to their antibacterial activity trough reduced bacterial adhesion. Related mechanism and the reason that nanopatterned surfaces encourage osteoblast adhesion and bone integration, while at the same time discourage bacteria that cause infection to adhere on the surface was followed. Therefore, the achievement of controlling bacterial growth by bioactive ceramics as well smart composite structures highlighted (Karimi, Yazdanshenas, Khajavi, Rashidi, & Mirjalili, 2014; Perreault, De Faria, Nejati, & Elimelech, 2015). In complementary view of the required metallic surface modification to meat standard level of artificial bone tissue, many studies have been focused on biological issues (Vasilescu et al., 2011). Despite the obtained biocompatibility manner, infections after introduction into the body were relatively frequent and caused the bacteria colonization (Y. Chen et al., 2008). Mostly, various bacterial sources are existed which may insist the space of the operating room, worn clothes, surgical equipment, bacteria resident on patient's skin and inside body (Zilberman & Elsner, 2008). A combination of modern and conventional techniques have been applied to control the microbial contamination of implantable devises. The involves the possibility of bactericidal and antibacterial agents such Ag, Au and classified potential nanostructures (H.-L. Huang et al., 2010). Current nanoparticle morphologies provide beneficial antibacterial features, to help the healing process. With the relevance function of antibiotic in 1940s, the usability of Ag in particular as an antimicrobial agent decreased, but there has been a promote resurgence of these material as effective antimicrobial factor before the turn of the millennium. In recent decade, the trend was continued to attend AgNPs in anti-infection functions. Highlighting to bone application, the promising functionality in clinical operations is aimed to adjust the antimicrobial mediation. However, AgNPs has been widely used in medicine, photonics, sensing, antibacterial surfaces, catalysts, and kitchen utensils because at the nanometer level its metallic nanoparticles display uncommon properties (B. Liu, Zhao, Zhu, Luo, &

Cheng, 2008; Shrivastava et al., 2007; J. Yang, Yin, Jia, & Wei, 2011). Attachment of AgNPs with ceramic and polymer materials resulted to design hybrid composites serving as core or shell in modified alloys. AgNPs and AuNPs are able to decorate on another matrix templates for higher functionality by using various methods such thermal, photochemical, microwave, reduction and sonochemistry tarnishes (Watson, 2014). Based on recent reports, the usability of Ag materials is concerned cytotoxicity in contrary with its ideal bactericidal mediation (Prabhu & Poulose, 2012). On the other hand, synthesis of Ag materials in micro/nano scale morphologies is extensively concerned by economic limitations. Therefore, development of new smart organic antibacterial biomaterials is challenging. In this regards, a report shown the antibacterial performance of amino acid hybrid carbon nanotube composite (Zardini, Amiri, Shanbedi, Maghrebi, & Baniadam, 2012).

2.6.3 Human Osteoblastic Cell Proliferation

Generally, biometallic implants have been taken into consideration where the medical prosperity is directly relevant to the primitive connection between living bone and the load-bearing tissues. The important osseointegration is directly affected by bioactivity of implant surfaces (Minagar, Li, Berndt, & Wen, 2015). Chemical stability of bone implants also influence the biological and antibacterial functionality. Several studies were conducted to examine the improved interaction between real bone and integrated cement (Mazaheri et al., 2015). The effects of surface modification on metallic implant on clinical results were analyzed towards enhanced future implantations. The interaction of engineered Ti-based bioalloys with human osteoblastic (hFOB) cells has been widely checked (Y.-Y. Guo et al., 2016; Karoussis, Kyriakidou, Psarros, Lang, & Vrotsos, 2016; Mariscal-Muñoz et al., 2016; Martin et al., 1995; Mishra, Teotia, Kumar, & Kannan, 2016; Subramani, Pandruvada, Puleo, Hartsfield, & Huja, 2016). From literature, applied micro arc oxidation and hydrothermal coatings on Ti-based surface,

provided adequate osteoblast cell adhesion (YM Zhang et al., 2004). The quick osseointegration ability of oral tissues was considered as key factor in accelerating bone remodeling (Berglundh, Abrahamsson, Lang, & Lindhe, 2003). Also, chemical effects on rehabilitation were evaluated biological fixation in replaced bone-like tissues (Albrektsson & Wennerberg, 2003). These features are crucial through the bone healing step in peri-implant regions. The surface of treated prosthesis are mostly interfaced with direct contacts of body buffer and organs. The existed challenges in engineered tissues is to attract, osteoblastic assay that provide a bone extracellular matrix, which will ensure a successful bone regeneration with minimum failure risk. hFOB cell adhesion is addressed as the initial sign in case of successful human osteoblastic proliferation. It was confirmed that biocompatibility with osteoblast proliferation bioassay are to some extent related to elements of cultured surfaces (Masuda, Yliheikkilä, Felton, & Cooper, 1997). Many *in-vitro* osteoblastic experiments have been studied on Ti-based substrates, to obtain the optimum surface properties. The large-area porosity of bioceramic coatings encouraged to entrapment of fibrin protein, cell adhesion and mechanical stability of implants in host bone (Lauer et al., 2001; Mehrali et al., 2016). Recently, modification of osteoblast assay of biomedical Ti-alloys with various bioactive ceramic and carbon-based nanostructures have been noticed (Al Qahtani et al., 2016; Gopi, Shinyjoy, & Kavitha, 2015; Hyzy et al., 2016; Iaculli, Di Filippo, Piattelli, Mancinelli, & Fulle, 2016; Justin et al., 2016; Lotz et al., 2016). Study on probable benefits of various Ag concentrations as antibacterial agent in osteoblast proliferation of treated Ti-based surfaces was carried out (Gao et al., 2014). Based on background, such excellent bactericidal feature was obtained with appearing of cytotoxicity effects, incites immunological and disrupts cell growth. The saturation on cytotoxicity trend was slightly controlled by interfering anchored bioactive passive layers. According to major view on longer harmful effects of releasing Ag ions in implant systems two-side feasible experimentations forwarded (Gao et al., 2014; M. V. Park et

al., 2011; Setyawati et al., 2014). Solving risky problem trough potential non-toxic organic biomaterials is still interesting. Highlights on smart topographies with controlled reasonable multifunctional balance of vital stability, antibacterial and mechanical characteristics fully aimed.

2.6.4 Smart Drug delivery

Artificial tissues infection associates devastating complications remarkably in orthopedic and dental surgeries, which may undesired outcomes such implant failure, poor properties, topical pains, chronic osteomyelitis or even death. Besides, promising techniques, such antibiotic prophylaxis, have been applied to reduce and to some extent prevent the postoperative infections (Campoccia, Montanaro, & Arciola, 2006). However, the percentage of postoperative infections is still rising mostly affected by bacteria attachment on implant surfaces (Antoci et al., 2008; Zimmerli, Trampuz, & Ochsner, 2004). An unmet necessity to generate modified strategies to control artificial tissues infections and prevent bacterial colonization. In this case, development of various smart organic and inorganic thin films and composite coatings have been explored for Ti-based orthopedic implants (Q. Chen et al., 2015; Kämmerer et al., 2016; Maher et al., 2016; Mazaheri et al., 2015). Some studies examined the effects of antibiotics loading in carbonated hydroxyapatite and bioactive multilayers coating designs to note the enhanced drug delivery and antibacterial potentials (Ordikhani et al., 2016; Stigter, Bezemer, De Groot, & Layrolle, 2004). Drug delivery is referred to approaches, formulations, technologies and systems that facilitate the introduction and transport of therapeutic compounds in to the body to achieve their desired therapeutic effect (Mohan, Anandan, & Rajendran, 2016).

In conventional way of smart drug delivery system (oral, parenteral, etc,) prepared medicines are distributing to whole of body without specific site of interest, wherever the

therapy is necessary. These routes also have many problems and limitations like poor bio-distribution, side effects, toxicity, drug solubility and unfavorable pharmacokinetics (Mainardes & Silva, 2004). The idea of localized drug delivery system has been executed in different clinical devices capable of affording, programmable, sustained, controlled and localized release of drug functions (Wolinsky, Colson, & Grinstaff, 2012). These methods have come out favorable as possible options to conventional administration of drug for a wide range of clinical treatments. Drug-releasing implants (DRI) based on the invention of nanoengineered surfaces on available medical implants have drawn immense interest (Wu & Grainger, 2006).

Recently, anodically fabrication of rod shaped figurations such nanotube and nanoporous on some metallic alloys are considered as main platforms for drug releasing (Losic & Simovic, 2009). Advanced nanoconfigurations modified implant devises is advantageous as it is cost effective, surface chemistry can be tailored, pore/tube morphologies (Mohan, Anandan, & Rajendran, 2015). The as-treated surfaces are versatile, mechanically rigid, chemically stable high with increased large-surface-area drug capsulation capacity and tunable release. They are exceptional biocompatible and more fascinatingly, they can be consistently fabricated on the surface of existing medical implants (Roy et al., 2011). Many researchers have investigated anodized Ti topography based drug-releasing implants (DRIs) in fields of orthopedic implants, vascular (coronary) stents and localized cancer therapy (Bauer, Schmuki, von der Mark, & Park, 2013). Several therapeutic agents such as antibiotics, antifungal, anti-inflammatory, anticancer drugs, bone proteins, peptides, enzymes, vitamins, hormones, genes, antibodies, neurotransmitters, drug carriers and nanoparticles have been applied in order to employ a wide range of therapies into smart engineered implants (Aw, Kurian, & Losic, 2014). Drugs with various sizes and properties as well as anti-biotic, anti-cancer feature

such indomethacin, gentamicin and vancomycin, doxorubicin and paclitaxel have also been studied (Aw et al., 2014).

The critical parameters required for clinical applications such as desired kinetics, drug release rate and concentration for different localized drug delivery therapies are successfully delivered by Ti-based nanotubes demonstrated by *in-vitro* studies. Quercetin is a flavonol found in many leaves, vegetables, fruits and grains. Quercetin's anti-oxidant and anti-inflammatory effects may help to treat rheumatoid arthritis (R. Wong & A. Rabie, 2008) in which the immune system attacks the synovial membrane lining the joints and osteoarthritis, in which the cartilage between the bones deteriorates, causing the bones to rub against each other. Many reports described the beneficial effects of quercetin for antiinflammatory, anti-oxidant, anti-cancer activities (Joshi et al., 2011; R. W. Wong & A. B. M. Rabie, 2008) and osseointegration feasibility (R. W. Wong & A. B. M. Rabie, 2008). Chitosan is a cellulose-like biopolymer found mainly in the exoskeleton of marine animals. Numerous reports have illustrated the beneficial effects of chitosan for wound healing using *in- vitro* studies (Riva et al., 2011). From report, biodegradable polymers such as chitosan and PLGA have antibacterial and osseointegration properties (R. W. Wong & A. B. M. Rabie, 2008). Chitosan's hemostatic properties also allow it to reduce pain by blocking nerve endings. Its properties also allow it to be used in transdermal drug delivery in implant system (Ghadari & Kashefi, 2017; Jingquan Liu, Cui, & Losic, 2013).

In summary, this chapter reviewed technically the most possible coated biomaterials to improve the mechanical and biological and drug delivery property of Ti-based bone implants. Based on the literature, the bioactive nanostructures may contributes to enhance bio-implant systems with anti-infection performance. Extensive drug delivery applications of smart carbon-based materials are also able to be programmed with variety of antibiotics for minimizing risk of replacement.

CHAPTER 3: MATERIALS, METHODS AND PROCEDURE

This work is mainly focused on development of smart antibacterial nanostructures modified orthopedic and dental Ti67IMP with drug delivery potential. Physicochemical characterizations of multilayered metallic/ceramics/carbon-based biocomposites with and without amino acid functionalization performed comparably. The mechanical, corrosion, wettability, *in-vitro* bioactivity and antibacterial properties of treated Ti67IMP specimens were examined as well as biological hFOB cell performance of designed layer-by-layer composites. This chapter explained detailed account of experimental protocols from modeling to applications. Figure 3.1 presents Flow chart of research plan.

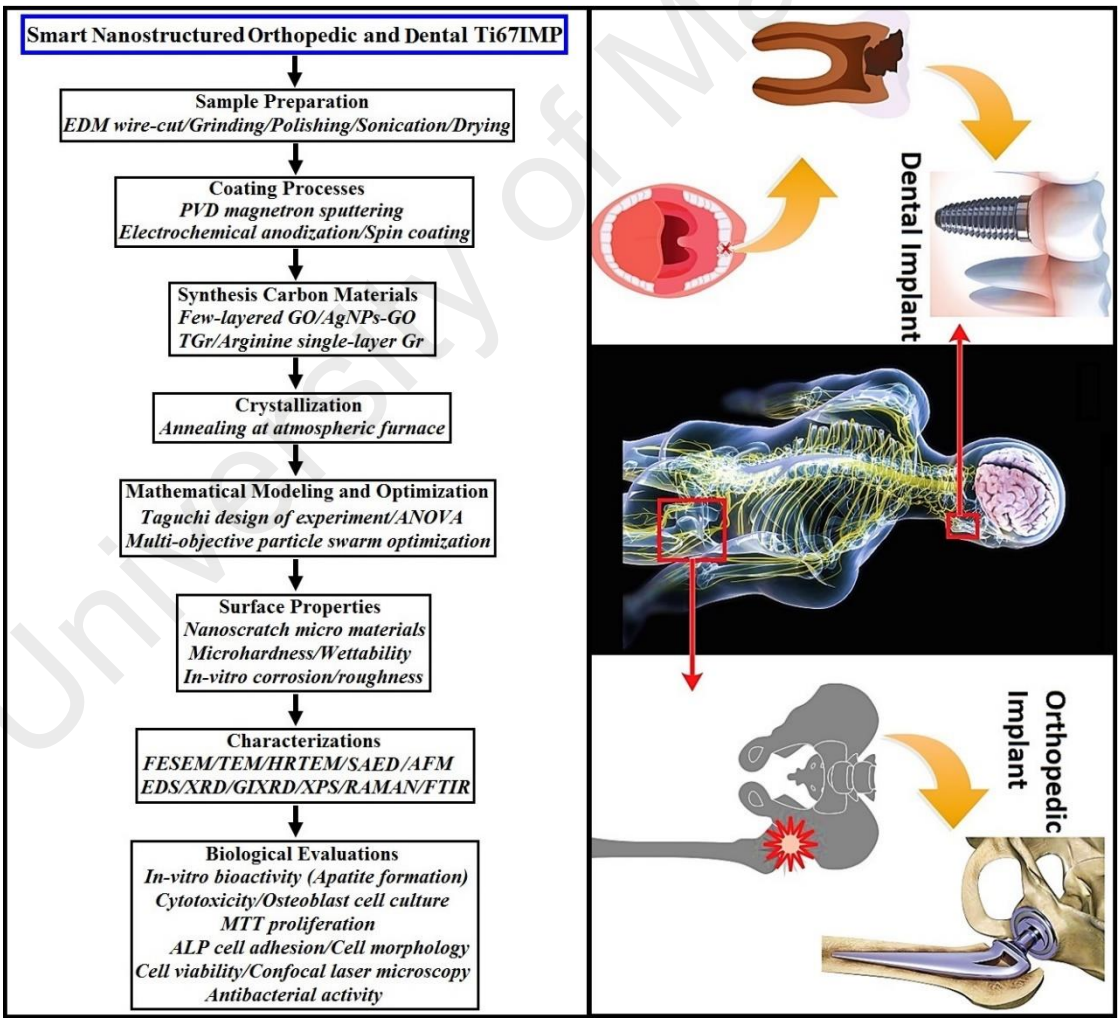

Figure 3.1: Flow chart and schematic application of research plan.

3.1 Experimental Procedures

3.1.1 Wire-cut EDM and Substrate Properties

The SPD-processed Ti67IMP sheet fixed in EDM holder to wire cut into laboratory size with dimensions of 20×10×2 mm^3 in this project. The specimens then were grinded to remove the oxide layer. Table 3.1 presents details of mechanical properties and elemental composition of Ti67IMP substrate.

Table 3.1: Properties of Ti-6Al-7Nb substrate.

Product	**Biomedical Ti67IMP Sheet**
Standard	ISO 5832-11/ GB 23102-2008
Application	Orthopedic and dental implants
Technology	Hot rolling, cold rolling, annealed
Surface	Pickling, sandblasting, polishing

Chemical Elements	Ti	Al	Nb	Ta	Fe	C	N	H	O
Ti67	Bal	5.5-6.5	6.5-7.5	0.50	0.25	0.08	0.08	0.009	0.20

		Mechanical Properties		
Material	Thickness	Tensile strength Rm/MPa	Yield strength Rp0.2/MPa	Elongation A%
Ti67	<100 mm	Min 900	Min 800	Min 10

3.1.2 PVD Magnetron Sputtering (PVDMS)

PVDMS is considered as physical vapor deposition technique (PVD) to sputter the dense layers through ejecting atoms from located targets onto substrates in high vacuum condition. Firstly, the sourced target is bombarded via energetic ions interfering an inert gas ions such Argon (Ar^+), which ions collision force lead to eject target atoms in chamber space. Then, the ejected atoms move to reach the substrate and start to condense the film. With increasing the time of deposition, more atoms are coalesced on substrates, motivate to molecular binding and forming a tightly-bound atomic layers allowing fabrication of precise homogenous thin films. Targets are produced from various materials that wish to deposit on surface of the components. DC or RF sputtering mode

settle depend on the targets and substrates. PVDMS provides such a closed magnetic field to trap electrons, enhancing the efficiency of initial ionization process and allowing a plasma to be generated at lower pressures which reduces both background gas incorporation in the growing film and energy loses in the sputtered atom through gas collisions. Hence, PVDMS method applies to coat thin films by sputtering a block of source material onto a substrate, so that, the sputtered atoms ejected into the gas phase are not in their thermodynamic equilibrium state, and tend to deposit on all surfaces in the vacuum chamber. Matched PVDMS potential, same mechanism of two or three materials can be sputtered simultaneously as hybrid or composite structures. Following the oxidation possibility, the oxide layer films may fabricate through adding oxygen to chamber within sputtering process. Herein, PVDMS machine (TF450 Sputtering System, SG Control Engineering, Singapore) was utilized to deposit homogenous Nb film on Ti67IMP substrate. The distance between the related targets and substrate was kept constant during the sputtering process. Accordingly, the experiments of Nb PVD coating were carried out under designed condition to obtain the optimum properties.

3.1.2.1 Taguchi Design of Experiment (DOE)

Design of experiments refers to the process of planning, designing and analyzing the experiment so that valid and objective conclusions can be drawn effectively and efficiently. In order to draw statistically sound conclusions from the experiment, it is necessary to integrate simple and powerful statistical methods into the experimental design methodology. Usually in performing biotechnological experiments such as; screening and optimization, Design-Expert software is used for such purposes, it makes a breakthrough improvements to a product or a process. Easily view response surfaces from all angles with rotatable 3D plots. Set flags and explore contours on interactive 2D graphs; and use the numerical optimization function to find maximum desirability for dozens of responses simultaneously. Here, the control parameters of PVD were DC

power, argon flow rate and DC Bias, which were investigated through three levels and the amounts of pressure, time and temperature were kept constant at 1.9×10^{-5}, 2 h and 220 °C, respectively. The applied parameter design followed a standard $L_9(3^3)$ orthogonal array, which was suggested from the possible variable response parameters via Taguchi DOE. Therefore, the PVD experiments were carried out nine times in combination of proposed factors. The designed parameters were summarized in Table 3.2.

Table 3.2: Factors and levels used in the PVD sputtering experiment.

Series	Factors		
	DC Power (w)	**Argon flow rate (sccm)**	**DC Bias (V)**
1	150	20	30
2	150	40	60
3	150	60	90
4	250	20	60
5	250	40	90
6	250	60	30
7	350	20	90
8	350	40	30
9	350	60	60

3.1.2.2 Preparation of Ti67IMP Substrate

Ti–6Al–7Nb plates (Baoji Liu Wei special Material and Equipment produce Co. Ltd China) were used as a substrate during all the experiments. Prior to any coating treatments, all the samples were ground via SiC emery paper (1000–2400 grit) and then wet-polished in a diamond slurry. Subsequently, the polished samples were sonicated in acetone at 40 °C for 14 min and washed three times with distilled deionized water and dried at 100 °C for 1.5 h.

3.1.2.3 Preparation of Nb Coating

A pure niobium (Nb) target (99.95% pure EX Ta, Kurt J. Lesker Company) was used in this work to coat Nb layer on Ti67IMP. The applied system possesses a vertical

configuration with dual switchable services (DC/RF targets) placed at a distance of 150 mm above a rotatable substrate holder. Prior to deposition, the substrate rinsed in acetone and preheated via digital heater until 300 °C. The target was pre-sputtered in an argon atmosphere to remove the oxide layer. The chamber of the machine was evacuated in order to reach the inside pressure less than 2.1×10^{-5} Torr. The process's working pressure, argon flow rate and chamber temperature also were kept at 3.6×10^{-3} Torr, 20 sccm and 220 °C respectively during 2 h process. For higher efficiency associated with deposition parameters statistical investigation was carried out. According to coating outputs, the analysis of data were evaluated through signal-to-noise (*S*/*N*) concept. Generally, in matter with adhesion strength of layers on substrate the large category was needed, which can be calculated by Equation 3.1 as follows:

$$S/N = 10log\left(\frac{1}{n}\sum_{i=1}^{n}\frac{1}{Y_i^2}\right) \quad (3.1)$$

where term of *y* is the obtained results and *n* represents the number of experiments. The schematic view and experiment set up of PVDMS to fabricate Nb film on Ti67IMP alloy was illustrated in Figure 3.2.

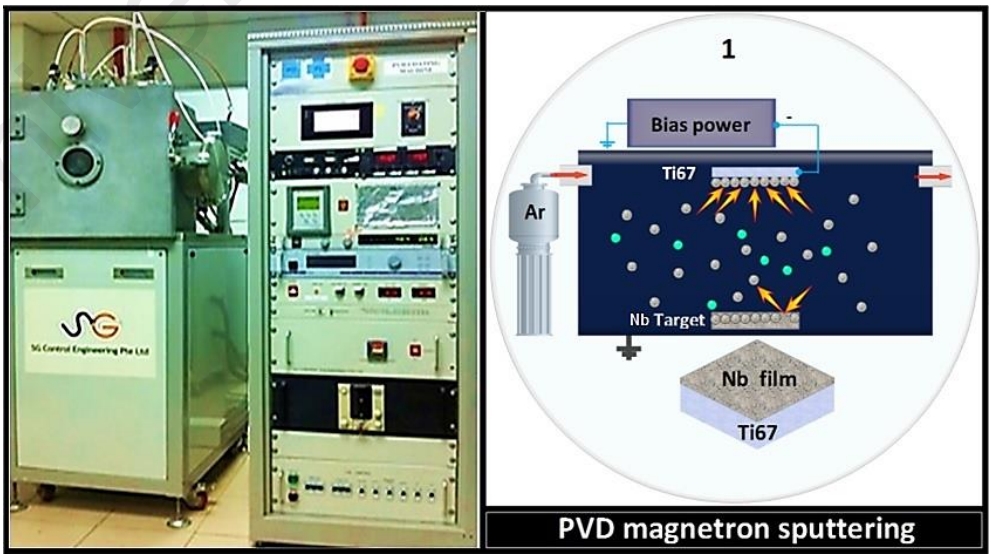

Figure 3.2: PVD magnetron sputtering devise and schematic view of process.

3.1.2.4 Modeling, Prediction and Optimization

(a) ***Particle Swarm Optimization and Multi-objective Approach***

As mentioned above, PSO as a population based metaheuristic technique has attracted significant attention to tackle the complexity of different optimization problems due to its simple concept with efficient search mechanism on real-valued numerical optimization. It is inspired by particles moving around in the search space. Each particle in PSO has a position and a velocity. Each particle keeps track of the overall best value, *gbest,* as well as its previous best position, *pbest*. The new position of the particle is computed as Equations 3.2 and 3.3. Moreover, in order to facilitate better understanding of PSO algorithm the schematic view of particles movement within the 2-dimentions search space toward the global position is illustrated in Figure 3.3:

$$v_i(t+1) = w.\ v_i\ (t) + c_1\ .\ rand\ _1.\Big(\ p_{best}\ _i(t) \quad x_i(t)\Big) + c_2.\quad rand\ _2.\ (g_{best}\ _i(t) \quad x_i(t)) \tag{3.2}$$

$$x_i\ (t+1) = x_i(t) + v_i(t+1) \qquad (i = 1 \dots \dots N) \tag{3.3}$$

where *rand1* and *rand2* are the random values distributed uniformly between 0 and 1, c_1 and c_2 are the acceleration factors, which determine the relative pull for particles towards *pbest* and *gbest*. *w* is the inertia weight used to control global exploration and local exploitation of the particles and usually varied linearly and descendingly from 0.9 to 0.4. Moreover, Figure 3.4 presents the flow chart algorithm of PSO to explain the concept of conducted optimization.

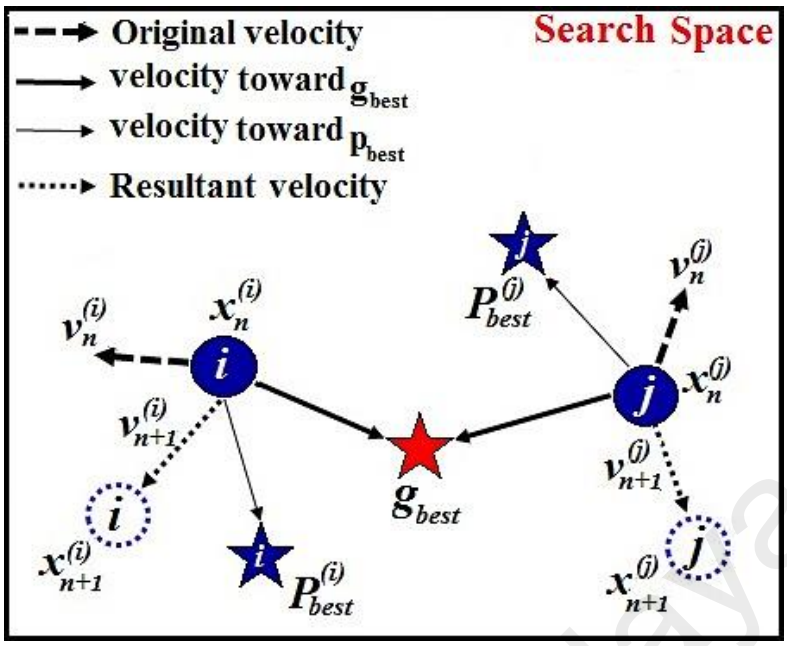

Figure 3.3: The mechanism of particles (i & j) movement toward the global position (gbest) within 2-dimensions search space.

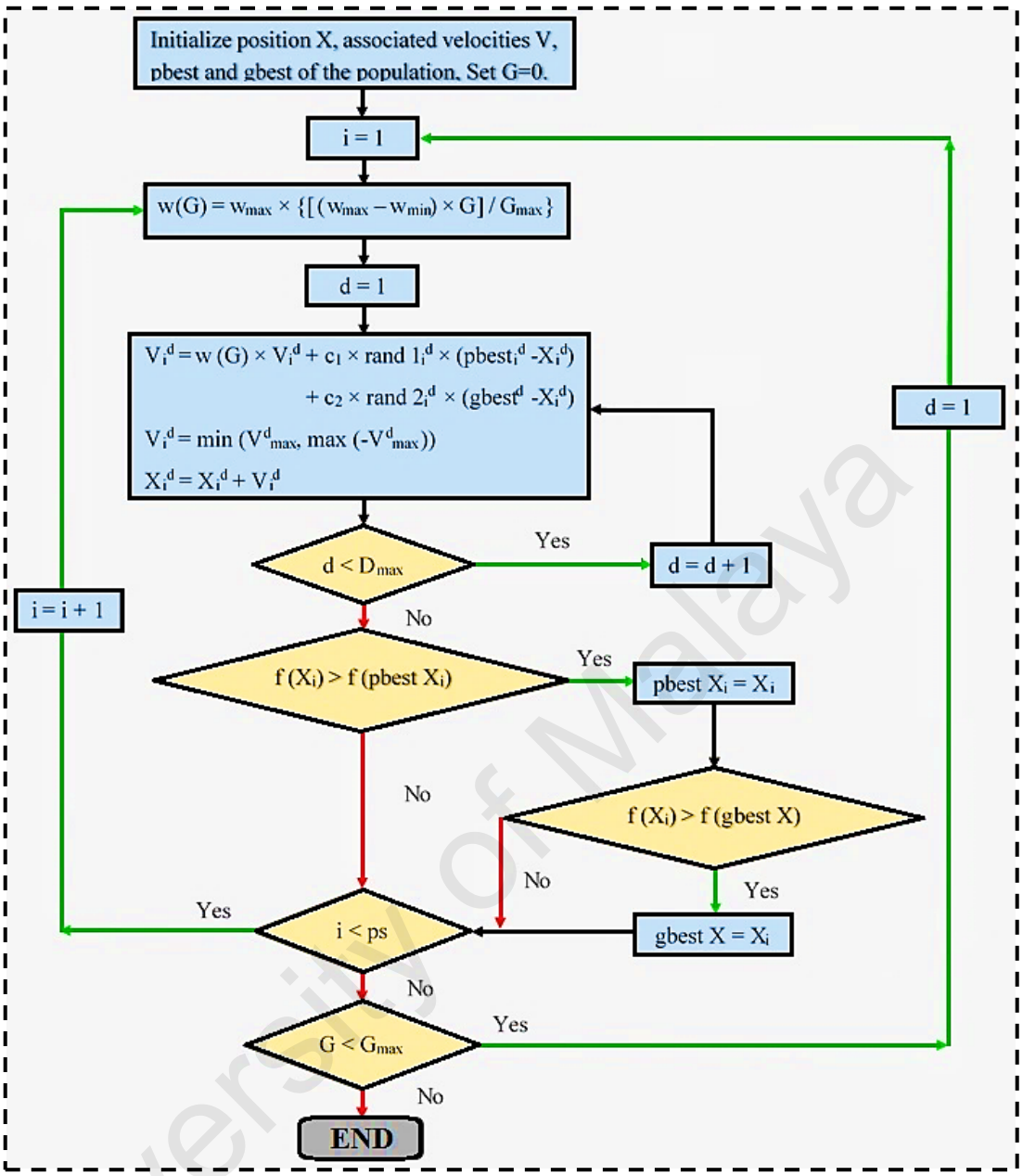

Figure 3.4: The flow chart of PSO.

Multi-objective particle swarm optimization (MOPSO) is implemented widely to optimize the several objectives simultaneously (Borhanazad, Mekhilef, Ganapathy, Modiri-Delshad, & Mirtaheri, 2014). Though, finding a unique optimum result is not possible, which maximizes both objectives, it is more appropriate to utilize the Pareto-optimal. Without sacrificing one of the considered objective function is not possible to improve another objective functions. Hence, the general form of multi-objective problems subjected to its inequality and equality constrains, which is provided in Equation 3.4.

$$Maximizing_{\ X\in\varphi}\ \boldsymbol{Y} = (f_1(X), f_2(X), \dots, f_k(X)) = F(X) \quad (3.4)$$

where,

$$\varphi = \{X\varepsilon R^k\ : g(X) \geq 0, h(X) = 0\} \quad (3.5)$$

$$F: R^n \rightarrow R^k$$

In multi-objective optimization, there is no unique results which represent the optimal value of each objective. As an alternative, there exists the Pareto-optimal solutions, which are a set of candidate results known as non-dominated solution. Supposing that $\Theta = (\Theta_1, \dots, \Theta_n)$ and $\Psi = (\Psi_1, \dots, \Psi_n)$ are two obtained results within the Pareto-optimal set. The result Θ is dominated by the result Ψ, represented by $\Theta > \Psi$ or $F(\Theta) > F(\Psi)$, if and only if the followed described conditions of Equations 3.6 and 3.7 are satisfied. Thus, the solution Θ will be considered as non-dominated result.

$$\forall i \in \{1, \dots, k\}: \qquad f_i(\theta) \geq f_i(\Psi) \quad (3.6)$$

$$\exists i \in \{1, \dots, k\}: \qquad f_i(\theta) > f_i(\Psi) \quad (3.7)$$

The red circled points shows the Pareto-optimal set (non-dominated solutions) for two considered objectives. Furthermore, the blue circled points are represented as the dominated solutions (Figure 3.5.a). Also, Equation 3.8 represents the set of Pareto-optimal solutions denoted by *P*.

$$P(Y) = \{Y_1 \in \Phi: \{Y_2 \in \Phi: Y_2 > Y_1, Y_2 \neq Y_1\} = 0\} \quad (3.8)$$

where

$$\Phi = \{Y \in R^k: Y = F(X), X \in \varphi \quad (3.9)$$

The multi-objective optimization algorithms are yielded Pareto-optimal as a series of the optimized results despite of a single solution. All results in Pareto-optimal are not superior to each other and the enhancement of one objective without sacrificing the other cannot be obtained. Thus, the theory of Fuzzy is implemented to achieve a candidate Pareto front (Pareto-optimal) solution, which potentially has the highest impact on the final result. Within the Pareto front, the considered Fuzzy theory to derive a single optimum solution, which is labeled as the best compromise result (Modiri-Delshad, Kaboli, Taslimi-Renani, & Rahim, 2016; Modiri-Delshad & Rahim, 2016). A relation between the achieved solutions must conduct to the best compromise result. The mechanism of choosing the best compromise result is considered using the Fuzzy theory, which highlights the best candidate. Generally, listing all non-dominated results in Pareto front in ascending order based on their membership functions, which can be provide a priority list of results. Accordingly, a Fuzzy-based membership functions are allocated to all objective functions followed by Equation 3.10.

$$\mu_{i,j} = \begin{cases} 0 & f_j(X_i) \le f_j^{min} \\ \frac{f_j^{min} - f_i(X_i)}{f_j^{max} - f_j^{min}} & f_j^{min} \le f_j(X_i) \le f_j^{max} \\ 1 & f_j(X_i) \ge f_j^{max} \end{cases} \quad (3.10)$$

Where f_i^{min}, f_i^{max} and fj (Xi) are presented the minimum, maximum amounts of the i^{th} objective function and the value of the j^{th} objective function for the i^{th} solution X_i, respectively. The Fuzzy-based membership function demonstrates the objective function's degree of optimum result ranged from 0 to 1 (Figure 3.5.b). For all non-dominated solutions, normalized membership function are computed via Equation 3.11.

$$\mu_k = \frac{f_i(X_i) - f_j^{max}}{f_j^{max} - f_j^{min}} \quad (3.11)$$

where the highest value of μ_k is considered as Fuzzy best compromise solution.

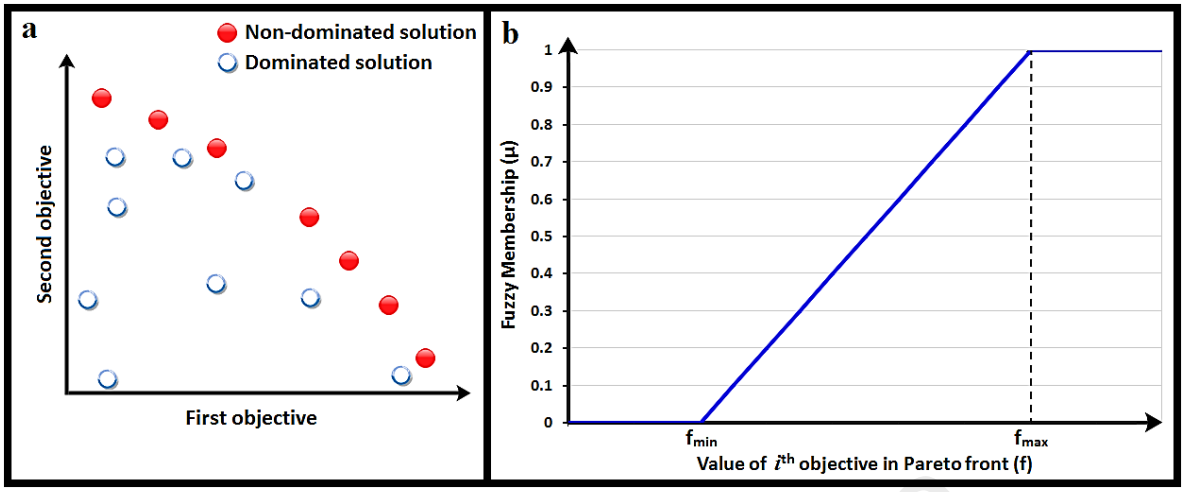

Figure 3.5: (a) The Pareto-optimal set for the two objective functions and (b) the fuzzy-based membership function.

Generally, the response surface methodology (RSM) defines the existing relation between dependent and independent variables. The main concept of RSM is to utilize the observed data from experimental procedures to achieve the optimum response of problems. In order to model the experimental procedures, more precisely and facilitate the formulation procedures dependent and independent variables which are measured on various scales, are normalized to a notionally common scale according to Equation 3.12.

$$X' = a + \frac{(X - X_{min})(b - a)}{X_{max} - X_{min}} \tag{3.12}$$

The second-degree polynomial model followed by Equation 3.13, is widely used in RSM to formulate and model the experimental outputs due to its flexible approximation. Even though this model is considered as an approximation, is easy to estimate and apply even when few findings are available about the current process. Moreover, it is able to be formed as wide variety of functions to determine its co-efficient waiting parameters (β's) easily.

$$Y' = \sum_{i=1}^{k-1} \sum_{j=2}^{k} \beta_{ij} X'_i \, X'_j + \sum_{i=1}^{k} \beta_{ii} X'^2_i + \sum_{i=1}^{k} \beta_i X'_i + \beta_0 \tag{3.13}$$

where Y' and β_{ij}, β_{ii} and β_i are considered as normalized independent variable and the second-degree polynomial regression coefficients for the intercept, linear, quadratic and interaction terms, respectively. Also, the normalized independent variables are represented by X'_I and X'_j while k denotes the number of these variables in this equation and β_0 is referred to renaming unexpected error. The regression coefficients of this model are determined through the least absolute deviation. The global search optimization algorithms, are tried to define the optimal values of the weighting factors by which the used model can fit to observed data through the least absolute deviation. For this aim, the objective function is defined by Equation 3.14 for minimizing the differences between the observed and estimated outputs based on the considered model (the second-degree polynomial model).

$$F(\beta) = \sum_{i=1}^{n} |(Y_i'\ (observed) - (Y_i'\ (estimated))| \tag{3.14}$$

Where $F(\beta)$ is considered as the objective function value, β is a vector which contains the regression weighting parameters and n is the total number of observations. The nonlinearity of the experimental procedures make this estimation as a complex optimization problem, which requires an efficient technique to find optimal or near values of weighting factors given by Equation 3.15:

$$\beta = \arg\min F(\beta) \tag{3.15}$$

To quantify the prediction performance of models, several evaluation criteria are employed; coefficient of determination (R-squared), mean absolute percentage error (MAPE), percentage of model accuracy (A), root mean square error (RMSE) and Thiel's inequality coefficient (U-statistic) followed by Equations. 3.16 to 3.20.

$$R^2 = \frac{(\sum_{i=1}^{n}((Y_i'\ (observed) - \overline{Y_i'}(observed)\ (Y_i'\ (estimated) - \overline{Y_i'}(estimated))^2}{\sum_{1=1}^{n}((Y_i'\ (observed) - \overline{Y_i'}(observed))^2 \sum_{i=1}^{n}((Y_i'\ (estimated) - \overline{Y_i'}(estimated))^2} \tag{3.16}$$

$$MAPE\ (\%) = \frac{1}{n}\sum_{i=1}^{n} \frac{(Y_i'\ (observed) - (Y_i'\ (estimated))}{Y_i'(observed)} \times 100 \quad (3.17)$$

$$A = \frac{1}{n}\sum_{i=1}^{n} \left(1 - \frac{(Y_i'\ (observed) - (Y_i'\ (estimated))}{Y_i'(observed)}\right) * 100\% \quad (3.18)$$

$$RMSE = \sqrt{\frac{1}{n}\sum_{1}^{n}(Y_i'\ (observed) - (Y_i'\ (estimated))^2} \quad (3.19)$$

$$U = \frac{RMSE}{\sqrt{\frac{1}{n}\sum_{1}^{n}(Y_i'\ (observed))^2} + \sqrt{\frac{1}{n}\sum_{1}^{n}(Y_i'\ (estimated))^2}} \quad (3.20)$$

In above mentioned equations, Thiel's inequality coefficient affords a measure of how well fitted a responsible sets of observed data to predicted values. This performance indicator is locate between amounts of 0 and 1. Though, closer value to 1 indicates the estimation is no more than a simple guess, whether the amount closer 0 means greater estimating accuracy with an optimum fitting.

(b) ***Sensitivity Analysis using Pearson coefficient analysis***

Here, the sensitivity analysis of PVDMS parameters using Pearson coefficient have been analyzed. A coefficient analysis has been proposed to indicate the measure for correlation of linear dependence between two different variables dented by *X* and *Y* (Zahedi, Azizi, Bahadori, Elkamel, & Alwi, 2013).

$$r = \frac{\sum(X-\bar{X})(Y-\bar{Y})}{\sqrt{\sum(X-\bar{X})^2 \sum(Y-\bar{Y})^2}} \quad (3.21)$$

Where, $\bar{Y}$and $\bar{X}$ are considered as the mean values of variables *Y* and *X* in sequence. The Pearson correlation factor is extensively utilized in the variety of studies as a method to measure the strength of linear dependence between two different variables. This factor is normally known as "*r*", which is varied from -100% to 100%. While, the value is more closed to 100% indicates correlation between *Y* and *X*. A multi-objective

optimization can be constructed in order to specify the optimal value of each decision variables aimed at maximization the output objectives. Herein, three independent variables labeled as DC power, argon flow rate and DC bias, which were bounded by maximum and minimum amounts of PVDMS machine parameters.

(c) *Maximizing Adhesion Strength and Hardness of Nb PVD via MOPSO*

A multi-objective optimization can be constructed in order to specify the optimal value of each decision variables aimed at maximization the output objectives. Herein, three independent variables labeled as DC power, argon flow rate and DC bias, which were bounded by maximum and minimum amounts of PVDMS machine parameters. The multi-objectives optimization method was implemented to enhance the adhesion strength and hardness of Nb PVD coating through alerting the independent variables of experimental design. As, the considered objectives cannot be taken from negative values, also exceed from a specific logical level, they were bounded in this constraint. In case of violation the constraint, the multi-objective optimization reiterates until reach a valid solution. Within the multi-objective optimization, the main objective is finding the set of non-dominated solutions, which cannot be further improved. These set of solutions are considered as the Pareto-optimal front. In spite of weighted sum method as a conventional method which, suggests only a single optimum solution, multi-objective optimization method can be widely applied to generate the Pareto-optimal front. While finding a unique optimal solution that maximize both objectives is a difficult task, there is a possibility of using a Pareto-optimal front, which may enhance one of the objective functions without sacrificing the optimality of other objective function. Due to the simple structure, efficient mechanism, robust and more likely to locate global optimum solution within searching the decision variable space, the MOPSO has been applied to obtain the highest logic values of Nb PVD coating's output properties (adhesion strength and hardness). It is remarkable that, in compared with weighted aggregation technique,

MOPSO is highly potential to predict the set of possible solutions know as Pareto-optimal front. In MOPSO, a random set of populations are generated within the decision variable space boundary and the objective values corresponding to those random solutions can be calculated by the PSO optimized second-degree polynomial models.

3.1.2.5 Response Surface Methodology

According to JMP *2005*, response surface methodology is in modeling a curved quadratic surface to continuous factors. It can locate any minimum or maximum response exists inside the factor region. In order to fit a quadratic function, three different values for each factor are essential for this purpose. However, the standard two-level designs are not capable of fitting curved surfaces (Lenth, 2009). Among the commonly used response surface designs in statistical analysis is the central composite design which combines a two-level fractional factorial, center points and axial points, as illustrated in Figure 3.6.

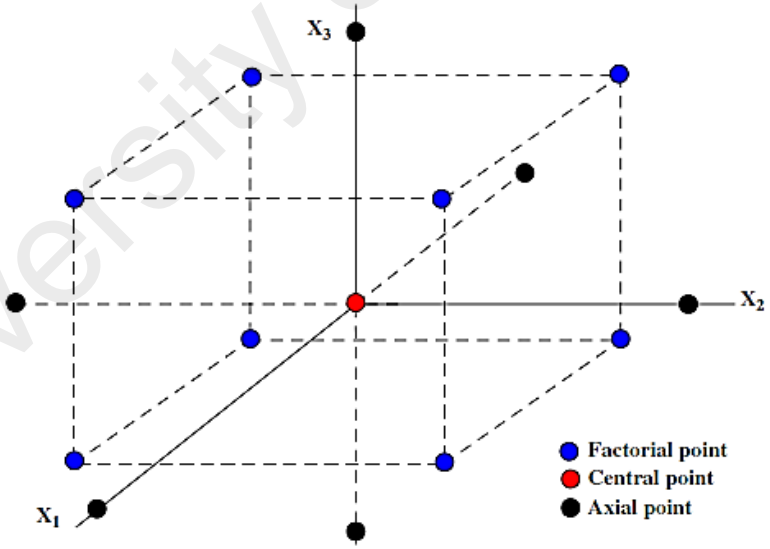

Figure 3.6: Central composite design (CCD) (Cho & Zoh, 2007).

3.1.3 Anodically Fabrication of Mixed Oxide TiO_2-Nb_2O_5-Al_2O_3 Nanotubes

To growth the ternary oxide TiO_2-Nb_2O_5-Al_2O_3 nanotubular arrays, optimized Nb as-prepared surfaces were electrochemically anodized at 50 °C stirred fluoride-based (0.5 wt% NH_4F, R&M Chemical) electrolyte contains 95:5 v% ethylene glycol (EG), purity >

99%, Merck and distilled water. The two electrode electrochemical cell (20 mm cathode/anode distance) was designed using 7 mm diameter of graphite cathodic counter electrode. The 240 min anodic process was done with DC power supply (E3641AModel, Agilent Technologies, Palo Alto, USA) at a steady potential of 20 V. The samples were washed with deionized water to remove surface residual materials after the anodization process. Finally, the formed amorphous mixed oxide nanotubes were annealed for 30 min at 440 °C with low heating rate to crystallize the coatings. The schematic view of the fabrication of highly ordered Ti-Nb-Al-O bioceramic layer on Ti67IMP is demonstrated in Figure 3.7.

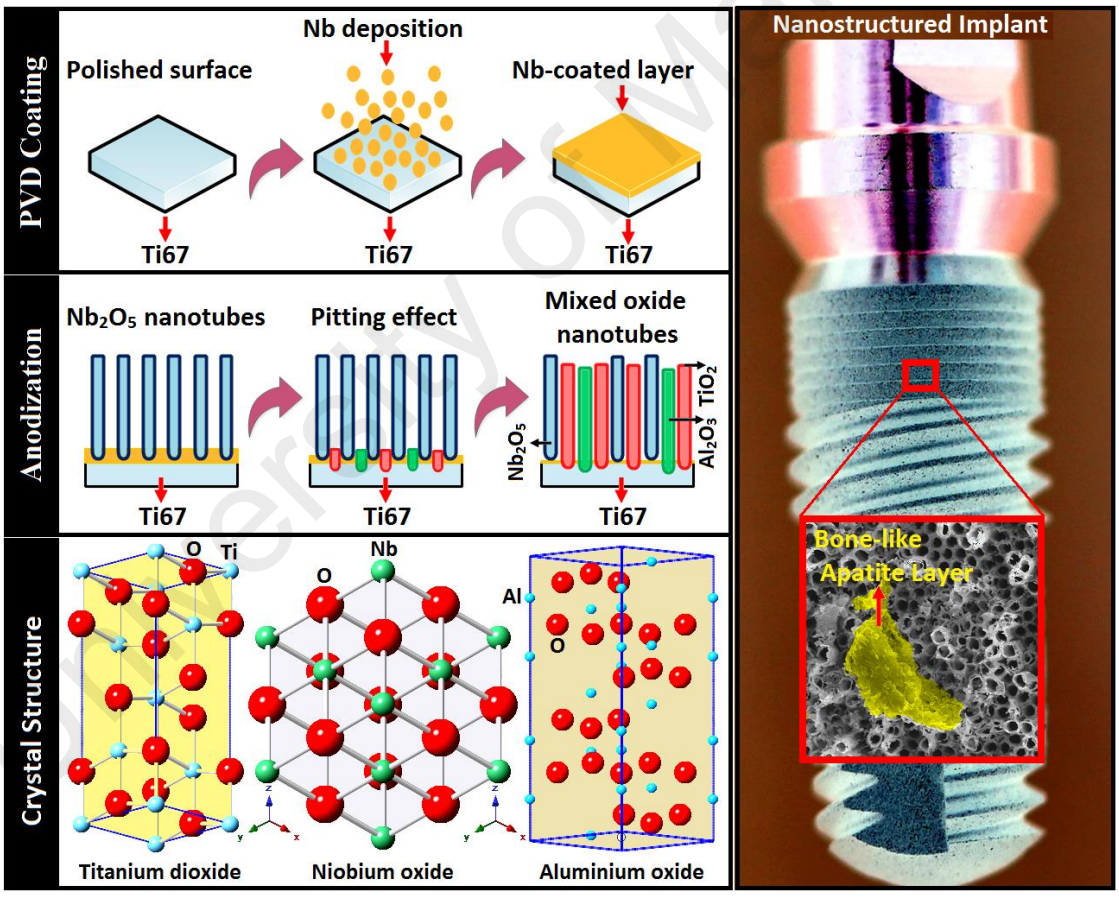

Figure 3.7: A schematic view of the fabrication process of mixed oxide nanotube arrays.

3.1.4 Spin Coating

3.1.4.1 Synthesis of Graphene Oxide (GO) Suspensions

The micron-sized graphite flakes used in this project were purchased from Ashbury Inc. The sulfuric acid (H_2SO_4, 94%), phosphoric acid (H_3PO_4, 98%), potassium permanganate (KMnO4, 99.9%), hydrogen peroxide (H_2O_2, 30%) and hydrochloric acid (HCl, 37%) were purchased from Merck (Malaysia). All of the aqueous solutions were prepared using double distilled water (ddH_2O). The GO was prepared from the graphite flakes using a simplified Hummers' method (Azarang, Shuhaimi, Yousefi, & Sookhakian, 2014; J. Chen, Yao, Li, & Shi, 2013; Fu, LIU, ZOU, & LI, 2005; Ming, 2011). Initially, mixture of H_2SO_4 (360 ml) and H_3PO_4 (40 ml) were gradually added into a beaker contained 3 g of graphite at room temperature. Then, $KMnO_4$ (18 g) was added to mixture and stirred for 4320 min to ensure complete oxidation of graphite. Then, the prepared suspension was diluted and cooled by adding 400 ml of ice water and wait for 10 minutes. Subsequently, H_2O_2 with purity of 30% was added until the gas evolution ceased. This action was conducted to ensure the reduction of residual permanganate into soluble manganese ions. Meanwhile, the synthesized GO suspension washed with diluting 1M HCl and ddH_2O repeatedly until reaching pH 5 via 10 min centrifuging at 4000 rpm for three times. The product was separated from the considered mixture via a centrifuge spinning at 11000 rpm and 5 min sonication to exfoliate graphite oxide. The treated material was centrifuged for 10 min to separate the GO sheets from supernatant. Then the GO powder was obtained by drying at 60 °C in an oven under night condition for 48 h. To fabricate thin films from synthesized GO, the dried powder was subsequently suspended in water followed by sonication and centrifuging at 14000 rpm to remove the multilayer species. Hence, the recovered supernatant included few-layer GO sheets at concentration of 15 mg/mL can be remained stable without precipitation for a long period of time. GO nanosheets are naturally hydrophobic which is caused by oxygen-based

functional group. So, GO nanosheets have a great colloidal stability in different solvents particularly polar ones, e.g. DI water, ethylene glycol, methanol and etc.

3.1.4.2 Preparation of GO/Mixed Oxides Nanocomposite

For thin-film fabrication from GO, the powder was first suspended in water by ultrasonication and centrifuged at 14000 rpm to remove multilayer species, which constituted -10% of the powder by weight. The carefully recovered supernatant is a solution of few-layer GO with concentration as high as 15 mg/mL and is stable against precipitation for several months. We used few-layer GO solutions to deposit the GO films on piranha-cleaned (caution: piranha mixture is a strong oxidizer), (aminopropyl)triethoxysilane (APTES) treated, glass and quartz surfaces. Testing film deposition by spin coating, drop casting, and solvent-induced precipitation revealed that spin-coating produces more uniform and thinner films than the other methods, and this technique was used for all films presented here. Typically, the substrate was completely covered with sufficient amount of the 1 mg/ml GO solution, which was allowed to stand in static condition around 60s for better surface absorption and spin coated at 600, 800 and 1600 rpm for 60s each. Accordingly, the transparent deposited GO film on mixed nanotubular array dried at 95 °C in a vacuum oven and kept in ambient cabinet drier conditions in sealed plastic containers.

3.1.4.3 Silver Nanoparticles Decorated Graphene Oxide (AgNPs-GO)

The synthesized graphene oxide (GO) nanosheets were used to pattern with decorated AgNPs. Chemicals such as $AgNO_3$, HNO_3 (nitric acid), H_2SO_4 (sulphuric acid) and NaOH (sodium hydroxide) were procured from Sigma–Aldrich Co., Selangor, Malaysia. The synthesized Ag-GO structure with different concentrations of AgNPs were prepared via dispersing the nanocomposite in distilled water without using a non-covalent e.g. surfactants. It is well known that GO has a lot of oxygen-containing species on its

main structures. It is therefore expected that oxygen attachment to Gr in any chemical form (epoxide, hydroxyl, carboxyl and ketonic-type functional groups) both on the basal plane and at the edges increases the hydrophilicity. To have higher degree of functional groups, an additional acid treatment process was conducted via dispersing GO in a 1:3 ratio of HNO_3 and H_2SO_4 solution (strong acid medium) for 3 h by a bath-ultrasonication. After 3 h, GO nanosheets were washed several times by DI water and then dried in an oven at the temperature of 70^{o} C for more than 24 h. Later the functionalized GO nanosheets were decorated with 17% Ag by a chemical reaction method. Subsequently, the solution of ammonia-silver was prepared by adding drop wise ammonia (1 wt%) to 0.01 L silver nitrate solution (0.05 M) until fully reacted and silver color disappeared. The Ag $(NH_3)_2OH$ solution (0.04 M) was mixed with 120 ml functionalized GO (1 mg/mL) solution, at the weight ratios of 1:12 and 1:6 of Ag-GO concentrations. The irradiation of final solution was done under vigorous stirring for 4 h. Then, different concentrations of Ag were collected after centrifuge at 11,000 rpm for 40 min. The obtained composite was washed well with distilled water several times to remove unreacted materials. Afterward, the different concentrations of prepared Ag-GO materials were used to coat on the surface of mixed oxides/Nb/Ti67IMP specimens. The resulting suspensions were stable and no sedimentation of particles was found for up to 60 days. Testing film deposition by spin-coating, drop-casting, and solvent-induced precipitation revealed that spin-coating produces more uniform although thinner films than the other methods, and thus considered technique was used for all films presented herein. Then, the substrate was completely covered with sufficient amount of the 1:12 and 1:6 Ag-GO solutions comparable. To assess mechano-biological analysis, synthesized nanostructures spin-coated on tubular topographies. All the dropped nanostructures were allowed to stand in static condition around 60s for better surface absorption and coated at 600, 800 and 1600

rpm for 60s each. Accordingly, the decorated Ag-GO films were dried at 95 °C in a vacuum oven and kept in drying cabinet.

3.1.4.4 Thermally Exfoliated Mono-layer Graphene (TGr)

Generally, GO is a compound of carbon, oxygen, and hydrogen in variable ratios. GO mostly has different functional groups such as epoxide groups, carbonyl (C=O), hydroxyl (-OH), phenol, and carboxyl groups (COOH). The presence of different oxygen-based functional groups provide good colloidal stability for this material, however, the main structure is full of defects which deteriorate the main structural properties. So, GO is heavily chemically oxidized with many permanent functional groups, leading to numerous defects such as holes into the basal plane. These defects are not readily healed even upon annealing (Ruoff, 2008). Therefore, reduction of graphene oxide was suggested as a promising method for restoration of main structure. However, even with most effective reducing agents such as H2 or hydrazine, and even annealing at very high temperature, the original crystalline structure of graphene is not restored (Sun, Kohama, Zhang, Lomeda, & Tour, 2010). After introducing liquid phase exfoliation of graphite in the presence of high surface-tension organic solvents, a promising method was born to produce pure single-layer graphene with original crystalline structure (Hernandez et al., 2008). Owning original crystalline structure and lack of defects, pure mono-layer Gr showed superior mechanical, biological, electrical and thermal properties as compared with other carbon allotropes such as GO, Gr Nanoplatelets and etc. In this projects, thermally exfoliated mono-layer Gr sheet was synthesized as following. Firstly, the bulk graphite (10 mg) and $AlCl_3$ (185.4 mg) were mixed and poured into a Teflon reaction vessel. Then tetrahydrofurfuryl polyethylene glycol (PEG, 200 ml) was added and sonicated for 30 min at room temperature to reach a back suspension under nitrogen atmosphere. Once adding the PEG, small amount of white smoke was observed. In order to speed the reaction and increase the degree of functionalization, 0.5 ml of concentrated

hydrochloric acid were added dropwise to the suspension over the sonication stage. After 30 min sonication, the Teflon vessel was sealed and transferred into an industrial microwave and irradiated at 150 °C at an output power of 700 W for 20 min (with frequently of 5 min sonication and 5 min placed under microwave irradiation). In the presence of $AlCl_3$ and concentrated hydrochloric acid, PEG can be protonated and an electrophilic species was achieved, which is a cationic electrophilic reagent with significantly superior reactivity (Amiri et al., 2016a). An electrophilic addition reaction occurred between the PEG and graphite, resulting in the attachment of the PEG groups and hydroxyl groups to the exposed edges and side of the expanded graphite flakes, thereby producing functionalized, expanded graphite. Microwave irradiation was used to increase the speed of the reaction and the functionalization yield. Note that microwave irradiation was employed to enhance the reaction speed and amplify the degree of functionalization. Then, the resulting mixture was left for 24 h to separate large unstable graphite aggregates. Subsequently, the resulting black ink-like dispersion was left to sit for 24 h to separate large unstable graphite aggregates. The functionalized graphite without unstable graphite aggregates was expanded and was much more soluble in such DMF and EG than the pristine graphite (Lotya et al., 2009; Lv et al., 2009). After functionalization, the expanded graphene had the great colloidal stability in EG than the pristine graphite (Amiri et al., 2016b). Then, the homogeneous suspension of PEG-treated expanded graphite in EG was sonicated for 2 h to exfoliate the graphene layers. Then, the mixture was centrifuged at 3000 rpm for 30 min and the supernatant was collected. After filtering and, washing the supernatant, thermal treatment up to 500 °C under a nitrogen atmosphere was applied for 15 min to remove all functional groups to produce pure graphene without functional groups. The product was labeled as pure mono-layer Gr aimed at functionalization with Arg amino acid group.

3.1.4.5 Functionalized Arginine-graphene (Arg-Gr) Composite

The mechanism for functionalization of mono-layer thermally exfoliated Gr with Arg includes the generation of semi-stable diazonium ions, which then initiate a radical reaction with the TGr sheet. To this end, TGr and deionized water were poured into a vessel. The reaction vessel was sonicated after adding arginine, isoamyl nitrite and concentrated HCl, and the resulting black mixture was again poured into a Teflon vessel for doing the reaction under microwave irradiation at 700 W for 30 min (with frequently of 5 min sonication and 5 min placed under microwave irradiation). Subsequently, to have the functionalization degree of almost 20%, the resulting suspension was mixed vigorously for 48 h, and, after cooling to room temperature, it was filtered and washed thoroughly with DI-water, followed by drying for 48 h at 50 ^{o}C water.

3.1.4.6 Arg-Gr/Mixed Oxides Nanocomposite

Herein, to fabricate Gr-Arg/TiO_2-Nb_2O_5-Al_2O_3 composite reinforced Ti67IMP alloy, spin coating technique has been utilized. The dropped functionalized nanostructures was attached on the anodic mixed bioceramics with leaving 60s static condition for better surface absorption and coated at 600, 800 and 1600 rpm for 60s each. Then, transparent multilayer coating dried at 95 °C in a vacuum oven and kept in ambient drying cabinet.

3.2 Characterization Techniques

3.2.1 Physico-chemical Characteristics (FESEM/TEM/SAED/EDS/XRD/GIXRD/XPS/RAMAN/FT-IR)

In this project, the microstructure and morphological features of the synthesized materials and coating layers were assessed via field emission scanning electron microscopy (FESEM; SU8000/SU8200, Hitachi, Japan) with an acceleration voltage of 10 kV attached with Energy-dispersive X-ray spectrometry (EDS) and elemental mapping

analysis equipment to examine the chemical constituents and the spatial distribution of elements. Also, transmission electron microscopy (TEM, HT7700, Hitachi, Japan) with an acceleration voltage of 2 and 120 kV and high resolution TEM with selected-area electron diffraction (SAED) to characterize the crystal structure. Besides, phase analysis were performed with a X-ray diffractometer (XRD, PANalytical Empyrean, Netherlands) using a Cu–Kα radiation at 30 kV and 35 mA over a 2θ range from 20° to 80° and Grazing incidence X-ray diffraction (GIXRD) PANalytical Empyrean system with *Cu–Kα* radiation over a 2*θ* range from 20° to 80°. To examine the XRD reflections, "*PANalytical X'Pert HighScore*" software was used wherein the reflections were contrasted to the standards gathered by the Joint Committee on Powder Diffraction and Standards (JCPDS). Moreover, X-ray photoelectron spectroscopy (XPS, ULVAC-PHI Quantera II) with $Al_{K\alpha}$ radiation (hv = 1486.6 eV) as the excitation source operated at 25.6 W (beam diameter of 100 µm) was used at room temperature to measure the elemental composition and atomic ratio of corresponding elements and fitting analysis (wide and narrow scan) have been presented via attached software to machine The characteristic peaks corresponding to each materials and bounding of fabricated ceramic and carbon-based nanostructures to find the crystallographic orientation, defect density and crystallinity via Raman spectroscopy analysis using Model, In-Via Raman Microscope, Renishaw, England with 30-40% laser power of 20 mW. The applied parameters for Raman analysis such laser wavelength, grating, laser power and exposure were considered as 514, 1800, 10%, and 10s respectively in each sample analysis. Moreover, the mutual absorbance bands to hydroxyl functional groups stretching. The position of the characteristic bands related to fabricated nanostructures were assessed via 64 scans Fourier transform infrared spectroscopy (FTIR) analysis (Bruker IFS 66/S, Germany, MIR-source, resolution 4cm^{-1}) in room temperature. Figure 3.8 represents schematic illustration of physico-chemical characterization.

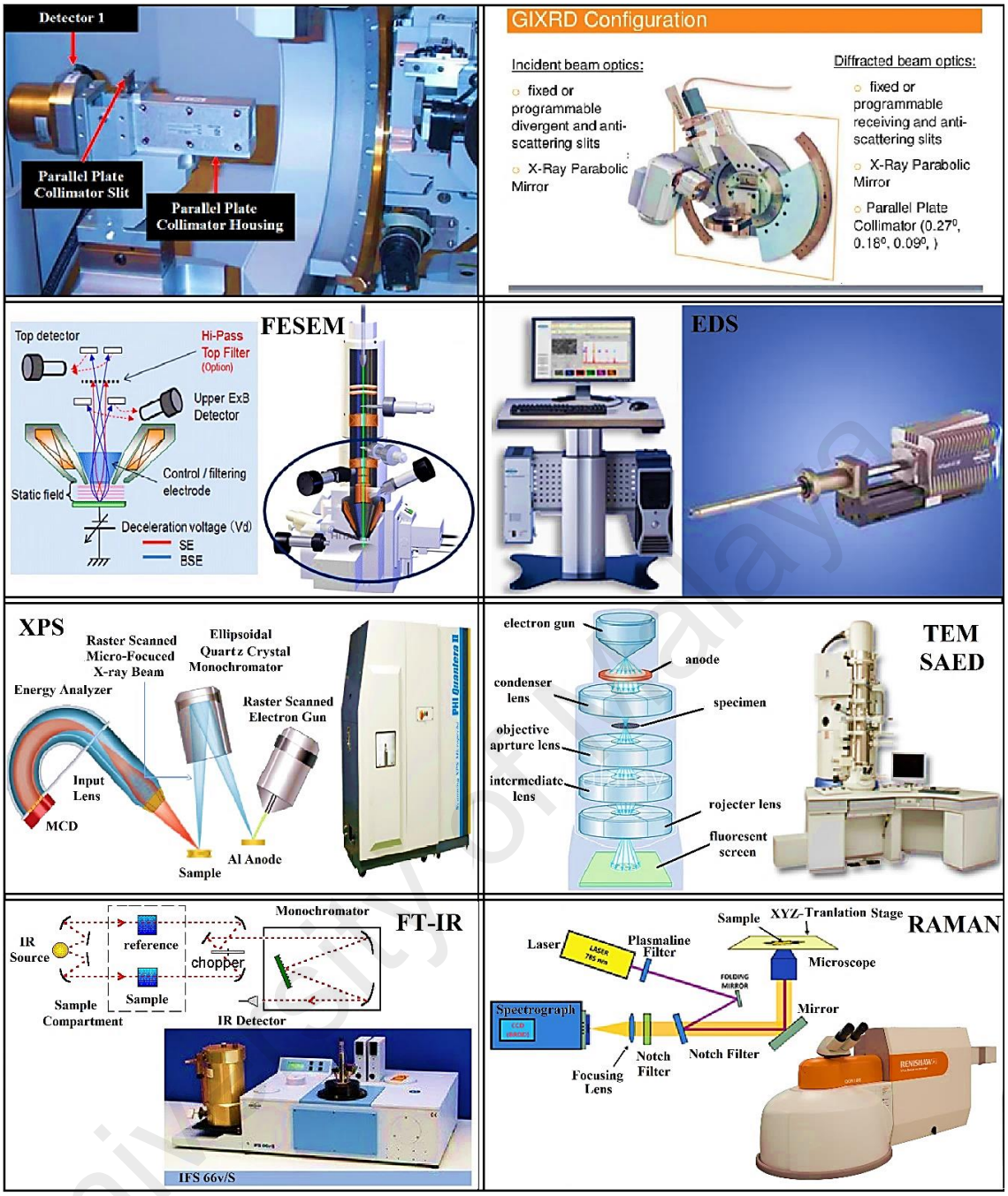

Figure 3.8: Schematic illustration and devise of physico/chemical characterization. ***[With academic permission of The collimation system in PANalytical X'pert Pro Gazing Incidence X-ray (User Manual, University of Minnesota, College of Science and Engineering Characterization Facility, Hi-Tech Instruments, Co., BRUKER Co., Encyclopædia Britannica, Inc., CHEMICOOL.COM, EVISA databases, ULVAC-PHI, Inc., ANDOR Ins. Co. and Iuliana Cernatescu PANalytical Inc.].***

3.2.2 Mechanical Properties

3.2.2.1 Scratch Assessment

The adhesion strength between coatings and substrate was measured by a Micro Materials nano-scratch tester (Wrexham, U.K.) within the specified load operation (1500, 2000 and 2500 mN) by means of a diamond indenter (25.0 ± 2.0 μm in radius and 90.0 ± 5.0° in angle). Throughout the examination, the deepness of probe diffusion and tangential load were incessantly checked. During the analysis, the probe-penetration depth also frictional loads were monitored continuously and plotted the depth, load and friction graphs versus around 1000 μm distance of scratch line. To appraise baseline specimen topography, a pre-analysis was conducted by an ultra-low contact force. After that, the measurements were conducted at a constant speed of 2 μm s^{-1} and each measurement was repeated three times to get average values of the adhesion strength. Then, for determining the damaged profiles affected by scratch test, a light optical microscope (Olympus BX61, Japan) has been used to investigate the failure point position.

3.2.2.2 Microhardness Evaluation

The coatings' mechanical properties were followed by hardness assessment as well as adhesion strength. The Vickers microhardness of the substrate and coated specimens was determined using microhardness measurement equipment (Shimadzu Newage Micro Hardness Tester HMV-2T). The harness-duration and applied load were 5 s and 98.07 mN, respectively. Three indentations per each experiment were performed to determine the average microhardness values. The schematic view of performed mechanical analysis was illustrated in Figure 3.9.

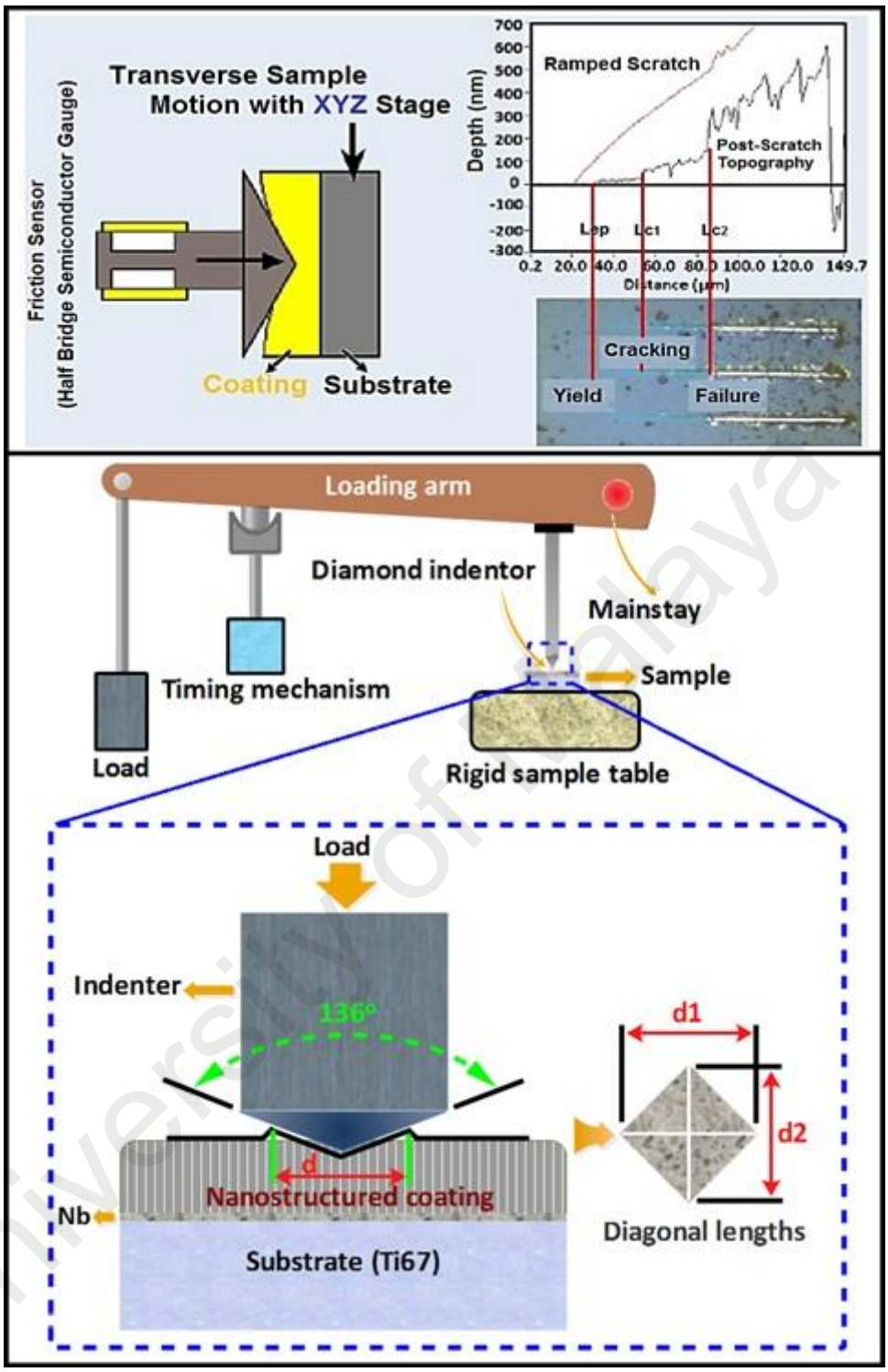

Figure 3.9: A schematic illustration of the Micron Material Nano Test equipment and a scratch test with 3 µm end radius probe scanning over a 150 µm track at a scan speed of 2 µm/s (Upper part) *[With academic permission of NanoTest Vantage. Co]* and Vickers microhardness (Down).

3.2.3 Surface Topography and Wettability Measurement

Herein, atomic force microscope (AFM, ScanAsyst mode, Frequency 1 Hz, Bruker) was employed to examine the topographical texture of functional carbon-based

structures. AFM analysis was mostly investigated the changing of flake thicknesses after amino acid functionalization. To prepare AFM samples, the synthesized Gr-based materials were sonicated in DMF without any additives and then drop-cast on mica. The surface wettability was analyzed with measuring the contact angle (CA) with a sessile drop of deionized water deposited on to the specimen's surface, where the hydrophilic or hydrophobic balance of the nanostructured layers was estimated by a video-based optical CA measuring instrument (OCA 15EC; Data Physics Instruments GmbH; Germany). The liquid volume and dropping velocity were fixed to 5 µl and 2 µl sec^{-1} throughout the measurement, respectively with an accuracy of ±1° at 26±1 °C. The droplet height "*h*" and width "*d*" were measured to calculate the CA "θ" as followed in equation 3.28 (Elias, Oshida, Lima, & Muller, 2008).

$$\theta(^{\circ}) = 2tan^{\ 1}\frac{2h}{d} \tag{3.22}$$

3.2.4 In-vitro Corrosion Resistance

In-vitro corrosion analysis of the samples was performed by electrochemical Tafel polarization technique, i.e. DC using a potentiostat/galvanostat model Auto Lab PGSTAT30 from Ecochemie (Netherlands), which was controlled by frequency response analyzer (FRA). The polarization behavior was recorded after immersion in Phosphate-buffered saline (PBS) for 60 min using a three-electrode cell, where the specimens, platinum (Pt) wire and saturated calomel electrode (*SCE*) were the working, counter and reference electrodes, respectively. In this test, the corrosion potentials (E_{corr}), corrosion current (I_{corr}), corrosion rate (*CR*) and anodic/cathodic Tafel slopes (β_A and β_C) were obtained from the Tafel plots with the scan rate of 0.001 Vs^{-1}. The measurement region of Tafel slopes was through range of~ ±4 V_{SCE} for coated samples. The polarization resistance (R_p) values were determined using Equations 3-23 to 3-26 (Ranganatha & Venkatesha, 2014).

$$I_{corr} = \frac{\beta}{R_p} \tag{3-23}$$

where β was considered a constant as below:

$$\beta = \frac{\beta_A \beta_C}{2.3(\beta_A + \beta_C)} \tag{3-24}$$

where β_A and β_C (V^{-1}) and R_p (Ω) were labeled as Tafel polarization slopes rand elated resistance, which *CR* was calculated by following equation.

$$CR\ (mmyear^{-1}) = \frac{0.13 I_{corr}(E.W.)}{d} \tag{3-25}$$

where *E.W.*, *d*, and I_{corr} are equivalent weight of the corroding species in g, density of the corroding species in g cm^{-3}, and corrosion current in A cm^{-2}. Also, *P.E.* was determined to evaluate the effectiveness of corrosion protection by the specimens using the Equation 3-26.

$$P.E(\%) = \frac{I^0_{corr} \quad I^C_{corr}}{I^0_{corr}} \times 100 \tag{3-26}$$

where I^0_{Corr} and I^C_{Corr} are the corrosion current of the IMPTi67 in the absence and presence of the thin film layers, respectively. The schematic view of *in-vitro* corrosion test was shown in Figure 3.10.

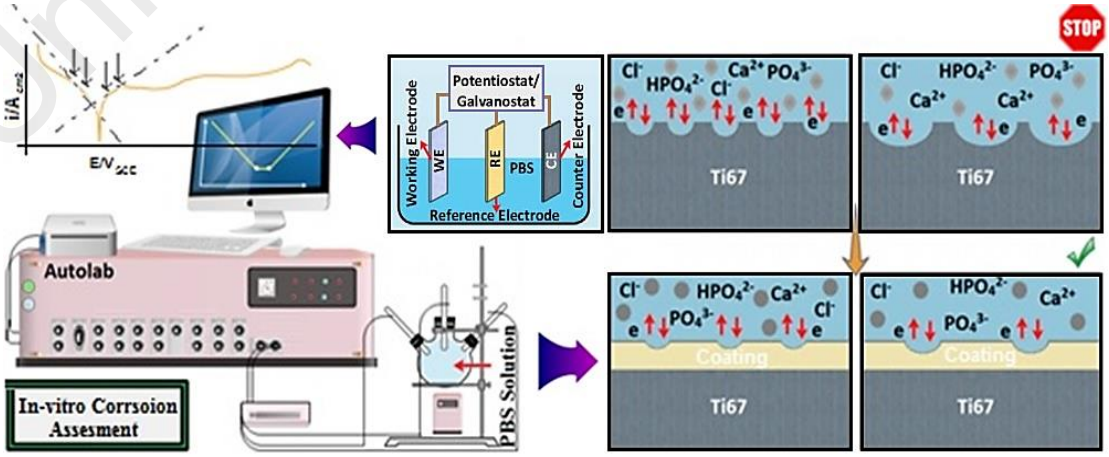

Figure 3.10: A schematic illustration of the in-vitro corrosion test in PBS.

3.2.5 Biological Evaluation

3.2.5.1 Soaking in Simulated Body Fluid (SBF)

In-vitro bioactivity of the structured thin films and composites was examined by appraising the bone-like apatite layer formation on the surface of the specimens after immersion into the simulated body fluid (SBF). The considered media with ion concentrations similar to those in human blood plasma were prepared in accordance with the described method (Kokubo, 1990; Kokubo & Takadama, 2006). Briefly, reagent grade $CaCl_2$, $K_2HPO_4.3H_2O$, NaCl, KCl, $MgCl_2.6H_2O$, $NaHCO_3$, and Na2SO4 were dissolved in distilled water and the pH adjusted to 7.3. The specimens were soaked in SBF and kept at 37 °C in a humidified atmosphere containing 5% CO_2 for time period of 10 days at a surface area to volume ratio of 1 cm^2 ml^{-1}. Afterwards, the specimens were gently rinsed with double deionized water and PBS to remove SBF and then dried at 80 °C for 10 h. To examine the microstructure of formed apatite layer, the sample surface were analyzed by FESEM and EDS characterization.

3.2.5.2 Antibacterial Activity

Antibacterial activity of bare Ti67IMP alloy and different concentrations Ag-GO samples on anodic mixed oxide nanotubes were assessed using a Gram-negative bacteria *Escherichia coli* (*E. coli*, ATCC 15597) and a Gram-positive bacteria *Staphylococcus aureus* (*S. aureus*, NCTC 6571), cultivated in Luria-Bertani broth at 37 °C for 12 h. Before performing the test, the specimens were sterilized by autoclaving at 126 °C for 15 min. Then, 1 ml of bacteria culture at a concentration of 10^8 CFU ml^{-1} was slowly dripped onto the sample surface. The specimens were then incubated at 37 °C for 24 h with shaking at 120 rpm using an orbital shaker incubator (Benchtop, Ind. & Vac. Instrument). At end of the incubation time, the culture medium was sampled to determine the viable counts of bacteria. The samples were gently rinsed with PBS in order to eliminate non-adherent bacteria, and the adhered bacteria on each specimen were detached using

ultrasonic vibration for 5 min with the resulting bacterial suspension in 1 ml of LB broth, after which the bacterial counts of viable bacteria that adhered on the specimens were performed. The viable bacteria in the sampled suspensions were counted using the serial dilution method and platted on to LB agar plates and incubated at 37 °C overnight. The antibacterial activity of bacteria in the culture medium and the antibacterial activity for adhered bacteria on the specimens were calculated based on the following formulae:

(I) Antibacterial activity for bacteria in the medium (R*p*) = (B - A)/B × 100%. and,

(II) Antibacterial activity for adherent bacteria on the specimen (R*a*) = (D - C)/D × 100%.

where, A is the average of viable bacteria number in culture medium inoculated with the samples, B indicates the average viable bacteria number in the culture medium inoculated with no specimen (blank control), C and D are the average number of viable bacteria on the modified specimens and plain sample respectively.

Herein, the average viable bacteria number in the culture medium inoculated with or without the specimen (blank control) and modified Ti67IMP alloy specimens were investigated for antibacterial activity. Besides, the antibacterial performance of the functionalized Arg-Gr composite was assessed in comparison to pure GO, 1:12 and 1:6 Ag-GO nanostructures using *E. coli* (ATCC 15597) and *S. aureus* (NCTC 6571). Both bacterial strains were cultured overnight in Luria Bertani (LB) medium at 37˚C. The bacterial optical density using the nanospectrophotometer (Implem, USA) was adjusted to 1 X 10^5 cfu/ml using LB broth, after which, a sterile cotton swab was used to lawn the nutrient agar (NA) plates with the bacterial culture. Wells (0.35mm) were bored into the surface of the agar. The antibacterial immunity was assessed in presences 0.15ml of synthesized structures which were placed into each well. A well filled with sterile

phosphate buffered saline served as a negative control. The NA plates were then incubated at 37°C for 17 hours after which the resulting inhibition zones were measured. All tests were performed three times in triplicates under the same conditions.

3.2.5.3 Human Osteoblastic Cell Culture

The hFOB 1.19 derived cell-line from osteoblasts human source purchased from ATCC, Rockville, MD, American Type Culture Collection. The cells were kept and propagated in DMEM/F-12 (Himedia) cell culture medium supplemented with 10% fetal bovine serum (Biowest, France), 5 ml penicillin-streptomycin (100ug/ml) at 37 °C in 5% CO_2 humidified atmospheric condition. The capability of hFOB to stich and proliferate on the nanostructured composites and materials was determined through culturing the cells on specimens in compare with Ti67IMP substrate. The related samples, were sterilized using 70% ethanol, followed by washing with sterile PBS and then dried in an oven at 70 °C. In the next step, the bulk substrates and nanostructured samples were washed with the cell culture medium prior to placement in a 12-well tissue culture plate (Corning, USA). The cells were then seeded at 1×10^4 cells/well in wells containing specimens.

3.2.5.4 Cell attachment proliferation using MTT assay

The hFOB were seeded on sterilized surfaces of specimens at 1×10^4 cells ml^{-1} in 12-well 200 μL media culture plates in each well processed for period times of 1, 3, 5 and 7 days. The bone cell proliferation on cultured sterilized pellets was characterized by the methyl thiazole tetrazolium (MTT) assay. A 5 mg mL^{-1} MTT stock solution (St. Louis, MO, Sigma Aldrich) was prepared by dissolving MTT in PBS, filtering the solution with a 0.2 μm filter, and storing at 4 °C. When the 12-well plates were removed from the incubator, 20 μL of MTT stock solution was added to each well. The cells were incubated for 4 h at 37 °C in an atmosphere of 100% humidity and 5% CO_2. Following

incubation, the MTT solution was removed and replaced with 100 µL of DMSO. At each time point (1, 3, 5 and 7 days), the related solutions were removed to a 96-well plate and optical density (OD) absorbance was measured at 570 nm using a TECAN Sunrise microplate reader. Each tests were performed three times in triplicates under the same conditions.

3.2.5.5 Alkaline Phosphatase Activity Assay

The hFOB 1.19 cells (1×10^4 cells ml^{-1}) were seeded onto the sterilized surfaces of specimens in 12-well culture plates containing 200 µL media. Following culture at 1, 3, 5 and 7 days, alkaline phosphatase (ALP) activity was determined using the ALP assay Kit (Colorimetric) (ab83369, Abcam) according to the manufacturer's instruction. Briefly, all materials and prepared reagents were standardized to room temperature prior to use. Standards, samples and background control (for coloured samples) wells were set up as instructed. ALP activity in the sample background control wells were terminated using 20 µL of stop solution. After that, 50 µL of 5mM pNPP solution was been added to each well containing sample and background controls without adding solution to standard wells. Ten µL of ALP enzyme solution was added to each pNPP standard wells. Following these steps, the plate was incubated in the dark at 25 °C for 60 minutes. The enzyme converts pNPP substrate to an equal amount of colored p-Nitrophenol (pNP). Then, the sample and standard reactions (except backround controls) were stopped by adding 20 µL stop solution. Finally, the plate was gently shake d output measured immediately on a microplate reader (Thermo Scientific Varioskan® Flash) at OD 405nm. Three-sample of each states were tested, and each experiment was conducted in triplicate.

3.2.5.6 Statistical Analysis

Three samples were used in each group by reporting the results as means ± standard deviations. One-way analysis of variance (ANOVA) followed by Tukey−Kramer post hoc test. $P < 0.05$ was considered statistically significant.

3.2.5.7 Cell Morphology

In order to observe the adherence of the hFOB cells to the sample surfaces after 24 h cell seeding, the cells were fixed on the bare substrate, multilayered thin films and loaded liquid-materials on silicon wafer using FESEM characterization. First, the surfaces fixed with 2% O_SO_4 overnight. The samples were then brought to room-temperature followed by two washes in dH2O Dehydration steps were performed using a series of graded ethanol-water, ethanol-acetone and pure acetone solutions (15 min ethanol 10%, 20%, 30%, 40%, 50%, 60%, 70%, 80%, 90%, 95% 2×100%, ratio of 3:1, 1:1, 1:3 ethanol-acetone and 20 min 3×100% acetone, respectively), then followed by critical point drying (CPD) process for 90-120 min. Finally, the samples were mounted on stubs with carbon adhesive cement or double sided tape and morphology of the fixed cells were viewed using the FESEM model QUANTA FEG 450.

3.2.5.8 Confocal Laser Scanning Microscopy

The hFOB cells were seeded on un-treated substrate and multilayered composites on Ti67IMP in well plate. For the synthesized carbon-based materials, the hFOB cells were grown to confluency on glass cover slips (thickness of 0.13-0.17 mm) in well plate, before the material was loaded into the wells. Following incubation, the specimens were washed with 1×PBS before staining with 200 μg/mL acridine orange (Sigma Aldrich) at constant room temperature for 20 min. Accordingly, excess stain removed by two-time washing with 1× PBS for 10 min each. The stained cells were then characterized using confocal microscopy (Micro-system, Mannheim, Germany, Leica TCS-SP5 II, Leica) and

the images were processed with Leica LAS X software. The live cells are distinguished by the presence of intact nuclease (green), determined by the enzymatic conversion of the virtually non-fluorescent cell-permeant to the intense fluorescence of the nucleus. The dye will be well retained within the live cells, producing uniform green fluorescence in live cells.

It is imperative to follow the standard laboratory safety measures during cell culture experiments and tissue engineering. To this end, the standardized instruction of ***Safety Operating Procedure (SOP) Biosafety Level 2*** was adopted for all the biological experiments conducted for the purpose of this study.

CHAPTER 4: RESULTS AND DISSCUSIONS

4.1 Mechanical Properties

4.1.1 Adhesion Strength of Taguchi Designed Nb Layer

Reasonable mechanical properties which lead to long-term durability are commonly considered as the most important characteristics of replacement of artificial tissues. Application of stable thin coatings can efficiently modify the implant functionality with increasing the specific surface area. So, adequate adhesion strength has large impact on stability of applied materials and interfaces. In this study, adhesion strength of as-sputtered Nb PVD coating on Ti67IMP was quantitatively assessed with scratch tester, while the related curves and optical images determined the critical load (L_c). The analysis as followed microscopic observation, depth, load and friction to indicate the failure points through scratch experiments. The critical load was issued to the load-displacement scratch graph directed from left side while, L_{c1} defined as prior critical load, and dedicates to cohesive failure. Gradually, by increment of scratch load and indenter pressure, delamination may happen on both sides of failure point and resulted to trackside labeled as L_{c2}. It is remarkable that there was not any clear delamination of coated layers along scratch path, but cracking can be appeared. In case of higher applied load, the crack wholes and delaminated points will become bigger and thin film started to remove eventually as L_{c3} area (Brace, 1968; Tomsia, Saiz, Song, & Bertozzi, 2005). According to literature, with increment of DC voltage in PVDMS coating, the rate of sputtering, ionized particles, distance of atoms and related energy will be increased and resulted in enhancing the adhesion strength also the collisions of sputtered particles. Moreover, by increase of bias voltage, the distance between coated layers remarkably decreases, which lead to more compatibility and improvement of coating adhesion. Herein, the adhesion strength between as-deposited Nb samples and Ti67IMP substrates followed Taguchi experiments (See Table 3.2) were measured by scratch tests. Therefore,

in the present case, the film-to-substrate adhesion strength designed by Taguchi L(3^3) method was quantitatively measured by a scratch tester, where an acoustic signal, friction curve and microscope observation were applied to obtain the critical load (Lc). Graphs of depth, load, friction, and coefficient of friction (COF) versus distance as well as the scratch lengths and failure points of the specimens during the scratch experiments are presented accordingly. It is clear from the results that the seventh design has the best adhesion strength, where the total scratch length, distance of the failure point area, load and COF under the 2500 mN applied load were 965.41 µm, 795.63 µm, 2000.81 mN and 0.3, respectively. Meanwhile, the lowest adhesion measurement was addressed to sixth design with poor amount of 780.77 mN strength with substrate. This effect can be linked directly to PVD processing parameters (Gangopadhyay, Acharya, Chattopadhyay, & Paul, 2010; W.-Y. Zhang, Li, Li, Yu, & Xi, 2007). It has been found that with increase of DC voltage in PVD coating, the rate of sputtering, ionized particles, distance of atoms and related energy increase and lead to a rise in the adhesion strength also the collisions of sputtered particles. By increasing the bias voltage, the distance between coated layers decreases significantly, which leads to more compatibility and improvement of coating adhesion. Figure 4.1 (a-i) illustrates the performed scratch analysis of fabricated Nb films through parametric design of experiments.

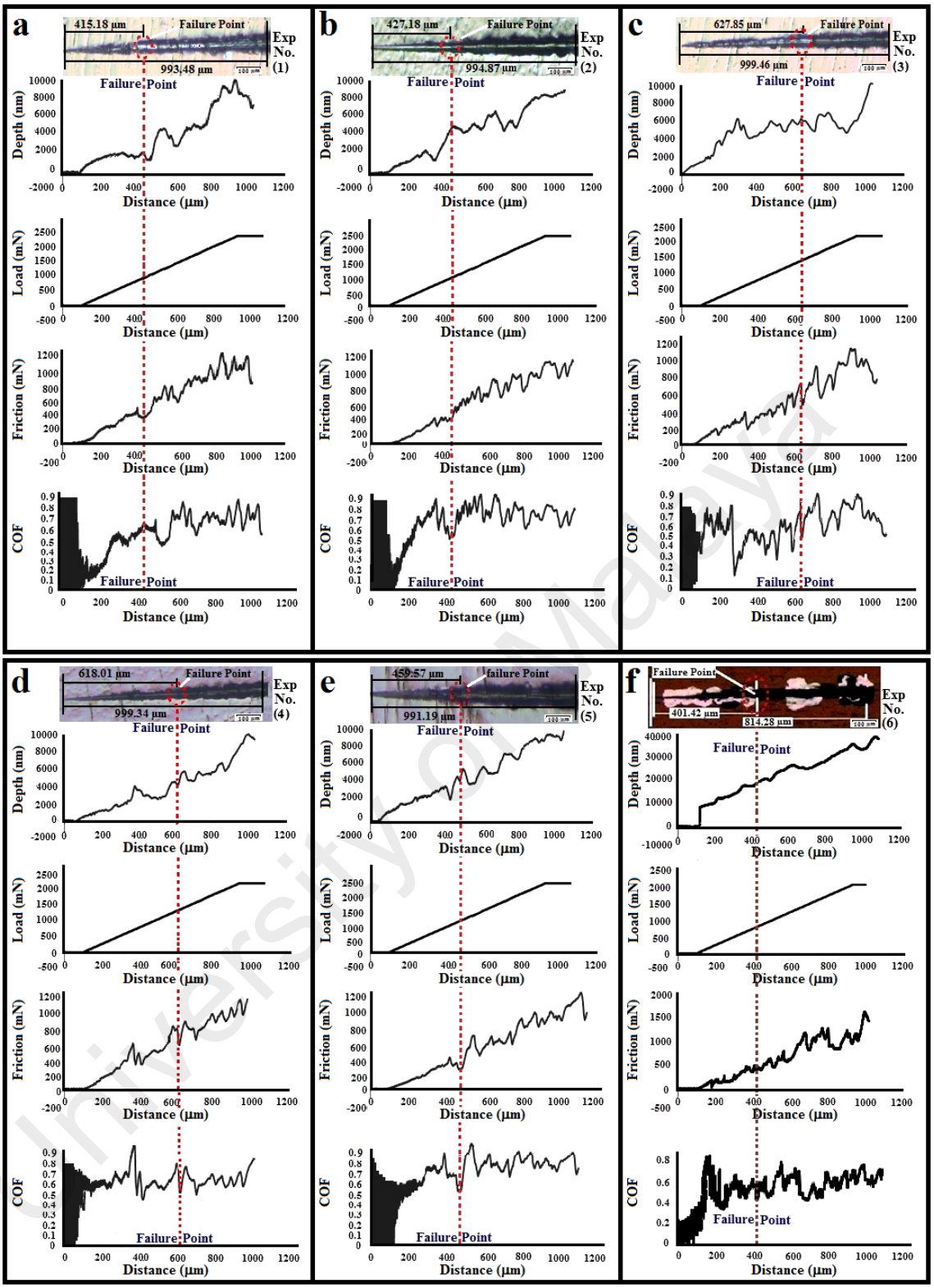

To be continued…

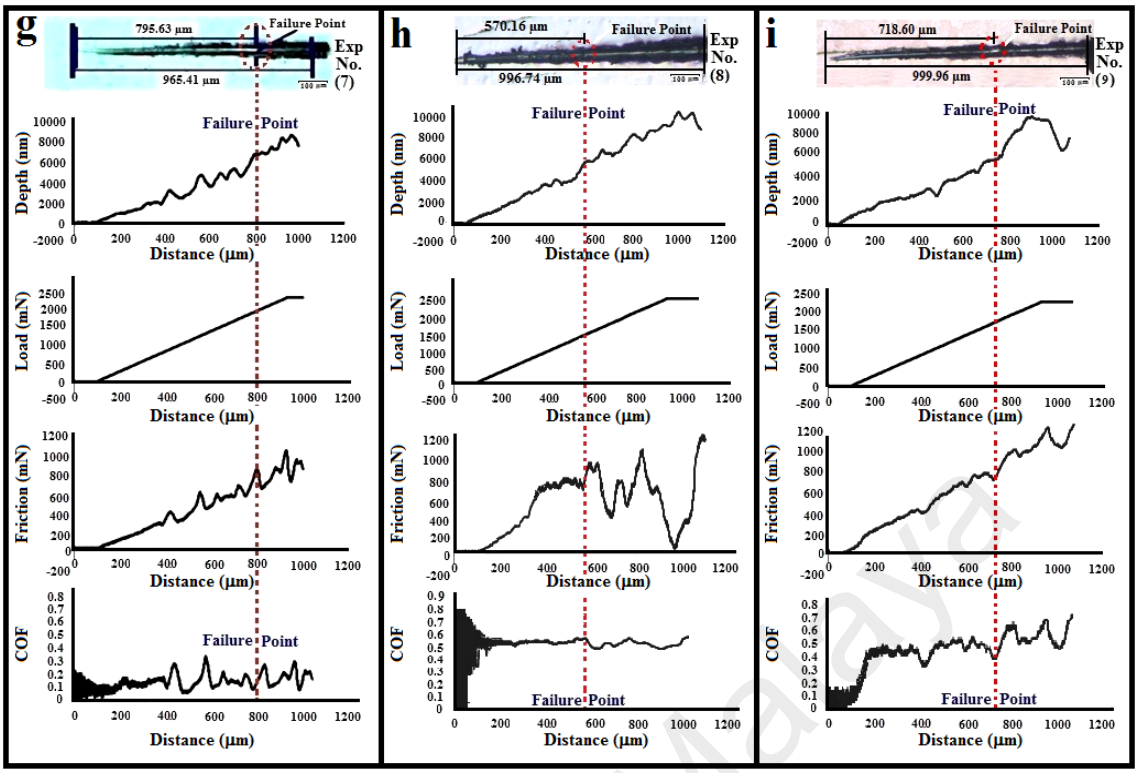

Figure 4.1: Optical micrograph of scratch track, profiles of depth, load, friction and coefficient of friction for different designs of Taguchi against scan distance after Nb coating on Ti67IMP substrate; (a) No. 1, (b) No. 2, (c) No. 3, (d) No. 4, (e) No. 5, (f) No. 6, (g) No. 7, (h) No. 8, and (i) No. 9.

The details adhesion strength values of as-deposited Nb film and calculated signal-to-noise (S/N) ratio analysis of variance (ANOVA) were summarized in Tables 4.1 and 4.2 respectively. The *S/N* response values for adhesion strengths are shown in Figure 4.2. It should be mentioned that the validation experiment was completely matched under applied PVDMS condition with the highest value labeled seventh experiments. The confirmation parameters set for DC power, argon flow rate, DC bias, temperature and time at 350, 20, 90, 220 and 120 min, respectively.

Table 4.1: The measured thickness and adhesion of Nb film as well as calculated S/N ratio.

Series	Nb coating thickness (nm)	Scratch Force (mN)				
		First (L = 1500)	Second (L = 2000)	Third (L=2500)	Ave	Calculated S/N ratio
1	3573.85	862.03	895.16	873.91	877.03	58.86
2	4072.03	938.52	1104.85	1189.43	1077.6	60.64
3	5938.01	1395.12	1274.13	1626.96	1432.07	63.11
4	4488.63	1271.19	1332.46	1574.7	1392.78	62.87
5	5611.85	1277.95	1219.63	1335.72	1277.76	62.12
6	2710.12	720.18	810.31	780.77	770.42	57.73
7	**6411.76**	**1985.14**	**1853.93**	**2000.81**	**1946.35**	**65.78**
8	5893.19	1408.12	1583.14	1519.63	1503.63	63.54
9	6133.92	1617.15	1617.15	1761.79	1658.31	64.39

Table 4.2: The S/N response values for the adhesion strength.

Coating parameters	S/N response		
	Level 1	*Level 2*	*Level 3*
DC Power (W)	60.87	60.90	64.54
Argon flow rate (sccm)	62.50	62.10	61.74
DC Bias (v)	60.04	62.63	63.67

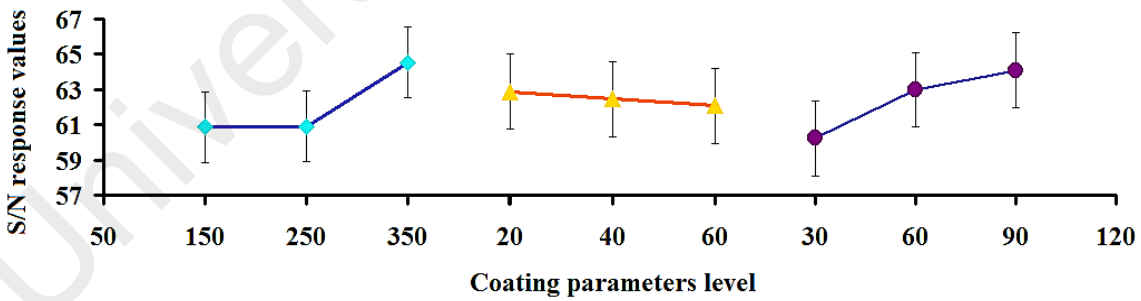

Figure 4.2: The S/N response graph for the adhesion strength.

4.1.2 Hardness of Taguchi Designed Nb Layer

The Vickers hardness analysis were conducted for all Taguchi designed experiments to evaluate the effect of PVDMS parameters on microhardness of fabricated Nb film. Based on the obtained results and *S/N* response, it can be concluded that the

maximum value is also dedicated to seventh experiment. While, corresponding to sputtered Nb layer on Ti67IMP substrate the Vickers hardness was shifted from 183 HV (1.795 GPa) in substrate to 335 HV (3.285 GPa) following the adhesion strength trend in 7^{th} experiment. This change is corresponded to density of coating and the surface roughness which emphasized the role of applying exact independent variables setting. The details of extracted measurements and surface roughness data were presented in Tables 4.3 and 4.4.

Table 4.3: The measured Vickers hardness of coated Nb and calculated S/N ratio.

Series	**Surface roughness**	**Hardness (HV)**				
		First	Second	Third	Ave (HV/GPa)	Calculated *S/N* ratio
1	0.022	256	258	260	258/2.53	48.23
2	0.018	290	291	289	290/2.84	49.24
3	0.013	247	241	253	247/2.42	47.85
4	0.014	269	270	271	270/2.64	48.62
5	0.014	274	278	276	276/2.70	48.81
6	0.025	232	235	229	232/2.27	47.30
7	**0.011**	**335**	**334**	**336**	**335/3.28**	**50.50**
8	0.013	293	297	301	297/2.91	49.45
9	0.012	264	269	259	264/2.58	48.43

Table 4.4: The S/N response values for the microhardness (HV).

Coating parameters	S/N response		
	Level 1	Level 2	Level 3
DC Power (W)	48.44	48.24	49.46
Argon flow rate (sccm)	49.16	49.11	47.86
DC Bias (v)	48.32	48.76	49.05

4.1.3 Maximizing Adhesion and Hardness via Multi-objective PSO Algorithm

4.1.3.1 Modeling and Formulation

With target of enhancement in adhesion strength and hardness aimed at higher stability of fabricated structure the PVDMS parameters were normalized as Table 4.5 to find the mathematical models. For this, PSO optimization was applied to find the optimum variables based on the resulted outputs, training/testing procedures and provided models. Due to the required simultaneous optimization of dependent variables, MOPSO algorithm proposed to find the new design of PVDMS experiment suggested as a validation test.

Table 4.5: The Taguchi design of Nb PVD parameters, obtained adhesion strength and hardness and the normalized related values.

No.	Adhesion (mN)	Hardness (HV)	Normalized values				
			DC Power	*Argon Rate*	*DC Bias*	*Adhesion*	*Hardness*
1	877	258	1.0	1.0	1.0	1.090	1.252
2	1077	290	1.0	1.5	1.5	1.261	1.563
3	1432	247	1.0	2.0	2.0	1.562	1.145
4	1392	270	1.5	1.0	1.5	1.529	1.368
5	1277	276	1.5	1.5	2.0	1.431	1.427
6	770	232	1.5	2.0	1.0	1.000	1.000
7	**1946**	**335**	**2.0**	**1.0**	**2.0**	**2.000**	**2.000**
8	1503	297	2.0	1.5	1.0	1.623	1.631
9	1658	264	2.0	2.0	1.5	1.755	1.310

Basically, the smart PSO model obtains an accurate formulations which can predict the PVDMS dependent variables such adhesion strength and hardness of coated Nb layer on Ti67IMP simultaneously. Training and testing procedures with estimate relation of 75 and 25 % respectively were provided to formulate the considered parameters. After finding the optimum PVD parameters, PSO algorithm offers the mathematical formulations for the considered outputs. The derived AI-models for adhesion strength and hardness of Nb coating in PVDMS process resulted in the following models in Equations 4.1 and 4.2. These formulations can predict the PVD coating dependent variables based on the selected independent variables.

$$\boldsymbol{Adhesion\ Strength} = ((Argon\ Flow\ Rate) \times (-2.711)) + (DC\ Bias \times (5.022)) + ((DC\ Power) \times (-2.136)) + ((Argon\ Flow\ Rate) \times (DC\ Bias) \times (-0.771)) + ((Argon\ Flow\ Rate) \times DC\ Power) \times (0.787)) + ((DC\ Bias) \times (DC\ Power) \times (-1.519)) + ((Argon\ Flow\ Rate)^2) \times (0.740)) + ((DC\ Bias)^2) \times (-0.337)) + ((DC\ Power)^2) \times (1.140)) + (0.875) \quad (4.1)$$

$$\boldsymbol{Hardness} = ((Argon\ Flow\ Rate) \times (2.076)) + (DC\ Bias \times (-0.258)) + ((DC\ Power) \times (-0.930)) + ((Argon\ Flow\ Rate)^2) \times (0.798)) + ((DC\ Bias)^2) \times (0.156)) + ((DC\ Power)^2) \times (0.422)) + (0.583) \quad (4.2)$$

In this step, using the proposed formulations lead to predict reliably with determining the considered scores. So, the PSO training, testing procedures and the errors between observed and estimated data for modeled adhesion strength and hardness are presented in Figure 4.3a and b, respectively. To find the best models and minimize the error between observed and estimated data the convergence characteristics of both PSO models were used (Figure 4.4a).

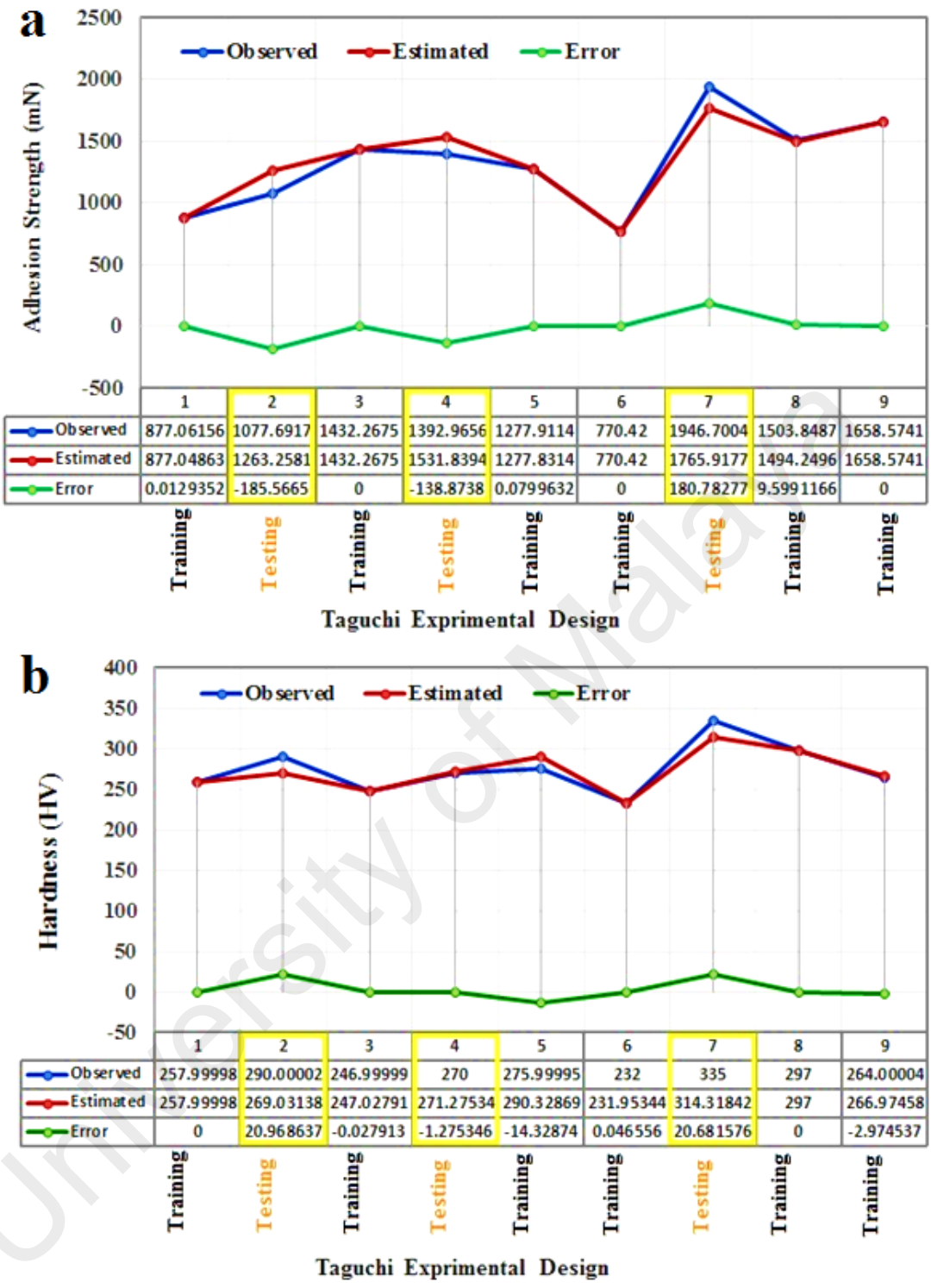

Figure 4.3: The comparable results of the experimental observed and PSO estimated (training and testing) (a) adhesion strength and (b) hardness.

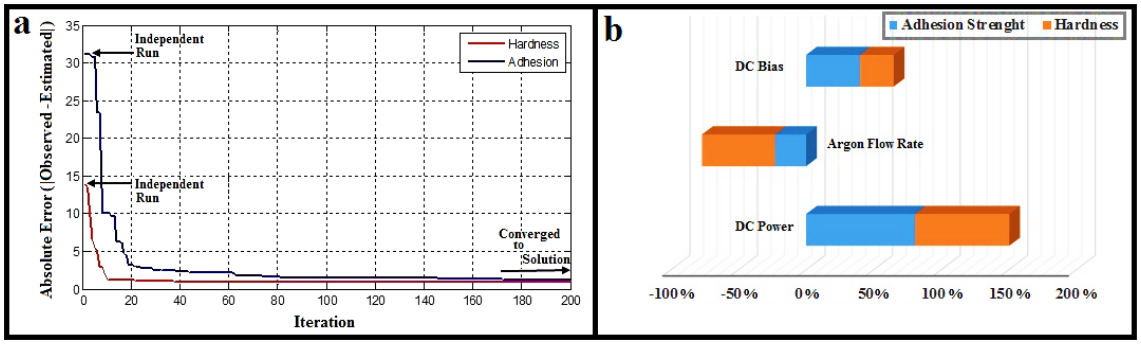

Figure 4.4: (a) Convergence characteristics of PSO algorithm to model the adhesion and hardness of Nb PVD coating and (b) the frequency values of the predictor variables.

4.1.3.2 Performance Evaluations of Obtained Models

In this section approximation power of the proposed PSO algorithm was evaluated and the considered dependent variables computed by obtained models is compared with the actual experiments designed by Taguchi. The performance indexes of models such as absolute error, the coefficient of determination (*R*-squared), mean absolute percentage error (MAPE), percentage of model accuracy (A), mean square error (MSE), root mean square error (RMSE) and Thiel's inequality coefficient (*U*-statistic) measured values were gathered in Table 4.6. The above-mentioned performance of index values proposed for adhesion strength and hardness of NB PVD film were presented in details.

Table 4.6: The performance index of proposed adhesion strength and hardness models optimized by PSO.

Performance Index of Proposed Models	Adhesion Strength	Hardness
Absolute Error	0.512	0.585
MSE	0.006	0.010
RMSE	0.082	0.101
MAPE (%)	3.142	3.599
U-statistic	0.025	0.033
A (%)	96.857	96.400
R2 (%)	96.02	92.00

4.1.3.3 Sensitivity Analysis

Nevertheless, optimization of the related parameters of PVDMS process is challenged owing to the considered nonlinear properties of coated materials. Therefore, to design an adhesive layers, these models explored the application of sensitivity analysis (SA) extracted by PSO algorithm for the optimization of adhesion strength and hardness. Mainly, SA is utilized to identify the most important parameters of PVD coating to enhance the accuracy and simplification of the optimization. Figure 4.4b presents the total sensitivity indices for PVDMS parameters of current mechanical properties. Base on the SA results DC power, DC bias and Ar flow rate and had higher significant effects on the adhesion strength respectively. Whereas, regarding to hardness the sequence of parameters sensitivity was changed to DC power, Ar flow rate and DC bias accordingly. The value of the index for the DC power of both adhesion strength and hardness indicated that the most sensitivity was related to this parameters. The applied DC bias and Ar flow rate factors had almost similar histograms, which confirmed that they have similar effects on the adhesion strength and hardness of Nb PVD coating. So, contribution of optimized variables in MOPSO validated test was completely in agreement with previous actual experiments evaluated. It should be notified that the considered variables were identified after proposing and generating various models through different aspects of mechanical properties in concern with PVDMS process. To conduct sensitivity analysis, the related values to independent variables frequency near and up to 100% were appeared of the best performed MOPSO program. Moreover, response surface methodology (RSM) analysis was also investigated to distinguish the effects of PVDMS parameters on adhesion strength and hardness of Nb PVD coating. The controlled factors of PVDMS process within performed Taguchi experiments were utilized to provide the combination of parameter settings. The extracted data from experimental procedures was set for RSM results in order to analyze the quality of predictor as well as optimization aspects. Both

tow indexes were associated with MOPSO algorithm to search for the optimum combination of PVD process. The RSM analysis regarding to the adhesion strength and microhardness of controlled Nb PVD coating via MOPSO algorithm illustrated in Figure 4.5a.

Additionally, in accordance with the RSM plots, more analysis were conducted to generate the quality of considered models for adhesion strength and hardness extracted from Equations 4.1 and 4.2. Based on the presented responses DC power were fixed in its minimum and maximum possible values versus the other PVDMS parameters. The RSM was also plotted for DC bias and Ar flow rate to distinguish the relation of changing PVDMS parameters to each other and coating outputs. The presented RSM responses were in agreement with sensitivity analysis and confirmed the most effective independent variables of Nb PVD coating allocated to DC power resulted to achieve maximum possible adhesion strength of coated thin film. (Figure 4.5b and c). The following sensitivity results include the surface response (RSM) of optimized models with PSO to continuous changes the variables (Argon flow rate-DC Bias) for adhesion strength and hardness while DC Power were fixed in its minimum and maximum possible values; (b) RSM of optimized models with PSO to continuous changes the variables (DC Power-DC Bias) for adhesion and hardness while argon flow rate were fixed in its min and max possible values; (c) RSM of optimized models with PSO to continuous changes the variables (DC Power-argon flow rate) for adhesion and hardness while DC Bias were fixed in its min and max values.

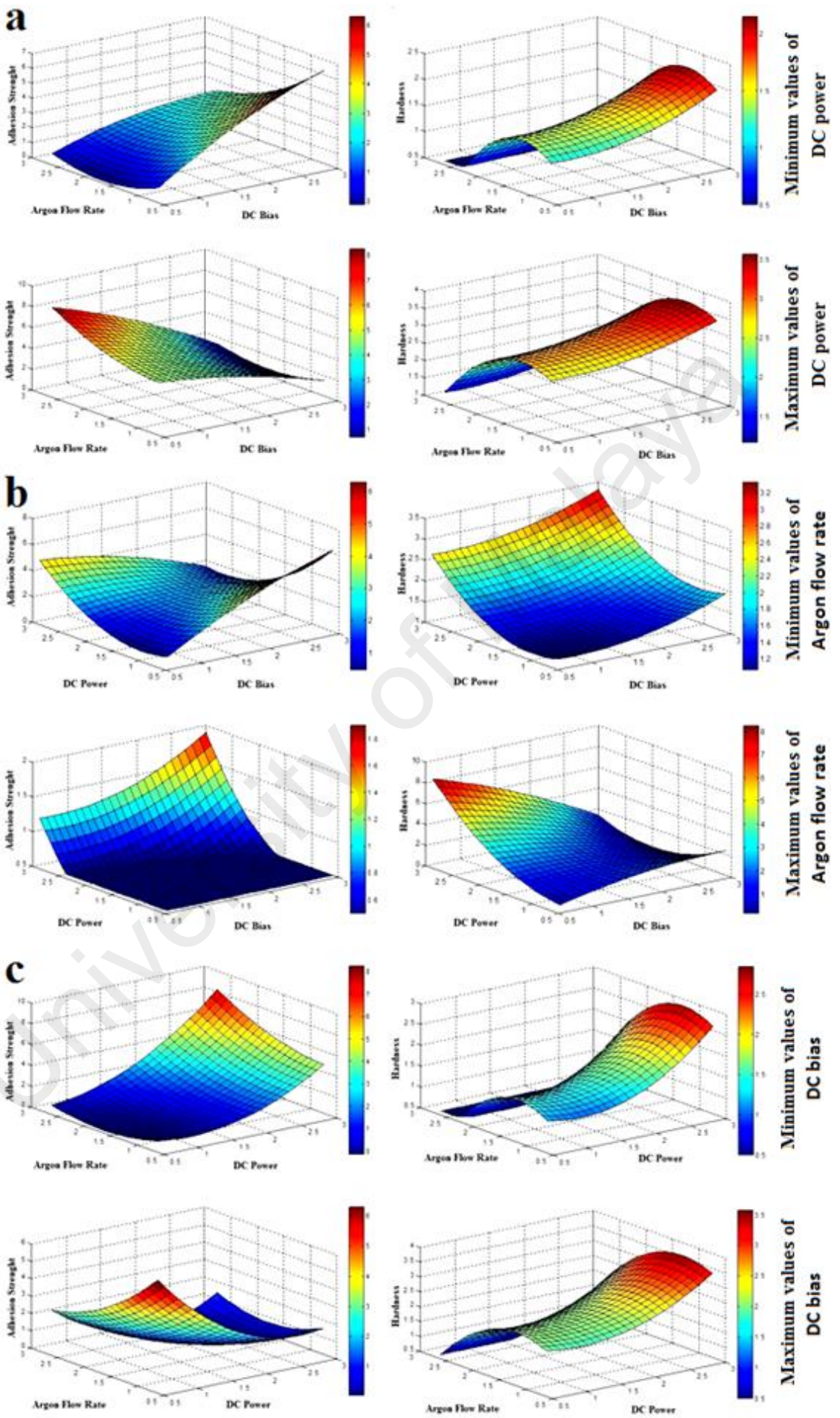

Figure 4.5: The surface response (RSM) of optimized models with PSO.

4.1.3.4 Forecasting and validation of the optimum values

The non-dominated approaches are applied to propose MOPSO algorithm and the Pareto front values owing to adhesion strength and hardness were developed as the optimization model. The maximum applied iteration numbers and population were set to 500 and 250 respectively. In addition, the parameters setting of used PSO algorithm have been fixed at $c_1 = c_2 = 2$, $w_0^{max} = 0.9$ and $w_0^{min} = 0.4$. Figure 4.6 demonstrates the solutions related to Pareto front for functioned MOPSO algorithm. The best compromise solution is chosen through the Pareto members based on applied fuzzy decision maker. While, the 40 non-dominated solutions of the Pareto front are listed in Table 4.7 with the indexes as μ_k, $\mu_{adhesion}$, $\mu_{hardness}$ and the best compromise solution were shown in bold format and considered as the results of validated MOPSO test.

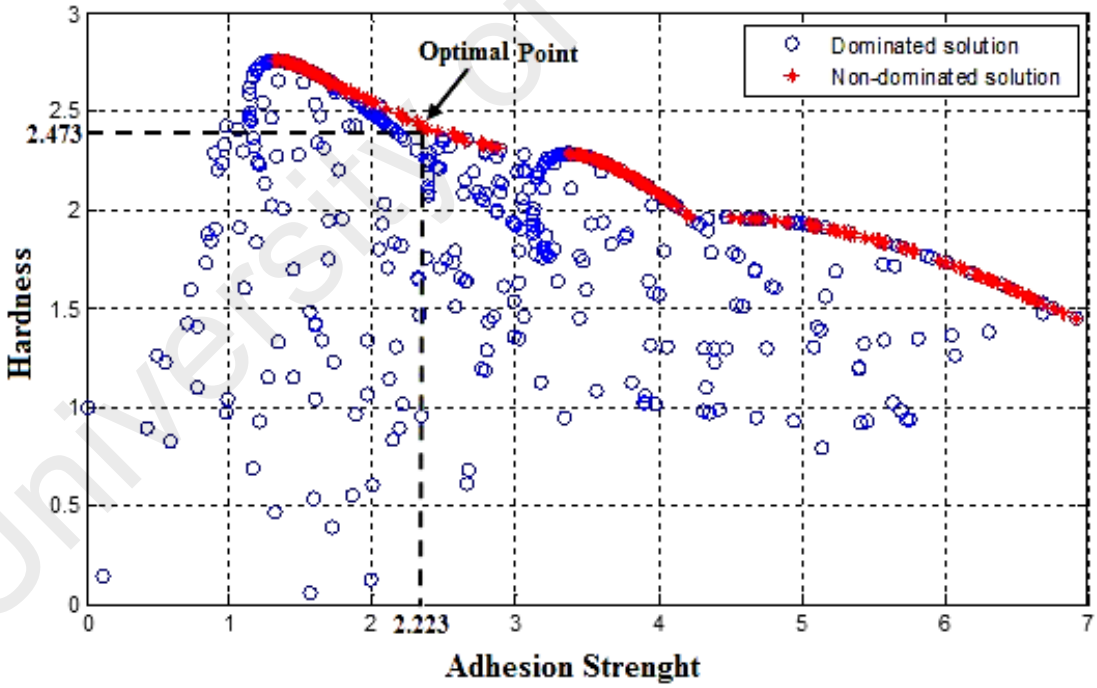

Figure 4.6: Pareto front obtained by multi-objective PSO aimed at maximizing the objective functions (adhesion strength and hardness).

Table 4.7: The performance index of proposed adhesion strength and hardness models optimized by PSO.

Non-Dominated Solution	Normalized Adhesion Strength	Normalized Hardness	Fuzzy Membership of Adhesion ($\mu_{adhesion}$)	Fuzzy Membership of Hardness ($\mu_{hardness}$)	μ_k
1	1.316	2.754	0.000	1.000	0.528
2	1.361	2.752	0.008	0.998	0.470
3	1.460	2.734	0.025	0.984	0.435
4	1.515	2.717	0.035	0.971	0.463
5	1.590	2.688	0.048	0.949	0.542
6	1.635	2.672	0.056	0.937	0.579
7	1.677	2.654	0.064	0.923	0.635
8	1.768	2.621	0.080	0.898	0.715
9	1.883	2.587	0.101	0.872	0.764
10	2.094	2.511	0.138	0.814	0.946
11	**2.223**	**2.473**	**0.161**	**0.785**	**1.000**
12	2.945	2.331	0.260	0.676	0.998
13	3.391	2.281	0.370	0.638	0.447
14	3.48	2.271	0.386	0.631	0.374
15	3.543	2.258	0.397	0.621	0.362
16	3.581	2.248	0.404	0.613	0.370
17	3.617	2.238	0.410	0.605	0.380
18	3.641	2.23	0.415	0.599	0.397
19	3.692	2.213	0.424	0.586	0.431
20	3.747	2.192	0.433	0.570	0.487
21	3.811	2.166	0.445	0.550	0.562
22	3.845	2.152	0.451	0.540	0.604
23	3.890	2.131	0.459	0.524	0.675
24	3.949	2.104	0.470	0.503	0.765
25	4.188	2.034	0.512	0.449	0.862
26	4.405	1.971	0.551	0.401	0.946
27	4.705	1.953	0.604	0.388	0.590
28	5.076	1.920	0.671	0.362	0.224
29	5.257	1.894	0.703	0.343	0.113
30	5.572	1.835	0.759	0.297	0.013
31	5.790	1.786	0.798	0.260	0.000
32	6.140	1.695	0.861	0.190	0.063
33	6.312	1.644	0.891	0.152	0.137
34	6.460	1.599	0.918	0.117	0.208
35	6.604	1.553	0.943	0.082	0.292
36	6.846	1.470	0.987	0.019	0.472
37	6.918	1.445	1.000	0.000	0.528
38	6.918	1.445	1.000	0.000	0.528
39	6.918	1.445	1.000	0.000	0.528
40	6.918	1.445	1.000	0.000	0.528

Based on the proposed PSO models for adhesion strength and hardness, the independent variables were found as 452 W, 30 sccm and 60 V for DC power, Ar flow

rate and DC bias, respectively, which resulted in optimum values and maximizing the PVDMS outputs (See Figure 4.6 and Table 4.7). The scratch and microhardness assessment were carried out for validation tests in compare with untreated case. From the obtained results, both adhesion and hardness were significantly improved by optimization. Currently, the scratch test on 1 mm line and applied load of 2500 mN was failed at point of 934.21 µm which provided 2501 mN related to adhesion strength illustrated in Figure 4.7. It is remarkable that the used optimization algorithm was predicted this output as 2.223 as normalized value, which is close to actual data and corresponded 2208.582 mN according to Equation 3.12. Moreover, the PSO estimated microhardness value for as-sputtered Nb specimen was offered normalized 2.473, which is equal to 383 HV (3.756 GPa) which was raised from 335 HV (3.285 GPa) and confirmed the strength enhancement for multi-layered Nb/Ti67IMP surface. In addition to adhesion strength, the estimated value of hardness was matched with validated actual data after optimization treatment. In brief, adhesion strength and hardness of Nb/Ti67IMP were improved simultaneously affected by multi-objective PSO application.

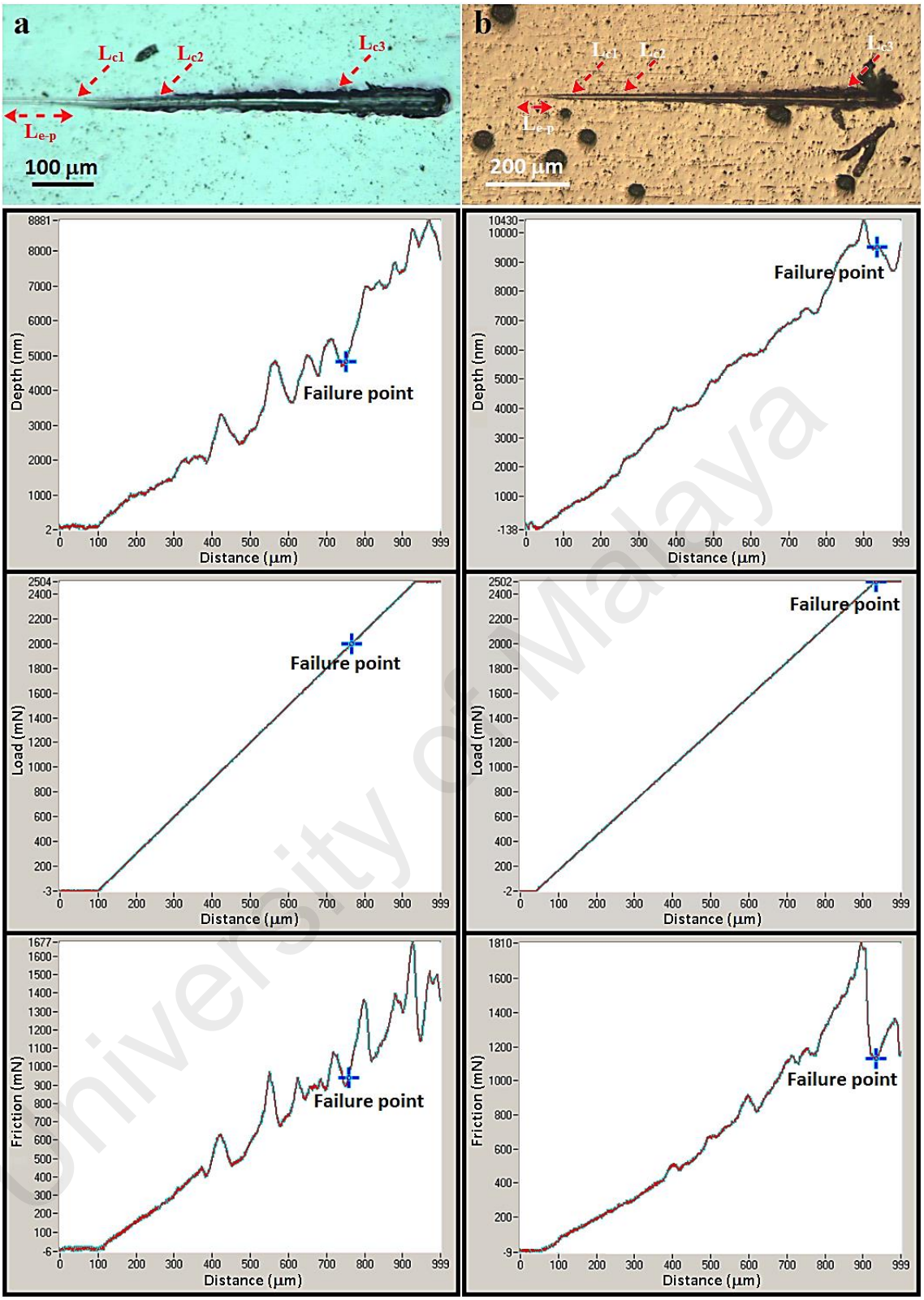

Figure 4.7: Optical image, Load, depth and friction vs distance graphs as well as the failure points for: (a) as-prepared Nb thin film (b) treated sample.

4.2 Fabrication of Mixed Oxide Bioceramics on Ti67IMP

4.2.1 Mechanism of formation

Generally, the physical and chemical properties of nanotube layer are controllable by altering the fabrication process parameters (Kunze et al., 2008). Anodizing has been utilized to grow homogeneous oxide films on valve metals for decades (Baradaran et al., 2013). In general, highly-ordered nanostructure arrays could be formed on valve metals when they are subjected to suitable electrolytes. In such situation, oxidizationing will begin at the interface of M-oxide as $M \rightarrow M^{n+} + ne^-$ and the M^{n+} ions transfer to the outside under a practical voltage, where M represents a given metal. In the meantime, oxygen anions supplied by H_2O in the electrochemical cell move towards the interface of M-oxide, and create a dense MO_x layer where *x* counts on the metal valence (Figure 4.8). This process is typically executed at an invariable practical voltage. Considering that the metal-oxide layer shows a higher resistivity than the undercoat and electrolyte, the applied electric field within oxide layer is gradually diminished by thickening the oxide film. Even though the oxide layer keeps thickening, until the practical field is sufficiently high to make the transmission of ion throughout the oxide, the procedure incessantly decelerates and finishes up in the equilibrium of the metal-oxide layer. Specific empirical circumstances may cause additional developing of the porous oxide layer, and in more particular terms, highly-ordered nanostructure arrays could be developed.

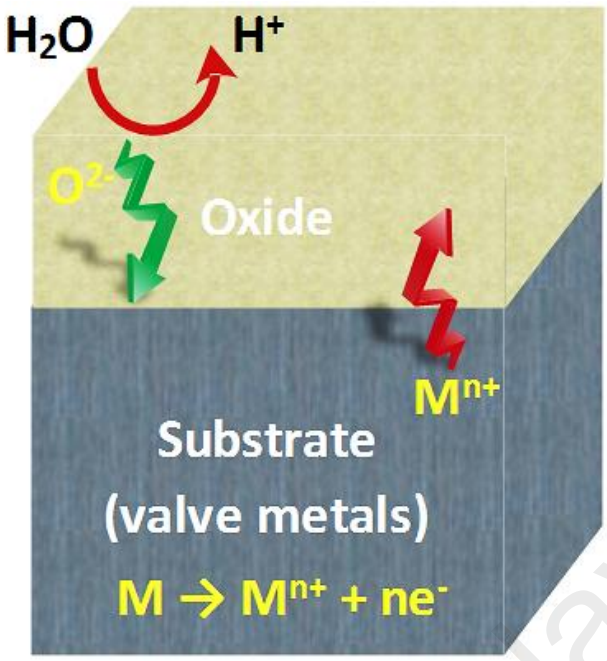

Figure 4.8: Schematic illustration of oxide formation on a valve metal.

As mentioned above, in consequence of the anodizing in acidic solutions, a dense, homogeneous oxide thin film is developed on the surface of the valve metals. Given that the oxide films surface alters at the microscopic scale, the propagation of electric field in the oxide film is inconsistent, causing localized electric field at specific areas. Consequently, field-intensified dissolution in the oxide layer occurs and highly-ordered nanostructure arrays begin to develop. The process of growth sequentially arrives at steady-state, and homogeneously dispersed pores are formed. This growth mechanism can be valid for the development of highly-ordered nanostructure arrays on metals with anodizing potential. However, in some cases, contrary to Al, an acidic solution is not adequate to form self-ordered nanostructure arrays but only to create a dense oxide film. In such a situation, to develop self-ordering nanostructure arrays, the existence of fluoride in electrochemical cell is strongly preferred due to its capability to create water soluble metal-fluoride compounds. The development of these complexes assists the debarment of metal-oxide films from forming underneath the tube. This prevention causes gentle but stable chemical dissolution of the metal-oxide layer. Furthermore, owing to the small

ionic radii, fluoride is capable to go into the growing oxide lattices and to be transferred via the practical field throughout the oxide (competing with O^{2-}) to the interface of M–oxide. The elimination of the impurities together with the electropolishing, which led to gradual reduction of surface roughness, played a crucial role in uniform electric field scattering over the whole metal surface during anodizing; hence, highly-ordered nanotubes grew on a regular basis on the whole surface. Herein, the development of the mixed oxide nanotubular configuration in F^- comprising electrolyte is because of the two challenging electric field-assisted procedures: (i) Nb/Ti67IMP hydrolysis and (ii) mixed oxide dissolution at the interface of MO_x/electrolyte was proposed. In reality, owing to the chemical dissolution of the components, the pore underneath is self-acidified. This results in the generation of a pH profile in the pore growth direction where the rate of chemical dissolution at the pore underneath is higher than that of the pore top. This causes the length of tubes generally increases over time. On the other hand, to further increase surface area of the nanotubular configuration, several attempts have been conducted on the fabrication of bamboo-type anodic nanotubular arrays. The parametric effects of electrochemical anodization on morphology-controlled TiO_2 nanotubes using pulsed voltage were analyzed (D. Kim, Ghicov, Albu, & Schmuki, 2008) reported. They showed that the bamboo-type TiO_2 nanotubes can provide enhanced light-harvesting outputs in comparison with the smooth-walled nanotube arrays. However, these bamboo-type TiO_2 nanotubes were produced by anodizing in an electrolyte comprising environmentally harmful HF and a rather high voltage for a long period of time (> 10 h). In most previous studies, for preparing bamboo-type nanotubes, voltage-sources have been utilized to provide alternating voltage (AV) waves during anodizing. In addition, AC anodizing has been proposed for the production of a very homogeneous structure (Guan & Wang, 2012). However, the growth mechanism of bamboo-type mixed oxide nanotubes has not been explored in detail.

When an invariable voltage is used, various morphologies of an oxide film become apparent consecutively on the substrate. At the start of the process, a dense oxide film is developed. Afterward, a porous structure is formed as a result of pits and pores development in the dense oxide film. In the final step of the process, the pores are detached by interpore cavities that generate an arranged tubular structure. To achieve such morphological development, three processes include nine chemical reactions take place concurrently as follows: (1) Ti, Nb and Al field-assisted oxidation, where H_2O decomposes in the vicinity of the metal and O^{2-}/H^+ ions; the oxygen ions then transfer upon an solution−oxide interface to oxidize components (Luan, Guan, & Wang, 2012):

$$H_2O \rightarrow 2H^+ + O^{2-} \quad (4.3)$$

$$Ti + 2O^{2-} \rightarrow TiO_2 + 4e \quad (4.4)$$

$$2Nb + 5O^{2-} \rightarrow Nb_2O_5 + 10e \quad (4.5)$$

$$2Al + 3O^{2-} \rightarrow Al_2O_3 + 6e \quad (4.6)$$

(2) Mixed oxides field-assisted dissolution as a result of electric field, where the Ti–O bond endures polarization and is weakened, encouraging dissolution of the oxides. (3) Mixed oxides chemical dissolution in which Ti^{4+}, Nb^{5+}, and Al^{3+} cations become soluble complexes $[TiF_6]^{2-}$, $[NbF_6]^-$, and $[AlF_6]^{3-}$ that move into the solution, whereas the free O^{2-} ions transport to the interface of oxide–metal and react with Zr, Ti, Nb, and Al as follows:

$$TiO_2 + 6F^- + 4H^+ \rightarrow [TiF_6]^{2-} + 2H_2O \quad (4.7)$$

$$Nb_2O_5 + 12F^- + 10H^+ \rightarrow 2[NbF_6]^- + 5H_2O \quad (4.8)$$

$$Al_2O_3 + 12F^- + 6H^+ \rightarrow 2[AlF_6]^{3-} + 3H_2O \quad (4.9)$$

Figure 4.9 shows the schematic representation of TiO_2–Nb_2O_5–Al_2O_3 nanotubes formation by one-pot electrochemical anodization. It can be displayed (Figure 4.9a) that the ion outlines inward three tubes with different chemical composition on Nb/Ti67IMP surface and the steady pH gradient (selected area) decreasing from the underneath of tube to tube entry. As the anodization begins, pH and ion diffusion gradients are rapidly initiated inside the nanotubes, causing a steady growth of the mixed oxide nanotubular arrays at applied voltage. In such a situation, H^+ ions generally originate from H_2O decomposition at the tube bottom (Equation 4.3). A number of H^+ ions scatter outward to make a steady pH gradient while the others take part in the dissolution of encircling oxides together with fluoride from outside. Under the constant-voltage anodization (20 V), the sample is incessantly oxidized (Equations 4.3 to 4.6) and the barrier layer at the underneath holds moving, headed for the undercoat, causing a steady growth of the mixed oxide nanotubes. In return, tube-bottom oxides are dissolved (Equations 4.7 to 4.9) and the interface of solution/oxide shifts headed for the substrate as well. Concerning the bamboo-type configuration, it is very likely that a sudden drop in voltage occurs and consequently fewer H^+ ions is supplied and the pH profile is altered to a less steep gradient (Figure 4.9b). This effect decelerates the oxides dissolution at the underneath of tube, producing a thicker dense barrier film there. After a given time, small pits and pores are developed in the barrier film under low voltage, very similar to the first step of the generation of tube described above. In these circumstances, a succeeding stage back to the high voltage would regenerate the growth of previous tubes headed for the undercoat, and the organized pits and pores (in the barrier film) are used up by them. Nevertheless, part of the compact barrier film between two neighboring arrays continues to exist and remains on the tube walls to create ridges as illustrated above, yielding bamboo-shape nanotubes (Figure 4.9c). It has been established that if the low-voltage anodizing is applied for extended period of time, the barrier film thickness decreases and the pits and

pores turn into small nanotubes (Figure 4.9d). Accordingly, the H^+ ions significantly decrease because of external dispersion and participation in the oxide dissolution, and the gradient of pH is much less steep. At a crucial point, the structure is capable of provoking a second development of longer mixed oxide nanotubular arrays under a subsequent high-voltage, as shown in Figure 4.9.e. This leads to the formation of a double layer nanotubular configuration, where the presented small nanotubes wrap the newly-produced inferior coating, and a quantity of them are even merged into the walls of longer nanotubes in the inferior layer. In schematic representation of bamboo-type and double-layer mixed nanotubes electrochemical tuning (a) ion diffusion profiles inside four nanotubes and pH gradient profile in nanotubes; (b) less-steep pH gradient and pit or pore formation under low voltage; (c) the development of bamboo-type nanotubes; (d) further less-steep pH gradient and tube formation in a specified time range with low voltage; (e) formation of double-layer mixed oxide nanotubes; and (f) cross sectional FESEM image of the bamboo-type mixed oxide nanotubes provided.

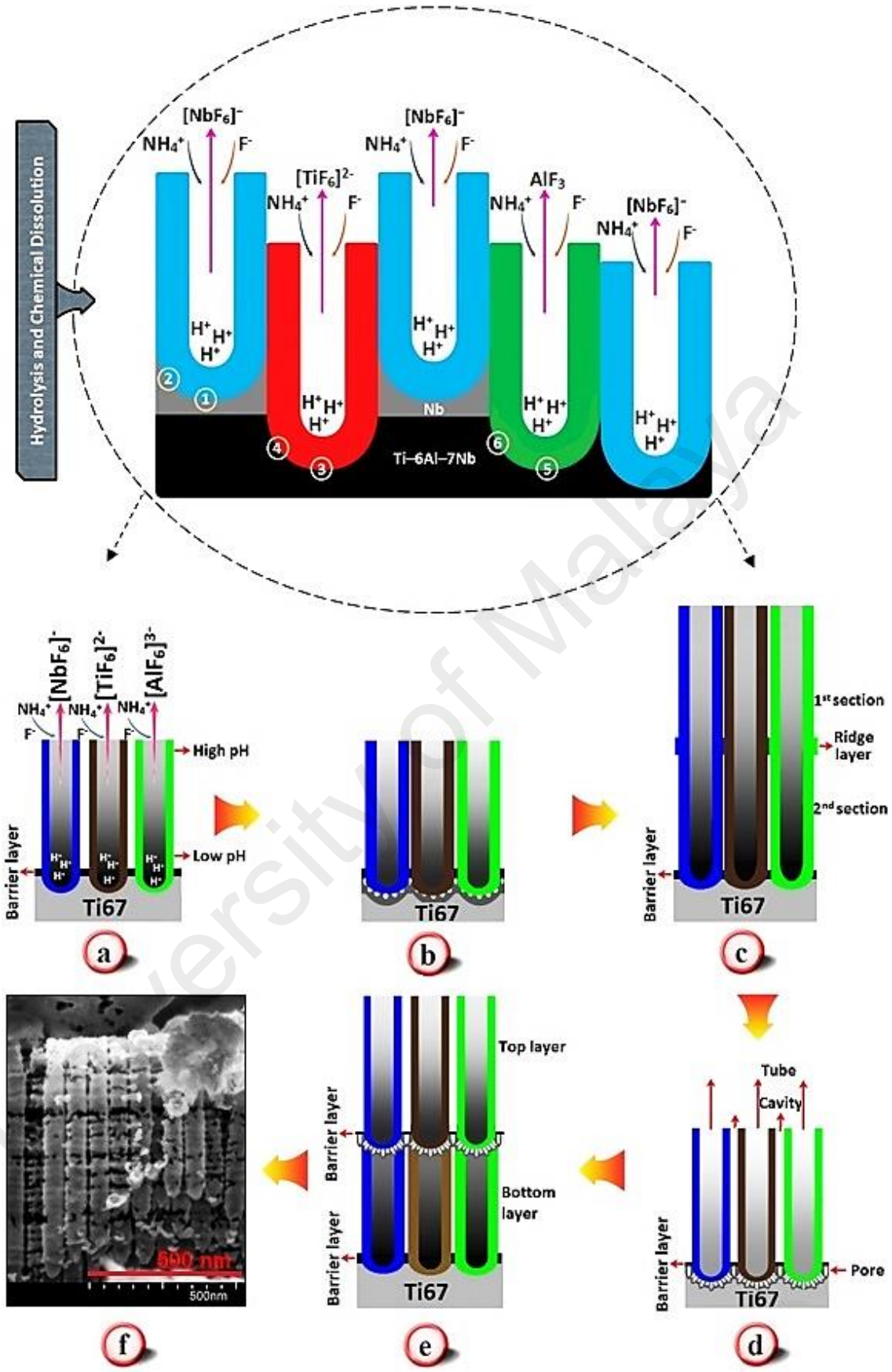

Figure 4.9: Schematic representation of bamboo-type and double-layer TiO2–Nb2O5–Al2O3 nanotubes formation by one-pot electrochemical anodization (a-f explained in text).

4.2.2 Morphological, Structural and Elemental Characterization

In brief, the microstructural features of anodic configurations could be regulated by altering the procedure variables like voltage, electrolyte composition and anodization period (Rafieerad et al., 2016). Since the morphological features, chemical composition and elemental distribution of the nanostructured coatings have considerable effects on the biomedical functionality, the morphological features, phase purity and chemical constituents of the as-sputtered, anodized and annealed specimens were analyzed by FESEM/TEM, EDS imaging, XRD, and XPS techniques respectively. The morphology of the MOPSO treated Nb coating can be considered to be a homogenous structure (Figure 4.10a). It is obvious that no three-dimensional macroscopic or bulk defects, such as pores, cracks, or inclusions could be detected in the optimized Nb coating structure. From the SEM cross-section image in Figure 4.10b, the average coating thickness was 4.35 ± 0.03 μm. FESEM top view images of the mixed oxide nanotubes synthesized using anodic oxidation of as-sputtered Nb/Ti67IMP in EG-NH_4F-dH_2O electrolyte at 20 V for different anodization times are shown in Figure 4.10c to g. At the beginning of anodizing, the formation of compact oxide layers on the surface of the sample would be expected to be detected as the interaction within O^{2-} and OH^{-}. Subsequently, irregular pits were generated due to the localized dissolution of oxide layer and followed by the pits conversion to larger pores, while most of the areas covered with oxide layer. With elongated anodization time (4 h), the compact oxide layer collapsed, a porous oxide layer grew gradually, and the TiO_2–Nb_2O_5–Al_2O_3 mixed oxide nanotubular arrays were achieved. As shown in Figure 4.10g,h the highly-ordered nanotubes are uniformly distributed over the anodized sample at 4h. From FESEM image, it can be indicated that the average inner diameter and wall thickness are around 60 and 15 nm, respectively. Figure 4.10i-n represent FESEM/TEM/SAED patterns of crystalline mixed nanotubular morphology after subsequent annealing.

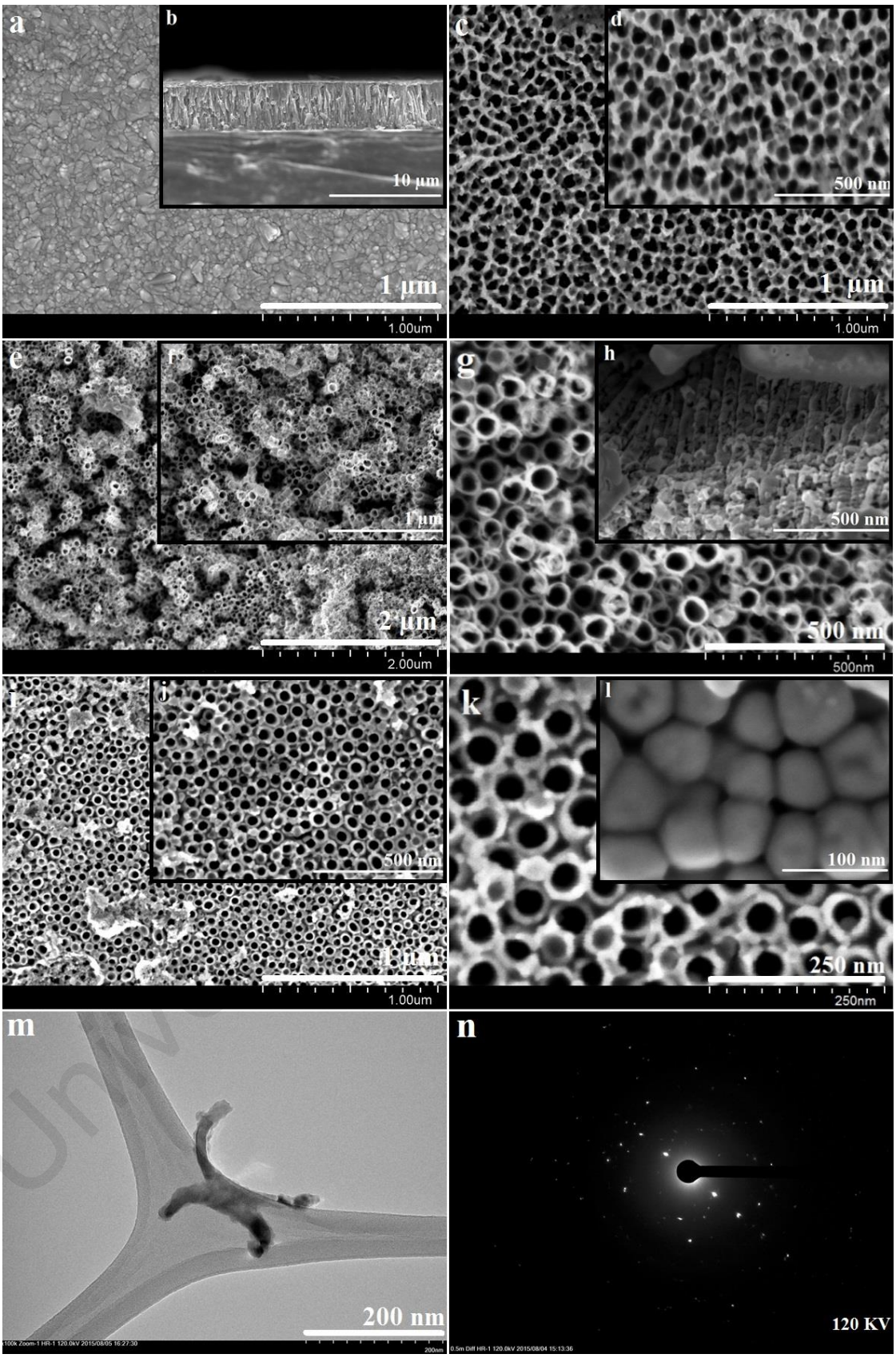

Figure 4.10: FESEM images of optimized Nb layer on Ti67IMP (a) top view, (b) cross section, and top view of Nb/Ti67IMP anodized for (c, d) 2, (e, f) 3, (g (top), f (cross)) 4 h at 20 V and (i-n) FESEM/TEM/SAED of annealed mixed nanotubes.

To prove the feasibility of the formation and growth of the TiO_2–Nb_2O_5–Al_2O_3 mixed oxide nanotubes on Ti67IMP, the anodic processes with the same condition as electrolyte concentration and anodization parameters were done on Ti67IMP before Nb sputtering, pure Ti and Al separately. Figure 4.11 shows the morphology of the obtained nanotubular structures on mentioned substrates. As can be seen, the morphological features of the nanotubes on various substrates can be easily distinguished. This proves that by attaching the Nb layer on Ti67IMP the electrochemical behavior of system was changed and led to the formation of the ternary mixed oxide nanotubular arrays. This can be justified by the anodization mechanism and pitting effect, which schematically was explained (See Figure 4.8 and 4.9). During the anodization process, as a result of the electrochemical dissolution of Nb the pore bottom is self-acidified, which causes the formation of a pH profile in the growth direction of the pore. With elongated anodization time, the thickness of Nb sputtered layer decreases gradually and Ti67IMP as main substrate is exposed to an acidic environment. Due to the electrochemical dissolution of Ti and Al, TiO_2 and Al_2O_3 nanotubes can be grown and set within the Nb_2O_5 nanotubes, wherein the composition of the oxide nanotubes was influenced strongly by the chemistry of the phases present in Ti67IMP. It would be reasonable that the number of TiO_2 nanotubes is more than the other oxides (Al_2O_3 and Nb_2O_5). From FESEM images in Figure 4.12a and b, the TiO_2 nanotubes have an average inner diameter of 44±12 nm and mean tube wall thickness of 12±2 nm. In the case of the anodized pure Al, a homogenous porous structure with an average pore size of 25±11 nm was achieved after 4 h of anodization at 20 V (Figure 4.12c and d). As shown in Figure 4.11e and f, the anodized Ti67IMP entailed nanotubes with an average inner diameter of 153±56 nm and mean tube wall thickness of 15±2 nm. FESEM cross-section images of the 4 h anodized specimens at 20 V indicates that the surface was completely filled with the self-organized nanotubes with a length of 2 μm in Ti and 4 μm in Ti67IMP (Figure 4.11g and h).

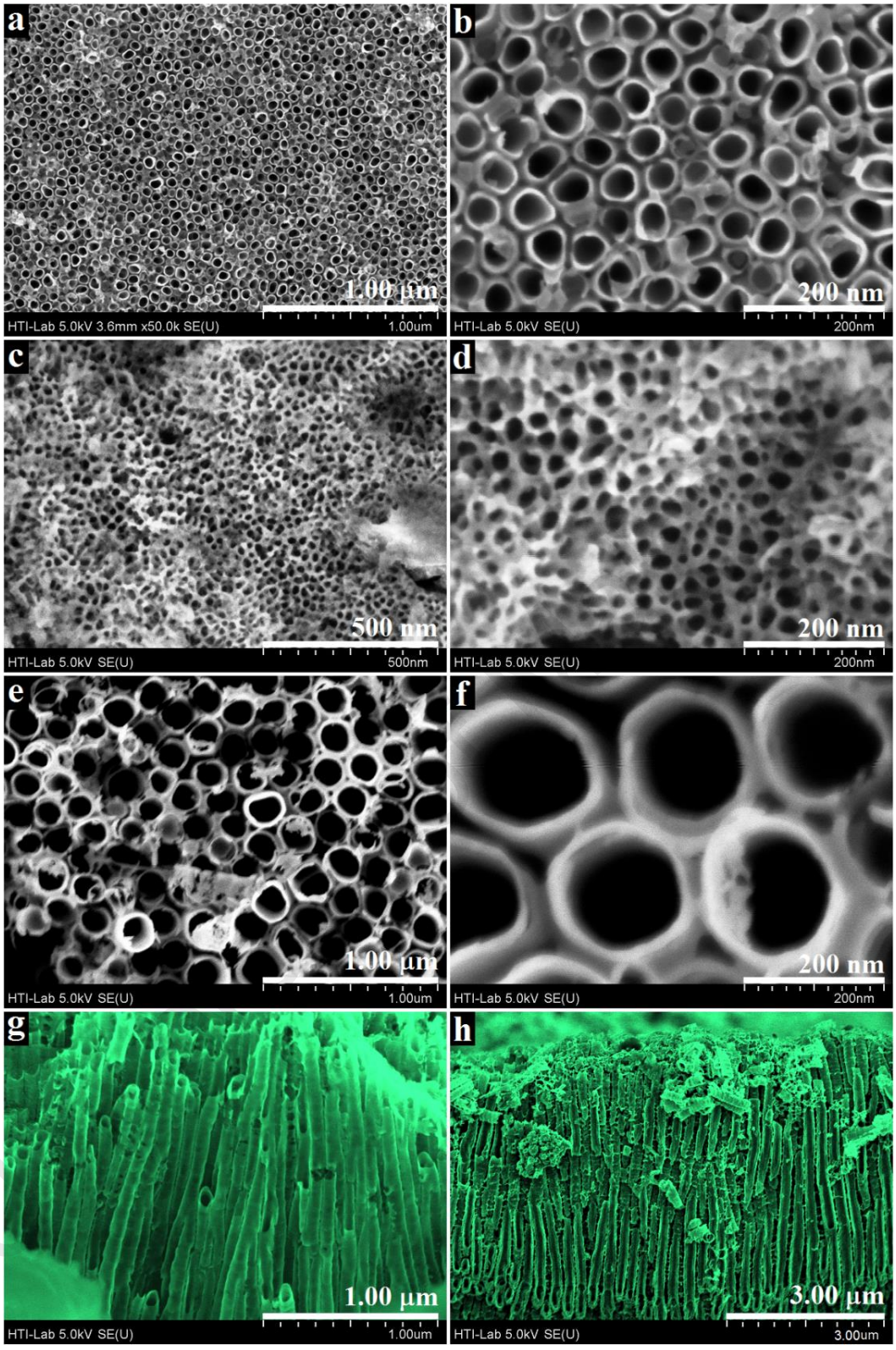

Figure 4.11: FESEM images of the anodized (a,b) pure Ti, (c,d) pure Al, and (e,f) Ti67IMP, as well as cross-sectional images of (g) pure Ti and (h) Ti67IMP.

Due to morphological stability of grown mixed nanotubular array after thermal annealing at 440 °C for 30 min, different magnifications of top view FESEM images as

well as cross sectional image were presented (Figure 4.10i to l). It is clear that a highly oriented arrays of TiO_2–Nb_2O_5–Al_2O_3 mixed oxide nanotubes was formed after thermal treatment. Nevertheless, no significant changes in the morphology of the anodized mixed oxide nanotubes were observed after annealing at 440 °C for 30 min. In this case, the average inner diameter and wall thickness are 45-50 and 10-11.5 nm, in order which is appropriate size for biomedical applications particularly cell adhesion (J. Park, Bauer, von der Mark, & Schmuki, 2007). The bottom of the mixed oxide nanotubes exhibits a series of evenly spaced ‘‘bumps’’, that represent the pore tips of each individual nanotube with low-spacing configuration in case of treated samples. The grown bamboo-shaped structure with good density, which could result in enhanced chemical activity, mechanical and biological properties. It should be mentioned that, in case of increment the optimum annealing temperature (440 °C) satisfied ternary oxides, significant morphological changes and sequential collapse of the nanotubes can be recorded which provide decomposed rough ceramic structure. This issue indicates that coarsening of the mixed oxide nanotubes may occur during annealing at high temperatures (> 600 °C). Furthermore, the TEM image and SAED pattern of the annealed sample are shown in Figure 4.10m and n respectively. The TEM observation indicate that the thickness of tube wall decreases gradually from the bottom to the top region (~ 10 nm). This effect can be explained by the origination of nanotubes during the electrochemical anodization, where the chemical dissolution of the tube wall close to the mouth by the F^- containing electrolyte for elongated anodization time resulted in thinning of the tube wall. Moreover, the SAED pattern of the annealed sample reveals its polycrystalline anatase structure.

From the EDS profile in Figure 4.12, the main elements in the mixed oxide nanotubes are Nb, Ti, Al, and O. In addition, no chemically stable impurity was found. Concerning the elemental area selected and line-scan mapping images (Figure 4.12b,c), a proper spatial distribution of elements was detected, showing the formation of

homogenous microstructure after electrochemical anodization for 4 h at 20 V. However, the elemental mapping displays that the Nb element is mainly distributed on the bottom. This effect can be linked to the dissolution kinetic in fluoride-containing solutions. According to literature, the various transition-metal oxides have very different dissolution kinetics in fluoride-containing solutions (Ghicov et al., 2006). In particular, Nb_2O_5 produced at the anode is significantly more resistant to F^- ions than TiO_2 so that the dissolution rate of Nb_2O_5 is 1 $nmmin^{-1}$, whereas that of TiO_2 is 20 $nmmin^{-1}$. Given that the dissolution rate of Nb_2O_5 in a fluoride containing electrolyte is lower than that of TiO_2, it was anticipated that the elemental mapping of Nb (preferential accumulation on bottom) would differ significantly from that of Ti.

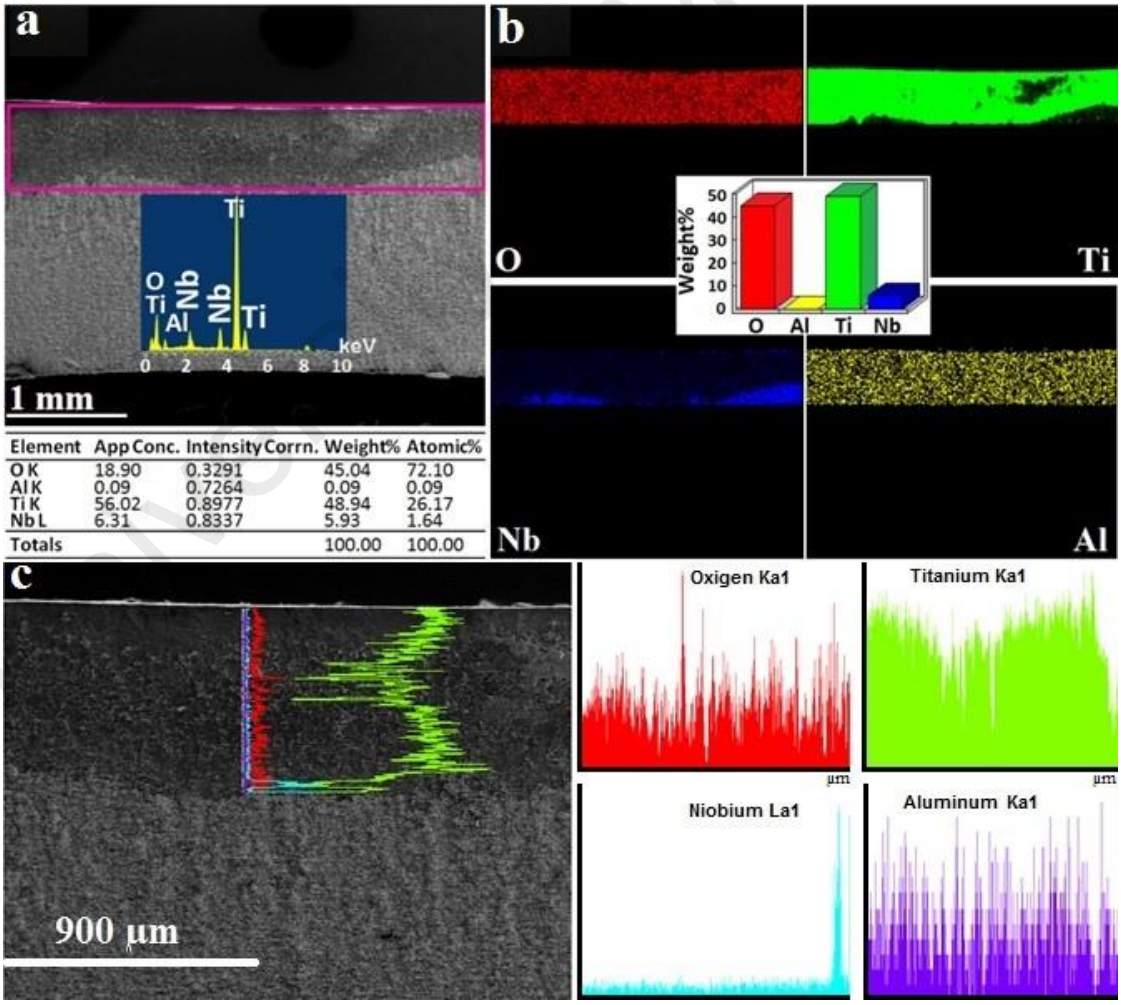

Figure 4.12: (a) EDS profile, (b) coating area and (c) line-scan elemental mapping of the optimized mixed oxides sample (4 h).

Phase analysis of the Ti67IMP substrate, as-sputtered Nb, 4h anodized sample after annealing treatment were presented in Figure 4.13. As can be seen, the XRD profile of the substrate shows merely the characteristic peaks of Ti (JCPDS#005-0682) located around at 2θ = 35.1°, 38.4°, 40.2°, 53.1°, 63.1°, 70.6° and 76.4°, which are ascribed, to the (1 0 0), (0 0 2), (1 0 1), (1 0 2), (1 1 0), (1 1 2) and (2 0 1) planes, respectively. After the PVD deposition, new diffraction peaks, i.e. (1 1 0) plane at 2θ = 38.3°, (2 0 0) plane at 2θ = 55.4°, and (2 1 1) plane at 2θ = 69.4°, corresponding to the single-phase Nb film with a body-centered cubic (bcc) structure (*Im*3*m*) became obvious in the XRD diffractogram (Figure 4.13b). The crystallite size of the specimen was estimated to be 16±3 nm from the FWHM of the main diffraction peaks using the Scherrer formula. After 1 h anodization (Figure 4.13c), the characteristic peaks of tetragonal TiO_2 (anatase: #004-0477; rutile: #01-072-1148), cubic Al_2O_3 (#0047-1292), and monoclinic Nb_2O_5 (#37-1468) were perceived, which confirm the successful development of the mixed oxide nanotubes on Ti67IMP substrate. Peaks typically positioned at 25.4, 37.9, 48.1, and 62.9° were assigned to the (1 0 1), (0 0 4), (2 0 0), and (2 0 4) planes of the anatase phase. The growth orientation of the (1 0 1) plane is favored among planes for all specimens, as evidenced by its dominant intensity compared with that of the other anatase peaks. Moreover, the peaks located at 27.5, 36.1, 41.3 and 54.3° correspond to the (1 1 0), (1 0 1), (1 1 1), and (2 1 1) planes of rutile, respectively (Hanaor & Sorrell, 2011; Kar et al., 2015; SANTOS, OGASAWARA, & CORRÊA, 2009). Hereon, it seems that the anodization electrolyte acted as a chemical catalyst during the preparation process where it provides an alternative route for the generation of highly crystalline TiO_2 phases at room temperature without post-thermal treatment. Based on results, the percentage of anatase and rutile phases in the mixed oxide nanotubes was 57 and 43%, respectively. It has been reported that the amount of rutile formed can be increased when the applied voltage increases up to 200 V because of the greater amount of energy provided at higher

voltage (Cheong, Yam, Ooi, & Hassan, 2014). From the schematic views of the Ti (1 0 0) and Nb (1 0 0) surfaces in Figure 4.13d, there are three dissimilar, high-symmetry adsorption positions involving (i) top, (ii) hollow and (iii) bridge sites, which shows that the mixed oxide nanostructures can be generated on the Nb/Ti67IMP after immersing the specimen in the anodizing bath. As can be seen, both anatase (space group *I*41/*amd*) and rutile (space group *P*42/*mnm*) are tetragonal in structure and comprise of TiO_6 octahedra, sharing four edges in anatase and two in rutile (Hanaor & Sorrell, 2011). In general, Al_2O_3 can crystallize with various crystal structures. Here, the phase obtained is γ-Al_2O_3 which has space group *Fd*3*m*, $a = b = c = 7.9448$ Å, V = 501.47 Å^3, $D = 3.59$ g/cm^3. In this structure, for the Al^{3+} ions (located on three different lattice positions) the site occupancy is not 1, but amounts to 0.58, 0.84, and 0.17 which means that in 58%, 84%, and 17% of the unit cells a given Al^{3+} position is actually occupied by an Al^{3+} ion (De Graef & McHenry, 2012). In the case of monoclinic Nb_2O_5, twenty-seven of the Nb atoms are in octahedral coordination and one is tetrahedral, where the structure possesses ReO_3-type blocks of two different sizes. At one level these are three octahedra wide and five long, and are joined, by sharing edges on both sides, into slabs running right through the structure in two directions. The second kind of block, three octahedra by four, cements these together by additional edge sharing, and leaves tetrahedral holes partly, but systematically, filled with niobium atoms (Gatehouse & Wadsley, 1964). Based on discussed results, crystallization behavior of mixed oxide nanopatterned bioceramics was affected by the subsequent annealing. Following XRD results include (a) Ti67IMP substrate, (b) mono-layered Nb coating, and mixed oxide nanotubes (c) as well as (d) schematic views of the Ti (1 0 0) and Nb (1 0 0) surfaces plus projections of the structures of tetragonal TiO_2 (A: anatase ; R: Rutile), cubic Al_2O_3, monoclinic Nb_2O_5.

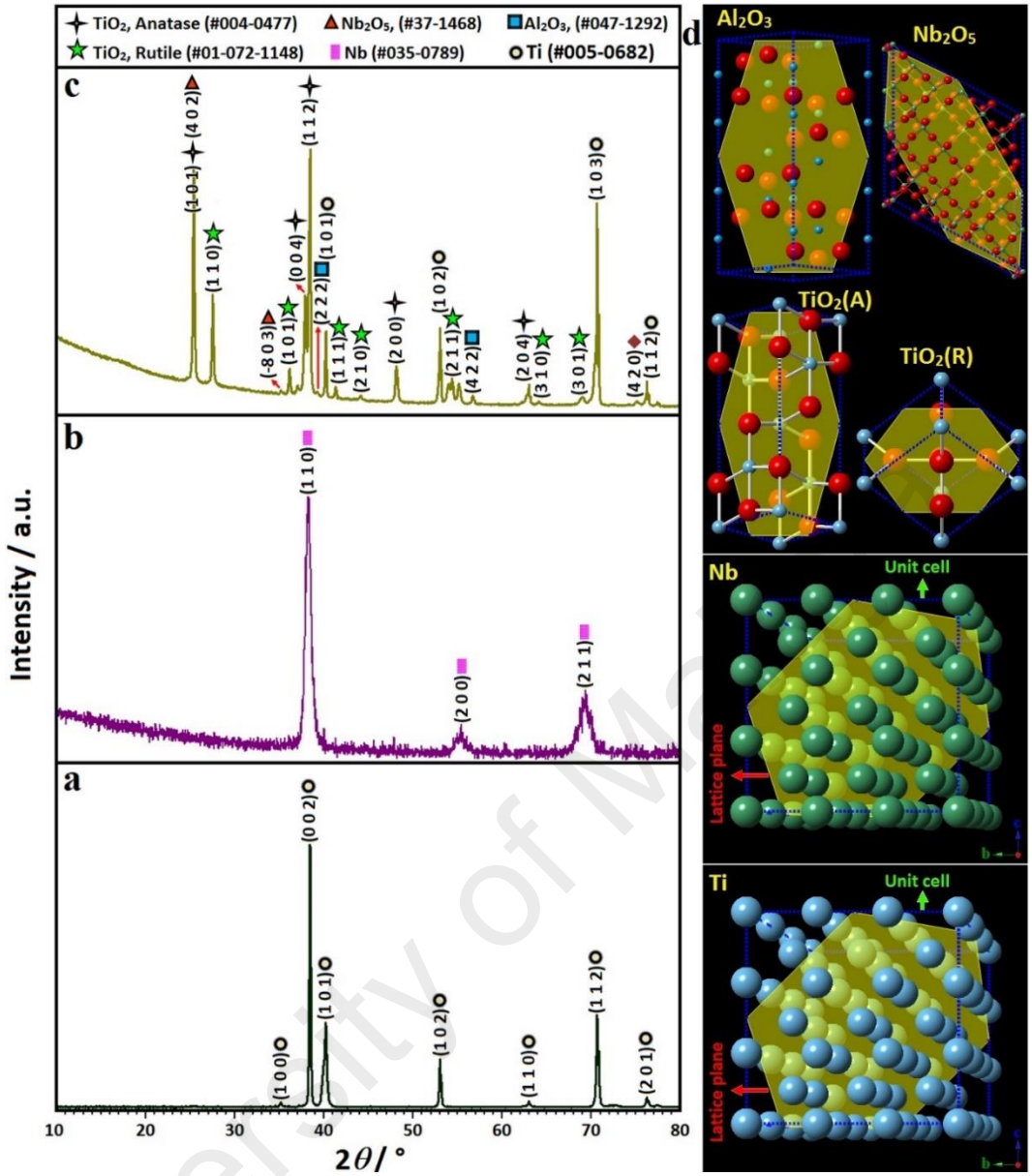

Figure 4.13: XRD patterns of Ti67IMP substrate, mono-layered Nb coating and mixed oxide nanotubes.

Moreover, to evaluate chemical constituents of anodically aligned mixed oxide nanopattern ceramics XPS analysis was examined to confirm XRD results. Figure 4.14 displays the XPS spectra (wide and narrow scan) of the 4 h anodized Nb/Ti67IMP at 20 V after thermal annealing. High-resolution XPS showed that the nanotubes formed on Nb/Ti67IMP are composed of a mixture of TiO_2, Nb_2O_5, and Al_2O_3 (Ghicov et al., 2006). According to the Ti 2p, Nb 3d and Al 2p peaks the Ti/Nb/Al/O atomic ratio of the nanotubes was determined as 16:6:2:59. The Ti 2p spectrum of nanotubular arrays is

matched $2p_{3/2}$ and $2p_{1/2}$ as the spin–orbit components of Ti 2p were deconvoluted into two peaks at binding energy of 458.6 and 464.06 eV. Note that the amount of the binding energy separation between the Ti $2p_{3/2}$ and Ti $2p_{1/2}$ peaks is ca. 5.5 eV, which is in well agreement with the binding energy separation of stoichiometric TiO_2 (Ghazzal, Chaoui, Genet, Gaigneaux, & Robert, 2011). The Nb 3d spectra of all the nanotube arrays show two peaks at 207.2 and 210.1 eV, which are assigned to Nb $3d_{5/2}$ and Nb $3d_{3/2}$, respectively (H. Liu, Gao, Liao, & Fang, 2015). This is in good agreement with the reported literature values for Nb $3d_{5/2}$ and Nb $3d_{3/2}$ in Nb_2O_5 based on the NIST database (Y. Zhao et al., 2012). Also, the XPS Al 2p spectrum of the nanotubular array has a single peak at around 74.5 eV, which is associated with Al-O bond (Nayak et al., 2014). From this spectra, the Ti/Nb/Al ratio of the oxide reflects the 8:3:1 atomic ratio of the Ti67IMP substrate. For all nanopatterned ternary oxide structure, the O 1s peaks represent three peaks at binding energy of 529.3, 530.5 and 531.8 eV, which assigned to oxygen component in the Ti-O, Nb-O, Al-O and O-H bonds respectively. These panels confirm the successful preparation of TiO_2-Nb_2O_5-Al_2O_3 mixed oxide ceramic with confirmed elemental compositions. The obtained result is also in agreement with EDS analysis (which has a larger analysis area and a much higher penetration depth than XPS), signifying that the composition stays nearly constant over the entire tube length. Following XPS results include (a) XPS spectra (wide scan) of the 4h anodized mixed oxide sample at 20 V after annealing at 440 °C for 30 min and XPS high-resolution spectra (narrow fitting) of (b) Ti(2p), (c) Nb(3d), (d) Al(2p), and (e) O(1s).

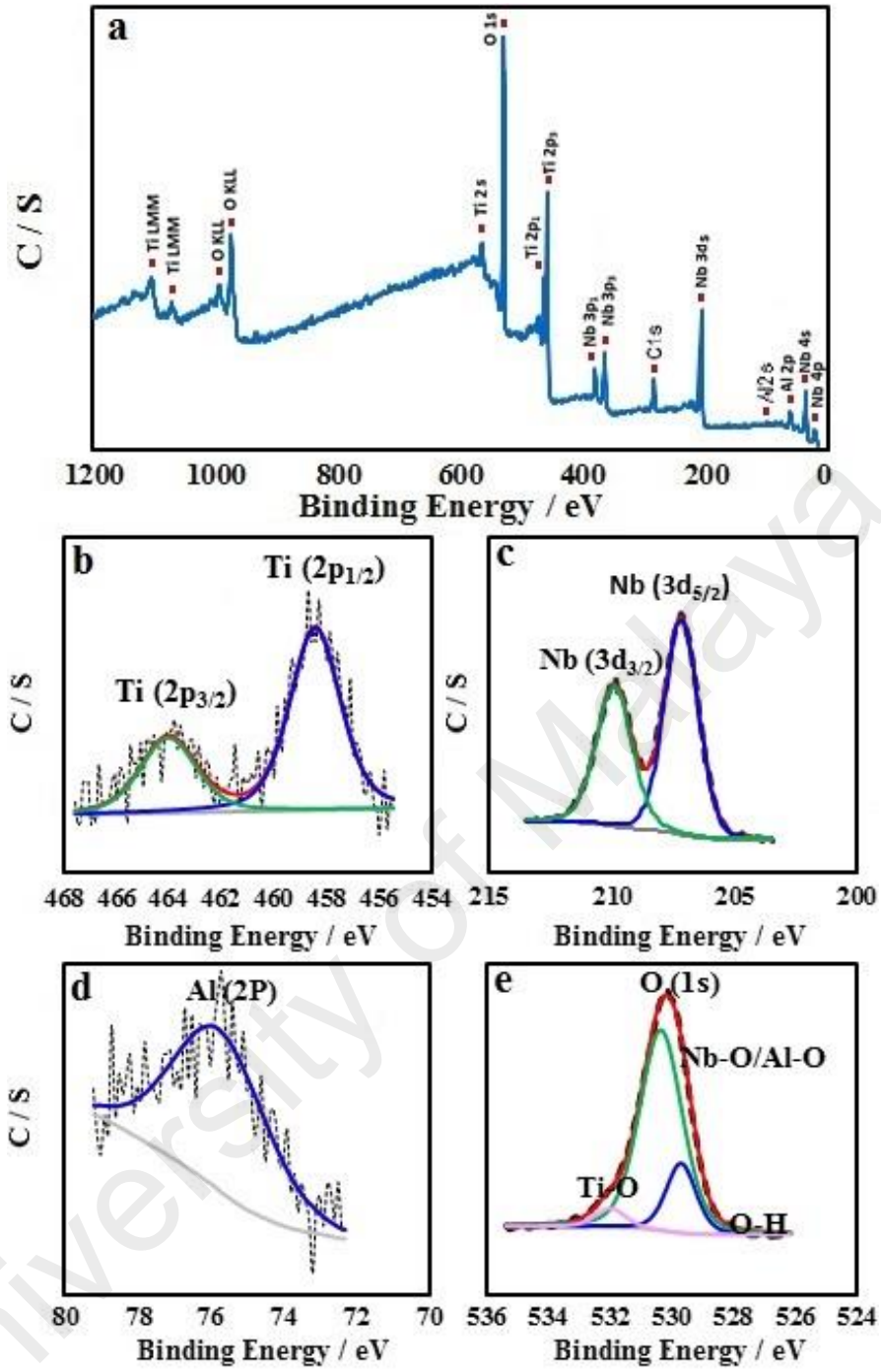

Figure 4.14: XPS spectra wide and narrow fitting scan of crystalline mixed oxides.

4.3 Multilayered GO and Ag-GO on Grown Mixed Bioceramics

4.3.1 Morphological Study

Firstly, the obtained GO suspension were prepared and transparently coated on grown ternary oxide nanotubes to develop ceramic/carbon-based nanocomposite on Ti67IMP. The top-view different magnification TEM/FESEM micrographs of the

attached GO layer on crystallized mixed TiO_2-Nb_2O_5-Al_2O_3 bioceramics are shown in Figure 4.15a to d. As can be seen, a hybrid composite of nanotubular arrays and GO was formed transparently through loading treatment. Applied surface modification via mixed oxide nanotubes and GO nanosheets contributes to enhance the surface area of grown andic configuration. This issue, can generate more active sites of chemical and physical interactions which lead to enhance the bonding between NTs and the host material (N. Liu et al., 2008). Due to antibacterial background of Ag materials, biological performance of hybrid AgNPs-GO topographies may enhance by multilayer attachment of mixed oxides nanotubes. Figure 4.15e to l presents the obtained morphology of 1:12 and 1:6 as-decorated Ag-GO before and after coating comparably. From the obtained results, homogenous covering of carbon-based thin films was generated on nanotubes with and without presence of AgNPs. It is notified that the obtained morphologies are in good agreement with distribution of both concentrations of AgNPs through GO nanosheet in case of synthesized and composite materials. The fabricated nanocomposites were aimed to evaluate the probable biological and corrosion activity of GO-based structures as well as antibacterial effects for bone tissue regeneration.

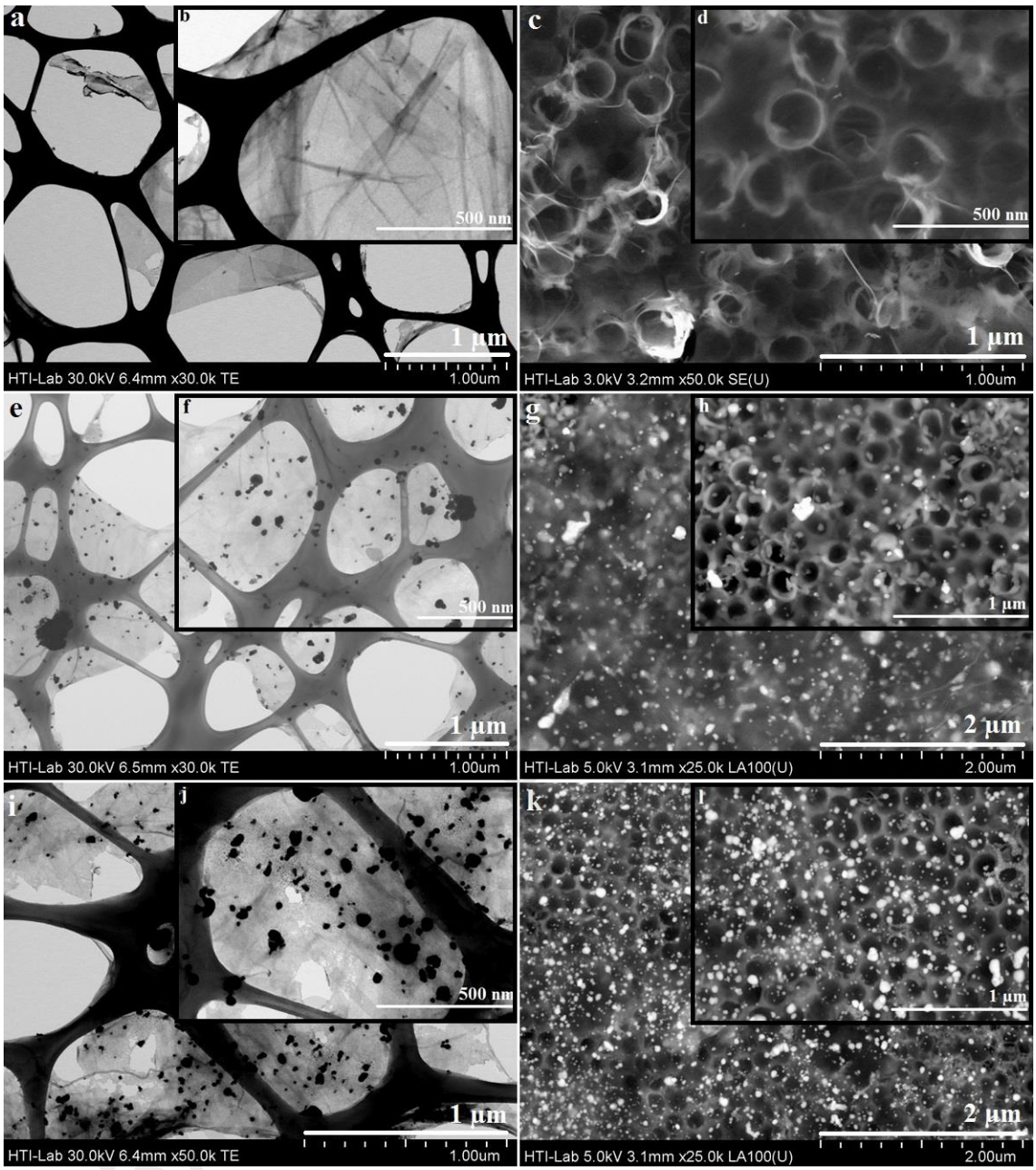

Figure 4.15: TEM/FESEM micrograph of the synthesized and multilayer thin film composites (a-d) GO (e-h) 1:12 Ag-GO and (i-l) 1:6 Ag-GO loaded mixed nanotubular bioceramics on Ti67IMP.

4.3.2 Structural and Elemental Characterization

Figure 4.16 illustrates the XRD patterns and schematic drawings of the single-layer graphene, graphene oxide (GO) and Ag decorated GO nanostructures. The XRD profile of graphene displays the (0 0 2), (1 0 1), and (0 0 4) graphite diffraction peaks, as labeled in Figure 4.16a. The structure is preserved after the functionalization process. The broad diffraction peaks of graphene implied that the ionic liquid groups can influence the

crystallization of the graphene nanosheets in the functionalization process as also reported by Liu *et al.* 2008 (Lambert et al., 2009). As shown in the schematic drawing in Figure 4.16a, graphene is a single-layer of sp^2 hybridized carbon atoms in a 2D honeycomb lattice. The surface area value and aspect ratio of a single-layer of graphene can reach 2600 $m^2 g^{-1}$, which is much higher than those of carbon nanotubes (CNTs) and fullerenes. This feature can generate more active sites for expediting chemical and physical interactions, consequently enhancing the bonding between graphene and the host material (N. Liu et al., 2008; Z. Pan et al., 2015). From the standard database (Blanton & Majumdar, 2013), it is expected that the (0 0 1) GO diffraction peak appears in a range of 2θ ~7–12° dependent on the residual water amount intercalated between basal planes in a GO (Blanton & Majumdar, 2012). From Figure4.16b, the reflection mode geometry X-ray diffraction pattern for a neat GO has a strong (0 0 1) characteristic peak at 2θ = 10.6° with the interlayer spacing of 0.83 nm, which is much wider than that of the graphite narrow peak located at 26.8° with an interlayer spacing of 0.33 nm. This shows that GO has been successfully exfoliated from the raw graphite. Besides, a broad diffraction peak appeared at a lower 2θ than bulk graphite in the range of 23–24°, which is related to (0 0 2) peak of reduced graphene oxide (RGO) with interlayer spacings of 0.36 nm. According to the schematic representation in Figure 4.16b, GO as a type of functionalized graphene is a single-layer of sp^2-hybridized carbon atoms with the presence of carboxyl, carbonyl, hydroxyl and epoxy functional groups, attached to the edges and the basal planes of the graphene sheets (Xu & Shi, 2011). It has been reported that the presence of the functional groups change the van der Waals interactions between the sheets, enhanced dispersion in water, N-methylpyrrolidone, dimethylformamide, tetrahydrofuran and other polar solvents (J. Kim et al., 2010). In the case of Ag decorated GO (Figure 4.16c), the intensity of (0 0 1) characteristic peak of GO fell sharply and a broad diffraction peak corresponding to RGO appeared in the range of 23–24° (Sookhakian, Amin, & Basirun,

2013). In addition to GO and RGO peaks, new crystalline peaks relevant to Ag (JCPDS#004-0783) including (1 1 1) plane at 2θ = 38.4°, (2 0 0) plane at 2θ = 44.1°, (2 2 0) plane at 2θ = 64.1°, and (3 1 1) plane at 2θ = 77.3° with a face-centered cubic (fcc) configuration (*Fm*3*m*) are evident in the XRD profile.

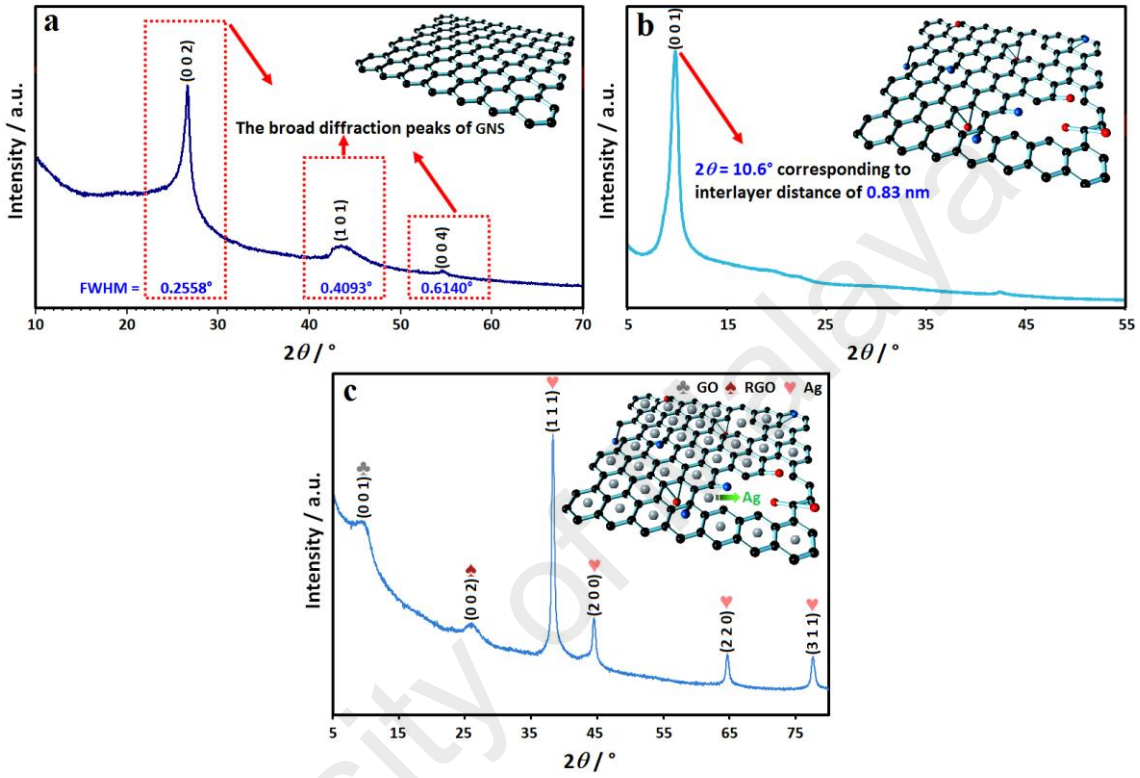

Figure 4.16: XRD patterns and schematic drawings of the (a) single-layer graphene, (b) graphene oxide (GO) and (c) AgNPs-decorated GO nanostructures.

As shown in Figure 4.17, after the deposition of synthesized GO-based materials such Ag-GO with the different ratios of 1:6 and 1:12 on the external surface of the mixed oxide vertically aligned bioceramics, a similar phase structures was obtained. From Figure 4.17 a and b, it was verified the existence of tetragonal TiO_2, cubic Al_2O_3, monoclinic Nb_2O_5 phases together with minor cubic Ag after the Ag-GO deposition confirmed with attached schematic views of GO and Ag surfaces. Based on the presented figure, Ag crystallizes in a face-centered cubic lattice with bulk coordination number 12. It is also clear that GO is a single-atomic layered material. In fact, Go is an oxidized form of graphene, laced with oxygen-containing groups. Although graphene contains of only

sp^2 carbons, GO consists of some sp^3 carbons and structural defects giving insulating properties (Chua & Pumera, 2014). The following XRD results includes graphs of mixed bioceramics on Ti67IMP in presence of Ag-GO with the ratio of (a) 1:6 and (b) 1:12 as well as (c) schematic of cubic Ag and idealized structure proposed for GO.

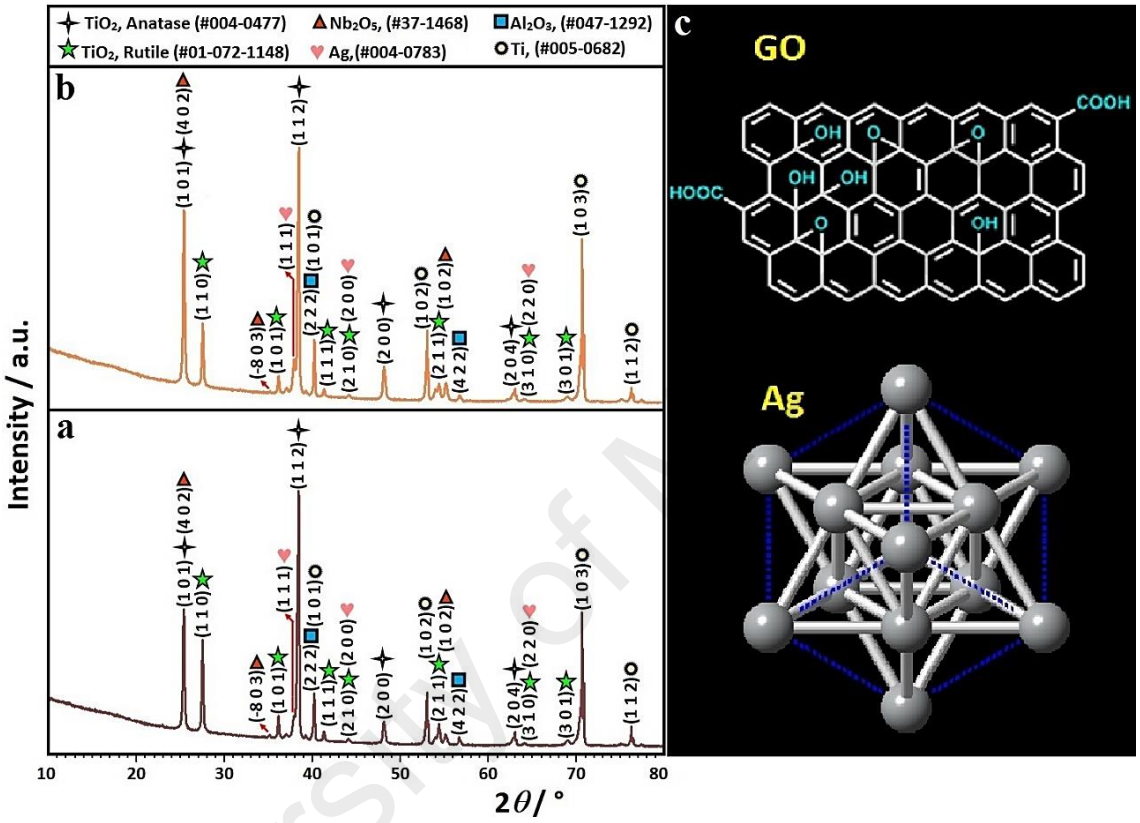

Figure 4.17: XRD patterns of mixed bioceramics on Ti67IMP in presence of Ag-GO.

Designed GO and Ag-GO topographies were anchored on the surface of patternd nanotubular bioceramics. As shown fitting XPS spectra in Figure 4.18a after appearing GO nanosheet, the deconvolution of C 1s peak investigated in four peaks. The first peak at 283.4 was attributed to the sp^2-hydridized carbon. Oxidized forms of carbons were the main reason for appearing the other peaks at ca. 285.0, 285.8 and 286.98 eV, which are usually related to the C–O, C=O and O–C=O bonds (Z. Wang et al., 2014). Hence, the presence of these peaks clearly confirms the successful decomposition of GO on the designed multilayer metallic-ceramic composition. Accordingly, the transparently coated

Ag-GO structure on the surface of nanotubular morphology was characterized as a new layer. Therefore, a new peak was added to XPS spectra of fabricated TiO_2-Nb_2O_5-Al_2O_3 nanotubes on Ti67 substrate. The narrow-scan fitting of Ag 3d in Figure 4.18b presents a couple peak at 368.0 and 374.0 eV, which were attributed to the binding energies of Ag $3d_{5/2}$ and Ag $3d_{3/2}$, respectively. In addition, the spin energy separation between the aforementioned peaks is 6.0 eV, representing the successful decoration of Ag nanoparticles on GO surface (Figure 4.18a and b) as well as characteristic of considered metallic Ag (S.-K. Li, Yan, Wang, & Yu, 2013). The following XPS results include (a) narrow spectra of loaded GO nanosheet (C 1s) and (b also a) decorated Ag-GO (Ag 3d and C 1s) attachment on the surface of anodic mixed nanotubes configuration coated Ti67IMP substrate.

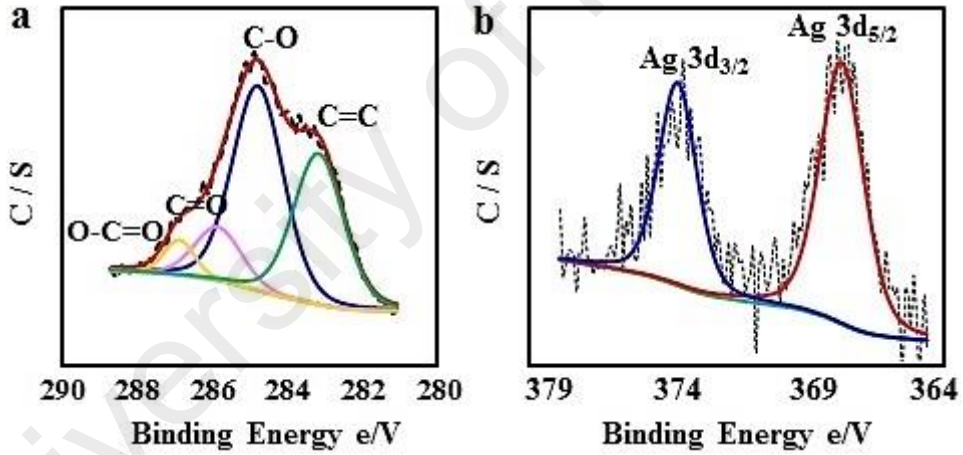

Figure 4.18: (a) XPS narrow spectra of loaded GO nanosheet and decorated Ag-GO attachment on the surface of mixed bioceramics.

As well as XRD and XPS characterization, to verify the GO and decorated of Ag-GO composite, FT-IR and Raman spectroscopies were employed. Figure 4.19a demonstrates the current spectra of pristine GO and Ag-GO nanostructures. First, a broad peak at the range of 3200-3400 cm^{-1} is attributed to the stretching vibration of OH groups. Also, two peaks in the range of 2800-2950 cm^{-1} are related to the stretching vibration of C-H groups (Vasconcelos, Nunes, Gasparon, & Vasconcelos, 2011). The strong peaks at

1733, 1624, 1366 and 1049 cm^{-1} are assigned to the stretching vibration of C=O, COOH, C–O–C (epoxide) and C–O groups, respectively (Acik et al., 2010). In contrast, the FTIR spectrum of Ag-GO shows some weak peaks as compared to GO. Adding silver nanoparticles to the GO surface change the KBr pellet opaque, resulting in reduction of transmission infrared light as well as the removal of some weak bands (Amiri, Shanbedi, Eshghi, Heris, & Baniadam, 2012; Chook et al., 2012). Noteworthy, a significant band at ~ 485 cm^{-1} is related to the characteristic stretching mode of Ag-O.

Raman spectroscopy is considered as a strong characterization method to analyze the structural and electronic properties of carbon allotropes (A. Das et al., 2008; B. Das, Voggu, Rout, & Rao, 2008). Figure 4.19b illustrates the Raman spectra of GO and Ag-GO. It can be seen that Raman spectra of GO and GO-Ag show two sharp peaks at 1363 and 1598 cm^{-1}, which were attributed to the D and G bands, respectively. Note that the D band is arises from the amorphous/disordered carbon (sp^3- hybridized carbon atoms), which can be sourced by functionalization and electron doping, whereas the G band is associated to the in-plane bond stretching of the graphitic carbon (sp^2 band) (Amiri et al., 2015; Amiri et al., 2016a). It can be seen that the intensities of both D- and G-bands were increased significantly after the decoration of silver nanoparticles on the surface of GO structure. These increases in intensities are attributed to a short-range chemical effect between AgNPs and GO (Amiri et al., 2016a). Likewise, the ratio of the intensities of the D-band to the G-band (I_D/I_G), which is the amount of sp^3-hybridized carbon relative to sp^2-hybridized carbon increased, which can be confirmed the successful decoration of AgNPs on GO material (Amiri et al., 2012).

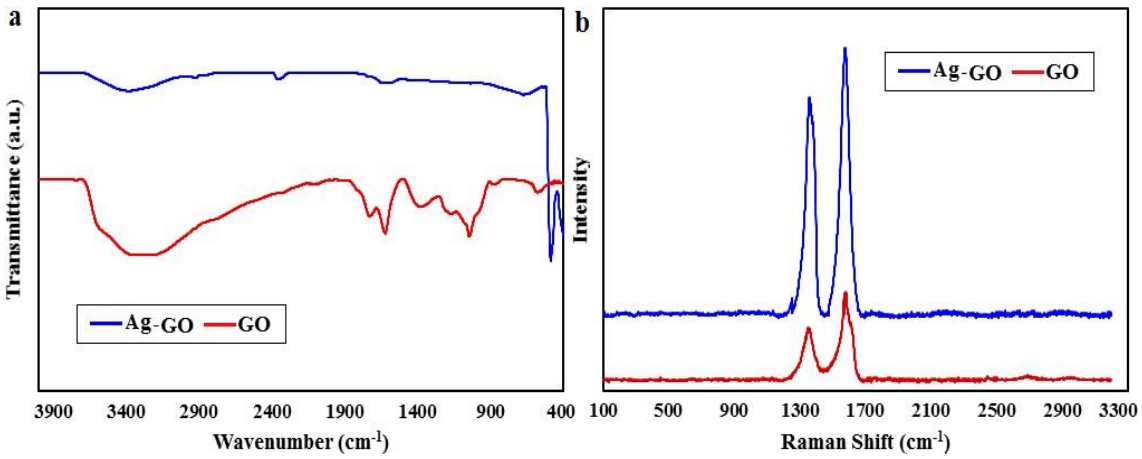

Figure 4.19: (a) FT-IR and (b) Raman spectra of GO nanosheet also decorated Ag-GO composite.

4.4 Arginine-pure Graphene (Arg-Gr)/Mixed Oxides Nanobiocomposite

4.4.1 Morphological Study

Herein, due to superior characteristics, pure mono layer Gr and functionalized Arg-Gr before and after attachment on mixed nanotubes was presented to assess the multilayer morphology of metallic/ceramics/carbon-amino acid biocomposites. Figure 4.20 presents TEM/FESEM micrograph images of nanopatterned Gr and Arg-Gr composite. Clearly, all related TEM images demonstrate some few-layered graphene flakes with diameter around 2 µm. It is remarkable that, obtained images of the pure Gr show some sheets with more or less smooth layer's surface. Although TEM image is not able to distinguish very small functional groups, some surface changes and the presence of wrinkles in sheets can be considered as a reason for the attachment of functional groups. From the TEM images of the Arg-Gr, the resulting sheets preserved their shape and size as compared with the pure graphene. Figure 4.20c and d demonstrates the images of the functionalized Arg-Gr, which were comprised of a few-layered graphene with wrinkled morphology and folded edges. Arg-Gr sheets are attributed to the inherent instability of the graphene structures and the enhanced flexibility of sheets after chemical functionalization. Clearly, higher tendency for wrinkling shows a growth in the wettability of graphene surface due to covalent functionalization with amino acid. In

addition, a set of highly-crumpled, individual graphene flakes with suitable transparency and without observable graphite crystalline structure in current results confirmed that these wrinkles resulted from the crumpling of graphene rather than stacking. Likewise, the morphology of reinforced mixed nanotubular bioceramics with Arg-Gr functionality was resulted to fabricate the multilayer composite (Figure 4.20e and f).

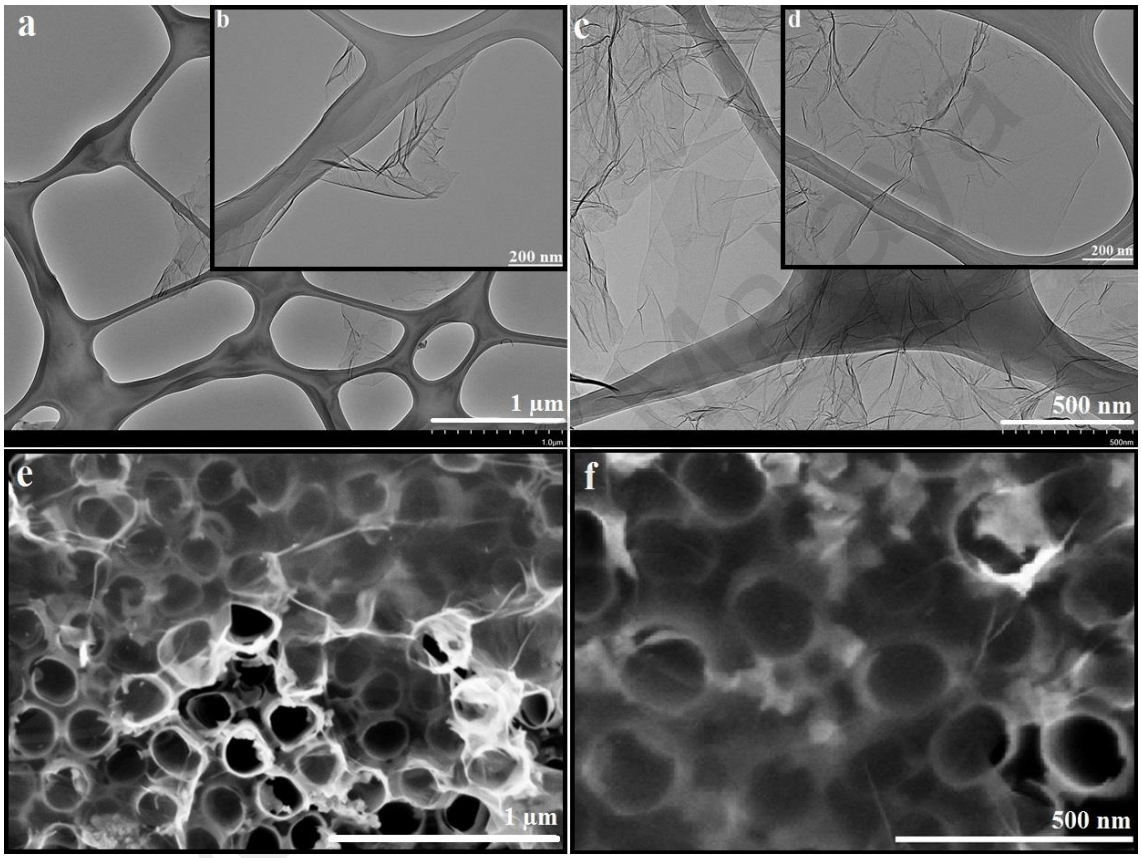

Figure 4.20: TEM/FESEM different magnifications micrograph of (a, b) synthesized mono-layer pure Gr, (b, c) functionalized Arg-Gr composites and (e, f) reinforced Arg-Gr/ mixed nanotubes/Nb/Ti67IMP.

AFM images (left) and cross-section contour (right) of functionalized Arg mono-layer Gr are shown in Figure 4.21a and b. AFM analysis was employed to investigate the thicknesses of the flakes after and before amino acid functionalization. According to the results, the pure Gr sample indicated a sheet with the thicknesses of less than 1 nm, representing the thickness of one layer which is in agreement by recent work (Amiri et al., 2016a). The obtained results are in agreement with the recent report regarding to

thermally exfoliation of single layered Gr nanosheet. Herein, after novel functionalization of mono-layer Gr with Arginine (Arg), the thickness of sheets was increased accordingly. Based on AFM analysis by Park and Ruoff, mono-layer Gr without any modification has a thickness between 0.6 and 0.9 nm (Nemes-Incze, Osváth, Kamarás, & Biró, 2008; S. Park & Ruoff, 2009). Therefore, the increase in Gr layer thickness was attributed to the functional groups across the surface of Gr sheets. They also reported the thickness of 1.5 nm for functionalized mono layer Gr sheets from AFM images. An increment in thickness of layer confirmed the successful amino acid functionalization procedure.

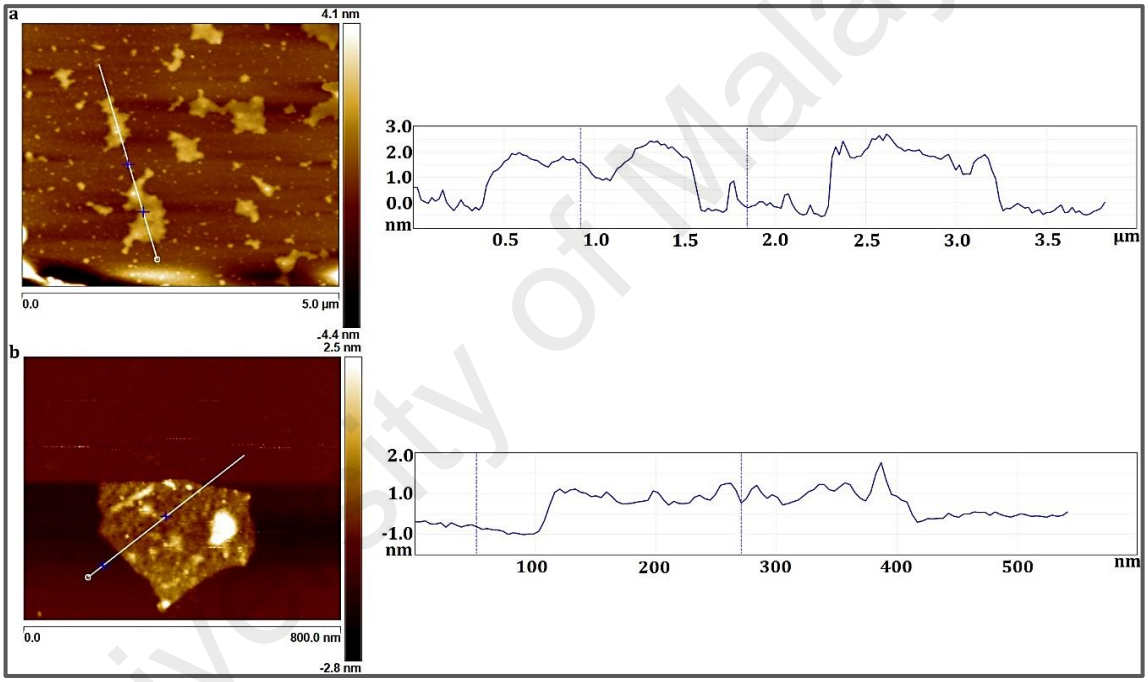

Figure 4.21: (a, b) AFM and cross-section contour of functionalized Arg-mono layer Gr.

4.4.2 Elemental and Structural Characterization

Microstructural characteristics of modified bioceramics with Arg-Gr composite was examined with analyzing the functional amino acid group with pure Gr. XPS spectra of C1s and N1s were described to conduct elemental characterization. The C1s spectra for both synthesized structure and thin film composites including Arg-Gr which provided characteristic features of sp^2 C (284.7) and sp^3 C (283.4 eV), C−N (285.9 eV),

C−O (287.9 eV) and C=O (290.6 eV) groups (Amiri et al., 2016a). It can be seen in Figure 4.22a that the main component at 284.7 eV is originated by elemental carbon atoms. The shoulder at 285 eV - 291 eV is originated by carbon atoms bonded to oxygen and nitrogen atoms by single bonds. Therefore, XPS spectra clearly show that functionalization of pure mono-layer Gr introduce additional functionalities to the surface and/or edges. Moreover, Figure 4.22b illustrates the N1s XPS spectra of Arg-Gr composite loaded anodically grown mixed oxide nanotubes on Ti67IMP. As shown, the deconvolution of N 1s peak was resulted in four peaks at 398.7, 400.5, 401.3 and 402.6 eV, which were commonly attributed to the N-C, amino groups (NH2) (G. Liu, Wang, Liu, & Song, 2012), N=C, and N-C-N bonds, respectively (H. J. Kim et al., 2012; Teng et al., 2014). So, the presence of nitrogen (N) atoms with four different binding energies indicates in related narrow fitting. Noteworthy, there is a well-agreement between the details of different carbon functionalities determined from the C 1s and N 1s high-resolution XPS spectra including nanopatterned organic structure. The Following XPS results include narrow spectra of treated Arg-Gr composite (a) (C 1s) and (b) N 1s attachment on the surface of anodic mixed nanotubes configuration coated Ti67IMP.

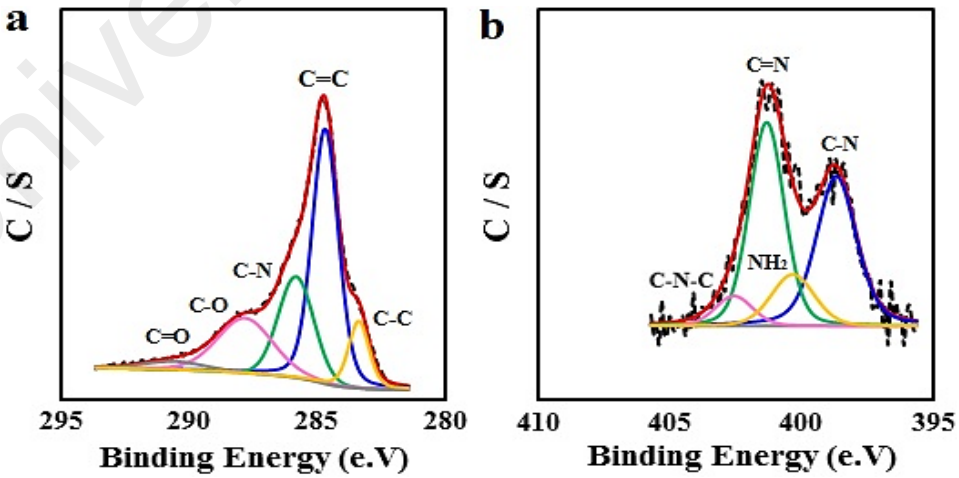

Figure 4.22: XPS narrow spectra of treated Arg-Gr composite attachment.

To study the functional groups, the synthesized samples were characterized by FTIR and Raman spectroscopy. Figure 4.23a illustrates the FTIR spectra of pure Gr and treated Arg-Gr. It can be seen that the current spectrum of pure Gr provided no evidence of functional groups. From the result only two weak peaks were detected in the range of 2800-3000 cm^{-1}, which associated with the C-H stretching vibration. Likewise, the -OH stretching vibration presented a weak peak at 3455 cm^{-1}, indicating the presence of hydroxyl groups on the edge and basal plane of the pure mono-layer Gr structure. In contrast, the FTIR spectrum of treated Arg-Gr had numerous peaks, confirming the successful functionalization of pure Gr with Arg amino acid. The detailed list of peaks and their assigned groups are presented in Table 4.8. It was observed in FTIR spectrum of Arg-Gr that there is a board peak at 3300–3600 cm^{-1}, which is associated with the -OH, and -NH of primary amine stretching vibration. Also, two peaks in the range of 2800-2950 cm^{-1} were associated with the C-H stretching vibration. The peak at 1714 cm^{-1} was consistent with C=O stretching vibrations, which is infrared-activated by the attachment of the arginine groups to the surfaces of the graphene. The FTIR spectrum of the treated samples also had a peak at 1465 cm^{-1}, representing the bending vibration of the CH_2 group. The peaks at 1157 and 1124 cm^{-1} were in agreement with the stretching vibration of the C–N and C–O groups. From Gr-Arg spectrum, decorated amino acid on mono-layer Gr surface show peaks at ~ 1157 and 1552 cm^{-1}, representing the stretching vibration −C−N and −NH bending vibration of primary amine, respectively. The presented peaks were confirmed the successful functionalization of the Gr material with amino acid structure.

The Raman spectra of samples are shown in Figure 4.23b. It is notified that, Raman characterization is a powerful measurement instrument for analyzing structure and sp^2 and sp^3 hybridized carbon atoms in different allotropes. As could be seen, the Raman spectra of pure Gr and Arg-Gr illustrate the D and G bands at around 1342 and 1575 cm^{-1}, respectively. The ratio of the D- to G-band intensities (I_D/I_G) is the best evidence for

measuring the amount of sp^3-hybridized carbon relative to sp^2-hybridized carbon. Therefore, the amount of I_D/I_G can show an increase or decrease in the amount of disruption of aromatic π-π electrons in carbon allotropes or the partial damage of graphitic carbon. As well, while the pure mono-layer Gr demonstrates no sharp D band, Arg-Gr sample is shown strong D bands and higher I_D/I_G ratios, implying structural deformation by functionalization. The ratio of the I_D/I_G for pure mono-layer Gr and Arg-Gr is listed in Table 4.9. It is noteworthy that the I_D/I_G value of Arg-Gr is significantly larger than that of pure Gr. The higher I_D/I_G of Arg-Gr shows that the diazonium reaction was completely successful.

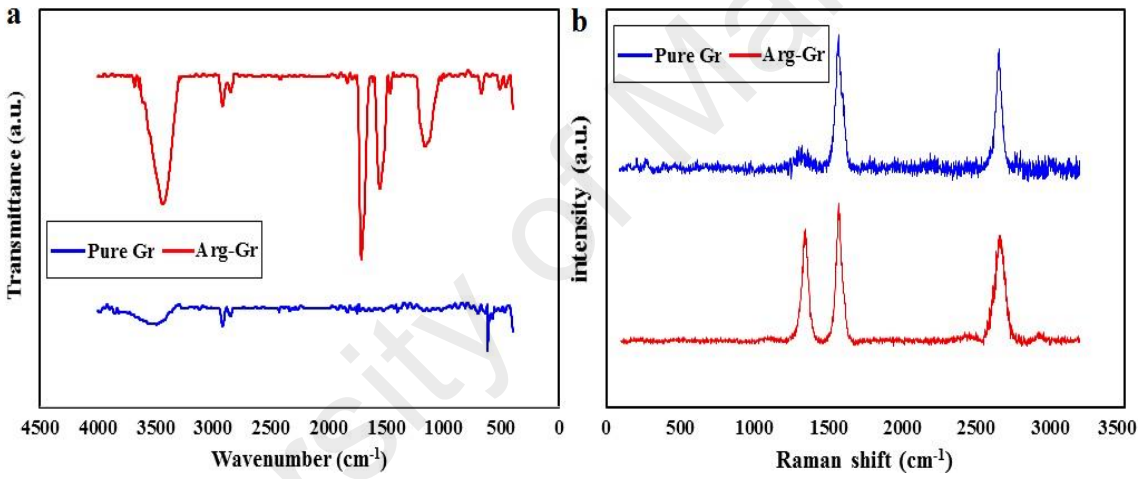

Figure 4.23: (a) FT-IR and (b) Raman spectra of pure Gr and Arg-Gr composite.

Table 4.8: FT-IR detailed peaks and interpretation group of pure Gr and Arg-Gr composite.

Samples	Peak (cm^{-1})	Interpretation
Pure Graphene (Gr)	2800-2950	CH_2 stretching vibration
	3200-3400	υ (C-OH, COOH, H_2O)
	1124	C−O stretching vibration
Arginine-treated Graphene (Arg-Gr)	1157	−C−N stretching vibration
	1465	−CH_2 bending vibration
	1552	−NH bending vibration of primary amine
	1714	−C=O stretching vibration
	2800-2950	CH_2 stretching vibration
	3300–3600	-OH, and -NH of primary amine stretching vibration

Table 4.9: Raman analysis, the ratio of the ID/IG for pure Gr, and treated Arg-Gr composite.

Sample	Amount of I_D/I_G
Pure Graphene (Gr)	0.140674
Arginine-treated Graphene (Arg-Gr)	0.812139

4.5 *In-vitro* Corrosion Resistance

Basically, the elimination and coarse debris removal of corroded surface cause to change in the surface topography which provides biomaterials with low stability. Herein, due to importance of corrosion resistance in bone-like materials, *in-vitro* evaluation of metallic, ceramic and carbon-based nanocomposites on Ti67IMP was conducted via potentiodynamic polarization in phosphate buffered saline (PBS). Figure 4.24 demonstrates the plotted Tafel polarization profiles of the specimens. The corrosion potential (E_{corr}), corrosion current density (I_{corr}), polarization resistance (R_p) and anodic/cathodic Tafel slopes values of the specimens were summarized in Table 4.10. Based on the obtained data, the measured corrosion potential of Ti67IMP was around −0.198 V_{SCE}, where corresponded current density was approximately 4.833×10^{-5} A cm^{-2} which caused active dissolution of the bare substrate. In the case of the optimized as-sputtered Nb film, the measured corrosion potential reached -0.063V_{calc}. From obtained results, the corrosion potentials of the anodized Nb/Ti67IMP, annealed mixed oxide nanotubes, as well as attached GO, 1:12 Ag-GO, 1:6 Ag-GO and Arg-Gr on nanotubular bioceramics samples are around -0.096, -0.086, 0.036, 0.084, -0.059 and 0.015 V_{SCE}, respectively, which are more positive than that of the Ti67IMP substrate. Moreover, the anodic current density of the 440 °C annealed sample is lower than that of the bare substrate which changed to 7.646×10^{-6}, where the hyperbolic curve shifts towards a lower current density. Accordingly after carbon-based materials reinforcement, the related amounts were recorded as 1.299×10^{-8}, 1.659×10^{-8}, 6.958×10^{-8} and 3.207×10^{-9} thorough presented details. This issue indicates that the protective effects of Ti67IMP increase after

thermal treatment of anodically grown mixed bioceramics also GO, Ag-GO 1:12, Ag-GO 1.6 and functionalized Arg-Gr attachments. In accordance to the measured data, the corrosion rate of the crystalline mixed oxides nanotubes, GO, 1:12 Ag-GO, 1:6 Ag-GO and Arg-Gr topographies on Ti67IMP substrate exhibited a reduction of 84.17, 99.97, 99.96, 99.85 and 99.99% respectively. It can be concluded that crystallization of the as-anodized coating and carbon-amino acid reinforcement led to improve the corrosion resistance of Ti67IMP for long term usability. The following corrosion results include polarization curves of corroded (a) Ti67IMP substrate, (b) as-sputtered Nb film, (c) anodized optimum Nb/Ti67IMP, (d) annealed mixed oxide nanotubes, (e) GO/mixed oxides/Nb/Ti67IMP, (f) 1:12 Ag-GO/mixed oxides/Nb/Ti67IMP, (g) 1:6 Ag-GO/mixed oxides/Nb/Ti67IMP and (h) Arg-Gr/mixed oxides/Ti67IMP multilayered specimens, (the related values of i / A cm^{-2} were varied from 10^{-9} to 1).

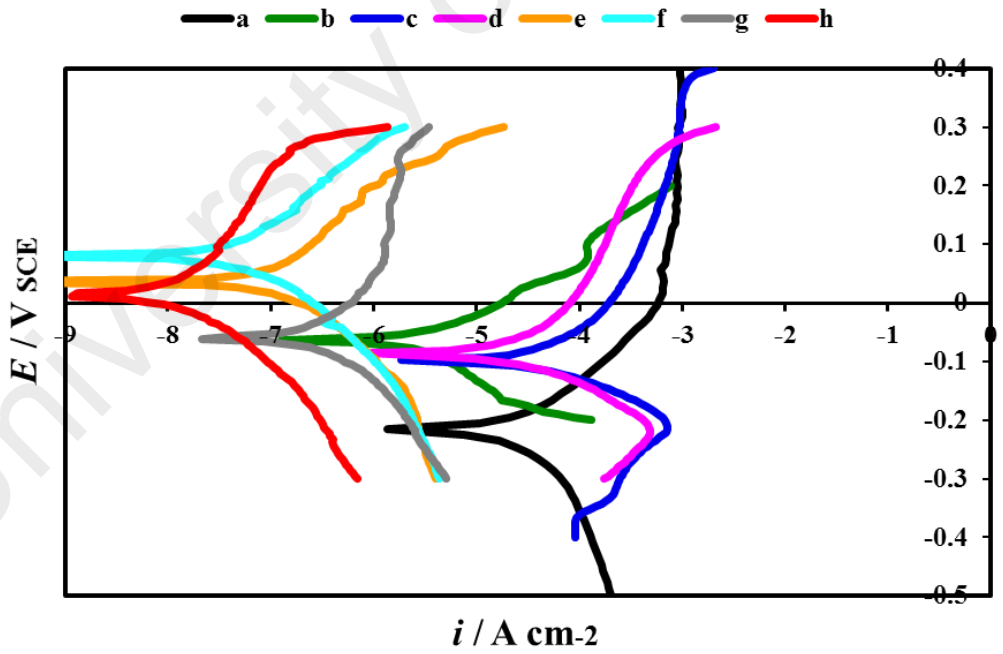

Figure 4.24: Polarization curves of corroded Ti67IMP substrate before and after coating treatments.

Table 4.10: The measured electrochemical parameters of in-vitro corrosion analysis.

Electrode	Ecorr (VSCE)	Banode (V dec-1)	Bcathode (V dec-1)	Icorr (A cm-2)	Rp (Ohm)	CR (mm/year)
Ti67IMP substrate	-0.198	0.177	0.480	4.833×10^{-5}	7.639×10^{2}	7.719×10^{-1}
As-sputtered Nb film	-0.063	0.061	0.044	5.672×10-7	8.053×102	1.919×10-3
Anodized Nb/Ti67	-0.096	0.112	0.069	1.721×10-5	9.810×101	2.009×10-3
Annealed mix oxides	-0.086	0.104	0.060	7.646×10-6	1.759×102	8.923×10-4
GO/mixed oxides/Nb/Ti67IMP	0.036	0.038	0.035	1.299×10-8	2.235×104	1.516×10-6
1:12 Ag-GO/mixed oxides/Nb/Ti67IMP	0.084	0.105	0.085	1.659×10-8	1.173×105	1.936×10-6
1:6 Ag-GO/mixed oxides/Nb/Ti67IMP	-0.059	0.086	0.066	6.958×10-8	1.788×104	8.121×10-6
Arg-Gr/mixed oxides/Nb/Ti67IMP	0.015	0.092	0.076	3.207×10-9	4.746×105	3.743×10-7

From the results, development of highly crystalline mixed oxides nanotubes was significantly improved the corrosion behavior of Ti67IMP. The trend of anticorrosion modification was continued by transparent loading of GO thin film on the surface of grown nanotubular bioceramics. Notably, presence of Ag ions in such stable doped-composite coating structures with high chemical bonding may improve the corrosion resistance of substrates (Chaudhary, Singh, Vankar, & Khare, 2016; Faraji & Mohaghegh, 2016; Khalid et al., 2016). Also, in case of modified metal oxides with corporation AgNPs-decorated carbon structures, the anticorrosion performance enhanced. It should be notified that slight decrease in corrosion rate of 1:12 and 1:6 Ag-GO composites in compared with other carbon-based samples was corresponded to lower molecular bonding which lead to partially release of decorated AgNPs into media through polarization analysis. The higher corrosion behavior was recorded for Arg-Gr sample due to desired homogenous morphology of synthesized mono layer Gr. The corrosion superiority of mono-layer Gr compared with GO composites (defective surface) was directly attributed to its high purity structure with no hole. The extensive corrosion modification of Ti67IMP substrate was confirmed for stable multilayer Arg-Gr/mixed

oxides/Nb/Ti67IMP nanostructured implant which changed from 7.719×10^{-1} to 3.743×10^{-7} mm/year.

4.6 Hardness Assessment

The mechanical hardness measurement of bare Ti67IMP substrate, optimized as-sputtered Nb specimens and multilayered composite-implant systems were followed. Based on the obtained results, the applied modification resulted to enhance mechanical properties as well as microhardness. This improvement is due to more uniformed and adhesive deposited Nb layer by PVDMS process. The coated surfaces with optimized microstructural characteristics were electrochemically anodized to evaluate the effect nanotubular arrays development on mechanical properties of nanostructured Ti67IMP. The fundamental principles of Vickers hardness test operation shows that the load is applied to the indentor by a simple weighted lever. Before the thermally induced crystallization of anodic bioceramics, the Vickers hardness of the as-sputtered Nb and anodized specimens was 362 and 382 HV (3.550 and 3.746 GPa), respectively. In the case of the 440 °C annealed sample, the Vickers hardness was shifted to 415 HV (4.070 GPa) affected by phase transformation of mixed anodic nanotubular array from amorphous to highly crystalline state. This improvement can be linked to the decreased amount of chemisorbed liquid. The achieved enhancement is in good agreement with the microstructural analysis, where the mixed nanostructures were established a stable configuration after annealing treatment. Notably, the validation test predicted the optimal value of hardness for Nb PVD sample (383 HV ~ 3.756 GPa) similar to range of actual data (362 HV ~ 3.550 GPa), which shows the validity of proposed method. Accordingly, the loaded GO thin film also led to enhance the hardness of grown mixed nanatubes. From the measured analysis, the microhardness rose to 481 HV (4.717 GPa). In case of reinforced mix bioceramics with Ag-GO composites, it can be seen that the remarkable decrease was recorded as 333 and 293 HV (3.266 and 2.873 GPa) corresponding to 1:12

and 1:6 conditions respectively. This feature may be addressed to the fact that the softening effect of Ag on coating matrix (C.-F. Huang et al., 2011; Ou, Weng, Lin, & Huang, 2017). Afterward, due to effect of pure TGr and its amino acid-containing structures on strength improvement, the measured value of microhardness was intensively increased in case of amino acid functionalized carbo-based nanocomposite on mixed bioceramics (L. Guo et al., 2016; Kalisz et al., 2016). From the hardness analysis, the highest value was absolutely related to Arg-Gr (545 HV= 5.345 GPa) due to mono-layer Gr morphology and Arg amino acid modification. The variation of Vickers microhardness amounts before and after carbon-based loading are shown in Figure 4.25. the following results include strength of (a) Ti67IMP substrate, (b) as-sputtered Nb film, (c) anodized optimum Nb/Ti67IMP, (d) annealed mixed oxide nanotubes, (e) GO/mixed oxides/Nb/Ti67IMP, (f) 1:12 Ag-GO/mixed oxides/Nb/Ti67IMPIMP, (g) 1:6 Ag-GO/mixed oxides/Nb/Ti67IMP and (h) Arg-Gr/mixed oxides/Nb/Ti67IMP layer-by-layered specimens.

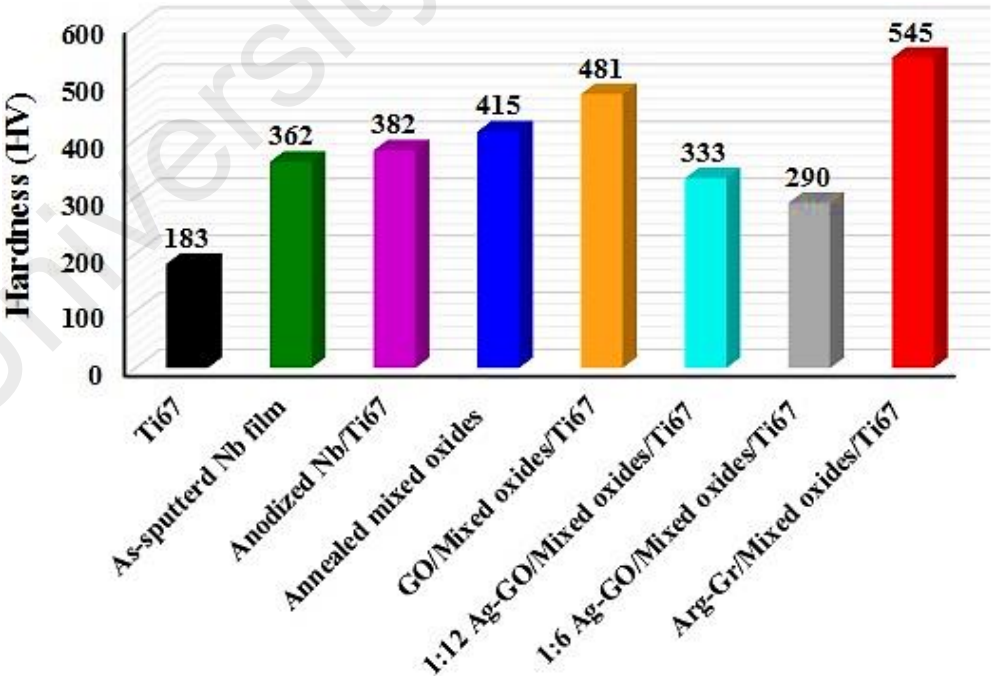

Figure 4.25: Vickers hardness of Ti67IMP substrate before and after coatings.

4.7 Wettability Analysis

Generally, the physical surface features and the surface energy can be specified by the wettability specifications and obtained CA of dropped surfaces (Elias et al., 2008). The CA values signify whether the in hydrophilic or hydrophobic modes. The wettability behavior refers to surface energy and is most determined by the CA (θ) (Tryba, Morawski, & Inagaki, 2003). The drop's form is directly governed by the action of forces pulling at the contact line between the drop and the solid plane, where the solid (S)/liquid (L), liquid (L)/vapor (V) and solid (S)/vapor (V) interfaces meet. The CA is also defined by an equilibrium state between the forces acting on the contact line separating the wetted and non-wetted portions of a homogenous smooth solid surface. Each interface is described by a certain free energy per unit area (γ_{SL}, γ_{LV}, and γ_{SV}). The CA on a smooth and flat surface can be expressed using the Young's model ($\cos(\theta) = (\gamma_{SV} - \gamma_{SL})/\gamma_{LV}$). Figure 4.26a to h shows the schematic view of wettability analysis (part a) and variation of the ultra-pure deionized water CA on the as-sputtered Nb layer on Ti67IMP substrate, anodized Nb/Ti67IMP, crystalline mixed oxides nanotubular array, as well as multilayered carbon-based attached nanocomposites on clinical Ti67IMP alloy. Based on the obtained results, the sputtered Nb layer exhibits a CA of 82.8 ° (Figure 4.26b). While, the CA was changed to 78.6 ° in the case of the anodized optimum Nb/Ti67IMP, (Figure 4.26c). In case of the anodized surfaces, electrolyte conditions played an important role in the wetting phenomenon. EG has a hydrophilic quality due to the hydrogen bonding, which is based on the OH bond in the molecular structure. The dipole-dipole forces among the OH bonds between EG and water bring them together easily. Thus, EG absorbs the water molecule from the air due to the presence of two pairs of OH groups. This suggests that the formation of mixed oxide nanotubes in EG/Fluoride-based electrolyte can enhance the hydrophilicity of the product, thereby the cell attachment, extension and spreading, as well as cytoskeletal organization may improve on the hydrophilic surfaces

of metallic implants (Z. He et al., 2014; Yaghoubi, Taghavinia, Alamdari, & Volinsky, 2010). On the other hand, thermal treatment is an effective manner to improve the hydrophilicity of the metallic implants owing to the high-density oxygen-related defects by this process. Accordingly, improved hydrophilicity (34.2 °) of the annealed sample at 440 °C for 30 min was detected (Figure 4.26d). It has been proven that, amino acids and chained proteins biofunctionality of artificial bone tissues affect the surface features remarkably adsorption and adhesion properties (Elias et al., 2008). Likewise, the wetting behavior of implant surface influences cell feasibility in the primary osseointegration steps. Truthfully, the mineralization mechanism begins when the implant gets in contact with the blood and body fluids. Concerned hydrophobic surfaces, the antibodies signs decrease cell adsorption. In contrary, for hydrophilic surfaces, the signs of the antibodies are to some extent predominant and adsorption is stimulated (Macak et al., 2007). It is remarkable that the surface modification can alter topography, composition, wettability and roughness which amplify cell behavior in bone regeneration.

Transparent loading of carbon-based nanomaterials on crystalline mixed nanotubes enhanced the hydrophilicity feature of designed implant. From the results, the measured CA values decreased to 14.3, 17.1, 26.0 and 30.6 ° for GO/mixed oxides, 1:12 Ag-GO/mixed oxides, 1:6 Ag-GO/mixed oxides and Arg-Gr/mixed oxides specimens on Nb/Ti67IMP surfaces respectively (Figure 4.26f to h). Due to the hydrophilic superiority of GO material rather than pure Gr, higher CA was recorded for Arg-Gr/mixed tubes/Ti67IMP specimen. This superior hydrophilicity of GO, is corresponded to carboxyl, hydroxyl, epoxy and ester groups. Regarding to decorated AgNPs structures, since, it shares ions with just carboxyl group, the lower concentration (1:12) provided near wettability behavior with GO condition. While, for 1:6 Ag-GO, the measured values has been increased affected by metallic nanoparticle distributed on GO nanosheets. These findings indicate that the surface wettability of the Ti67IMP is influenced notably by the

electrochemical anodization, subsequent thermal treatment and carbon-materials loading. The following wettability results include (a) schematic view of the wettability effect. The droplet shape is characterized by the CA (θ), which is defined by three interfacial energies γSV (surface/vapor), γSL (surface/ liquid), and γLV (liquid/vapor). Shown variation of the deionized water CA on the (b) as-sputtered Nb film on Ti67IMP substrate, (c) anodized optimum Nb/Ti67IMP, (d) annealed mixed oxide nanotubes, (e) GO/mixed oxides/Nb/Ti67IMP, (f) 1:12 Ag-GO/mixed oxides/Nb/Ti67IMP, (g) 1:6 Ag-GO/mixed oxides/Nb/Ti67IMP and (h) Arg-Gr/mixed oxides/Nb/Ti67IMP multilayered specimens.

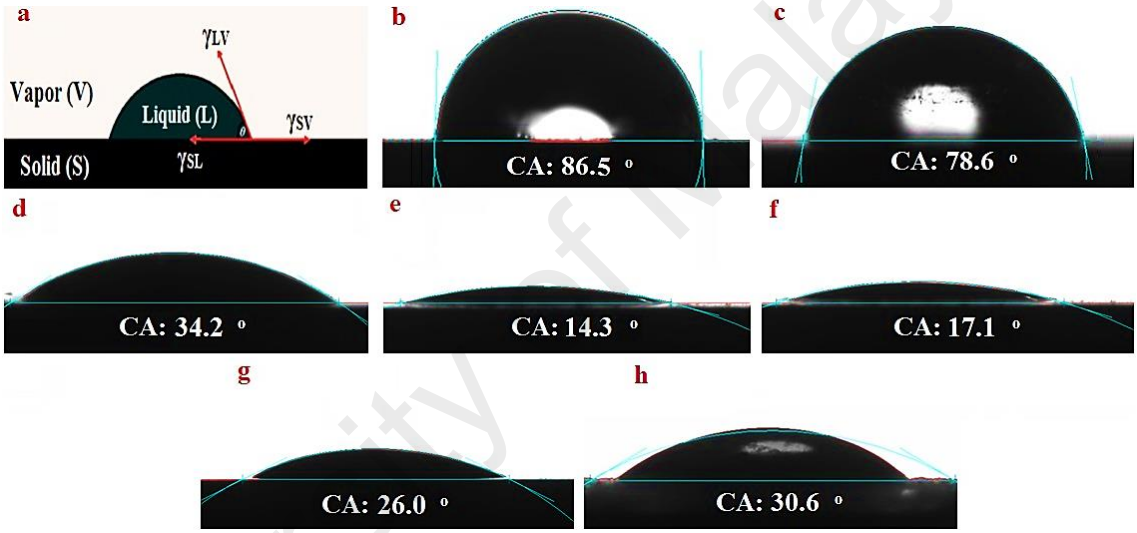

Figure 4.26: (a) Schematic view of the wettability effect and the measured contact angle of bare Ti67IMP and multilayered specimens.

4.8 Biological Studies

4.8.1 *In-vitro* Bioactivity and Mineralization in Simulated Body Fluid (SBF)

Apart from the positive mechanical and corrosion characteristics associated with Arg-Gr/mixed oxides/Nb composite, the good biocompatibility of modified Ti67IMP is also vital for clinical applications. Thus, a quick bio-integration of prosthesis can be a main key feature to form bone-like apatite layer in the vicinity of body media. The apatite formability on metallic implants is on the basis of heterogeneous nucleation phenomenon. If the solution supersaturation and the substrate condition are appropriately controlled,

nucleation and crystallization of apatite layer could happen on the surface of the sample. Therefore, *in-vitro* bioactivity of nanoengineered biometals can be addressed in view of apatite-induced effects on biocompatibility function. From, wettability results, the hydrophilicity of anodic mixed oxides before and after annealing at 440 °C was higher rather than un-treated Ti67IMP substrate. This issue is due to large-surface area of grown mixed oxide nanotubular array which alter the nucleation site. It can be found that, the apatite formation can effectively accelerated on the surface of mixed nanotubes in compare with flat metal surfaces. Figure 4.27 presents the FESEM images and EDS characterization of annealed nanotubes after 10 days soaking in SBF. As shown, a thick layer of bone-like apatite with Ca/P ratio of 1.2 to 1.6 was introduced on mixed bioceramics without any pretreatment of nanotubes in alkaline solution. Therefore, the apatite film has an important effect on bone ingrowth and implant fixation. Obtaining such a uniform apatite layer, is highly affected by morphological stability and dimension of nanotubes. Therefore, development of highly ordered nanotubular bioceramics with the average inner diameter of 46±2 nm resulted to provide appropriate potential. It is remarkable that, within the preliminary phase of soaking, the treated sample interacts with the simulated body media. Furthermore, the wettability features of the artificial tissues can have a significant influence on more expansion of the apatite film. Afterward, the nanopatterned surface was increasingly covered by a coarse layer of bone-like apatite over time, which is in direct contact with media. To examine the effect of the formed apatite layer on hydrophilicity, the CA analysis was repeated with the same condition for the annealed samples. As shown, the CA value dramatically reduced from 34.2° to 12.80° affected by crystalline apatite. This shows that optimized nanostructure coatings improved the hydrophilicity of Ti67IMP. Whereby, the current bioactivity can be linked to higher cell attachment, extension and spreading, as well as cytoskeletal organization and biomedical functionality (Z. He et al., 2014; Yaghoubi et al., 2010).

The *in-vitro* bioactivity analysis was followed for multilayered GO, 1:12 Ag-GO, 1:6 Ag-GO and Arg-Gr layer on anodized Nb/Ti67IMP surfaces. From the results, same thick bone-like apatite layers were formed on all multilayered composites. Figure 4.27e-p illustrates the morphological view of apatite formality potential of nanostructured Ti67IMP systems. It can be seen that bioactivity of GO-based and Arg-Gr specimens very attractive to accomplish promotion of osseointegration. It is notified that higher bio-integration was provided rather than the GO-based nanostructures due to greater specific surface area of synthesized single-layer Gr as well as the effect of functionalized group. The superior apatite formability of Arg-Gr resulted in higher concentration of apatite structure throughout the oxides nanotubular array. Furthermore, the wettability behavior of treated surfaces was increased affected by formed apatite. It can be seen that, the CA decreased from 14.3 to 6.6° in case of GO/mixed oxides/Nb/Ti67IMP sample, which, referred to the hydrophilicity feature of GO nanosheets ant its integration with apatite film. The CA measurement was 7.9 and 11.0° for 1:12 and 1:6 Ag-GO/mixed oxides/Nb/Ti67IMP respectively. The wetting performance of reinforced nanotubular surface with Arg-Gr composite, defined the CA with amount of 13.9 °. The superior hydrophilicity of GO nanosheet rather than Gr structure was confirmed the obtained results. The *in-vitro* bioactivity in simulated body media states osseointegration potential of designed surfaces. To meet the real interaction with body cell, the bioassay evaluations of nanostructures will assess the biocompatibility with hFOB proliferation accordingly. The following results include different magnification FESEM images and variation of the deionized water CA (e, f, m) GO/mixed oxides/Nb/Ti67IMP, (g, h, n) 1:12 Ag-GO/mixed oxides/Nb/Ti67IMP, (i, j, o), 1:6 Ag-GO/mixed oxides/Nb/Ti67IMP and (k, l, p) Arg-Gr/mixed oxides/Nb/Ti67IMP multilayered specimens.

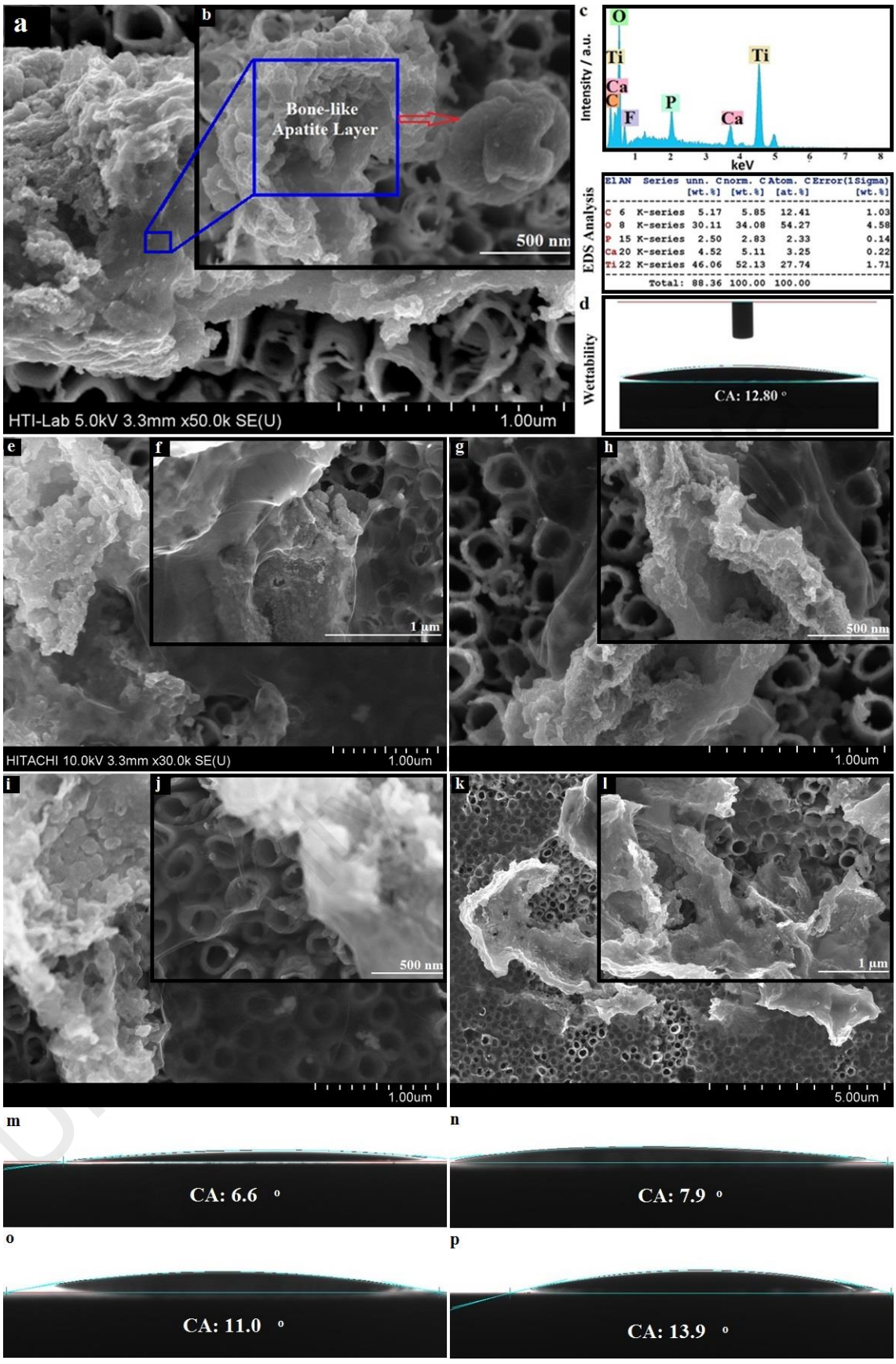

Figure 4.27: (a,b) FESEM observations, (c) EDS results and (d) hydrophilicity measurement of annealed mixed oxide nanotubes after soaking in SBF and(e-p) obtained results multilayered structures modified Ti67IMP.

4.8.2 Antibacterial Activity

Generally, metallic implants are expected to satisfy the high standard of antibacterial immunity as well as biocompatibility properties. Hence, bioactive ceramic and carbon-based nanostructures have been applied in biomedical engineering to obtain bacterial resistance, antibacterial and bactericidal characteristics against Gram-positive and Gram-negative cell wall. To this end, the large-area nanotubular topographies such as TiO_2 and hybrid structures incorporated AgNPs provide current mediation due to specific physico-chemical features (Uhm et al., 2014; Verdier, Coutand, Bertron, & Roques, 2014; H. Yang, Mei, Zhao, & Zhang, 2016). Among carbon-based materials, GO and rGO has been attributed to membrane stress induced by sharp edges of Gr nanosheets, which appear physical damages on bacterial membranes, loss of integrity and the leakage of RNA (Omid Akhavan & Ghaderi, 2010). Based on conducted research, antibacterial activity of GO is higher than graphite (Gt), graphite oxide (GtO) or even rGO is clear (S. Liu et al., 2011). Likewise, it was proposed that Gr structure may induce oxidative stress on neural cells (Yongbin Zhang et al., 2010). GO nanosheets hybrid TiO_2 also can largely enhance the immunity against *E. coli* bacteria (O Akhavan & Ghaderi, 2009). This positively charged surfaces are able to enter the membrane of bacteria and damage the cytoplasm of bacteria. The bacterial cytotoxicity may thus attribute to the both membrane and oxidative stress.

Herein, the antibacterial assessment in the culture medium and adhered bacteria on treated and un-treated Ti67IMP were measured. Table 4.11 and Figure 4.28 present the details of R*p* and R*a* values against *E. coli* and *S. aureus* bacteria. From the results, there is large differences between antibacterial mediation of bare Ti67IMP compared with the coated substrates and synthesized nanostructures. The similar-condition plate assay was carried out to examine the antibacterial behaviour of specimens. The measurement of activity in medium against *E. coli* in LB broth, bare substrate as well as coated mixed

oxide nanotubes, GO, 1:12 Ag-GO and 1:6 Ag-GO on mixed oxides/Nb/Ti67IMP was recorded. From average triplicated results, favorable bactericidal performance (around 100%) was achieved in associated with 1:6 Ag-GO/mixed oxides/Nb/Ti67IMP samples most affected by presence of AgNPs. It is clear that, the attached GO and 1:12 Ag-GO thin films on mixed nanotubular configurations offered lower bactericidal functionality compared with that of 1:6 specimens. Notably, the microstructural stability of mixed ceramics, corresponded as passive layer to enhance the antibacterial activity. Due to this, the anchored GO sheets on the surface of vertically aligned nanotubes compromise in moderate antibacterial activity. So, the undesired potential of defected GO nanosheet, comprised the challenging possibility of using GO-based structure for implemented bone tissues. Moreover, the optical micrographs of plate assay represented differences in antibacterial activity of investigated surfaces. As shown in Figure 4.29, the remarkable bactericidal mediation of Ag-GO samples (particularly 1:6 concentration) was achieved to satisfy the antibacterial requirement of bone-like implants. In contrast, concern with the probable toxicity of Ag-GO materials in body systems, development of potential biocompatible materials are useful to accomplish long-term antibacterial ability. Hence, positively charged surface of organic Arg-Gr nanocomposite can be anchored on the surface of multilayer mixed oxide/Nb as potential alternative to prevent implant infection.

Table 4.11: The details of antibacterial activity against E. coli and S. aureus bacteria in the medium (Rp), and (b) on the specimen (Ra).

Medium	Control (Ti67IMP substrate)	Mixed oxides/ Nb/Ti67	GO/mixed oxides/Nb /Ti67IMP	1:12 Ag-GO /mixed oxides /Nb/Ti67IMP	1:6 Ag-GO/ mixed oxides /Nb/Ti67IMP
E. coli (R*p*)	13.79	86.59	75.82	92.8	97.56
S. aureus (R*p*)	16.41	78.27	91.44	94.31	98.15
E. coli (R*a*)	-----	89.18	95.45	97.50	98.20
S. aureus (R*a*)	-----	91.30	94.97	96.92	99.61

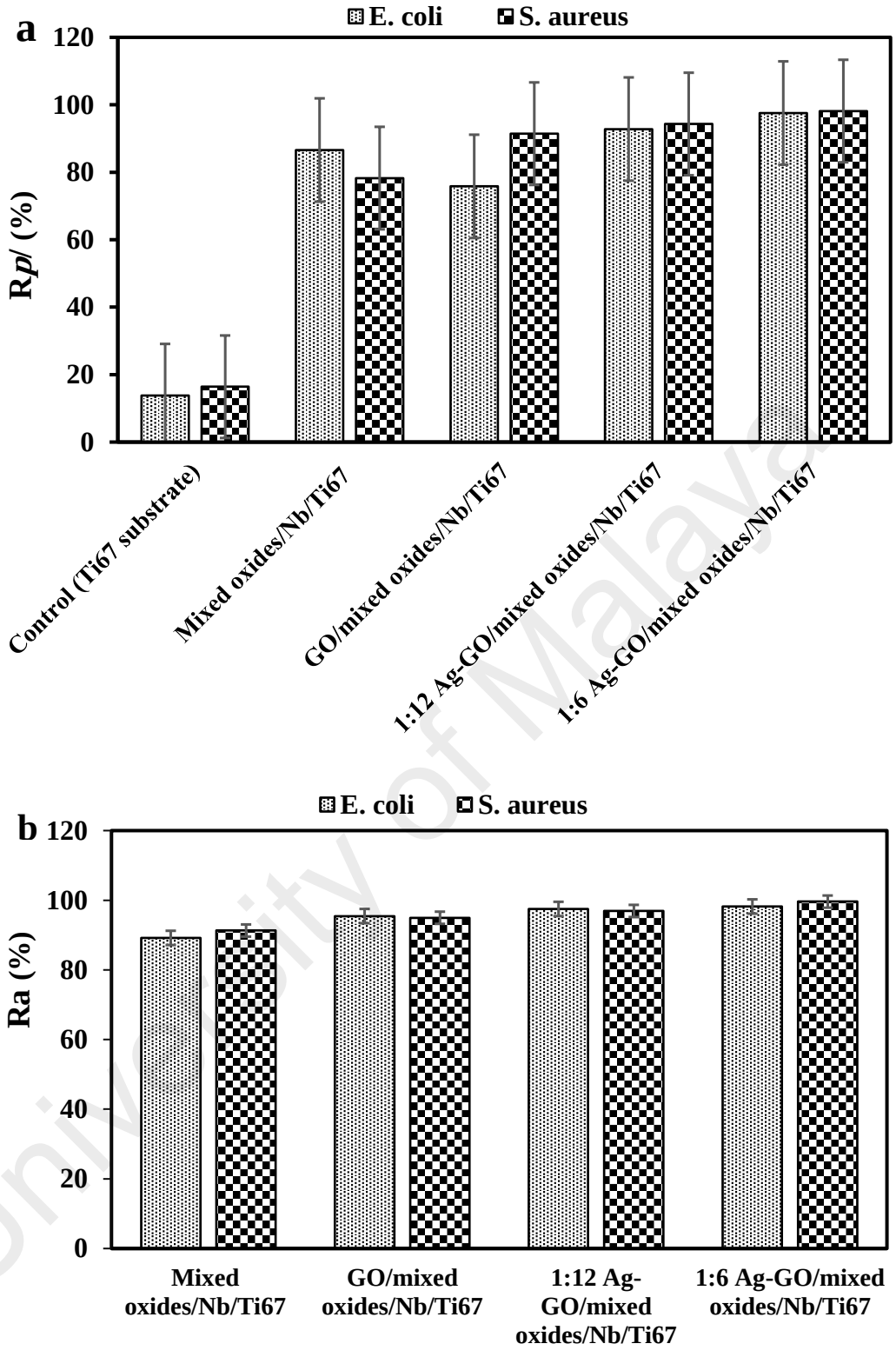

Figure 4.28: (a) Antibacterial rates against E. coli and S. aureus bacteria in the medium (Rp), and (b) Antibacterial rates against adherent bacteria on the specimen (Ra).

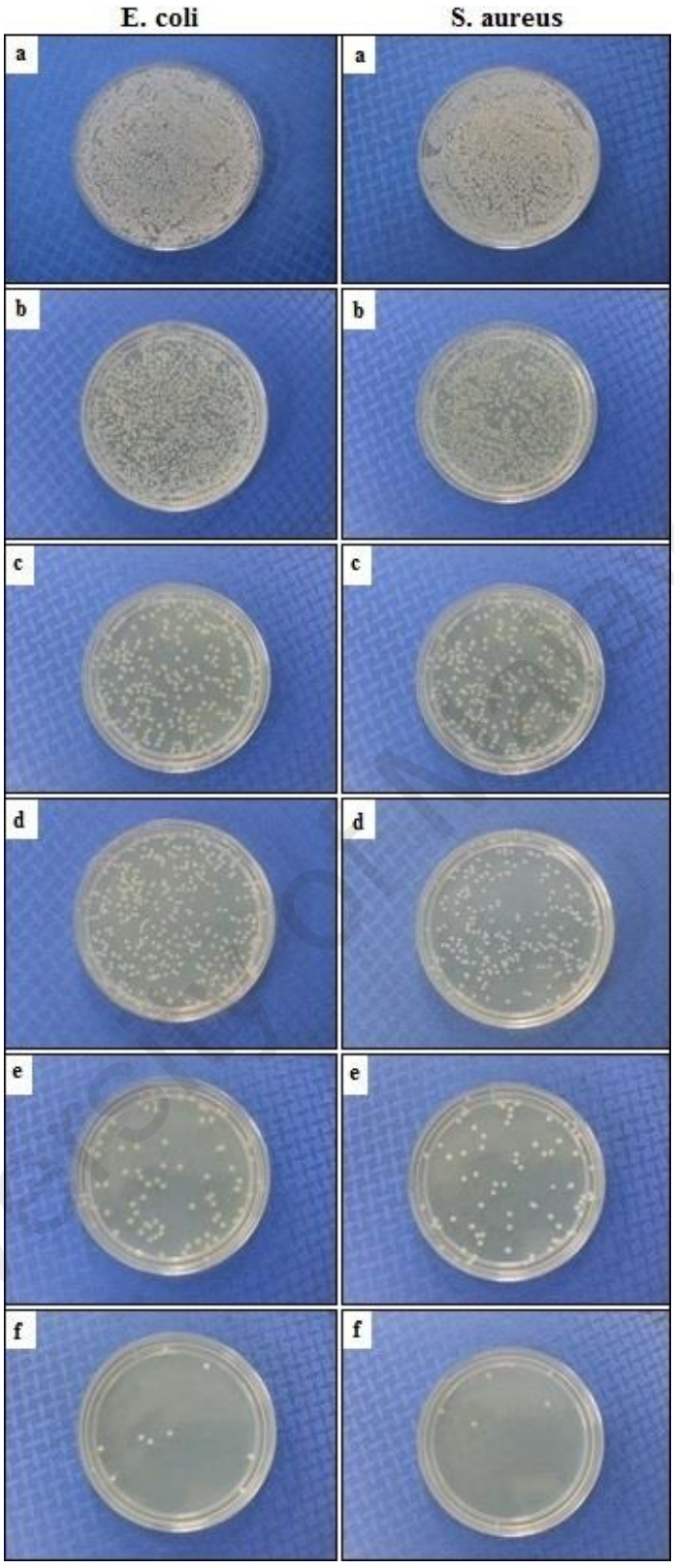

Figure 4.29: Plate assay of E. coli and S. aureus using (a) LB broth, (b) bare Ti67IMP implant, (c) crystalline mixed oxide/Nb/Ti67IMP, (d) multi-layered GO/mixed oxides/Nb/Ti67IMP, (e) 1:12 Ag-GO/mixed oxides/Nb/Ti67IMP and (f), 1:6 Ag-GO/mixed oxides/Nb/Ti67IMP at 24 h.

The antibacterial potential of functionalized Arg-Gr composite was assessed for the synthesized GO, 1:12 Ag-GO and 1:6 Ag-GO samples. The inhibition assay was followed under similar conditions which included bacterial density and counts. To justify the bactericidal potential of Arg-Gr composite, the measured inhibition zones of synthesized specimens using both *E. coli* and *S. aureus* were compared with two Ag-samples. The details of triplicated antibacterial analysis were presented in Table 4.12.

It was noted that, functionalization of pure mono-layer Gr with amino acid group provided strong cytotoxicity toward both bacteria used in this study. A mechanism of Arg-Gr in higher density of functional groups and smaller size involved more chances of interaction with bacteria and resulting cell deposition. By direct contact, the large-surface area Gr nanostructure can induce membrane stress by disrupting and damaging cell membranes, leading to cell death. The amino acid reinforcement of carbon-based nanomaterial to kill bacteria seems to correspond the interaction with the cell membrane. In similar antibacterial application of amino acids, positively-charged Arg and lysine (Lys) groups reported to operate as electrostatic adsorbents of negatively-charged bacteria membranes (Ernst et al., 2000). Elsewhere, other study emphasized on direct effects of electronic-structure-dependent bacterial cytotoxicity of single wall carbon nanotube (SWCNT) (Vecitis, Zodrow, Kang, & Elimelech, 2010). It can be concluded that, higher membrane adsorption by charged functionalities leads to increased interaction with the membranes, penetrate the cell, increase the permeability across related membrane, reduce the metabolic activity and finally kill the bacteria (Zardini et al., 2012). Therefore, an optimum functionalization percent of carbon-based nanostructure is required to achieve long-term antibacterial mediation.

Table 4.12: The measured inhibition zone sizes of synthesized specimens using E. coli and S. aureus cultures, and relative difference to Ag-GO samples.

Specimens	***(E. coli)***			
	Inhibition Zone (mm)			
	Control (PBS)	**Test**	**Relative difference to 1:12 Ag-GO (%)**	**Relative difference to 1:6 Ag-GO (%)**
GO	-ve	-ve	NA	NA
1:12 Ag-GO	-ve	14.33±0.29	–––	-4.47
1:6 Ag-GO	-ve	15.00±0.00	4.68	–––
Arg-Gr	-ve	14.83±0.76	3.49	-1.13
	Staphylococcus aureus (S. aureus)			
	Inhibition Zone (mm)			
GO	-ve	-ve	NA	NA
1:12 Ag-GO	-ve	13.33±0.58	–––	-10.11
1:6 Ag-GO	-ve	14.83±0.29	11.25	–––
Arg-Gr	-ve	15.67±0.58	17.55	5.66

* Note: -ve (No zone of inhibition detected)

The analysis of antibacterial assays for cultured specimens demonstrated that were no significant antibacterial activity detected in GO sample and for the PBS control, there were no inhibition zones for the negative control. The highest inhibition was found using 1:6 Ag-GO and Arg-Gr composites competitively. Based on assessment, the slight antibacterial superiority was justified for functionalized Arg-Gr rather than the Ag samples affected by its chemical characteristics. For *S. aureus*, the highest inhibition was related to Arg-Gr material with measured value of 15.67±0.58. Accordingly, in case of *E. coli*, the Arg-Gr (14.83±0.76) was performed prior mediation than 1:12 Ag-GO (13.33±0.58) and in competitive trend with 1:6 Ag-GO (15.00±0.00) composite. Figure 4.30 illustrates the antibacterial activity of *E. coli* and *S. aureus* bacterial assays using the agar diffusion method. To sum, the bactericidal activity of functionalized amino acid hybrid carbon-based nanobiocomposites versus the negative PBS control was clearly improved with attractive implant functionality.

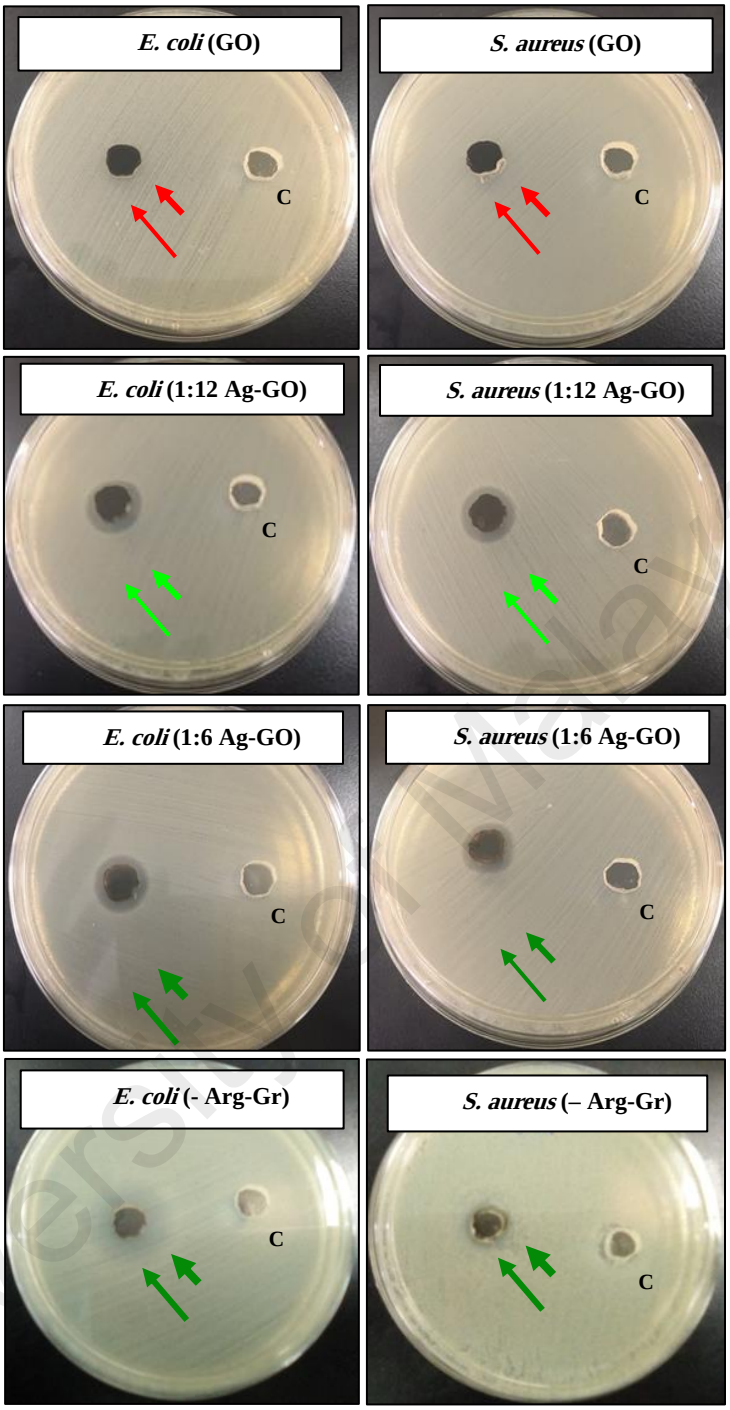

Figure 4.30: Antimicrobial activity of GO, 1:12 Ag-GO, 1:6 Ag-GO and functionalized Arg-Gr nanostructures against (a-d) E. coli and (a-d) S. aureus bacteria using the agar diffusion method, (Ctr: PBS used as the negative control).

4.8.3 *In-vitro* Biocompatibility with Human Osteoblasts Cell

4.8.3.1 Cell Attachment Proliferation using MTT Assay

The biological compatibility of un-treated Ti67IMP and fabricated nanostructures were investigated using hFOB cell culture. As acknowledged, bone-like materials were used to facilitate osseointegration by providing large-area bioactive surfaces for direct

cellular attachment, migration and proliferation. In this context, the multilayered thin film composites on Ti67IMP substrate and nanopatterned configurations may be expected to promote adhesion of hFOB to ensure successful joining. The reasonable bone interaction of organic Arg-Gr biocomposites, could suggest Arg-Gr/mixed oxides/Nb/Ti67IMP design for both antibacterial and bio-integration functionality with improved features.

Cell viability was studied with an MTT proliferation by seeding hFOB onto the surface of bare Ti67IMP, coated specimens and synthesized carbon-based nanostructures. Table 4.13 and Figure 4.31 present the cytotoxicity results of control, un-treated Ti67IMP, coated mixed oxide nanotubes, GO/mixed oxides, 1:12 Ag-GO/mixed oxides, 1:6 Ag-GO/mixed oxides on Nb/Ti67IMP as well as GO, 1:12Ag-GO, 1:6 Ag-GO and Arg-Gr composite for 1, 3, 5 and 7 days. The increase of the MTT activity with incubation time, indicate the proliferation of cells on the specimens. Interestingly, the number of cultured hFOB cells was significantly increased with multilayer attachment of the carbon-based materials on the surface of as-coated anodic mixed bioceramics. Proliferation of the cells on GO samples after day 5, which is preferred over an increase in osteoblast activity (from 0.407 to 0.521), highlights the initial proliferation and recruitment of cells to the implant surface. The cytotoxicity of Ti67IMP was clearly enhanced in seeded surfaces throughout the first day of culturing. From the results, the cells remained viable on nanotubular surfaces as well as on un-treated substrate surfaces. In case of 1:12 Ag-GO these results seem to be optimal concentrations of distributed AgNPs. In contrast, the 1:6 Ag-GO samples affected to increase the number of dead cells which associated to the toxicity potential of AgNPs on defected-GO sheets. The MTT assay demonstrated enhanced cell viability with increasing period of time when the osteoblast cells were co-cultured with thin film composites and synthesized nanostructures. The similarity in the absorbance values suggests that the cells were healthy and viable on all specimens over 24 h of analysis. The longer culturing results declared the number of alive cell was

changes due to the materials cytotoxicity. It can be seen, results, the optimum condition of hFOB cell bioassay was related to day 5 for all specimens. Among the multilayered thin films, the highest biocompatibility was recorded for GO (0.512) and 1:12 Ag-GO (0.434) samples with absolute better performance rather than un-treated Ti67IMP (0.289), mixed oxides (0.407) and 1:6 Ag-GO (0.123) conditions. From day-5 results, functionalized Arg-Gr (0.592) provided the optimum overall bioactivity in all cultured periods rather than GO (0.514), 1:12 Ag-GO (0.589) and 1:6 Ag-GO (0.241). Likewise, the 1:12 GO-Ag was also performed reasonable interaction with body cells after 1, 3 and 5 days. Afterward, due to limitation of space, oxygen and food in flask, the number of alive cell in all sample was remarkably decreased in day 7. While, the obtained trend of cytotoxicity was continued. The analysis indicated that results of day 5 culturing corresponded the most trustable cytotoxicity within assays higher than 24 h. In a summery view of MTT analysis, The OD measurements at 570 nm were briefly decreased in both coated and un-coated 1:6 Ag-GO samples for all days. Notably, cultured finding reported that the cytotoxicity agent of AgNPs was appeared negative effect on cell viability. On the other hand, the reasonable OD values of functionalized Arg-Gr composite proposed reasonable biocompatibility. The quantitative MTT finding are followed by alkaline phosphatase activity (ALP) Assay accordingly

Table 4.13: MTT assay details of cultured hFOB cell for 1, 3, 5 and 7 day.

Specimens	Day 1	Day 3	Day 5	Day 7
Control solid	0.652	0.499	0.289	0.289
Ti67IMP Substrate	0.296	0.206	0.178	0.178
Mixed oxide nanotubes/Nb/Ti67IMP	0.280	0.345	0.407	0.407
GO/mixed oxides/Nb/Ti67IMP	0.249	0.456	0.512	0.512
1:12 Ag-GO/mixed oxides/Nb/Ti67IMP	0.290	0.367	0.434	0.434
1:6 Ag-GO/mixed oxides/Nb/Ti67IMP	0.170	0.132	0.123	0.123
Control liquid	0.838	0.682	0.456	0.456
GO	0.674	0.634	0.514	0.514
1:12 Ag-GO	0.556	0.669	0.589	0.589
1:6 Ag-GO	0.381	0.295	0.241	0.241
Arg-Gr	0.538	0.642	0.592	0.592

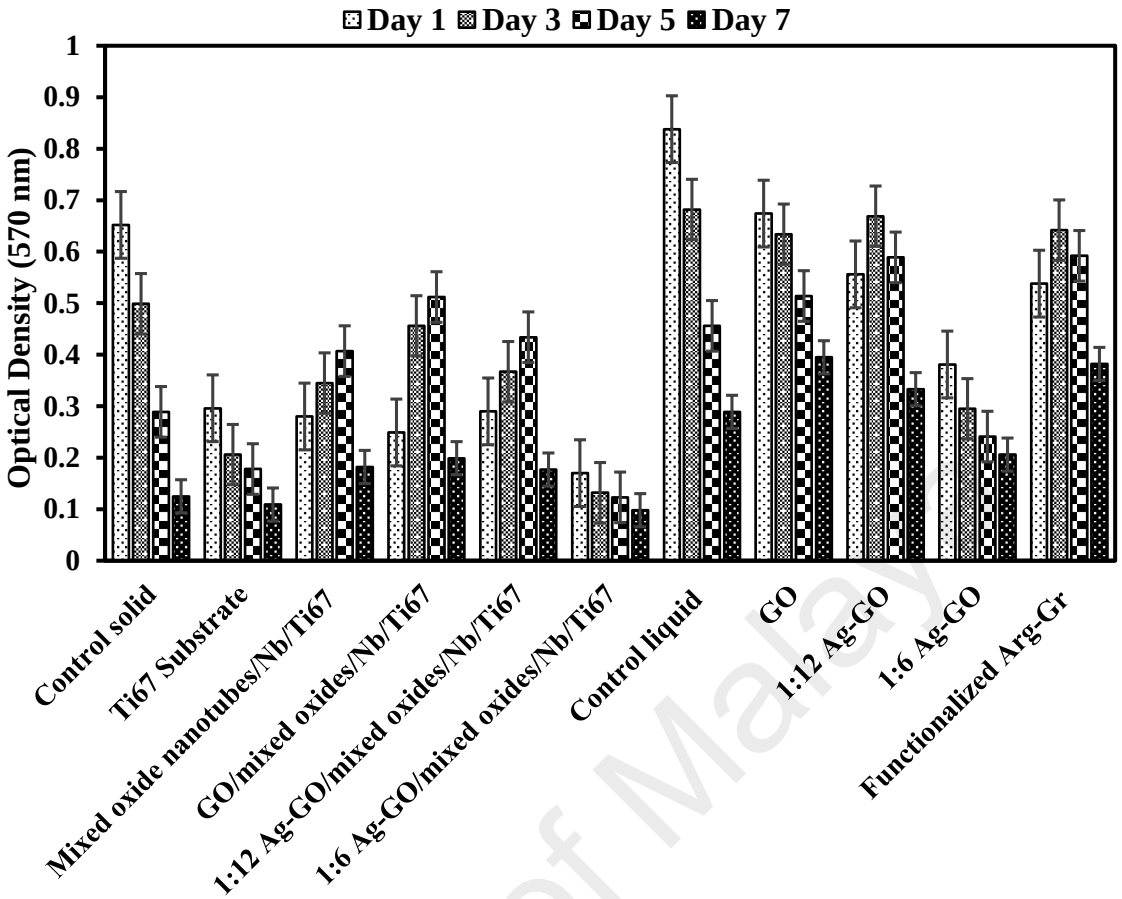

Figure 4.31: The hFOB cell culture results for multilayered thin films and synthesized carbon-based nanostructures after 1, 3, 5 and 7 days.

4.8.3.2 Alkaline Phosphatase Activity (ALP) Assay

To better understand the effect of developed nanostructures on the behavior of the hFOB cells, osteoblast differentiation is one of the most important steps in overall cellular activity and bone formation ability. The effects of culture time on performance of hFOB on samples were evaluated using an alkaline phosphate enzyme activity (ALP) assay, which elevated an early marker of osteoblast differentiation. On day 1, 3, 5 and 7 ALP results were in good agreement with the conducted MTT assay. From the results, it may be concluded that the presence of AgNPs in cultured bio-system led to cytotoxicity effects. Both coated and un-coated samples with higher concentration of AgNPs, logically resulted in higher toxicity rather than the 1:12 Ag-GO composite. Although, the optimum Ag structures seemed to somewhat provide reasonable interaction with body cells within

5 days, but the cytotoxicity trend cannot be ignored. The harmful agent may boost release of Ag^{+} ions in implant systems following longer duration of exposure. The ALP analysis clearly confirmed the superiority of organic Arg-Gr structure and GO samples in both coated and un-coated conditions suited with the economic aspect. In concern with the undesired defected GO nanosheets in chemical stability and microstructural characteristics, an overall priority of Arg-Gr is preferred. Table 4.14 and Figure 4.32 present the ALP activity of the hFOB cells cultured on multilayered thin films and synthesized nanostructure for 1, 3, 5 and 7 days of culture. The bioassay results significantly demonstrated that the ALP activity of coated Ti67IMP was modified as compared to the un-treated substrates. Similarly with MTT results, the optimum analysis was measured for 5 days due to the *in-vitro* culturing limitation. The ALP activity of the cells on the Ti67IMP moderately increased with developing large-area mixed oxide nanotubes. Previous studies indicated the effect of carbon-based materials on the cell viability and gene expression of osteoblasts. Therefore, reinforcement of Arg-Gr structure with mixed nanotubular configuration can easily generate the reasonable cytocompatibility, osteoblast spreading, proliferation and differentiation. As an overall point of view, The Ag-GO samples were not desirable as a structure for bone regeneration due to the poor mechanical and corrosion performance. Besides, the longer cell culture experiments and in-vivo justification are required to surely reject the possibility of GO/mixed oxides/Nb/Ti67IMP that are associated with insufficient antibacterial and mechanical features of bone implant. Thus, the degradable Arg-Gr may attract as an organic economic material with adequate biofunctionality of bone-like tissue. The performed bioassays were followed by morphological characterization of cell spreading and attachment accordingly. The fluorescence microscopy analysis also conducted to examine the number of alive cells and integrated state.

Table 4.14: ALP activity of hFOB after 1, 3, 5 and 7 days cultivation on specimens.

Specimens	Day 1	Day 3	Day 5	Day 7
Ti67IMP Substrate	1.0633	3.0124	3.2542	2.0514
Mixed oxide nanotubes/Nb/Ti67IMP	2.6941	3.2367	4.3154	3.0652
GO/mixed oxides/Nb/Ti67IMP	3.1781	5.3872	6.7421	3.9512
1:12 Ag-GO/mixed oxides/Nb/Ti67IMP	2.8795	4.6408	6.41032	3.4216
1:6 Ag-GO/mixed oxides/Nb/Ti67IMP	2.1541	3.2597	4.8665	3.1953
GO	3.3754	5.5788	6.5416	4.9825
1:12 Ag-GO	2.9551	5.2151	5.6982	4.4239
1:6 Ag-GO	1.0444	1.9532	3.5671	2.8632
Arg-Gr	3.3454	5.9473	6.5016	4.8517

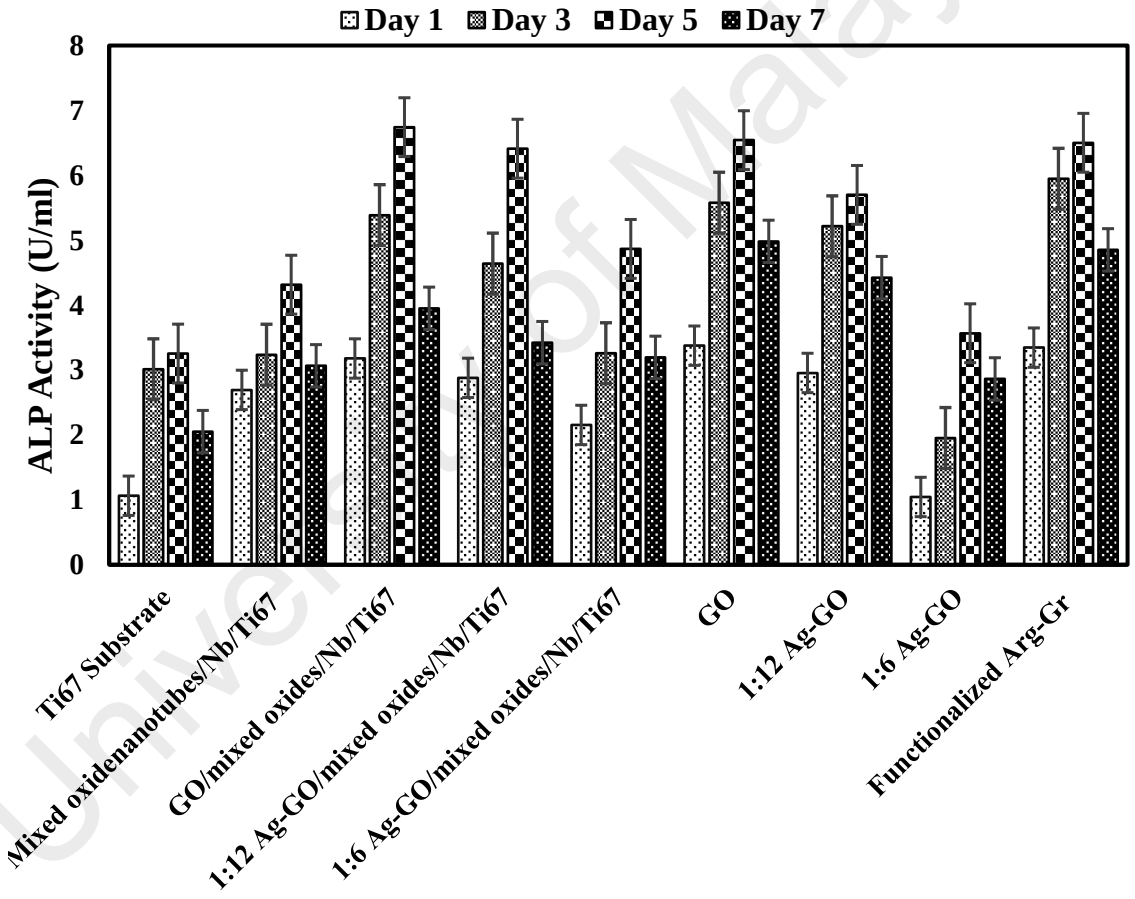

Figure 4.32: ALP activity of hFOB after cultivation on specimens for 1, 3, 5 and 7 days.

4.8.3.3 Cell Morphology

The multilayered thin films on Ti67IMP substrate and potential of synthesized nanostructures are intended for use as artificial bone materials. Generally, osteoblastic

cells are capable to attach to the metallic implants with bioactive surface. They actively participate in bone regeneration by first forming a collagen matrix and then assisting in the deposition of apatite crystal on the current matrix. The effect of nanostructures on the growth and proliferation of hFOB was continuously assessed qualitatively by observing the current population on the treated surfaces.

In this regards, the osteoblast growing on bone-like tissue largely associated the osseointegration promotion and implant durability (Lahiri et al., 2011; Mehrali et al., 2014). To conduct more confirmation on MTT and ALP results, the morphology of fixed hFOB cells was conducted accordingly. The possibility of cell attachment on the surface of designed structures was assessed after 24 h of incubation. Figure 4.33 and 4.34 demonstrate the obtained observation extracted from the seeded bare Ti67IMP substrate and multilayered thin film specimens. It can be seen in the images that the cells have attached properly and spread on all specimens affected by the bioactivity features of cultured surface. From the observation, the cells were alive as demonstrated by a typical polygonal osteoblastic cell morphology and seemed healthy following the first day of culture. As shown the cells were mostly confluent in most nanotubular morphologies. The bioassay analysis demonstrated that, cell populations attached on the surface of bare Ti67IMP influenced with bioactivity of its elemental compositions. It was proven that the nanoporous Ti-based surface promotes the maturation of focal adhesions and the formation of filopodia with distinctive nanoscale protrusions by osteogenic cells (Bello, Fouillen, Badia, & Nanci, 2017). The extensive spread of bone cells on porous surfaces achieved by nanotubular configuration was observed under lower magnifications of microscopical observations. Besides, the higher magnification FESEM images demonstrated that throughout the specimens, abundant pronounced finger-like protrusions and filopodia stretched out from the bone cells to interact with designed nanotopography. The considered biocompatibility had clearly improved with cell

appearance more closely to ideal state in case of seeded nanostructures. The performance on day 1 of the bioassay was kept steady with no significant difference in cell morphology at this time-point. Moreover, the anchored hFOB cells to the surface of cultured Arg-Gr seemed to have a good integrated shape in the cement. Such adequate cell integration with synthesized nanocomposite on anodized Nb/Ti67IMP may provide conditions of real bone extension after replacement. By doing these extensions, the reasonable spreading consequently were looking at effects of the enhanced cell in the vicinity of large-area bioactive nanopatterned structures. It can be revealed that the widespread of hFOB was influenced by cytotoxicity ratio. Herein, the best biological viability referred to GO, 1:12 Ag-GO (as optimum Ag concentration) and Arg–mono layer Gr samples after 24 h. Notably, the probable risk of releasing toxic Ag ions into the implemented systems is still existed. Well-orgnized decoration of AgNPs on GO nanosheets is provided through a weak semi-covalent bonding which can be easily released to the surrounded tissue and body organs. Based on literature, the non-degradable Ag ions may be released into the blood circulation as toxic agents with long-term undesired biological consequences. Another challenge is the same interaction of Ag nanomaterials with normal and cancer cells which might cause cell damaging effects in any concentration (AshaRani, Low Kah Mun, Hande, & Valiyaveettil, 2008; Foldbjerg, Dang, & Autrup, 2011). Elsewhere, it was reported that, the coated and uncoated AgNPs were distributed in the cells differently and caused different levels of DNA damage (Ahamed et al., 2008). The exposure of hFOB *in-vitro* to AgNPs with the average size of around 18 nm results in nanoparticle uptake and changes in cell ultrastructure leading to apoptosis and necrosis. It is notified that, even the low concentration of AgNPs materials can somewhat effect in toxicity for human osteoblasts. So, wide researches were carried out through molecular mechanism of AgNPs to decrease the toxicity effects slightly (Zielinska, Tukaj, Radomski, & Inkielewicz-Stepniak, 2016). Another issue related to economical superiority of

synthesized organic biomaterials such Arg-Gr rather than Ag-GO nanostructures needs to be highlighted with regards to commercialization aspects. As an overall view, the degradable Arg-Gr materials is more expected to meet the reasonable biofunctionality in longer interaction with body cells. The following results include different magnifications FESEM illustrating the morphology of fixed hFOB cells on (a-c) un-treated Ti67IMP substrate, (d-e) crystalline mixed oxide nanotubes/Nb/Ti67IMP, (g-i) GO/mixed oxides/Nb/Ti67IMP, (j-l) 1:12 Ag-GO/mixed oxides/Nb/Ti67IMP, (m-o), 1:6 Ag-GO/mixed oxides/Nb/Ti67IMP multilayered specimens after 24 h. More evolution of attached osteoblast populations in various culturing periods (day 1, 3 and 5) was assessed by confocal analysis accordingly.

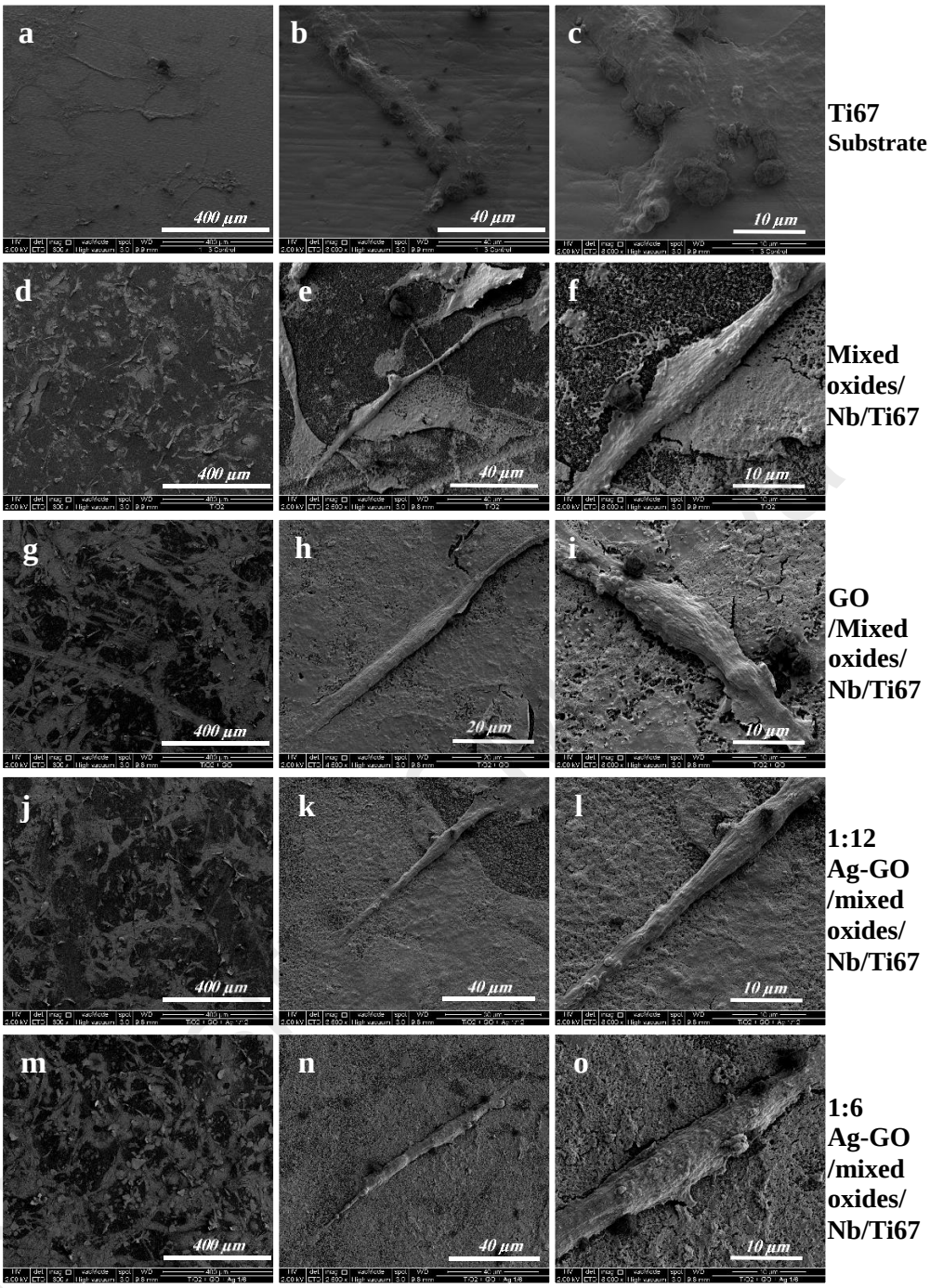

Figure 4.33: Different magnifications FESEM illustrating the morphology of fixed hFOB cells on multilayered specimens after 24 h.

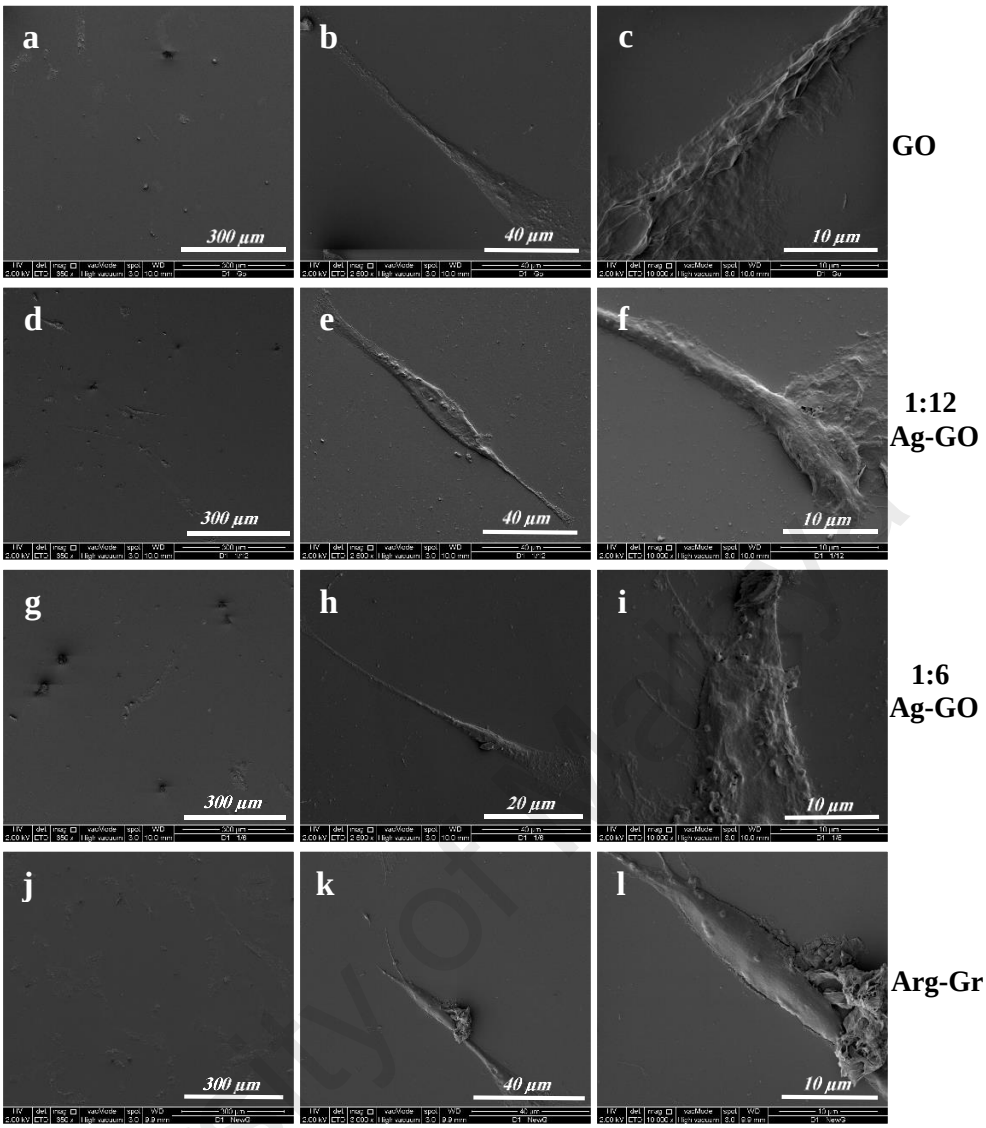

Figure 4.34: Different magnifications FESEM illustrating the morphology of fixed hFOB cells on (a-c) GO, (d-f) 1:12 Ag-GO, (g-i) 1:6 Ag-GO and (j-i) functionalized Arg-Gr nanostructures on silicon wafer after 24 h.

4.8.3.4 Confocal Laser Scanning Microscopy Analysis

In order to observe the cell viability, the seeded cells were stained using acridine orange. It is a faster, less expensive and more sensitive indicator of cytotoxic events. Figure 4.35 illustrates the fluorescence microscopy images of stained Ti67IMP, multilayer thin films and synthesized nanosurfaces. In agreement with MTT-ALP assay, the confocal images suggest that the cells still are viable on treated surfaces after 1, 3 and 5 days of growth respectively. The images show the population of bone cells on the surface of thin films and carbon-based nanostructures. The seeded hFOB cells in the

confocal images illustrate the typical lens-shaped characteristic of the live osteoblasts with normal cell growth behavior. As shown in the images of day 1 the live cell exist in all specimens even un-treated Ti67 substrate. The number of detected alive cells demonstrated that GO and 1:12 Ag-GO films on anodized Nb/Ti67 provide higher biocompatibility. For the liquid carbon-based nanostructure also there is alive cells on GO, 1:12 Ag-GO, 1:6 Ag-GO and Arg-Gr. The differences between day 1 results, issued to the required time for seeded cell to attach on liquid surfaces. Based on images of day 3, a few healthy cells were detected for 1:6 Ag-GO samples and mixed oxide surfaces. While, the higher number of grown cell was detected on the surface of GO and 1:12 Ag-GO on the surface of mixed oxides/Nb/Ti67 specimens. From the observation, attachment of few-layered GO nanosheets on mixed nanotubular morphologies enhanced the cytotoxicity performance of Ti67IMP through the obtained larger bioactive surface-area. Qualitative images of synthesized carbon-based nanostructures indicates the priority of 1:12 Ag-GO rather than 1:6 concentration. Likewise, GO and Arg-Gr structures providing the increased specific-area and such biocompatibility. Amid day 5 confocal images, the seeded cells became more confluent and started forming dense islands following the similar trend. Interestingly, compared with day-3 results, after five days of growth, more osteoblast population covered the surface of bioactive samples (Figure 4.36). GO-based nanostructures compromise undesired microstructural stability, affecting their biofunctionality operation by longer periods. Based on biological evaluation, Arg-Gr and GO nanostructures matched with reasonable biocompatibility. In summary, an overall view on implant requirements, pointed impact for the attachment of Arg-Gr composite on the anodized morphology of Nb/Ti67IMP to accomplish both long-term antibacterial ability and bio-integration properties. The following results include confocal images of cultured hFOB cells on (a-c) un-treated Ti67IMP, (d-f) crystalline mixed oxide

nanotubes/Nb/Ti67IMP, (g-i) GO/mixed oxides/Nb/Ti67IMP, (j-l) 1:12 Ag-GO/mixed oxides/Nb/Ti67IMP, (m-o), 1:6 Ag-GO/mixed oxides/Nb/Ti67IMP.

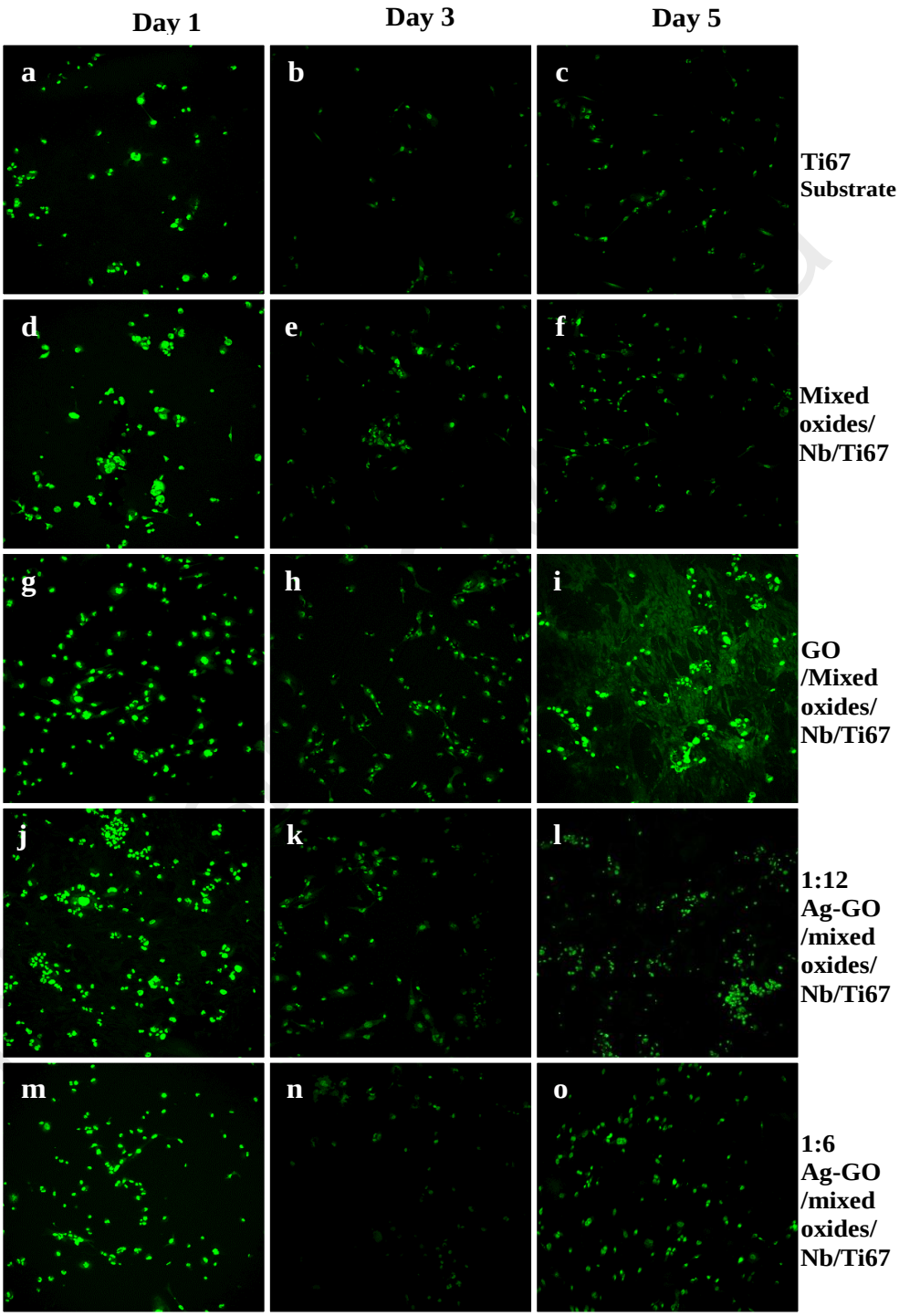

Figure 4.35:The Confocal images of adherent hFOB cells for 1, 3 and 5 days. All the scale bars represent 100 µm.

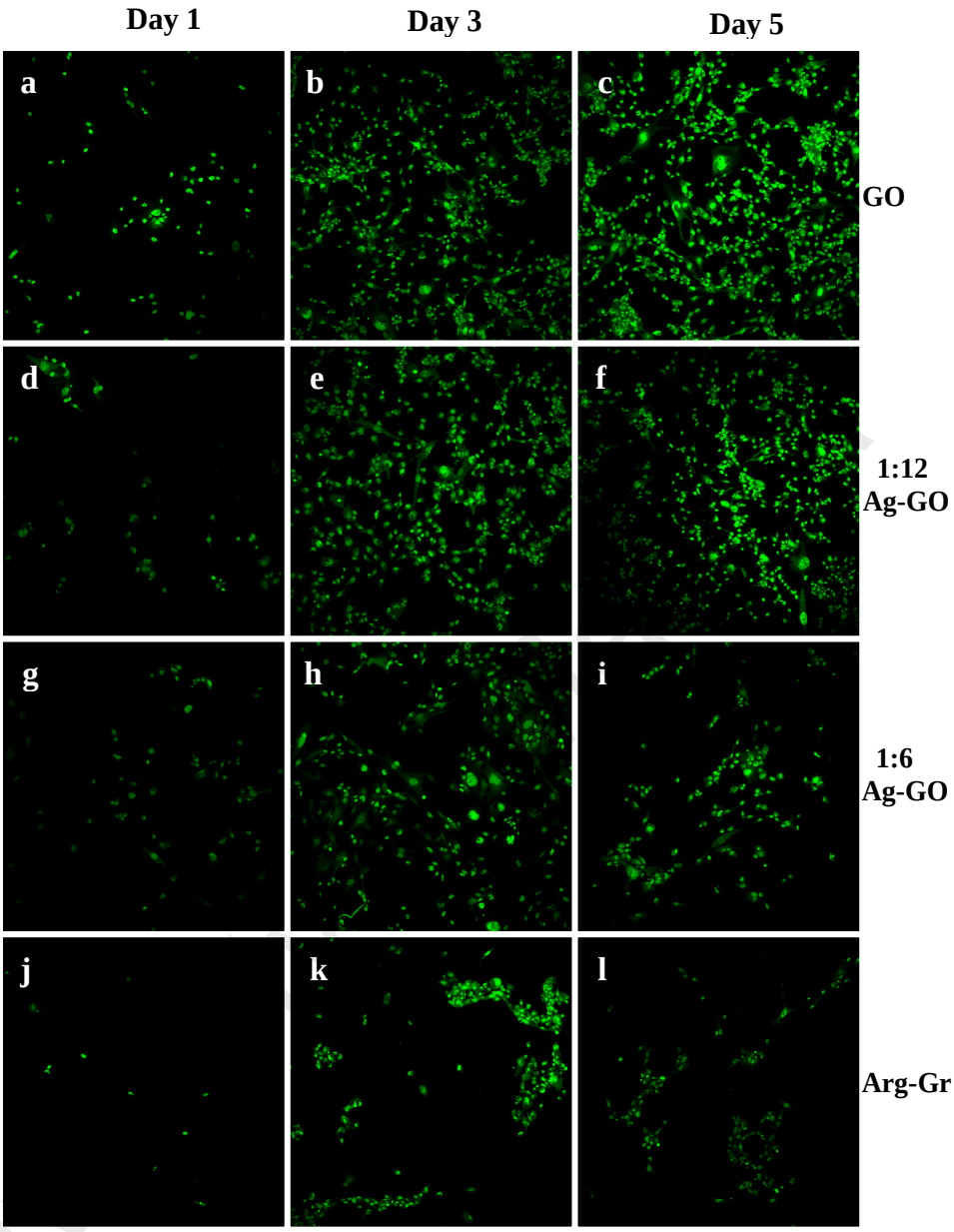

Figure 4.36: The Confocal images of adherent hFOB cells for 1, 3 and 5 days on synthesized (a-c) GO, (d-f) 1:12 Ag-GO, (g-i) 1:6 Ag-GO and (j-l) functionalized Arg-Gr. All the scale bars represent 100 µm.

CHAPTER 5: CONCLUSIONS AND SUGGESTIONS FOR FUTURE WORK

5.1 Conclusions

This study presents a comprehensive analysis in terms of modeling, optimization and synthesis towards improved microstructure, mechanical, corrosion, *in-vitro* bioactivity, antibacterial and biological properties. Surface modification of metallic Ti67IMP through development of large-area multilayer bionanomaterials was assessed. Based on bioassay analysis, the Ag-GO samples remarkably 1:6 concentration caused the cytotoxicity effects in contrary with the achieved bactericidal ability. Besides, mechanical and antibacterial ability of GO nanostructure was limited due to poor stability of defected GO sheets. The in-vitro biofunctionality clearly confirmed a bactericidal response of amino acid treated single-layer Gr composite along with reasonable bone cell activity. The transparent loading of Arg-Gr topography on the surface of optimized mixed nanotubes confirmed Ti67IMP reinforcement. Main conclusions highlighted as below:

i. Application of Taguchi-MOPSO maximized mechanical outputs of as-sputtered Nb PVD film (4.35 ± 0.03 μm thickness) on Ti67IMP surface.
ii. The obtained mathematical formulations of adhesion strength and hardness were satisfied the prediction aspect of future experiments.
iii. The microstructural stability of grown TiO_2-Nb_2O_5-Al_2O_3 mixed nanotubular topography on Nb/Ti67 surface was obtained after performed thermal annealing. There is no any significant change in morphology of mixed oxides after the crystallization treatment.
iv. Transparent attachment of GO, Ag-GO and Arg-Gr films on the anodized Nb/Ti67IMP surfaces clearly improved the mechanical, corrosion, hydrophilicity, *in-vitro* bioactivity and antibacterial activity compared with bare Ti67 substrate.

a) GO/nanotubes/Nb/Ti67IMP provided higher properties than both Ag-GO/nanotubes/Nb/Ti67IMP specimens except antibacterial mediation. Raised characteristics found in Arg-Gr sample compared with single-phase GO configuration. According to slight decrease on CA wettability of Arg-Gr sample, superiority in Gr hydrophobicity detected rather than most hydrophilic GO.

b) Almost same trend of mineralization in SBF within bone-layer formability was observed on the surface of nanotubes, GO and Ag-GO samples. In multilayered Arg-Gr, thick apatite layer was almost formed throughout treated surface due to larger bioactive specific-area.

v. From antibacterial results, the anodic nanotubes somehow increased Ti67IMP performance. Whereas, the excellent antibacterial results against both Gram-positive and Gram-negative bacteria of Ag-GO specimens remarkably 1:6 concentration (around 100%) was obtained affected by decorated AgNPs agent.

a) Likewise, the positively-charged organic Arg-Gr composite shown the great mediation. The-triplicate inhibition analysis against both cultured media confirmed the significant bactericidal capability of synthesized material in both Gram-positive and Gram-negative bacteria, which is quite competitive with risky Ag.

vi. The osteoblastic proliferation of multilayered thin films and carbon-materials clearly demonstrated the toxicity of Ag-GO samples after few hours of *in-vitro* bioassay. The quantitative and qualitative results of 1, 3, 5 and 7 days hFOB cell culture specified.

a) In first-day MTT, the most appropriate biocompatibility feature of treated structures was belonged to GO and 1:12 Ag-GO/mixed oxides/Nb/Ti67IMP

samples by sequence. From OD measurements of coated and un-coated samples the most toxicity effect referred to 1:6 Ag-GO surfaces (0.170 versus control at 0.652, and 0.381 versus control at 0.838). Whereas, such reasonable results was recorded for Arg-Gr samples (0.538) in close competition with GO (0.556).

b) Increased times to days 3, similar trend was almost observed accordingly. The interaction of hFOB cell with structures in longer culture time, was investigated through 5 and 7 days analysis. The results clarify that herein, the studied day 5 was the optimum proliferation time. The bioactive priority still was referred to Arg-Gr composite and GO materials at day 5. After day 7 due to the experimental limitation, the number of alive cell for all samples was gradually decreased. Whether, the following similar sequence for cytotoxicity of samples was examined at this time.

c) The performed cell adhesion analysis (:ALP) has confirmed the results of cytotoxicity for multilayered thin films on Ti67IMP and carbon-based nanostructures. The highest amounts of assessed first day ALP activity were related to functionalize Arg-Gr and GO samples competitively. For coated samples also GO/nanotubes/Nb/Ti67IMP was performed appropriately. In similar sequences with MTT, the optimum ALP results also were provided in day 5. The cytotoxicity of Ag-GO composites was clearly proved duo to releasing the Ag ions in implant material-hFOB systems. Remarkably, 1:6 Ag-GO thin films as composites for performed with the highest toxicity. In day 5 the amounts also pointed as desired cell interaction of Arg-Gr and GO samples.

d) Cell Morphology successfully observed the population of seeded cells on the surface of multilayered thin films on Ti67IMP and loaded carbon-based nanostructures after 24 h.

e) Confocal laser microscopy images also qualitatively analyzed the cytotoxicity behavior and viability of seeded cells after 1, 3 and 5 days.

vii. Attachment of mixed nanotubes with GO, 1:12 Ag-GO, 1:6 Ag-GO layers, can be concluded that contrary with their antibacterial and reasonable short-term controlled cytotoxicity, releasing the Ag ions in still concerned. In case of GO materials, appropriate biological was recorded, while largely suffer from poor antibacterial and mechanical performance.

viii. In a nutshell, development of all multilayered metallic-ceramic-carbon nanostructures was significantly enhanced the properties of Ti67IMP versus before-coating status. Within these morphologies, Arg-Gr/nanotubes/Nb composite greatly corresponded to enhance the mechanical hardness (1.795 to 5.345 GPa), corrosion resistance (7.719×10-1 to 3.743×10-7) and *in-vitro* bioactivity of Ti67IMP have been enormously enhanced. Based on findings, multilayered metallic/ceramic/carbon-amino acid biocomposite on clinical Ti67IMP alloy may contribute as the new generation of smart antibacterial implant material with drug programing potential to facilitate safe bone-regeneration with low risk of infection after implantation.

5.2 Suggestions for Future Work

The findings of this study mostly established not-yet-designed smart antibacterial nanostructured Arg-Gr/mixed oxides/Nb/Ti67 composite-implant for orthopedic and dental tissue regeneration. However, some of the topic need further *vitro/vivo* investigations for clinical translation. Based on the medical reports, in real life, the implants are in the living body for >15 years, in most of the cases. It is therefore important to assess the fate of current improved bone materials, for longer *in-vivo* exposure, to assure their safe use. A systematic study of implanting the smart antiracial nanocomposite

in animal model for longer exposure period (3-6 months and 1 year) followed by histocompatibility studies is recommended. Also, with the current potential of Gr nanosheets the induced pluripotent stem cell (iPSC) culture also is attractive to be examined. Moreover, the implant biofunctionality compaction of Arg-Gr with generation of functionalized graphene quantum dots (GQDs) is aimed.

REFERENCES

Abbasi, S., Golestani-Fard, F., Mirhosseini, S., Ziaee, A., & Mehrjoo, M. (2013). Effect of electrolyte concentration on microstructure and properties of micro arc oxidized hydroxyapatite/titania nanostructured composite. *Materials Science and Engineering: C, 33*(5), 2555-2561.

Acik, M., Lee, G., Mattevi, C., Chhowalla, M., Cho, K., & Chabal, Y. (2010). Unusual infrared-absorption mechanism in thermally reduced graphene oxide. *Nature materials, 9*(10), 840-845.

Ahamed, M., AlSalhi, M. S., & Siddiqui, M. (2010). Silver nanoparticle applications and human health. *Clinica chimica acta, 411*(23), 1841-1848.

Ahamed, M., Karns, M., Goodson, M., Rowe, J., Hussain, S. M., Schlager, J. J., & Hong, Y. (2008). DNA damage response to different surface chemistry of silver nanoparticles in mammalian cells. *Toxicology and applied pharmacology, 233*(3), 404-410.

Akhavan, O., & Ghaderi, E. (2009). Photocatalytic reduction of graphene oxide nanosheets on TiO2 thin film for photoinactivation of bacteria in solar light irradiation. *The Journal of Physical Chemistry C, 113*(47), 20214-20220.

Akhavan, O., & Ghaderi, E. (2010). Toxicity of graphene and graphene oxide nanowalls against bacteria. *ACS nano, 4*(10), 5731-5736.

Al Qahtani, W., Schille, C., Spintzyk, S., Al Qahtani, M. S., Engel, E., Geis-Gerstorfer, J., . . . Scheideler, L. (2016). Effect of surface modification of zirconia on cell adhesion, metabolic activity and proliferation of human osteoblasts. *Biomedical Engineering/Biomedizinische Technik*.

Albayrak, O., El-Atwani, O., & Altintas, S. (2008). Hydroxyapatite coating on titanium substrate by electrophoretic deposition method: effects of titanium dioxide inner layer on adhesion strength and hydroxyapatite decomposition. *Surface and Coatings Technology, 202*(11), 2482-2487.

Albrektsson, T., & Wennerberg, A. (2003). Oral implant surfaces: Part 2--review focusing on clinical knowledge of different surfaces. *The International journal of prosthodontics, 17*(5), 544-564.

Albu, S. P., Ghicov, A., Macak, J. M., & Schmuki, P. (2007). 250 μm long anodic TiO2 nanotubes with hexagonal self- ordering. *physica status solidi (RRL)-Rapid Research Letters, 1*(2), R65-R67.

Alsawat, M., Altalhi, T., Gulati, K., Santos, A., & Losic, D. (2015). Synthesis of Carbon Nanotube–Nanotubular Titania Composites by Catalyst-Free CVD Process: Insights into the Formation Mechanism and Photocatalytic Properties. *ACS applied materials & interfaces, 7*(51), 28361-28368.

Amiri, A., Ahmadi, G., Shanbedi, M., Savari, M., Kazi, S., & Chew, B. (2015). Microwave-assisted synthesis of highly-crumpled, few-layered graphene and

nitrogen-doped graphene for use as high-performance electrodes in capacitive deionization. *Scientific reports, 5*.

Amiri, A., Shanbedi, M., Ahmadi, G., Eshghi, H., Kazi, S., Chew, B., . . . Zubir, M. N. M. (2016a). Mass production of highly-porous graphene for high-performance supercapacitors. *Scientific reports, 6*.

Amiri, A., Shanbedi, M., Ahmadi, G., Eshghi, H., Kazi, S., Chew, B., . . . Zubir, M. N. M. (2016b). Mass production of highly-porous graphene for high-performance supercapacitors. *Scientific reports, 6*, 32686.

Amiri, A., Shanbedi, M., Eshghi, H., Heris, S. Z., & Baniadam, M. (2012). Highly dispersed multiwalled carbon nanotubes decorated with Ag nanoparticles in water and experimental investigation of the thermophysical properties. *The Journal of Physical Chemistry C, 116*(5), 3369-3375.

Antoci, V., Adams, C. S., Parvizi, J., Davidson, H. M., Composto, R. J., Freeman, T. A., . . . Shapiro, I. M. (2008). The inhibition of Staphylococcus epidermidis biofilm formation by vancomycin-modified titanium alloy and implications for the treatment of periprosthetic infection. *Biomaterials, 29*(35), 4684-4690.

AshaRani, P., Low Kah Mun, G., Hande, M. P., & Valiyaveettil, S. (2008). Cytotoxicity and genotoxicity of silver nanoparticles in human cells. *ACS nano, 3*(2), 279-290.

Assefpour-Dezfuly, M., Vlachos, C., & Andrews, E. (1984). Oxide morphology and adhesive bonding on titanium surfaces. *Journal of Materials Science, 19*(11), 3626-3639.

Audronis, M., Leyland, A., Kelly, P., & Matthews, A. (2008). Composition and structure-property relationships of chromium-diboride/molybdenum-disulphide PVD nanocomposite hard coatings deposited by pulsed magnetron sputtering. *Applied Physics A, 91*(1), 77-86.

Aw, M. S., Kurian, M., & Losic, D. (2014). Non-eroding drug-releasing implants with ordered nanoporous and nanotubular structures: concepts for controlling drug release. *Biomaterials Science, 2*(1), 10-34.

Azarang, M., Shuhaimi, A., Yousefi, R., & Sookhakian, M. (2014). Effects of graphene oxide concentration on optical properties of ZnO/RGO nanocomposites and their application to photocurrent generation. *Journal of Applied Physics, 116*(8), 084307.

Aziz-Kerrzo, M., Conroy, K. G., Fenelon, A. M., Farrell, S. T., & Breslin, C. B. (2001). Electrochemical studies on the stability and corrosion resistance of titanium-based implant materials. *Biomaterials, 22*(12), 1531-1539.

Bakheet, A. M. A. (2016). First principles study of the physical properties of pure and doped calcium phosphate biomaterial for tissue engineering. *Nanobiomaterials in Hard Tissue Engineering: Applications of Nanobiomaterials*, 215.

Baradaran, S., Basirun, W., Zalnezhad, E., Hamdi, M., Sarhan, A. A., & Alias, Y. (2013). Fabrication and deformation behaviour of multilayer Al 2 O 3/Ti/TiO 2 nanotube arrays. *Journal of the mechanical behavior of biomedical materials*, *20*, 272-282.

Baradaran, S., Zalnezhad, E., Basirun, W., Hamouda, A., Sookhakian, M., Sarhan, A. A., & Alias, Y. (2014). Statistical optimization and fretting fatigue study of Zr/ZrO 2 nanotubular array coating on Ti–6Al–4V. *Surface and Coatings Technology*, *258*, 979-990.

Barletta, M., Gisario, A., Palagi, L., & Silvestri, L. (2014). Modelling the Electrostatic Fluidised Bed (EFB) coating process using Support Vector Machines (SVMs). *Powder Technology*, *258*, 85-93.

Bauer, S., Schmuki, P., von der Mark, K., & Park, J. (2013). Engineering biocompatible implant surfaces: Part I: Materials and surfaces. *Progress in materials science*, *58*(3), 261-326.

Becerril, H. A., Mao, J., Liu, Z., Stoltenberg, R. M., Bao, Z., & Chen, Y. (2008). Evaluation of solution-processed reduced graphene oxide films as transparent conductors. *ACS nano*, *2*(3), 463-470.

Bello, D. G., Fouillen, A., Badia, A., & Nanci, A. (2017). A nanoporous titanium surface promotes the maturation of focal adhesions and formation of filopodia with distinctive nanoscale protrusions by osteogenic cells. *Acta biomaterialia*.

Beranek, R., Hildebrand, H., & Schmuki, P. (2003). Self-organized porous titanium oxide prepared in H 2 SO 4/HF electrolytes. *Electrochemical and solid-state letters*, *6*(3), B12-B14.

Berger, S., Jakubka, F., & Schmuki, P. (2009). Self-ordered hexagonal nanoporous hafnium oxide and transition to aligned HfO2 nanotube layers. *Electrochemical and solid-state letters*, *12*(7), K45-K48.

Berglundh, T., Abrahamsson, I., Lang, N. P., & Lindhe, J. (2003). De novo alveolar bone formation adjacent to endosseous implants. *Clinical Oral Implants Research*, *14*(3), 251-262.

Bhardwaj, G., & Webster, T. J. (2017). Reduced bacterial growth and increased osteoblast proliferation on titanium with a nanophase TiO2 surface treatment. *International journal of nanomedicine*, *12*, 363.

Biasetto, L., Elsayed, H., Bonollo, F., & Colombo, P. (2016). Polymer-derived sphene biocoating on cpTi substrates for orthopedic and dental implants. *Surface and Coatings Technology*.

Black, J. (2005). *Biological performance of materials: fundamentals of biocompatibility*: CRC Press.

Blanton, T. N., & Majumdar, D. (2012). X-ray diffraction characterization of polymer intercalated graphite oxide. *Powder Diffraction*, *27*(02), 104-107.

Blanton, T. N., & Majumdar, D. (2013). Characterization of X-ray irradiated graphene oxide coatings using X-ray diffraction, X-ray photoelectron spectroscopy, and atomic force microscopy. *Powder Diffraction, 28*(02), 68-71.

Boccaccini, A., Keim, S., Ma, R., Li, Y., & Zhitomirsky, I. (2010). Electrophoretic deposition of biomaterials. *Journal of The Royal Society Interface, 7*(Suppl 5), S581-S613.

Böke, F., Giner, I., Keller, A., Grundmeier, G., & Fischer, H. (2016). Plasma-Enhanced Chemical Vapor Deposition (PE-CVD) yields better Hydrolytical Stability of Biocompatible SiOx Thin Films on Implant Alumina Ceramics compared to Rapid Thermal Evaporation Physical Vapor Deposition (PVD). *ACS applied materials & interfaces, 8*(28), 17805-17816.

Boland, E. D., Espy, P. G., & Bowlin, G. L. (2004). Tissue engineering scaffolds *Encyclopedia of biomaterials and biomedical engineering* (pp. 1630-1638).

Borhanazad, H., Mekhilef, S., Ganapathy, V. G., Modiri-Delshad, M., & Mirtaheri, A. (2014). Optimization of micro-grid system using MOPSO. *Renewable Energy, 71*, 295-306.

Brace, A. W. (1968). *The Technology of Anodising Aluminium*: Robert Draper.

Brunette, D. M. (2001). Principles of cell behavior on titanium surfaces and their application to implanted devices *Titanium in medicine* (pp. 485-512): Springer.

Bull, S., & Berasetegui, E. (2006). An overview of the potential of quantitative coating adhesion measurement by scratch testing. *Tribology International, 39*(2), 99-114.

Calciolari, E., Donos, N., & Mardas, N. (2016). Osteoporotic Animal Models of Bone Healing: Advantages and Pitfalls. *Journal of Investigative Surgery*, 1-9.

Campoccia, D., Montanaro, L., & Arciola, C. R. (2006). The significance of infection related to orthopedic devices and issues of antibiotic resistance. *Biomaterials, 27*(11), 2331-2339.

Carta, D., Pickup, D. M., Knowles, J. C., Smith, M. E., & Newport, R. J. (2005). Sol–gel synthesis of the P 2 O 5–CaO–Na 2 O–SiO 2 system as a novel bioresorbable glass. *Journal of Materials Chemistry, 15*(21), 2134-2140.

Cha, B.-K., Choi, D.-S., Jang, I., Choe, B.-H., & Choi, W.-Y. (2016). Orthodontic tunnel miniscrews with and without TiO2 nanotube arrays as a drug-delivery system: In vivo study. *Bio-Medical Materials and Engineering, 27*(4), 375-387.

Chandanshive, B. B., Rai, P., Rossi, A. L., Ersen, O., & Khushalani, D. (2013). Synthesis of hydroxyapatite nanotubes for biomedical applications. *Materials Science and Engineering: C, 33*(5), 2981-2986.

Chaudhary, D., Singh, S., Vankar, V., & Khare, N. (2016). A ternary Ag/TiO 2/CNT photoanode for efficient photoelectrochemical water splitting under visible light irradiation. *International Journal of Hydrogen Energy*.

Checchetto, R., Bazzanella, N., Patton, B., & Miotello, A. (2004). Palladium membranes prepared by rf magnetron sputtering for hydrogen purification. *Surface and Coatings Technology, 177*, 73-79.

CHEMISTS, C. H. (1992). WE PROVIDE BUILDING BLOCKS FOR SUCCESSFUL R&D. *Organomet. Chem, 441*, 457.

Chen, C., Huang, Z., Yuan, W., Li, J., Cheng, X., & Chi, R.-a. (2011). Pressure effecting on morphology of hydroxyapatite crystals in homogeneous system. *CrystEngComm, 13*(5), 1632-1637.

Chen, J., Yao, B., Li, C., & Shi, G. (2013). An improved Hummers method for eco-friendly synthesis of graphene oxide. *Carbon, 64*, 225-229.

Chen, Q., Li, W., Goudouri, O.-M., Ding, Y., Cabanas-Polo, S., & Boccaccini, A. R. (2015). Electrophoretic deposition of antibiotic loaded PHBV microsphere-alginate composite coating with controlled delivery potential. *Colloids and Surfaces B: Biointerfaces, 130*, 199-206.

Chen, W.-C., Chen, Y.-S., Ko, C.-L., Lin, Y., Kuo, T.-H., & Kuo, H.-N. (2014). Interaction of progenitor bone cells with different surface modifications of titanium implant. *Materials Science and Engineering: C, 37*, 305-313.

Chen, W., Liu, Y., Courtney, H., Bettenga, M., Agrawal, C., Bumgardner, J., & Ong, J. (2006). In vitro anti-bacterial and biological properties of magnetron co-sputtered silver-containing hydroxyapatite coating. *Biomaterials, 27*(32), 5512-5517.

Chen, Y., Zheng, X., Xie, Y., Ding, C., Ruan, H., & Fan, C. (2008). Anti-bacterial and cytotoxic properties of plasma sprayed silver-containing HA coatings. *Journal of Materials Science: Materials in Medicine, 19*(12), 3603-3609.

Cheong, Y., Yam, F., Ooi, Y., & Hassan, Z. (2014). Room-temperature synthesis of nanocrystalline titanium dioxide via electrochemical anodization. *Materials Science in Semiconductor Processing, 26*, 130-136.

Cho, I.-H., & Zoh, K.-D. (2007). Photocatalytic degradation of azo dye (Reactive Red 120) in TiO 2/UV system: optimization and modeling using a response surface methodology (RSM) based on the central composite design. *Dyes and Pigments, 75*(3), 533-543.

Chook, S. W., Chia, C. H., Zakaria, S., Ayob, M. K., Chee, K. L., Huang, N. M., . . . Rahman, R. M. F. R. A. (2012). Antibacterial performance of Ag nanoparticles and AgGO nanocomposites prepared via rapid microwave-assisted synthesis method. *Nanoscale research letters, 7*(1), 1-7.

Chua, C. K., & Pumera, M. (2014). Chemical reduction of graphene oxide: a synthetic chemistry viewpoint. *Chemical Society Reviews, 43*(1), 291-312.

Ciganovic, J., Stasic, J., Gakovic, B., Momcilovic, M., Milovanovic, D., Bokorov, M., & Trtica, M. (2012). Surface modification of the titanium implant using TEA CO 2 laser pulses in controllable gas atmospheres–Comparative study. *Applied Surface Science, 258*(7), 2741-2748.

Cools, P., De Geyter, N., Vanderleyden, E., Barberis, F., Dubruel, P., & Morent, R. (2016). Adhesion improvement at the PMMA bone cement-titanium implant interface using methyl methacrylate atmospheric pressure plasma polymerization. *Surface and Coatings Technology, 294*, 201-209.

Cotolan, N., Rak, M., Bele, M., Cör, A., Muresan, L., & Milošev, I. (2016). Sol-gel synthesis, characterization and properties of TiO 2 and Ag-TiO 2 coatings on titanium substrate. *Surface and Coatings Technology*.

Dale, G., Hamilton, J., Dunlop, P., Lemoine, P., & Byrne, J. (2009). Electrochemical growth of titanium oxide nanotubes: the effect of surface roughness and applied potential. *Journal of nanoscience and nanotechnology, 9*(7), 4215-4219.

Danaher, S., Dudziak, T., Datta, P., Hasan, R., & Leung, P. S. (2013). Long-term oxidation of newly developed HIPIMS and PVD coatings with neural network prediction modelling. *Corrosion Science, 69*, 322-337.

Das, A., Pisana, S., Chakraborty, B., Piscanec, S., Saha, S., Waghmare, U., . . . Ferrari, A. (2008). Monitoring dopants by Raman scattering in an electrochemically top-gated graphene transistor. *Nature Nanotechnology, 3*(4), 210-215.

Das, B., Voggu, R., Rout, C. S., & Rao, C. (2008). Changes in the electronic structure and properties of graphene induced by molecular charge-transfer. *Chemical Communications*(41), 5155-5157.

Das, I., Chattopadhyay, S., Mahato, A., Kundu, B., & De, G. (2016). Fabrication of a cubic zirconia nanocoating on a titanium dental implant with excellent adhesion, hardness and biocompatibility. *RSC Advances, 6*(64), 59030-59038.

Datta, S., Pratihar, D. K., & Bandyopadhyay, P. (2013). Hierarchical adaptive neuro-fuzzy inference systems trained by evolutionary algorithms to model plasma spray coating process. *Journal of Intelligent & Fuzzy Systems, 24*(2), 355-362.

De Graef, M., & McHenry, M. E. (2012). *Structure of materials: an introduction to crystallography, diffraction and symmetry*: Cambridge University Press.

De Jong, W. H., Van Der Ven, L. T., Sleijffers, A., Park, M. V., Jansen, E. H., Van Loveren, H., & Vandebriel, R. J. (2013). Systemic and immunotoxicity of silver nanoparticles in an intravenous 28 days repeated dose toxicity study in rats. *Biomaterials, 34*(33), 8333-8343.

Ding, Y. F., Li, R. W., Nakai, M., Majumdar, T., Zhang, D. H., Niinomi, M., . . . Chen, X. B. (2016). Osteoanabolic Implant Materials for Orthopedic Treatment. *Advanced healthcare materials*.

Disegi, J. A., Kennedy, R. L., & Pilliar, R. (1999). *Cobalt-base alloys for biomedical applications*: ASTM International.

Dobrzański, L., Staszuk, M., & Honysz, R. (2010). Application of artificial neural networks in properties modelling of PVD and CVD coatings. *Archives of Computational Materials Science and Surface Engineering, 2*(3), 141-148.

Domb, A. J., & Kumar, N. (2011). *Biodegradable polymers in clinical use and clinical development*: John Wiley & Sons.

dos Santos Coelho, L. (2010). Gaussian quantum-behaved particle swarm optimization approaches for constrained engineering design problems. *Expert Systems with Applications, 37*(2), 1676-1683.

Durgalakshmi, D., Rakkesh, R. A., & Balakumar, S. (2015). Stacked bioglass/TiO 2 nanocoatings on titanium substrate for enhanced osseointegration and its electrochemical corrosion studies. *Applied Surface Science, 349*, 561-569.

El-Meliegy, E., & van Noort, R. (2011). *Glasses and Glass Ceramics for Medical Applications*: Springer Science & Business Media.

El Abedin, S. Z., Welz-Biermann, U., & Endres, F. (2005). A study on the electrodeposition of tantalum on NiTi alloy in an ionic liquid and corrosion behaviour of the coated alloy. *Electrochemistry Communications, 7*(9), 941-946.

Elias, C. N., Oshida, Y., Lima, J. H. C., & Muller, C. A. (2008). Relationship between surface properties (roughness, wettability and morphology) of titanium and dental implant removal torque. *Journal of the mechanical behavior of biomedical materials, 1*(3), 234-242.

Eliaz, N., Kopelovitch, W., Burstein, L., Kobayashi, E., & Hanawa, T. (2009). Electrochemical processes of nucleation and growth of calcium phosphate on titanium supported by real- time quartz crystal microbalance measurements and X- ray photoelectron spectroscopy analysis. *Journal of Biomedical Materials Research Part A, 89*(1), 270-280.

Emslie, A. G., Bonner, F. T., & Peck, L. G. (1958). Flow of a viscous liquid on a rotating disk. *Journal of Applied Physics, 29*(5), 858-862.

Ernst, W. A., Thoma-Uszynski, S., Teitelbaum, R., Ko, C., Hanson, D. A., Clayberger, C., . . . Ganz, T. (2000). Granulysin, a T cell product, kills bacteria by altering membrane permeability. *The Journal of Immunology, 165*(12), 7102-7108.

Evans, N. T., Irvin, C. W., Safranski, D. L., & Gall, K. (2016). Impact of surface porosity and topography on the mechanical behavior of high strength biomedical polymers. *Journal of the mechanical behavior of biomedical materials, 59*, 459-473.

Faraji, M., & Mohaghegh, N. (2016). Ag/TiO 2-nanotube plates coated with reduced graphene oxide as photocatalysts. *Surface and Coatings Technology, 288*, 144-150.

Farrokhi- Rad, M. (2016). Effect of Dispersants on the Electrophoretic Deposition of Hydroxyapatite- Carbon Nanotubes Nanocomposite Coatings. *Journal of the American Ceramic Society*.

Fenker, M., Kappl, H., Banakh, O., Martin, N., & Pierson, J.-F. (2006). Investigation of Niobium oxynitride thin films deposited by reactive magnetron sputtering. *Surface and Coatings Technology, 201*(7), 4152-4157.

Fini, M., Giavaresi, G., Rimondini, L., & Giardino, R. (2002). Titanium alloy osseointegration in cancellous and cortical bone of ovariectomized animals: histomorphometric and bone hardness measurements. *International Journal of Oral & Maxillofacial Implants, 17*(1).

Foldbjerg, R., Dang, D. A., & Autrup, H. (2011). Cytotoxicity and genotoxicity of silver nanoparticles in the human lung cancer cell line, A549. *Archives of toxicology, 85*(7), 743-750.

Frigg, R., Schavan, R., & Hehli, M. (2001). Bone plate: Google Patents.

Fu, L., LIU, H.-b., ZOU, Y.-h., & LI, B. (2005). TECHNOLOGY RESEARCH ON OXIDATIVE DEGREE OF GRAPHITE OXIDE PREPARED BY HUMMERS METHOD [J]. *Carbon, 4*, 10-14.

Gangopadhyay, S., Acharya, R., Chattopadhyay, A., & Paul, S. (2010). Effect of substrate bias voltage on structural and mechanical properties of pulsed DC magnetron sputtered TiN–MoSx composite coatings. *Vacuum, 84*(6), 843-850.

Gao, A., Hang, R., Huang, X., Zhao, L., Zhang, X., Wang, L., . . . Chu, P. K. (2014). The effects of titania nanotubes with embedded silver oxide nanoparticles on bacteria and osteoblasts. *Biomaterials, 35*(13), 4223-4235.

García-Galván, F. R., Jiménez-Morales, A., Hickman, G. J., Perry, C. C., & Galván, J. C. (2016). *Sol-Gel TiO2 and ZrO2-Nanocomposite Thin Films for Enhancing in Vitro Biocompatibility and Bio-Corrosion Resistance of Ti6Al4V Orthopaedic Implants.* Paper presented at the Meeting Abstracts.

Gatehouse, B., & Wadsley, A. (1964). The crystal structure of the high temperature form of niobium pentoxide. *Acta Crystallographica, 17*(12), 1545-1554.

Geetha, M., Singh, A., Asokamani, R., & Gogia, A. (2009). Ti based biomaterials, the ultimate choice for orthopaedic implants–a review. *Progress in materials science, 54*(3), 397-425.

Ghadari, R., & Kashefi, A. (2017). A computational study on the usability of amino acid-functionalised nitrogen-doped graphene oxides as temperature-responsive drug delivery systems. *International Journal of Hyperthermia*, 1-11.

Ghazzal, M. N., Chaoui, N., Genet, M., Gaigneaux, E. M., & Robert, D. (2011). Effect of compressive stress inducing a band gap narrowing on the photoinduced activities of sol–gel TiO 2 films. *Thin Solid Films, 520*(3), 1147-1154.

Ghicov, A., Aldabergenova, S., Tsuchyia, H., & Schmuki, P. (2006). TiO2–Nb2O5 nanotubes with electrochemically tunable morphologies. *Angewandte Chemie International Edition, 45*(42), 6993-6996.

Ghicov, A., & Schmuki, P. (2009). Self-ordering electrochemistry: a review on growth and functionality of TiO 2 nanotubes and other self-aligned MO x structures. *Chemical Communications*(20), 2791-2808.

Giavaresi, G., Fini, M., Chiesa, R., Rimondini, L., Rondelli, G., Borsari, V., . . . Giardino, R. (2002). Osseointegration of sandblasted or anodised hydrothermally-treated titanium implants: mechanical, histomorphometric and bone hardness measurements. *The International journal of artificial organs, 25*(8), 806-813.

Gilbert, J. L., Buckley, C. A., & Jacobs, J. J. (1993). In vivo corrosion of modular hip prosthesis components in mixed and similar metal combinations. The effect of crevice, stress, motion, and alloy coupling. *Journal of biomedical materials research, 27*(12), 1533-1544.

Gonczy, S. T., & Randall, N. (2005). An ASTM standard for quantitative scratch adhesion testing of thin, hard ceramic coatings. *International Journal of Applied Ceramic Technology, 2*(5), 422-428.

Gonzalez, J., & Mirza-Rosca, J. (1999). Study of the corrosion behavior of titanium and some of its alloys for biomedical and dental implant applications. *Journal of Electroanalytical Chemistry, 471*(2), 109-115.

Gopi, D., Shinyjoy, E., & Kavitha, L. (2015). Influence of ionic substitution in improving the biological property of carbon nanotubes reinforced hydroxyapatite composite coating on titanium for orthopedic applications. *Ceramics International, 41*(4), 5454-5463.

Gopi, D., Shinyjoy, E., Kavitha, L., & Rajeswari, D. (2016). Carbon Nanotubes-reinforced Bioceramic Composite: An Advanced Coating Material for Orthopedic Applications. *Advanced Composite Materials*, 399.

Greer, A. I., Lim, T. S., Brydone, A. S., & Gadegaard, N. (2016). Mechanical compatibility of sol–gel annealing with titanium for orthopaedic prostheses. *Journal of Materials Science: Materials in Medicine, 27*(1), 1-6.

Guan, D., & Wang, Y. (2012). Synthesis and growth mechanism of multilayer TiO 2 nanotube arrays. *Nanoscale, 4*(9), 2968-2977.

Guo, L., Hu, Y., Yu, B., Davis, E., Irvin, R., Yan, X., & Li, D. (2016). Incorporating TiO2 nanotubes with a peptide of D-amino K122-4 (D) for enhanced mechanical and photocatalytic properties. *Scientific reports, 6*.

Guo, Y.-Y., Liu, B., Hu, B.-B., Xiao, G.-Y., Wu, Y.-P., Sun, P.-F., . . . Lu, Y.-P. (2016). Antibacterial activity and increased osteoblast cell functions of zinc calcium phosphate chemical conversion on titanium. *Surface and Coatings Technology, 294*, 131-138.

Guo, Y., Zhang, G., Wang, L., & Hu, Y. (2016). Optimization of parameters for EDM drilling of thermal-barrier-coated nickel superalloys using gray relational analysis method. *The International Journal of Advanced Manufacturing Technology, 83*(9-12), 1595-1605.

Hackenberg, S., Scherzed, A., Kessler, M., Hummel, S., Technau, A., Froelich, K., . . . Kleinsasser, N. (2011). Silver nanoparticles: evaluation of DNA damage, toxicity and functional impairment in human mesenchymal stem cells. *Toxicology letters, 201*(1), 27-33.

Hanaor, D. A., & Sorrell, C. C. (2011). Review of the anatase to rutile phase transformation. *Journal of Materials Science, 46*(4), 855-874.

He, S., Zheng, M., Yao, L., Yuan, X., Li, M., Ma, L., & Shen, W. (2010). Preparation and properties of ZnO nanostructures by electrochemical anodization method. *Applied Surface Science, 256*(8), 2557-2562.

He, Z., Xiao, J., Xia, F., Kajiyoshi, K., Samart, C., & Zhang, H. (2014). Enhanced solar water-splitting performance of TiO 2 nanotube arrays by annealing and quenching. *Applied Surface Science, 313*, 633-639.

Hench, L., & Ethridge, E. (1975). Biomaterials: the interfacial problem. *Adv Biomed Eng, 5*, 35-150.

Hench, L. L., & Polak, J. M. (2002). Third-generation biomedical materials. *Science, 295*(5557), 1014-1017.

Hench, L. L., & Wilson, J. (1993). *An introduction to bioceramics* (Vol. 1): World Scientific.

Hernandez, Y., Nicolosi, V., Lotya, M., Blighe, F. M., Sun, Z., De, S., . . . Gun'Ko, Y. K. (2008). High-yield production of graphene by liquid-phase exfoliation of graphite. *Nature Nanotechnology, 3*(9), 563-568.

Hoffman, R. (1988). *Nanomechanics of thin films: emphasis: tensile properties.* Paper presented at the MRS Proceedings.

Höland, W., Rheinberger, V., Apel, E., van't Hoen, C., Höland, M., Dommann, A., . . . Graf-Hausner, U. (2006). Clinical applications of glass-ceramics in dentistry. *Journal of Materials Science: Materials in Medicine, 17*(11), 1037-1042.

Holleck, H., & Schier. (1995). Multilayer PVD coatings for wear protection. *Surface and Coatings Technology, 76*, 328-336.

Horgnies, M., Willieme, P., & Gabet, O. (2011). Influence of the surface properties of concrete on the adhesion of coating: characterization of the interface by peel test and FT-IR spectroscopy. *Progress in Organic Coatings, 72*(3), 360-379.

Hu, Y., Shenderova, O. A., Hu, Z., Padgett, C. W., & Brenner, D. W. (2006). Carbon nanostructures for advanced composites. *Reports on Progress in Physics, 69*(6), 1847.

Huang, C.-F., Chiang, H.-J., Lan, W.-C., Chou, H.-H., Ou, K.-L., & Yu, C.-H. (2011). Development of silver-containing austenite antibacterial stainless steels for biomedical applications Part I: microstructure characteristics, mechanical properties and antibacterial mechanisms. *Biofouling, 27*(5), 449-457.

Huang, H.-L., Chang, Y.-Y., Lai, M.-C., Lin, C.-R., Lai, C.-H., & Shieh, T.-M. (2010). Antibacterial TaN-Ag coatings on titanium dental implants. *Surface and Coatings Technology, 205*(5), 1636-1641.

Hyzy, S. L., Cheng, A., Cohen, D. J., Yatzkaier, G., Whitehead, A. J., Clohessy, R. M., . . . Schwartz, Z. (2016). Novel hydrophilic nanostructured microtexture on direct metal laser sintered Ti–6Al–4V surfaces enhances osteoblast response in vitro and osseointegration in a rabbit model. *Journal of Biomedical Materials Research Part A*.

Iaculli, F., Di Filippo, E. S., Piattelli, A., Mancinelli, R., & Fulle, S. (2016). Dental pulp stem cells grown on dental implant titanium surfaces: An in vitro evaluation of differentiation and microRNAs expression. *Journal of Biomedical Materials Research Part B: Applied Biomaterials*.

Izman, S., Shah, A., Nazim, E., Hassan, M., Anwar, M., Abdul-Kadir, M. R., & Rosliza, R. (2012). *Surface modification techniques for biomedical grade of titanium alloys: Oxidation, carburization and ion implantation processes*: INTECH Open Access Publisher.

Janković, A., Eraković, S., Mitrić, M., Matić, I. Z., Juranić, Z. D., Tsui, G. C., . . . Park, S. J. (2015). Bioactive hydroxyapatite/graphene composite coating and its corrosion stability in simulated body fluid. *Journal of Alloys and Compounds, 624*, 148-157.

Jaya, A. S. M., Hashim, S. Z. M., & Rahman, M. N. A. (2010). *Fuzzy logic-based for predicting roughness performance of TiAlN coating.* Paper presented at the 2010 10th International Conference on Intelligent Systems Design and Applications.

Jia, Z., Xiu, P., Li, M., Xu, X., Shi, Y., Cheng, Y., . . . Cai, H. (2016). Bioinspired anchoring AgNPs onto micro-nanoporous TiO 2 orthopedic coatings: trap-killing of bacteria, surface-regulated osteoblast functions and host responses. *Biomaterials, 75*, 203-222.

Jimbo, R., Coelho, P. G., Bryington, M., Baldassarri, M., Tovar, N., Currie, F., . . . Ono, D. (2012). Nano hydroxyapatite-coated implants improve bone nanomechanical properties. *Journal of dental research, 91*(12), 1172-1177.

Johnston, H. J., Hutchison, G., Christensen, F. M., Peters, S., Hankin, S., & Stone, V. (2010). A review of the in vivo and in vitro toxicity of silver and gold particulates: particle attributes and biological mechanisms responsible for the observed toxicity. *Critical reviews in toxicology, 40*(4), 328-346.

Joshi, U. J., Gadge, A. S., D'Mello, P., Sinha, R., Srivastava, S., & Govil, G. (2011). Anti-inflammatory, antioxidant and anticancer activity of Quercetin and its analogues. *Int J Res in Pharma and Biomed Sci, 2*, 1756-1766.

Justin, D., Jin, S., Frandsen, C., Brammer, K., Bjursten, L., Oh, S., & Pratt, C. (2016). IN VITRO AND IN VIVO EVALUATION OF IMPLANT SURFACES TREATED WITH TITANIUM OXIDE (TIO2) NANOTUBE ARRAYS TO ENHANCE OSSEOINTEGRATION BETWEEN ARTHROPLASTY IMPLANTS AND SURROUNDING BONE. *Bone Joint J, 98*(SUPP 8), 71-71.

Justin, D., Pratt, C., Jin, S., Shivaram, A., Bose, S., & Bandyopadhyay, A. (2017). THE MECHANICAL STABILITY AND IN VITRO AND IN VIVO RESPONSE OF TITANIUM ARTHROPLASTY BONE INGROWTH MATERIALS

ENHANCED WITH TIO2 NANOTUBES AND ANTIMICROBIAL SILVER. *Bone Joint J, 99*(SUPP 4), 38-38.

Kaczmarek, M., Jurczyk, K., Koper, J. K., Paszel-Jaworska, A., Romaniuk, A., Lipińska, N., . . . Jurczyk, M. U. (2016). In vitro biocompatibility of anodized titanium with deposited silver nanodendrites. *Journal of Materials Science, 51*(11), 5259-5270.

Kalisz, M., Grobelny, M., Świniarski, M., Mazur, M., Wojcieszak, D., Zdrojek, M., . . . Kaczmarek, D. (2016). Comparison of structural, mechanical and corrosion properties of thin TiO 2/graphene hybrid systems formed on Ti–Al–V alloys in biomedical applications. *Surface and Coatings Technology, 290*, 124-134.

Kämmerer, T. A., Palarie, V., Schiegnitz, E., Topalo, V., Schröter, A., Al- Nawas, B., & Kämmerer, P. W. (2016). A biphasic calcium phosphate coating for potential drug delivery affects early osseointegration of titanium implants. *Journal of Oral Pathology & Medicine*.

Kar, P., Zhang, Y., Farsinezhad, S., Mohammadpour, A., Wiltshire, B. D., Sharma, H., & Shankar, K. (2015). Rutile phase n-and p-type anodic titania nanotube arrays with square-shaped pore morphologies. *Chemical Communications, 51*(37), 7816-7819.

Karimi, L., Yazdanshenas, M. E., Khajavi, R., Rashidi, A., & Mirjalili, M. (2014). Using graphene/TiO2 nanocomposite as a new route for preparation of electroconductive, self-cleaning, antibacterial and antifungal cotton fabric without toxicity. *Cellulose, 21*(5), 3813-3827.

Karoussis, I. K., Kyriakidou, K., Psarros, C., Lang, N. P., & Vrotsos, I. A. (2016). Nd: YAG laser radiation (1.064 nm) accelerates differentiation of osteoblasts to osteocytes on smooth and rough titanium surfaces in vitro. *Clinical Oral Implants Research*.

Khalid, N., Ahmed, E., Ahmad, M., Niaz, N., Ramzan, M., Shakil, M., . . . Majid, A. (2016). Microwave-assisted synthesis of Ag–TiO 2/graphene composite for hydrogen production under visible light irradiation. *Ceramics International, 42*(16), 18257-18263.

Khalili, V., Khalil-Allafi, J., Sengstock, C., Motemani, Y., Paulsen, A., Frenzel, J., . . . Köller, M. (2016). Characterization of mechanical properties of hydroxyapatite–silicon–multi walled carbon nano tubes composite coatings synthesized by EPD on NiTi alloys for biomedical application. *Journal of the mechanical behavior of biomedical materials, 59*, 337-352.

Khorasani, A. M., Asadnia, M., & Saadatkia, P. (2013). Modeling of TiC-N thin film coating process on drills using particle swarm optimization algorithm. *Arabian Journal for Science and Engineering, 38*(6), 1565-1571.

Khorasani, A. M., Faraji, M., & Kootsookos, A. (2012). CVD and PVD coating process modelling by using artificial neural networks. *Artificial Intelligence Research, 1*(1), p46.

Kim, B.-K., Jo, Y.-L., & Shim, J.-J. (2012). Preparation and antibacterial activity of silver nanoparticles-decorated graphene composites. *The Journal of Supercritical Fluids, 72*, 28-35.

Kim, D., Ghicov, A., Albu, S. P., & Schmuki, P. (2008). Bamboo-type TiO2 nanotubes: improved conversion efficiency in dye-sensitized solar cells. *Journal of the American Chemical Society, 130*(49), 16454-16455.

Kim, H. J., Bae, I.-S., Cho, S.-J., Boo, J.-H., Lee, B.-C., Heo, J., . . . Hong, B. (2012). Synthesis and characteristics of NH2-functionalized polymer films to align and immobilize DNA molecules. *Nanoscale research letters, 7*(1), 30.

Kim, J., Cote, L. J., Kim, F., Yuan, W., Shull, K. R., & Huang, J. (2010). Graphene oxide sheets at interfaces. *Journal of the American Chemical Society, 132*(23), 8180-8186.

Kim, W.-G., Choe, H.-C., Ko, Y.-M., & Brantley, W. A. (2009). Nanotube morphology changes for Ti–Zr alloys as Zr content increases. *Thin Solid Films, 517*(17), 5033-5037.

Kirmanidou, Y., Sidira, M., Drosou, M.-E., Bennani, V., Bakopoulou, A., Tsouknidas, A., . . . Michalakis, K. (2016). New Ti-alloys and surface modifications to improve the mechanical properties and the biological response to orthopedic and dental implants: a review. *BioMed research international, 2016*.

Kitsugi, T., Nakamura, T., Yamamura, T., Kokubu, T., Shibuya, T., & Takagi, M. (1987). SEM- EPMA observation of three types of apatite- containing glass- ceramics implanted in bone: The variance of a Ca- P- rich layer. *Journal of biomedical materials research, 21*(10), 1255-1271.

Kokubo, T. (1990). Surface chemistry of bioactive glass-ceramics. *Journal of Non-Crystalline Solids, 120*(1), 138-151.

Kokubo, T., & Takadama, H. (2006). How useful is SBF in predicting in vivo bone bioactivity? *Biomaterials, 27*(15), 2907-2915.

Kramar, D., Cica, D., Sredanovic, B., & Kopac, J. (2016). Design of fuzzy expert system for predicting of surface roughness in high-pressure jet assisted turning using bioinspired algorithms. *Artificial Intelligence for Engineering Design, Analysis and Manufacturing, 30*(01), 96-106.

Kunze, J., Müller, L., Macak, J. M., Greil, P., Schmuki, P., & Müller, F. A. (2008). Time-dependent growth of biomimetic apatite on anodic TiO 2 nanotubes. *Electrochimica Acta, 53*(23), 6995-7003.

Kuo, M., & Yen, S. (2002). The process of electrochemical deposited hydroxyapatite coatings on biomedical titanium at room temperature. *Materials Science and Engineering: C, 20*(1), 153-160.

Kwaśny, W., Sitek, W., & Dobrzański, L. (2007). Modelling of properties of the PVD coatings using neural networks. *Journal of Achievements in Materials and Manufacturing Engineering, 24*(2), 163-166.

Lacefield, W. R. (1998). Current status of ceramic coatings for dental implants. *Implant dentistry, 7*(4), 315-322.

Lahiri, D., Singh, V., Benaduce, A. P., Seal, S., Kos, L., & Agarwal, A. (2011). Boron nitride nanotube reinforced hydroxyapatite composite: mechanical and tribological performance and in-vitro biocompatibility to osteoblasts. *Journal of the mechanical behavior of biomedical materials, 4*(1), 44-56.

Lambert, T. N., Chavez, C. A., Hernandez-Sanchez, B., Lu, P., Bell, N. S., Ambrosini, A., . . . Huber, D. L. (2009). Synthesis and characterization of titania− graphene nanocomposites. *The Journal of Physical Chemistry C, 113*(46), 19812-19823.

Lane, W. A. (1895). Some remarks on the treatment of fractures. *British medical journal, 1*(1790), 861.

Lauer, G., Wiedmann-Al-Ahmad, M., Otten, J., Hübner, U., Schmelzeisen, R., & Schilli, W. (2001). The titanium surface texture effects adherence and growth of human gingival keratinocytes and human maxillar osteoblast-like cells in vitro. *Biomaterials, 22*(20), 2799-2809.

Laugier, M. T. (1984). An energy approach to the adhesion of coatings using the scratch test. *Thin Solid Films, 117*(4), 243-249.

Le Guéhennec, L., Soueidan, A., Layrolle, P., & Amouriq, Y. (2007). Surface treatments of titanium dental implants for rapid osseointegration. *Dental materials, 23*(7), 844-854.

Lee, D. K., Park, J. Y., Kim, M. R., & Jang, D.-J. (2011). Facile hydrothermal fabrication of hollow hexagonal hydroxyapatite prisms. *CrystEngComm, 13*(17), 5455-5459.

Lee, J. U., Park, B., Kim, B.-S., Bae, D.-R., & Lee, W. (2016). Electrophoretic deposition of aramid nanofibers on carbon fibers for highly enhanced interfacial adhesion at low content. *Composites Part A: Applied Science and Manufacturing, 84*, 482-489.

Lee, S.-S., Hong, J.-D., Kim, C. H., Kim, K., Koo, J. P., & Lee, K.-B. (2001). Layer-by-layer deposited multilayer assemblies of ionene-type polyelectrolytes based on the spin-coating method. *Macromolecules, 34*(16), 5358-5360.

Lei, W.-S., Mittal, K., & Yu, Z. (2016). Adhesion Measurement of Coatings on Biodevices/Implants: A Critical Review. *Reviews of Adhesion and Adhesives, 4*(4), 367-397.

Lenth, R. V. (2009). Response-Surface Methods in R, using rsm. *Journal of Statistical Software, 32*(7), 1-17.

Leskinen, J., Eskelinen, A., Huhtala, H., Paavolainen, P., & Remes, V. (2012). The incidence of knee arthroplasty for primary osteoarthritis grows rapidly among baby boomers: A population- based study in Finland. *Arthritis & Rheumatism, 64*(2), 423-428.

Lester, E., Tang, S. V., Khlobystov, A., Rose, V. L., Buttery, L., & Roberts, C. J. (2013). Producing nanotubes of biocompatible hydroxyapatite by continuous hydrothermal synthesis. *CrystEngComm, 15*(17), 3256-3260.

Li, J., Liu, C., Ye, Y., Zhu, J., Wang, S., Guo, J., & Sham, T.-K. (2016). Tracking the Local Effect of Fluorine Self-Doping in Anodic TiO2 Nanotubes. *The Journal of Physical Chemistry C, 120*(8), 4623-4628.

Li, S.-K., Yan, Y.-X., Wang, J.-L., & Yu, S.-H. (2013). Bio-inspired in situ growth of monolayer silver nanoparticles on graphene oxide paper as multifunctional substrate. *Nanoscale, 5*(24), 12616-12623.

Li, Y., Yang, C., Zhao, H., Qu, S., Li, X., & Li, Y. (2014). New developments of Ti-based alloys for biomedical applications. *Materials, 7*(3), 1709-1800.

Lima, L. M., Motisuki, C., Santos-Pinto, L. d., Santos-Pinto, A. d., & Corat, E. J. (2006). Cutting characteristics of dental diamond burs made with CVD technology. *Brazilian oral research, 20*(2), 155-161.

Liu, B., Zhao, X., Zhu, W., Luo, W., & Cheng, X. (2008). Multiple Pass- Band Optical Left- Handed Metamaterials Based on Random Dendritic Cells. *Advanced Functional Materials, 18*(21), 3523-3528.

Liu, C., Teng, Y., Liu, R., Luo, S., Tang, Y., Chen, L., & Cai, Q. (2011). Fabrication of graphene films on TiO 2 nanotube arrays for photocatalytic application. *Carbon, 49*(15), 5312-5320.

Liu, C., Wang, K., Luo, S., Tang, Y., & Chen, L. (2011). Direct Electrodeposition of Graphene Enabling the One- Step Synthesis of Graphene–Metal Nanocomposite Films. *Small, 7*(9), 1203-1206.

Liu, G., Wang, S., Liu, J., & Song, D. (2012). An electrochemical immunosensor based on chemical assembly of vertically aligned carbon nanotubes on carbon substrates for direct detection of the pesticide endosulfan in environmental water. *Analytical chemistry, 84*(9), 3921-3928.

Liu, H., Gao, N., Liao, M., & Fang, X. (2015). Hexagonal-like Nb2O5 nanoplates-based photodetectors and photocatalyst with high performances. *Scientific reports, 5*.

Liu, J., Cui, L., & Losic, D. (2013). Graphene and graphene oxide as new nanocarriers for drug delivery applications. *Acta biomaterialia, 9*(12), 9243-9257.

Liu, J., Yang, Y., Hassanin, H., Jumbu, N., Deng, S., Zuo, Q., & Jiang, K. (2016). Graphene–Alumina Nanocomposites with Improved Mechanical Properties for Biomedical Applications. *ACS applied materials & interfaces, 8*(4), 2607-2616.

Liu, J., Ye, X., Wang, H., Zhu, M., Wang, B., & Yan, H. (2003). The influence of pH and temperature on the morphology of hydroxyapatite synthesized by hydrothermal method. *Ceramics International, 29*(6), 629-633.

Liu, J., Zhang, W., Shi, H., Yang, K., Wang, G., Wang, P., . . . Chu, P. K. (2016). In situ plasma fabrication of ceramic- like structure on polymeric implant with enhanced

surface hardness, cytocompatibility and antibacterial capability. *Journal of Biomedical Materials Research Part A*.

Liu, N., Luo, F., Wu, H., Liu, Y., Zhang, C., & Chen, J. (2008). One- step ionic- liquid-assisted electrochemical synthesis of ionic- liquid- functionalized graphene sheets directly from graphite. *Advanced Functional Materials, 18*(10), 1518-1525.

Liu, S., Li, B., Liang, C., Wang, H., & Qiao, Z. (2016). Formation mechanism and adhesive strength of a hydroxyapatite/TiO 2 composite coating on a titanium surface prepared by micro-arc oxidation. *Applied Surface Science, 362*, 109-114.

Liu, S., Zeng, T. H., Hofmann, M., Burcombe, E., Wei, J., Jiang, R., . . . Chen, Y. (2011). Antibacterial activity of graphite, graphite oxide, graphene oxide, and reduced graphene oxide: membrane and oxidative stress. *ACS nano, 5*(9), 6971-6980.

Liu, X., Chu, P. K., & Ding, C. (2004). Surface modification of titanium, titanium alloys, and related materials for biomedical applications. *Materials Science and Engineering: R: Reports, 47*(3), 49-121.

Losic, D., & Simovic, S. (2009). Self-ordered nanopore and nanotube platforms for drug delivery applications. *Expert opinion on drug delivery, 6*(12), 1363-1381.

Lotya, M., Hernandez, Y., King, P. J., Smith, R. J., Nicolosi, V., Karlsson, L. S., . . . McGovern, I. (2009). Liquid phase production of graphene by exfoliation of graphite in surfactant/water solutions. *Journal of the American Chemical Society, 131*(10), 3611-3620.

Lotz, E. M., Olivares- Navarrete, R., Hyzy, S. L., Berner, S., Schwartz, Z., & Boyan, B. D. (2016). Comparable responses of osteoblast lineage cells to microstructured hydrophilic titanium–zirconium and microstructured hydrophilic titanium. *Clinical Oral Implants Research*.

Lu, M., Shao, D., Wang, P., Chen, D., Zhang, Y., Li, M., . . . Zhou, Y. (2016). Enhanced osteoblast adhesion on amino-functionalized titanium surfaces through combined plasma enhanced chemical vapor deposition (PECVD) method. *RSC Advances, 6*(86), 82688-82697.

Luan, X., Guan, D., & Wang, Y. (2012). Facile synthesis and morphology control of bamboo-type TiO2 nanotube arrays for high-efficiency dye-sensitized solar cells. *The Journal of Physical Chemistry C, 116*(27), 14257-14263.

Lv, W., Tang, D.-M., He, Y.-B., You, C.-H., Shi, Z.-Q., Chen, X.-C., . . . Yang, Q.-H. (2009). Low-temperature exfoliated graphenes: vacuum-promoted exfoliation and electrochemical energy storage. *ACS nano, 3*(11), 3730-3736.

Lynch, K. R., Mlack, R., Correia, P. J. F., Brown, S. B., & Muhlstein, C. L. (2000). System and method for performing bulge testing of films, coatings and/or layers: Google Patents.

Macak, J., Tsuchiya, H., Ghicov, A., Yasuda, K., Hahn, R., Bauer, S., & Schmuki, P. (2007). TiO 2 nanotubes: self-organized electrochemical formation, properties

and applications. *Current Opinion in Solid State and Materials Science, 11*(1), 3-18.

Mackenzie, J. D., & Bescher, E. P. (2000). Physical properties of sol-gel coatings. *Journal of Sol-Gel Science and Technology, 19*(1-3), 23-29.

Maher, S., Qin, J., Gulati, K., ElMekawy, A., Kaur, G., Lima-Marques, L., . . . Losic, D. (2016). 3D printed titanium implants with nano-engineered surface titania nanotubes for localized drug delivery. *Chemeca 2016: Chemical Engineering-Regeneration, Recovery and Reinvention*, 65.

Mainardes, R. M., & Silva, L. P. (2004). Drug delivery systems: past, present, and future. *Current drug targets, 5*(5), 449-455.

Maleki- Ghaleh, H., Khalil- Allafi, J., Aghaie, E., & Siadati, M. (2015). Effect of TiO2–Ti and TiO2–TiN composite coatings on corrosion behavior of NiTi alloy. *Surface and Interface Analysis, 47*(1), 99-104.

Manso, M., Jimenez, C., Morant, C., Herrero, P., & Martınez-Duart, J. (2000). Electrodeposition of hydroxyapatite coatings in basic conditions. *Biomaterials, 21*(17), 1755-1761.

Marimuthu, M., Veerapandian, M., Ramasundaram, S., Hong, S. W., Sudhagar, P., Nagarajan, S., . . . Yun, K. (2014). Sodium functionalized graphene oxide coated titanium plates for improved corrosion resistance and cell viability. *Applied Surface Science, 293*, 124-131.

Marin, E., Offoiach, R., Regis, M., Fusi, S., Lanzutti, A., & Fedrizzi, L. (2016). Diffusive thermal treatments combined with PVD coatings for tribological protection of titanium alloys. *Materials & Design, 89*, 314-322.

Marin, S., Mihail Vlasceanu, G., Elena Tiplea, R., Raluca Bucur, I., Lemnaru, M., Minodora Marin, M., & Mihai Grumezescu, A. (2015). Applications and toxicity of silver nanoparticles: a recent review. *Current topics in medicinal chemistry, 15*(16), 1596-1604.

Mariscal-Muñoz, E., Costa, C. A., Tavares, H. S., Bianchi, J., Hebling, J., Machado, J. P., . . . Souza, P. P. (2016). Osteoblast differentiation is enhanced by a nano-to-micro hybrid titanium surface created by Yb: YAG laser irradiation. *Clinical oral investigations, 20*(3), 503-511.

Martin, J., Schwartz, Z., Hummert, T., Schraub, D., Simpson, J., Lankford, J., . . . Boyan, B. (1995). Effect of titanium surface roughness on proliferation, differentiation, and protein synthesis of human osteoblast- like cells (MG63). *Journal of biomedical materials research, 29*(3), 389-401.

Masuda, T., Yliheikkilä, P. K., Felton, D. A., & Cooper, L. F. (1997). Generalizations regarding the process and phenomenon of osseointegration. Part I. In vivo studies. *The International journal of oral & maxillofacial implants, 13*(1), 17-29.

Mazaheri, M., Eslahi, N., Ordikhani, F., Tamjid, E., & Simchi, A. (2015). Nanomedicine applications in orthopedic medicine: state of the art. *International journal of nanomedicine, 10*, 6039.

Mazare, A., Dilea, M., Ionita, D., & Demetrescu, I. (2014). Electrochemical behavior in simulated body fluid of TiO2 nanotubes on TiAlNb alloy elaborated in various anodizing electrolyte. *Surface and Interface Analysis*, *46*(3), 186-192.

Mazare, A., Dilea, M., Ionita, D., Titorencu, I., Trusca, V., & Vasile, E. (2012). Changing bioperformance of TiO 2 amorphous nanotubes as an effect of inducing crystallinity. *Bioelectrochemistry*, *87*, 124-131.

Mehrali, M., Akhiani, A. R., Talebian, S., Mehrali, M., Latibari, S. T., Dolatshahi-Pirouz, A., & Metselaar, H. S. C. (2016). Electrophoretic deposition of calcium silicate–reduced graphene oxide composites on titanium substrate. *Journal of the European Ceramic Society*, *36*(2), 319-332.

Mehrali, M., Moghaddam, E., Shirazi, S. F. S., Baradaran, S., Mehrali, M., Latibari, S. T., . . . Osman, N. A. A. (2014). Synthesis, mechanical properties, and in vitro biocompatibility with osteoblasts of calcium silicate–reduced graphene oxide composites. *ACS applied materials & interfaces*, *6*(6), 3947-3962.

Meischel, M., Eichler, J., Martinelli, E., Karr, U., Weigel, J., Schmöller, G., . . . Stanzl-Tschegg, S. (2016). Adhesive strength of bone-implant interfaces and in-vivo degradation of PHB composites for load-bearing applications. *Journal of the mechanical behavior of biomedical materials*, *53*, 104-118.

Merritt, K., & Brown, S. A. (1988). Effect of proteins and pH on fretting corrosion and metal ion release. *Journal of biomedical materials research*, *22*(2), 111-120.

Meyerhofer, D. (1978). Characteristics of resist films produced by spinning. *Journal of Applied Physics*, *49*(7), 3993-3997.

Minagar, S., Berndt, C. C., Gengenbach, T., & Wen, C. (2014). Fabrication and characterization of TiO 2–ZrO 2–ZrTiO 4 nanotubes on TiZr alloy manufactured via anodization. *Journal of Materials Chemistry B*, *2*(1), 71-83.

Minagar, S., Li, Y., Berndt, C. C., & Wen, C. (2015). The influence of titania–zirconia–zirconium titanate nanotube characteristics on osteoblast cell adhesion. *Acta biomaterialia*, *12*, 281-289.

Ming, H. N. (2011). Fabrication and characterization of graphene hydrogel via hydrothermal approach as a scaffold for preliminary study of cell growth. *International journal of nanomedicine, 6*.

Mishra, S. K., Teotia, A. K., Kumar, A., & Kannan, S. (2016). Mechanically tuned nanocomposite coating on titanium metal with integrated properties of biofilm inhibition, cell proliferation, and sustained drug delivery. *Nanomedicine: Nanotechnology, Biology and Medicine*.

Miura, C., Shimizu, Y., Imai, Y., Mukai, T., Yamamoto, A., Sano, Y., . . . Oikawa, M. (2016). In vivo corrosion behaviour of magnesium alloy in association with surrounding tissue response in rats. *Biomedical Materials, 11*(2), 025001.

Modiri-Delshad, M., Kaboli, S. H. A., Taslimi-Renani, E., & Rahim, N. A. (2016). Backtracking search algorithm for solving economic dispatch problems with valve-point effects and multiple fuel options. *Energy, 116*, 637-649.

Modiri-Delshad, M., & Rahim, N. A. (2016). Multi-objective backtracking search algorithm for economic emission dispatch problem. *Applied Soft Computing, 40*, 479-494.

Mohamed, A. E. R., & Rohani, S. (2009). *Synthesis of titania nanotube arrays by anodization.* Paper presented at the AIDIC Conf. Ser.

Mohan, L., Anandan, C., & Rajendran, N. (2015). Electrochemical behaviour and bioactivity of self-organized TiO 2 nanotube arrays on Ti-6Al-4V in Hanks' solution for biomedical applications. *Electrochimica Acta, 155*, 411-420.

Mohan, L., Anandan, C., & Rajendran, N. (2016). Drug release characteristics of quercetin-loaded TiO 2 nanotubes coated with chitosan. *International journal of biological macromolecules*.

Mohseni, E., Zalnezhad, E., Bushroa, A., Hamouda, A. M., Goh, B., & Yoon, G. (2015). Ti/TiN/HA coating on Ti–6Al–4V for biomedical applications. *Ceramics International, 41*(10), 14447-14457.

Mollahasani, A., Alavi, A. H., & Gandomi, A. H. (2011). Empirical modeling of plate load test moduli of soil via gene expression programming. *Computers and Geotechnics, 38*(2), 281-286.

Moon, I. K., Kim, J. I., Lee, H., Hur, K., Kim, W. C., & Lee, H. (2013). 2D graphene oxide nanosheets as an adhesive over-coating layer for flexible transparent conductive electrodes. *Scientific reports, 3*.

Morra, M., Cassinelli, C., Meda, L., Fini, M., Giavaresi, G., & Giardino, R. (2005). Surface analysis and effects on interfacial bone microhardness of collagen-coated titanium implants: a rabbit model. *International Journal of Oral & Maxillofacial Implants, 20*(1).

Moussy, F. (2010). Biomaterials for the developing world. *Journal of Biomedical Materials Research Part A, 94*(4), 1001-1003.

Movassagh-Alanagh, F., Abdollah-zadeh, A., Aliofkhazraei, M., & Abedi, M. (2017). Improving the wear and corrosion resistance of Ti–6Al–4V alloy by deposition of TiSiN nanocomposite coating with pulsed-DC PACVD. *Wear, 390*, 93-103.

Mueller, H., & Greener, E. (1970). Polarization studies of surgical materials in Ringer's solution. *Journal of biomedical materials research, 4*(1), 29-41.

Musil, J., Zenkin, S., Čerstvý, R., Haviar, S., & Čiperová, Z. (2017). (Zr, Ti, O) alloy films with enhanced hardness and resistance to cracking prepared by magnetron sputtering. *Surface and Coatings Technology, 322*, 86-91.

Nayak, P. K., Caraveo-Frescas, J., Wang, Z., Hedhili, M., Wang, Q., & Alshareef, H. N. (2014). Thin film complementary metal oxide semiconductor (CMOS) device using a single-step deposition of the channel layer. *Scientific reports, 4*, 4672.

Nemes-Incze, P., Osváth, Z., Kamarás, K., & Biró, L. (2008). Anomalies in thickness measurements of graphene and few layer graphite crystals by tapping mode atomic force microscopy. *Carbon, 46*(11), 1435-1442.

Ng, C., Ye, C., Ng, Y. H., & Amal, R. (2010). Flower-shaped tungsten oxide with inorganic fullerene-like structure: synthesis and characterization. *Crystal Growth & Design, 10*(8), 3794-3801.

Niinomi, M., Hattori, T., & Niwa, S. (2004). Material characteristics and biocompatibility of low rigidity titanium alloys for biomedical applications. *Biomaterials in orthopedics*, 41-62.

Nouri, A., Hodgson, P. D., & Wen, C. e. (2010). *Biomimetic porous titanium scaffolds for orthopaedic and dental applications*: InTech.

Ogino, M., Ohuchi, F., & Hench, L. L. (1980). Compositional dependence of the formation of calcium phosphate films on bioglass. *Journal of biomedical materials research, 14*(1), 55-64.

Oldani, C., Dominguez, A., & Eli, T. (2012). *Titanium as a Biomaterial for Implants*: Citeseer.

Ong, J., Lucas, L., Lacefield, W., & Rigney, E. (1992). Structure, solubility and bond strength of thin calcium phosphate coatings produced by ion beam sputter deposition. *Biomaterials, 13*(4), 249-254.

Ooi, C., Hamdi, M., & Ramesh, S. (2007). Properties of hydroxyapatite produced by annealing of bovine bone. *Ceramics International, 33*(7), 1171-1177.

Ordikhani, F., Zustiak, S. P., & Simchi, A. (2016). Surface Modifications of Titanium Implants by Multilayer Bioactive Coatings with Drug Delivery Potential: Antimicrobial, Biological, and Drug Release Studies. *JOM, 68*(4), 1100-1108.

Oshida, Y. (2007). Materials Classification. *Bioscience and Bioengineering of Titanium Materials, Elsevier, Oxford*, 11-22.

Ou, K.-L., Weng, C.-C., Lin, Y.-H., & Huang, M.-S. (2017). A promising of alloying modified beta-type Titanium-Niobium implant for biomedical applications: Microstructural characteristics, in vitro biocompatibility and antibacterial performance. *Journal of Alloys and Compounds, 697*, 231-238.

Pan, J., Leygraf, C., Thierry, D., & Ektessabi, A. (1997). Corrosion resistance for biomaterial applications of TiO 2 films deposited on titanium and stainless steel

by ion-beam-assisted sputtering. *Journal of biomedical materials research, 35*(3), 309-318.

Pan, Z., He, L., Qiu, L., Korayem, A. H., Li, G., Zhu, J. W., . . . Wang, M. C. (2015). Mechanical properties and microstructure of a graphene oxide–cement composite. *Cement and Concrete Composites, 58*, 140-147.

Parcharoen, Y., Termsuksawad, P., & Sirivisoot, S. (2014). *Electrochemical Deposition of Novel Graphene Oxide-Hydroxyapatite Composite onto Titanium Dioxide Nanotubes for Orthopaedic Applications.* Paper presented at the International Conference on Advances in science and Technology, Pattaya, Chonburi.

Park, J., Bauer, S., von der Mark, K., & Schmuki, P. (2007). Nanosize and vitality: TiO2 nanotube diameter directs cell fate. *Nano letters, 7*(6), 1686-1691.

Park, M. V., Neigh, A. M., Vermeulen, J. P., de la Fonteyne, L. J., Verharen, H. W., Briedé, J. J., . . . de Jong, W. H. (2011). The effect of particle size on the cytotoxicity, inflammation, developmental toxicity and genotoxicity of silver nanoparticles. *Biomaterials, 32*(36), 9810-9817.

Park, S., & Ruoff, R. S. (2009). Chemical methods for the production of graphenes. *Nature Nanotechnology, 4*(4), 217-224.

Park, Y. J., Liu, L., Yoo, S.-H., & Park, S. (2012). Electrochemical Synthesis of Dumbbell-like Au-Ni-Au Nanorods and Their Surface Plasmon Resonance. *Journal of Electrochemical Science and Technology, 3*(2), 57-62.

Patil, K. R., Hwang, Y. K., Kim, M.-J., Chang, J.-S., & Park, S.-E. (2004). Preparation of thin films comprising palladium nanoparticles by a solid–liquid interface reaction technique. *Journal of colloid and interface science, 276*(2), 333-338.

Peláez-Vargas, A. (2005). Evaluación de la toxicidad in vitro, la adherencia y la nanotopografía de recubrimientos aplicados por sol-gel para implantes metálicos. *Master's Thesis*.

Perreault, F., De Faria, A. F., Nejati, S., & Elimelech, M. (2015). Antimicrobial properties of graphene oxide nanosheets: why size matters. *ACS nano, 9*(7), 7226-7236.

Pittenger, M. F., Mackay, A. M., Beck, S. C., Jaiswal, R. K., Douglas, R., Mosca, J. D., . . . Marshak, D. R. (1999). Multilineage potential of adult human mesenchymal stem cells. *Science, 284*(5411), 143-147.

Piveteau, L.-D., Gasser, B., & Schlapbach, L. (2000). Evaluating mechanical adhesion of sol–gel titanium dioxide coatings containing calcium phosphate for metal implant application. *Biomaterials, 21*(21), 2193-2201.

Popat, K. C., Leoni, L., Grimes, C. A., & Desai, T. A. (2007). Influence of engineered titania nanotubular surfaces on bone cells. *Biomaterials, 28*(21), 3188-3197.

Prabakar, S. R., Hwang, Y.-H., Bae, E. G., Lee, D. K., & Pyo, M. (2013). Graphene oxide as a corrosion inhibitor for the aluminum current collector in lithium ion batteries. *Carbon, 52*, 128-136.

Prabhu, S., & Poulose, E. K. (2012). Silver nanoparticles: mechanism of antimicrobial action, synthesis, medical applications, and toxicity effects. *International Nano Letters, 2*(1), 32.

Qin, H., Cao, H., Zhao, Y., Zhu, C., Cheng, T., Wang, Q., . . . Jin, G. (2014). In vitro and in vivo anti-biofilm effects of silver nanoparticles immobilized on titanium. *Biomaterials, 35*(33), 9114-9125.

Qiu, D., Wang, A., & Yin, Y. (2010). Characterization and corrosion behavior of hydroxyapatite/zirconia composite coating on NiTi fabricated by electrochemical deposition. *Applied Surface Science, 257*(5), 1774-1778.

Rafieerad, A., Bushroa, A., Nasiri-Tabrizi, B., Kaboli, S., Khanahmadi, S., Amiri, A., . . . Wasa, K. (2016). Toward improved mechanical, tribological, corrosion and in-vitro bioactivity properties of mixed oxide nanotubes on Ti–6Al–7Nb implant using multi-objective PSO. *Journal of the mechanical behavior of biomedical materials*.

Rafieerad, A., Bushroa, A., Zalnezhad, E., Sarraf, M., Basirun, W., Baradaran, S., & Nasiri-Tabrizi, B. (2015). Microstructural development and corrosion behavior of self-organized TiO 2 nanotubes coated on Ti–6Al–7Nb. *Ceramics International*.

Rahmati, B., Sarhan, A. A., Zalnezhad, E., Kamiab, Z., Dabbagh, A., Choudhury, D., & Abas, W. (2016). Development of tantalum oxide (Ta-O) thin film coating on biomedical Ti-6Al-4V alloy to enhance mechanical properties and biocompatibility. *Ceramics International, 42*(1), 466-480.

Ranganatha, S., & Venkatesha, T. (2014). Fabrication and electrochemical characterization of Zn–halloysite nanotubes composite coatings. *RSC Advances, 4*(59), 31230-31238.

Rangari, V. K., Mohammad, G. M., Jeelani, S., Hundley, A., Vig, K., Singh, S. R., & Pillai, S. (2010). Synthesis of Ag/CNT hybrid nanoparticles and fabrication of their nylon-6 polymer nanocomposite fibers for antimicrobial applications. *Nanotechnology, 21*(9), 095102.

Ratner, B. D., Hoffman, A. S., Schoen, F. J., & Lemons, J. E. (2004). *Biomaterials science: an introduction to materials in medicine*: Academic press.

Redlich, M., Gorodnev, A., Feldman, Y., Kaplan-Ashiri, I., Tenne, R., Fleischer, N., . . . Feuerstein, N. (2008). Friction reduction and wear resistance of electro-co-deposited inorganic fullerene-like WS 2 coating for improved stainless steel orthodontic wires. *Journal of Materials Research, 23*(11), 2909-2915.

Reidy, B., Haase, A., Luch, A., Dawson, K. A., & Lynch, I. (2013). Mechanisms of silver nanoparticle release, transformation and toxicity: a critical review of current knowledge and recommendations for future studies and applications. *Materials, 6*(6), 2295-2350.

Reyes, Y., Durán, A., & Castro, Y. (2016). Glass-like cerium sol-gel coatings on AZ31B magnesium alloy for controlling the biodegradation of temporary implants. *Surface and Coatings Technology*.

Rigo, E., Boschi, A., Yoshimoto, M., Allegrini, S., Konig, B., & Carbonari, M. (2004). Evaluation in vitro and in vivo of biomimetic hydroxyapatite coated on titanium dental implants. *Materials Science and Engineering: C, 24*(5), 647-651.

Riva, R., Ragelle, H., des Rieux, A., Duhem, N., Jérôme, C., & Préat, V. (2011). Chitosan and chitosan derivatives in drug delivery and tissue engineering *Chitosan for biomaterials II* (pp. 19-44): Springer.

Rodríguez-González, F. Á. (2009). *Biomaterials in Orthopaedic Surgery*: ASM International.

Roy, P., Berger, S., & Schmuki, P. (2011). TiO2 nanotubes: synthesis and applications. *Angewandte Chemie International Edition, 50*(13), 2904-2939.

Ruoff, R. (2008). Graphene: Calling all chemists. *Nature Nanotechnology, 3*(1), 10-11.

Sadollah, A., & Bahreininejad, A. (2011). Optimum gradient material for a functionally graded dental implant using metaheuristic algorithms. *Journal of the mechanical behavior of biomedical materials, 4*(7), 1384-1395.

Sahu, N., Parija, B., & Panigrahi, S. (2009). Fundamental understanding and modeling of spin coating process: A review. *Indian Journal of Physics, 83*(4), 493-502.

SANTOS, J. G. d., OGASAWARA, T., & CORRÊA, R. A. (2009). Synthesis of nanocrystalline rutile-phase titania at low temperatures.

Sarraf, M., Razak, B. A., Dabbagh, A., Nasiri-Tabrizi, B., Kasim, N. H. A., & Basirun, W. J. (2016). Optimizing PVD conditions for electrochemical anodization growth of well-adherent Ta 2 O 5 nanotubes on Ti–6Al–4V alloy. *RSC Advances, 6*(82), 78999-79015.

Sarraf, M., Zalnezhad, E., Bushroa, A., Hamouda, A., Baradaran, S., Nasiri-Tabrizi, B., & Rafieerad, A. (2014). Structural and mechanical characterization of Al/Al 2 O 3 nanotube thin film on TiV alloy. *Applied Surface Science, 321*, 511-519.

Sasikumar, Y., & Rajendran, N. (2017). Effect of Acid Treatment on the Surface Modification of Ti-6Al-7Nb and Ti-5Al-2Nb-1Ta and Its Electrochemical Investigations in Simulated Body Fluid. *Journal of Bio-and Tribo-Corrosion, 3*(3), 41.

Sekine, H. (1989). Illustrated encyclopedia and dictionary of dental science: Ishiyaku Publishers, Tokyo.

Setyawati, M. I., Yuan, X., Xie, J., & Leong, D. T. (2014). The influence of lysosomal stability of silver nanomaterials on their toxicity to human cells. *Biomaterials, 35*(25), 6707-6715.

Shalabi, M., Gortemaker, A., Van't Hof, M., Jansen, J., & Creugers, N. (2006). Implant surface roughness and bone healing: a systematic review. *Journal of dental research, 85*(6), 496-500.

Shi, L., Chen, J., Teng, L., Wang, L., Zhu, G., Liu, S., . . . Ren, L. (2016). The Antibacterial Applications of Graphene and Its Derivatives. *Small, 12*(31), 4165-4184.

Shim, G., Kim, M.-G., Park, J. Y., & Oh, Y.-K. (2016). Graphene-based nanosheets for delivery of chemotherapeutics and biological drugs. *Advanced drug delivery reviews*.

Shim, J., Hagerman, E., Wu, B., & Gupta, V. (2008). Measurement of the tensile strength of cell–biomaterial interface using the laser spallation technique. *Acta biomaterialia, 4*(6), 1657-1668.

Shimizu, T., Fujibayashi, S., Yamaguchi, S., Yamamoto, K., Otsuki, B., Takemoto, M., . . . Kokubo, T. (2016). Bioactivity of sol–gel-derived TiO 2 coating on polyetheretherketone: In vitro and in vivo studies. *Acta biomaterialia, 35*, 305-317.

Shin, K. R., Ko, Y. G., & Shin, D. H. (2011). Effect of electrolyte on surface properties of pure titanium coated by plasma electrolytic oxidation. *Journal of Alloys and Compounds, 509*, S478-S481.

Shrivastava, S., Bera, T., Roy, A., Singh, G., Ramachandrarao, P., & Dash, D. (2007). Characterization of enhanced antibacterial effects of novel silver nanoparticles. *Nanotechnology, 18*(22), 225103.

Siriphannon, P., Kameshima, Y., Yasumori, A., Okada, K., & Hayashi, S. (2000). Influence of preparation conditions on the microstructure and bioactivity of α-CaSiO3 ceramics: Formation of hydroxyapatite in simulated body fluid. *Journal of biomedical materials research, 52*(1), 30-39.

Siriphannon, P., Kameshima, Y., Yasumori, A., Okada, K., & Hayashi, S. (2002). Formation of hydroxyapatite on CaSiO 3 powders in simulated body fluid. *Journal of the European Ceramic Society, 22*(4), 511-520.

Søballe, K., Hansen, E. S., B- Rasmussen, H., Jørgensen, P. H., & Bünger, C. (1992). Tissue ingrowth into titanium and hydroxyapatite- coated implants during stable and unstable mechanical conditions. *Journal of Orthopaedic Research, 10*(2), 285-299.

Songsorn, K., Sriprateep, K., & Rittidech, S. (2016). Grey–Taguchi method to optimize the percent zinc coating balances edge joints for galvanized steel sheets using metal inert gas pulse brazing process. *Advances in Mechanical Engineering, 8*(6), 1687814016651194.

Sookhakian, M., Amin, Y., & Basirun, W. (2013). Hierarchically ordered macro-mesoporous ZnS microsphere with reduced graphene oxide supporter for a highly efficient photodegradation of methylene blue. *Applied Surface Science, 283*, 668-677.

Sridhar, T., Eliaz, N., Mudali, U. K., & Raj, B. (2002). Electrophoretic deposition of hydroxyapatite coatings and corrosion aspects of metallic implants. *Corrosion reviews, 20*(4-5), 255-294.

Staiger, M. P., Pietak, A. M., Huadmai, J., & Dias, G. (2006). Magnesium and its alloys as orthopedic biomaterials: a review. *Biomaterials, 27*(9), 1728-1734.

Stergioudi, F., Vogiatzis, C., Pavlidou, E., Skolianos, S., & Michailidis, N. (2016). Corrosion resistance of porous NiTi biomedical alloy in simulated body fluids. *Smart Materials and Structures, 25*(9), 095024.

Stigter, M., Bezemer, J., De Groot, K., & Layrolle, P. (2004). Incorporation of different antibiotics into carbonated hydroxyapatite coatings on titanium implants, release and antibiotic efficacy. *Journal of Controlled Release, 99*(1), 127-137.

Strąkowska, P., Beutner, R., Gnyba, M., Zielinski, A., & Scharnweber, D. (2016). Electrochemically assisted deposition of hydroxyapatite on Ti6Al4V substrates covered by CVD diamond films—Coating characterization and first cell biological results. *Materials Science and Engineering: C, 59*, 624-635.

Subramani, K., Pandruvada, S., Puleo, D., Hartsfield, J., & Huja, S. (2016). In vitro evaluation of osteoblast responses to carbon nanotube-coated titanium surfaces. *Progress in Orthodontics, 17*(1), 23.

Sun, Z., Kohama, S.-i., Zhang, Z., Lomeda, J. R., & Tour, J. M. (2010). Soluble graphene through edge-selective functionalization. *Nano Research, 3*(2), 117-125.

Tan, A., Pingguan-Murphy, B., Ahmad, R., & Akbar, S. (2012). Review of titania nanotubes: fabrication and cellular response. *Ceramics International, 38*(6), 4421-4435.

Tan, A. W., Liau, L. L., Chua, K. H., Ahmad, R., Akbar, S. A., & Pingguan-Murphy, B. (2016). Enhanced in vitro angiogenic behaviour of human umbilical vein endothelial cells on thermally oxidized TiO2 nanofibrous surfaces. *Scientific reports, 6*.

Tanurat, P., & Sirivisoot, S. (2015a). *Osteoblast proliferation on graphene oxide eletrodeposited on anodized titanium.* Paper presented at the Biomedical Engineering International Conference (BMEiCON), 2015 8th.

Tanurat, P., & Sirivisoot, S. (2015b). *Osteoblast proliferation on graphene oxide eletrodeposited on anodized titanium.* Paper presented at the 2015 8th Biomedical Engineering International Conference (BMEiCON).

Teng, X., Ma, C., Ge, C., Yan, M., Yang, J., Zhang, Y., . . . Bi, H. (2014). Green synthesis of nitrogen-doped carbon dots from konjac flour with “off–on” fluorescence by Fe 3+ and L-lysine for bioimaging. *Journal of Materials Chemistry B, 2*(29), 4631-4639.

Textor, M., Sittig, C., Frauchiger, V., Tosatti, S., & Brunette, D. M. (2001). Properties and biological significance of natural oxide films on titanium and its alloys *Titanium in medicine* (pp. 171-230): Springer.

Tian, Q., & Liu, H. (2015). Electrophoretic deposition and characterization of nanocomposites and nanoparticles on magnesium substrates. *Nanotechnology, 26*(17), 175102.

Tomsia, A. P., Saiz, E., Song, J., & Bertozzi, C. R. (2005). Biomimetic bonelike composites and novel bioactive glass coatings. *Advanced Engineering Materials, 7*(11), 999-1004.

Tran, P. A., Fox, K., & Tran, N. (2017). Novel hierarchical tantalum oxide-PDMS hybrid coating for medical implants: One pot synthesis, characterization and modulation of fibroblast proliferation. *Journal of colloid and interface science, 485*, 106-115.

Tripi, T. R., Bonaccorso, A., & Condorelli, G. G. (2003). Fabrication of hard coatings on NiTi instruments. *Journal of endodontics, 29*(2), 132-134.

Tripi, T. R., Bonaccorso, A., Rapisarda, E., Tripi, V., Condorelli, G. G., Marino, R., & Fragalà, I. (2002). Depositions of nitrogen on NiTi instruments. *Journal of endodontics, 28*(7), 497-500.

Tryba, B., Morawski, A., & Inagaki, M. (2003). A new route for preparation of TiO 2-mounted activated carbon. *Applied Catalysis B: Environmental, 46*(1), 203-208.

Tyona, M. (2013). A comprehensive study of spin coating as a thin film deposition technique and spin coating equipment. *Advances in materials Research, 2*(4), 181-193.

Uchida, M., Kim, H. M., Kokubo, T., Fujibayashi, S., & Nakamura, T. (2003). Structural dependence of apatite formation on titania gels in a simulated body fluid. *Journal of Biomedical Materials Research Part A, 64*(1), 164-170.

Uhlig, H. H. (1948). *The corrosion handbook*: J. Wiley.

Uhm, S. H., Song, D. H., Kwon, J. S., Lee, S. B., Han, J. G., & Kim, K. N. (2014). Tailoring of antibacterial Ag nanostructures on TiO2 nanotube layers by magnetron sputtering. *Journal of Biomedical Materials Research Part B: Applied Biomaterials, 102*(3), 592-603.

Upadhyay, R., Naskar, S., Bhaskar, N., Bose, S., & Basu, B. (2016). Modulation of Protein Adsorption and Cell Proliferation on Polyethylene Immobilized Graphene Oxide Reinforced HDPE Bionanocomposites. *ACS applied materials & interfaces, 8*(19), 11954-11968.

Usinskas, P., Stankeviciute, Z., Beganskiene, A., & Kareiva, A. (2016). Sol-gel derived porous and hydrophilic calcium hydroxyapatite coating on modified titanium substrate. *Surface and Coatings Technology*.

Vasconcelos, D. C. L., Nunes, E. H. M., Gasparon, M., & Vasconcelos, W. L. (2011). Infrared spectroscopy of titania sol-gel coatings on 316L stainless steel. *Materials sciences and applications, 2*(10), 1375.

Vasilescu, C., Drob, P., Vasilescu, E., Demetrescu, I., Ionita, D., Prodana, M., & Drob, S. (2011). Characterisation and corrosion resistance of the electrodeposited hydroxyapatite and bovine serum albumin/hydroxyapatite films on Ti–6Al–4V–1Zr alloy surface. *Corrosion Science, 53*(3), 992-999.

Vecitis, C. D., Zodrow, K. R., Kang, S., & Elimelech, M. (2010). Electronic-structure-dependent bacterial cytotoxicity of single-walled carbon nanotubes. *ACS nano, 4*(9), 5471-5479.

Verdier, T., Coutand, M., Bertron, A., & Roques, C. (2014). Antibacterial activity of TiO2 photocatalyst alone or in coatings on E. coli: the influence of methodological aspects. *Coatings, 4*(3), 670-686.

Verma, R., Kant, S., & Suri, N. M. (2016). Adhesion strength optimization of slurry sprayed mullite-based coating using Taguchi method. *Proceedings of the Institution of Mechanical Engineers, Part E: Journal of Process Mechanical Engineering, 230*(2), 87-96.

Veronesi, F., Giavaresi, G., Fini, M., Longo, G., Ioannidu, C. A., d'Abusco, A. S., . . . Palattella, A. (2017). Osseointegration is improved by coating titanium implants with a nanostructured thin film with titanium carbide and titanium oxides clustered around graphitic carbon. *Materials Science and Engineering: C, 70*, 264-271.

Vijayaraghavan, T., & Bensalem, A. (1994). Electrodeposition of apatite coating on pure titanium and titanium alloys. *Journal of materials science letters, 13*(24), 1782-1785.

Wang, L.-N., Jin, M., Zheng, Y., Guan, Y., Lu, X., & Luo, J.-L. (2014). Nanotubular surface modification of metallic implants via electrochemical anodization technique. *International journal of nanomedicine, 9*, 4421.

Wang, S.-H., Yang, C.-W., & Lee, T.-M. (2016). Evaluation of Microstructural Features and in Vitro Biocompatibility of Hydrothermally Coated Fluorohydroxyapatite on AZ80 Mg Alloy. *Industrial & Engineering Chemistry Research, 55*(18), 5207-5215.

Wang, X., Zhi, L., & Müllen, K. (2008). Transparent, conductive graphene electrodes for dye-sensitized solar cells. *Nano letters, 8*(1), 323-327.

Wang, Z., Dong, Y., Li, H., Zhao, Z., Wu, H. B., Hao, C., . . . Lou, X. W. D. (2014). Enhancing lithium–sulphur battery performance by strongly binding the discharge products on amino-functionalized reduced graphene oxide. *Nature communications, 5*.

Watson, V. G. (2014). *Decoration of Graphene Oxide with Silver Nanoparticles and Controlling the Silver Nanoparticle Loading on Graphene Oxide.* University of Dayton.

Wei, W., Berger, S., Hauser, C., Meyer, K., Yang, M., & Schmuki, P. (2010). Transition of TiO 2 nanotubes to nanopores for electrolytes with very low water contents. *Electrochemistry Communications, 12*(9), 1184-1186.

Weng, H.-A., Wu, C.-C., Chen, C.-C., Ho, C.-C., & Ding, S.-J. (2010). Preparation and properties of gold nanoparticle-electrodeposited titanium substrates with Arg-Gly-Asp-Cys peptides. *Journal of Materials Science: Materials in Medicine, 21*(5), 1511-1519.

Williams, B. E., & Stiglich Jr, J. J. (1992). Hafnium-and Titanium-Coated Tungsten Powders for Kinetic Energy Penetrators, Phase 1, SBIR: DTIC Document.

Williams, D. (1987). Tissue-biomaterial interactions. *Journal of Materials Science, 22*(10), 3421-3445.

Williams, R. L., Brown, S. A., & Merritt, K. (1988). Electrochemical studies on the influence of proteins on the corrosion of implant alloys. *Biomaterials, 9*(2), 181-186.

Winters, G. L., & Nutt, M. J. (2003). *Stainless steels for medical and surgical applications* (Vol. 1438): ASTM International.

Wolinsky, J. B., Colson, Y. L., & Grinstaff, M. W. (2012). Local drug delivery strategies for cancer treatment: gels, nanoparticles, polymeric films, rods, and wafers. *Journal of Controlled Release, 159*(1), 14-26.

Wong, J. Y., & Bronzino, J. D. (2007). CRC press: Taylor & Francis group, Boca Raton, London, New York.

Wong, R., & Rabie, A. (2008). Effect of quercetin on preosteoblasts and bone defects. *The open orthopaedics journal, 2*(1).

Wong, R. W., & Rabie, A. B. M. (2008). Effect of quercetin on bone formation. *Journal of Orthopaedic Research, 26*(8), 1061-1066.

Wu, P., & Grainger, D. W. (2006). Drug/device combinations for local drug therapies and infection prophylaxis. *Biomaterials, 27*(11), 2450-2467.

Xie, J., Zhang, Y., Han, Y., & Li, C. (2016). High-Capacity Molecular Scale Conversion Anode Enabled by Hybridizing Cluster-Type Framework of High Loading with Amino-Functionalized Graphene. *ACS nano, 10*(5), 5304-5313.

Xu, Y., & Shi, G. (2011). Assembly of chemically modified graphene: methods and applications. *Journal of Materials Chemistry, 21*(10), 3311-3323.

Yaghoubi, H., Taghavinia, N., Alamdari, E. K., & Volinsky, A. A. (2010). Nanomechanical properties of TiO2 granular thin films. *ACS applied materials & interfaces, 2*(9), 2629-2636.

Yallappa, S., Manjanna, J., Dhananjaya, B., Vishwanatha, U., Ravishankar, B., Gururaj, H., . . . Hungund, B. (2016). Phytochemically Functionalized Cu and Ag Nanoparticles Embedded in MWCNTs for Enhanced Antimicrobial and Anticancer Properties. *Nano-Micro Letters, 8*(2), 120-130.

Yan, Y., Zhang, X., Mao, H., Huang, Y., Ding, Q., & Pang, X. (2015). Hydroxyapatite/gelatin functionalized graphene oxide composite coatings deposited on TiO 2 nanotube by electrochemical deposition for biomedical applications. *Applied Surface Science, 329*, 76-82.

Yang, C.-C., Lin, C.-C., & Yen, S.-K. (2011). Electrochemical deposition of vancomycin/chitosan composite on Ti alloy. *Journal of The Electrochemical Society, 158*(12), E152-E158.

Yang, H., Mei, S., Zhao, L., & Zhang, Y. (2016). Effects of Ultraviolet Irradiation on the Antibacterial Activity of TiO2 Nanotubes. *Nanoscience and Nanotechnology Letters, 8*(6), 498-504.

Yang, J., Yin, H., Jia, J., & Wei, Y. (2011). Facile synthesis of high-concentration, stable aqueous dispersions of uniform silver nanoparticles using aniline as a reductant. *Langmuir, 27*(8), 5047-5053.

Yao, C., Slamovich, E. B., & Webster, T. J. (2008). Enhanced osteoblast functions on anodized titanium with nanotube- like structures. *Journal of Biomedical Materials Research Part A, 85*(1), 157-166.

Yelten, A., Yilmaz, S., & Oktar, F. N. (2012). Sol–gel derived alumina–hydroxyapatite–tricalcium phosphate porous composite powders. *Ceramics International, 38*(4), 2659-2665.

Yu, D., Wang, C., Cheng, X., & Zhang, F. (2008). Optimization of hybrid PVD process of TiAlN coatings by Taguchi method. *Applied Surface Science, 255*(5), 1865-1869.

Zadorozhnyy, V. Y., Shi, X., Gorshenkov, M., Kozak, D., Wada, T., Louzguine-Luzgin, D., . . . Kato, H. (2016). Ti–Ag–Pd alloy with good mechanical properties and high potential for biological applications. *Scientific reports, 6*.

Zahedi, G., Azizi, S., Bahadori, A., Elkamel, A., & Alwi, S. R. W. (2013). Electricity demand estimation using an adaptive neuro-fuzzy network: a case study from the Ontario province–Canada. *Energy, 49*, 323-328.

Zalnezhad, E., Maleki, E., Banihashemian, S., Park, J., Kim, Y., Sarraf, M., . . . Ramesh, S. (2016). Wettability, structural and optical properties investigation of TiO 2 nanotubular arrays. *Materials Research Bulletin, 78*, 179-185.

Zalnezhad, E., Sarhan, A. A., & Hamdi, M. (2013). A fuzzy logic based model to predict surface hardness of thin film TiN coating on aerospace AL7075-T6 alloy. *The International Journal of Advanced Manufacturing Technology, 68*(1-4), 415-423.

Zanin, H., Saito, E., Marciano, F. R., Ceragioli, H. J., Granato, A. E. C., Porcionatto, M., & Lobo, A. O. (2013). Fast preparation of nano-hydroxyapatite/superhydrophilic reduced graphene oxide composites for bioactive applications. *Journal of Materials Chemistry B, 1*(38), 4947-4955.

Zardiackas, L. D., Kraay, M. J., & Freese, H. L. (2006). *Titanium, niobium, zirconium, and tantalum for medical and surgical applications*: ASTM International.

Zardini, H. Z., Amiri, A., Shanbedi, M., Maghrebi, M., & Baniadam, M. (2012). Enhanced antibacterial activity of amino acids-functionalized multi walled carbon nanotubes by a simple method. *Colloids and Surfaces B: Biointerfaces, 92*, 196-202.

Zhang, L., & Webster, T. J. (2009). Nanotechnology and nanomaterials: promises for improved tissue regeneration. *Nano today, 4*(1), 66-80.

Zhang, W.-Y., Li, G.-Z., Li, Y.-N., Yu, Z.-T., & Xi, Z.-P. (2007). Fabrication of TiO2 nanotube arrays on biologic titanium alloy and properties. *Transactions of Nonferrous Metals Society of China, 17*(s1B), s692-s695.

Zhang, Y., Ali, S. F., Dervishi, E., Xu, Y., Li, Z., Casciano, D., & Biris, A. S. (2010). Cytotoxicity effects of graphene and single-wall carbon nanotubes in neural phaeochromocytoma-derived PC12 cells. *ACS nano, 4*(6), 3181-3186.

Zhang, Y., Bataillon- Linez, P., Huang, P., Zhao, Y., Han, Y., Traisnel, M., . . . Hildebrand, H. (2004). Surface analyses of micro- arc oxidized and hydrothermally treated titanium and effect on osteoblast behavior. *Journal of Biomedical Materials Research Part A, 68*(2), 383-391.

Zhao, B., Wang, H., Qiao, N., Wang, C., & Hu, M. (2017). Corrosion resistance characteristics of a Ti-6Al-4V alloy scaffold that is fabricated by electron beam melting and selective laser melting for implantation in vivo. *Materials Science and Engineering: C, 70*, 832-841.

Zhao, L., Chu, P. K., Zhang, Y., & Wu, Z. (2009). Antibacterial coatings on titanium implants. *Journal of Biomedical Materials Research Part B: Applied Biomaterials, 91*(1), 470-480.

Zhao, Y., Eley, C., Hu, J., Foord, J. S., Ye, L., He, H., & Tsang, S. C. E. (2012). Shape-Dependent Acidity and Photocatalytic Activity of Nb2O5 Nanocrystals with an Active TT (001) Surface. *Angewandte Chemie International Edition, 51*(16), 3846-3849.

Zhu, Y., Murali, S., Cai, W., Li, X., Suk, J. W., Potts, J. R., & Ruoff, R. S. (2010). Graphene and graphene oxide: synthesis, properties, and applications. *Advanced materials, 22*(35), 3906-3924.

Zielinska, E., Tukaj, C., Radomski, M. W., & Inkielewicz-Stepniak, I. (2016). Molecular mechanism of silver nanoparticles-induced human osteoblast cell death: protective effect of inducible nitric oxide synthase inhibitor. *PloS one, 11*(10), e0164137.

Zilberman, M., & Elsner, J. J. (2008). Antibiotic-eluting medical devices for various applications. *Journal of Controlled Release, 130*(3), 202-215.

Zimmerli, W., Trampuz, A., & Ochsner, P. E. (2004). Prosthetic-joint infections. *New England Journal of Medicine, 351*(16), 1645-1654.

Zwilling, V., Darque- Ceretti, E., Boutry- Forveille, A., David, D., Perrin, M.-Y., & Aucouturier, M. (1999). Structure and physicochemistry of anodic oxide films on titanium and TA6V alloy. *Surface and Interface Analysis, 27*(7), 629-637.

LIST OF PUBLICATIONS AND PAPERS PRESENTED

ISI Journals

1. Rafieerad, A. R., et al. "Toward improved mechanical, tribological, corrosion and in-vitro bioactivity properties of mixed oxide nanotubes on Ti–6Al–7Nb implant using multi-objective PSO." ***Journal of the mechanical behavior of biomedical materials*** 69 (2017): 1-18.

2. Rafieerad, A. R., et al. "Vertically oriented ZrO 2-TiO 2-Nb 2 O 5-Al 2 O 3 mixed nanopatterned bioceramics on Ti6Al7Nb implant assessed by laser spallation technique." ***Journal of Alloys and Compounds*** (2017).

3. Amiri, A., Shanbedi, M., **Rafieerad, A. R.,** Rashidi, M. M., Zaharinie, T., Zubir, M. N. M., ... & Chew, B. T. (2017). Functionalization and exfoliation of graphite into mono layer graphene for improved heat dissipation. ***Journal of the Taiwan Institute of Chemical Engineers***, 71, 480-493.

4. Rafieerad, AR, et al. "GEP-based method to formulate adhesion strength and hardness of Nb PVD coated on Ti–6Al–7Nb aimed at developing mixed oxide nanotubular arrays." ***Journal of the mechanical behavior of biomedical materials*** 61 (2016): 182-196.

5. Rafieerad, AR, et al. "Mechanical properties, corrosion behavior and in-vitro bioactivity of nanostructured Pd/PdO coating on Ti–6Al–7Nb implant." ***Materials & Design*** 103 (2016): 10-24.

6. Rafieerad, AR, et al. "Optimized fabrication and characterization of TiO 2–Nb 2 O 5–Al 2 O 3 mixed oxide nanotube arrays on Ti–6Al–7Nb." ***RSC Advances*** 6.13 (2016): 10527-10540.

7. Rafieerad, AR, et al. "Silver/silver oxide nanorod arrays from physical vapor deposition and subsequent anodization processes." ***Surface and Coatings Technology*** 302 (2016): 275-283.

8. Rafieerad, A. R, et al. "Self-organized TiO 2 nanotube layer on Ti–6Al–7Nb for biomedical application." ***Surface and Coatings Technology*** 265 (2015): 24-31.

9. Rafieerad, A. R, et al. "Microstructural development and corrosion behavior of self-organized TiO 2 nanotubes coated on Ti–6Al–7Nb." ***Ceramics International 41***.9 (2015): 10844-10855.

10. Rafieerad, A. R., et al. "Surface characterization and corrosion behavior of calcium phosphate-base composite layer on titanium and its alloys via plasma electrolytic oxidation: A review paper." ***Materials Science and Engineering: C*** 57 (2015): 397-413.

Conference Paper

11. Rafieerad, AR, et al. "Graphene Oxide Modified Anodic Ternary Nanobioceramics on Ti6Al7Nb Alloy for Orthopedic and Dental Applications***." Procedia Engineering*** 184 (2017): 409-417. ***International conference of AMPT 2016, Malayasia.***